ISSN 1300-3615 / e-ISSN 2667-7725 - https://dergipark.org.tr/tr/pub/isibted

ISI Bilimi ve Tekniği Dergisi

Journal of Thermal Science and Technology

TIBTD
TÜRK ISI BİLİMİ VE TEKNİĞİ DERNEĞİ
TURKISH SOCIETY FOR THERMAL SCIENCE AND TECHNOLOGY

ISI Bilimi ve Tekniği Dergisi

Journal of Thermal Science and Technology

(2024) Vol. 44, No. 2

https://dergipark.org.tr/tr/pub/isibted

Türk Isı Bilimi ve Tekniği Derneği tarafından yılda iki kez Nisan ve Ekim aylarında yayınlanır.

A publication of the Turkish Society for Thermal Sciences and Technology, published twice a year, in April and October.

TIBTD Adına Yayın Sahibi Sorumlu Yayımcı / *Publisher:*
Prof. Dr. Nuri YÜCEL, Gazi Üniversitesi

Sorumlu Yazı İşleri Müdürü - Editör / *Editor-in-Chief:*
Prof. Dr. M. Zeki YILMAZOĞLU, Gazi Üniversitesi
zekiyilmazoglu@gazi.edu.tr

Yayın Türü: Yaygın, süreli

Türk Isı Bilimi ve Tekniği Derneği (TIBTD)

Dernek ve bu dergi, Türkiye'de ısı bilimi ve tekniğini geliştirmek amacıyla 1976 yılında Prof. Dr. Yalçın A. GÖĞÜŞ tarafından kurulmuştur.

Turkish Society of Thermal Sciences and Technology

The association and the journal was founded by Prof. Dr. Yalçın A. GÖĞÜŞ in 1976 to improve thermal sciences and technology in Turkey.

Adresi / *Address:*
TIBTD, Mühendislik Fakültesi, Zemin Kat No.22,
Gazi Üniversitesi, 06570 ANKARA
www.tibtd.org.tr
ibtd@tibtd.org.tr

Üyelik aidatları için:
İş Bankası Maltepe Şubesi
Hesap No: 42120867567
IBAN: TR08 0006 4000 0014 2120 8675 67

ISSN: 1300-3615 / **e-ISSN:** 2667-7725

İçindekiler / *Contents*

Amaç / *Objective*
Isı bilimi ve tekniğinin geliştirilmesini teşvik etmek, ısı bilimi ve tekniği alanında özgün, teorik, sayısal ve deneysel çalışmaların yayınlanmasına olanak sağlamaktır.
To contribute to the improvement of thermal sciences and technology and publication of original, theoretical, numerical, and experimental studies in thermal sciences and technology.

İçerik / *Content*
Isı bilimi ve tekniği alanındaki özgün ve derleme makaleler.
Original and review articles in thermal sciences and technology.

Değerlendirme / *Evaluation*
Dergi hakemli bir dergi olup, her bir makale konusunda uzman en az iki hakem tarafından değerlendirilir.
Each article published in this journal is evaluated by at least two referees.

Science Citation Index Expanded (SCIE), Engineering Index (EI), EBSCO ve Mühendislik ve Temel Bilimler Veri Tabanı (TÜBİTAK-ULAKBİM) tarafından taranmaktadır.

Indexed by Science Citation Index Expanded (SCIE), Engineering Index (EI), EBSCO and Engineering and Natural Sciences Data Base (TÜBİTAK-ULAKBİM).

Journal Homepage: https://dergipark.org.tr/tr/pub/isibted

Isı Bilimi ve Tekniği Dergisi

Archive: https://tibtd.org.tr/dergi

The Effects of Nanofluids on The Energy Efficiency: Experimental Performance Investigation of Cooling Nanofluids in A Mini-Channel Shell and Tube Heat Exchanger

Murat ÜNVERDİ [1, *], Hasan KÜÇÜK [2], Mehmet Senan YILMAZ [3]

[1] *Aydın Adnan Menderes Üniversitesi, Aydın Meslek Yüksekokulu, Efeler, 09010, Aydın, Türkiye*
[2] *Sakarya Üniversitesi, Mühendislik Fakültesi, Makine Mühendisliği Bölümü, Serdivan, 54050, Sakarya, Türkiye*
[3] *Bolu Abant İzzet Baysal Üniversitesi, Gerede Meslek Yüksekokulu, Gerede, 14900, Bolu, Türkiye*

A R T I C L E I N F O

2024, vol. 44, no.2, pp. 259-279

doi: 10.47480/isibted.1563032

Research Article
Received: 09 April 2023
Accepted: 28 June 2024

* *Corresponding Author*
e-mail: munverdi@adu.edu.tr

Keywords:
Energy efficiency
Nanofluids
Shell and tube heat exchanger
Heat transfer
Pressure drop

ORCID Numbers in author order:
0000-0002-7045-509X
0000-0002-8825-7315
0000-0001-5644-6675

A B S T R A C T

Energy efficiency in thermal systems used in industrial engineering applications is an important topic that affects operating costs. The thermophysical properties of working fluids and geometric, thermal, and hydrodynamic design variables affect the energy efficiency of thermal systems. Nanofluids are recommended instead of conventional working fluids in order to enhance convective heat transfer in thermal systems. However, researchers have not adequately discussed the effects of nanofluids on overall energy efficiency compared to conventional working fluids. This study experimentally investigated the effects of Al_2O_3-water nanofluids cooling on the tube side on energy efficiency in a lab-made shell and tube heat exchanger manufactured with mini-channel tubes. We evaluated the effects of nanofluids in three volumetric concentrations (0.2%, 0.4% and 0.8%) on energy efficiency compared to conventional working fluid water based on two metrics (Performance Evaluation Criterion-PEC and Efficiency Evaluation Criterion-EEC). In addition, we calculated PECs and EECs to compare the effects of conventional working fluids and nanofluids on energy efficiency with experimental data in the literature, in which nanofluids were used in plate heat exchangers and shell and tube heat exchangers. We compared the energy efficiency results based on the experimental data from the literature with our experimental energy efficiency results. The average PECs of Al_2O_3-water nanofluids with 0.2%, 0.4% and 0.8% volumetric concentrations in our study were -38%, -27.1% and -38.1% lower than conventional working fluid water, respectively, while the average EECs of these nanofluids were 0.62, 0.73 and 0.61, respectively. The PEC and EEC results showed that conventional working fluids were superior to nanofluids in terms of energy efficiency. It has been concluded that nanofluids are not suitable for thermal systems of industrial plants in terms of energy costs. However, they can be used in extraordinary thermal systems where low energy efficiency and other disadvantages are negligible and high heat flux is required, by taking into account all precautions and solutions.

Nanoakışkanların Enerji Verimliliğine Etkileri: Mini Kanallı Gövde Borulu Isı Değiştiricide Soğuyan Nanoakışkanların Deneysel Performans İncelemesi

M A K A L E B İ L G İ S İ

Anahtar Kelimeler:
Enerji verimliliği
Nanoakışkanlar
Gövde borulu ısı değiştirici
Isı geçişi
Basınç düşümü

Ö Z E T

Endüstriyel mühendislik uygulamalarında kullanılan ısıl sistemlerde enerji verimliliği, işletme maliyetlerini etkileyen önemli konu başlıklarındandır. Isıl sistemlerin enerji verimliliğini; seçilen aracı akışkanların termo-fiziksel özelikleri ile sistemin geometrik, ısıl ve hidrodinamik tasarım değişkenleri etkilemektedir. Nanoakışkanlar, ısıl sistemlerde taşınımla ısı geçişinin iyileştirilmesi amacıyla konvansiyonel saf taşıyıcı sıvıların (KSTS) yerine önerilmektedir. Ancak, nanoakışkanların genel enerji verimliliğine etkileri, KSTSlarla karşılaştırmalı olarak yeterince tartışılmamıştır. Bu çalışmada, mini kanallı borularla üretilen prototip gövde borulu bir ısı değiştiricide, boru tarafında soğuyan Al_2O_3-su nanoakışkanlarının enerji verimliliğine etkileri deneysel incelenmiştir. Üç farklı hacimsel oranda (%0.2, %0.4 ve %0.8) hazırlanan nanoakışkanların, KSTS suya göre enerji verimliliğine etkileri iki farklı ölçütle (Performans Değerlendirme Ölçütü-PDÖ ve Verimlilik Değerlendirme Ölçütü-VDÖ) değerlendirilmiştir. Ayrıca sunulan çalışmaya benzer şekilde; literatürde yayımlanan, levhalı ısı değiştiricilerde (LID) ve gövde borulu ısı değiştiricilerde (GBID) nanoakışkanların kullanıldığı deneysel çalışmaların verileriyle, PDÖ ve VDÖ hesaplanarak, KSTSların ve nanoakışkanların enerji verimliliğine etkileri karşılaştırılmıştır. Literatürdeki deneysel verilerle hesaplanan enerji verimliliği sonuçları, sunulan çalışmanın deneysel enerji verimliliği sonuçlarıyla karşılaştırılarak tartışılmıştır. Sunulan çalışmadaki %0.2, %0.4 ve %0.8 hacimsel oranlı Al_2O_3-su nanoakışkanlarının PDÖlerinin ortalaması KSTS suya göre sırasıyla -%38, -%27.1 ve -%38.1 daha düşük iken, VDÖlerinin ortalaması da sırasıyla 0.62, 0.73 ve 0.61'dir. PDÖ ve VDÖ sonuçları, KSTSların enerji verimliliği bakımından, nanoakışkanlara göre daha üstün olduğunu göstermiştir. Sonuç olarak; nanoakışkanların enerji maliyetleri bakımından, endüstriyel tesislerin ısıl sistemlerinde KSTSların yerine kullanılmasının uygun olmadığı elde edilmiştir. Ancak nanoakışanlar, düşük enerji verimliliği ve diğer dezavantajlarının önemsiz olduğu, yüksek ısı akısı (taşınım katsayısı) istenen, özel amaçlı ısıl sistemlerde, gerekli tüm önlemler alınarak ve çözümler uygulanarak kullanılabilir.

SEMBOLLER

c_p	özgül ısı (J/kgK)
k	ısı iletim katsayısı (W/mK)
m	kütle (kg)
Pe	Peclet sayısı, (=RePr)
Pr	Prandtl sayısı, (=$\mu c_p/k$)
Q	ısıl güç, ısı geçişi (W)
Re	Reynolds sayısı (=$\rho uD/\mu$)
T	sıcaklık (^oC, K)
W_{pg}	pompalama gücü (W)
ΔT	sıcaklık farkı (^oC, K)
$\dot{\forall}$	hacimsel debi (l/sa., l/dk.)
Δp	basınç düşümü (Pa)

Yunan Harfleri

μ	dinamik viskozite (kg/ms)
ρ	yoğunluk (kg/m^3)
φ	hacimsel oran (-, %)

Kısaltmalar

GBID	gövde borulu ısı değiştirici
KSTS	konvansiyonel saf taşıyıcı sıvı
LID	levhalı ısı değiştirici
MK-GBID	mini kanallı gövde borulu ısı değiştirici
PDÖ	Performans Değerlendirme Ölçütü, (Q/W_{pg})
TS	taşıyıcı sıvı
VDÖ	Verimlilik Değerlendirme Ölçütü, $(Q_{na}/Q_{ts})/(W_{pg,na}/W_{pg,ts})$

Alt İndisler

b	boru
ts	taşıyıcı sıvı
g	gövde
grş	giriş
na	nanoakışkan
çkş	çıkış
np	nanopartikül

GİRİŞ

Yüksek performanslı ısıtma ve soğutma sistemleri, farklı endüstriyel alanlardaki ileri teknoloji uygulamalarının en önemli ihtiyaçlarındandır. Yüksek performanslı ısıtmada ve soğutmada, en önemli sınırlamalardan biri de konvansiyonel ısı geçişi sıvılarının (aracı akışkanların) ısı iletim katsayılarının doğaları gereği düşük değerli olmasıdır. Enerji verimli ısı geçişi sıvılarının geliştirilmesinde asıl amaçlardan biri de ısı iletim katsayısının yükseltilmesidir. Nanometre boyutlarındaki metalik veya metalik olmayan parçacıklar, gelişmiş üretim yöntemleriyle üretebilmektedir. Nanomalzemeler; alışılagelmiş malzemelerden farklı olarak, kendine özgü; mekanik, optik, elektriksel, manyetik ve termo-fiziksel özeliklere sahiptir (Chand, 2017).

Nanoakışkanlar (nanosıvılar: nanopartiküllü sıvı süspansiyonları); konvansiyonel saf ısı geçişi sıvılarından (su, yağ ve etilen glikol gibi) veya konvansiyonel parçacıklı-sıvı süspansiyonlarından daha üstün ısıl özelikler gösteren, nanoteknoloji tabanlı ısı geçişi sıvılarını tanımlamak amacıyla kullanılan bir kavramdır. Bir başka ifadeyle nanoakışkanlar; su, yağ ve etilen glikol gibi konvansiyonel saf ısı geçişi sıvılarına, çökelmeden askıda kalabilecek (ortalama boyutları 100 nm'nin altında) nanopartiküllerin eklenmesi fikriyle ortaya çıkmıştır (Choi, 2009; Minkowycz vd., 2016). Çok az miktardaki nanopartiküller, mümkün olduğunca homojen bir şekilde konvansiyonel ısı geçişi sıvılarında dağıtılıp/karıştırılıp ve kararlı bir şekilde süspanse edildiğinde, ısı geçişi sıvılarının bazı ısıl özeliklerinde önemli iyileşmeler sağlanabilmektedir. Nanoakışkan teknolojisi, 90'lı yılların ortasından itibaren bilinip uygulansa da nanoakışkanlar; nanobilim, nanoteknoloji ve ısı mühendisliğinin buluştuğu, disiplinler arası bir alandır ve son on yılda nanoakışkanlarla ilgili çalışmalar hızlanmıştır (Bianco vd., 2011 Gonçalves vd., 2021). Nanoakışkan tasarımlarında amaç; nanopartiküllerin mümkün olan en düşük konsantrasyonlarda (tercihen hacimce %1'den küçük), konvansiyonel ısı geçişi sıvılarına karıştırılarak, ısıl özelikleri olabildiğince iyileştirilmiş aracı akışkanlar (homojen dağılımlı ve kararlı süspansiyonlar) elde etmektir (Choi, 2009).

Konvansiyonel saf ısı geçişi sıvılarının bazı ısıl özelikleri, nanopartiküller eklenerek iyileştirilse de uygulamada nanoakışkanların bazı kritik dezavantajlarıyla da karşılaşılmaktadır. Bunlar arasında; nanopartiküllerin kümelenmesi (ya da topaklaşması) ve çökelmesi, aşındırıcılık, kısa süreli kararlılık (stabilite), daha yüksek viskozite (artan sürtünme basınç kaybı/pompalama gücü gereksinimi), daha düşük özgül ısı gibi sınırlamalar ve olumsuzluklar sayılabilir (Das vd., 2006, 2007; Ghadimi vd., 2011; Sekhar ve Sharma, 2015). Isıtma, soğutma, akıllı akışkanlar, otomotiv, elektronik, biyomedikal, enerji, mekanik, ısıl sistemler ve benzerleri, nanoakışkanların potansiyel uygulama alanları arasındadır (Minkowycz vd., 2016). Çalışmanın devamında, daha kısa olması nedeniyle konvansiyonel saf ısı geçişi sıvılarından, konvansiyonel saf taşıyıcı sıvı (KSTS) olarak bahsedilecektir.

Endüstriyel ısıl sistemlerde, en yaygın kullanılan pasif ısı geçişi iyileştirme yöntemleri; (1) ısı değiştirici cihazlarda ısı geçişi yüzey alanlarını arttırmak ve/veya (2) taşıyıcı sıvılara eklenen katı partikülleri mümkün olabildiğince homojen dağıtmaktır (Webb ve Kim, 2005). Bu nedenle, her iki pasif ısı geçişi iyileştirme yönteminin, ısıl sistemlerde birlikte kullanılmasıyla, ısı geçişinin daha da iyileştirilebileceği düşüncesi, teorik olarak mantıklı bir yaklaşımdır.

Endüstriyel ısıl süreçlerde çok yaygın kullanılan, gövde borulu ısı değiştiricilerde (GBID) (Gupta vd., 2022) ve levhalı ısı değiştiricilerde (LID) (Zhang vd., 2019), yukarıda bahsedilen iki pasif ısı geçişi iyileştirme yönteminin uygulandığı deneysel araştırmalar oldukça fazladır. Bu çalışmalarda, GBIDlerde (makro borulu) ve LIDlerde, ya sadece farklı konsantrasyonlarda hazırlanan nanoakışkanlar doğrudan kullanılmıştır ya da LIDlerde yukarıda bahsedilen iki iyileştirme yöntemi, birleşik etkinin incelenmesi amacıyla bir arada kullanılmıştır. Ancak, LIDlerde olduğu gibi genişletilmiş yüzeyleri bulunmayan ve makro borularla üretilen GBIDlerde, farklı pasif iyileştirme yöntemleri ve nanoakışkanların birleştirilmiş etkileri deneysel araştırmalarla yeterince incelenmemiştir. Literatürde, her iki ısı değiştiricide, farklı nanopartiküllerle hazırlanan nanoakışkanlar kullanıldığında, genellikle KSTSlara göre ısı taşınım katsayısındaki iyileşmeden ve sürtünme faktörünün (basınç düşümünün) değişiminden bahsedilmektedir. Ayrıca,

bahsi geçen iki pasif ısı geçişi iyileştirme yönteminin, ısıl sistemlerin ısıl ve hidrodinamik performansına yani faydalı ısıl güç ve pompalama gücü arasındaki dengeye etkilerinin incelendiği deneysel çalışmalar oldukça kısıtlıdır.

Bu nedenlerle, endüstriyel ısıl sistemlerde yaygın kullanılan GBIDlerin, ısı geçişi yüzeyi alan yoğunluklarının, makro borular yerine mini kanallarla artırılmasıyla yetinilmeyip, KSTSların termo-fiziksel özelikleri, KSTSlara eklenen nanopartiküllerle (nanoakışkanlarla) değiştirilerek, ısı taşınım katsayılarındaki iyileşme daha da artırılabilir. Ayrıca mini kanallarla, GBIDlerde sağlanan kompaktlık (yüzey alanı/hacim oranı) artışının yanında, kullanılacak metal malzeme kütlesi ve aracı akışkan miktarları da azaltılabilecektir. Bu yönüyle mini kanallar, çevreye zararlı ve/veya pahalı aracı akışkanların kullanıldığı uygulamalarda, ilk yatırım, işletme ve çevresel maliyetleri de azaltacaktır. Dolayısıyla, mini kanallarla üretilen GBIDlerde, termo-fiziksel özelikleri değiştirilmiş ancak yüksek maliyetli aracı akışkanlar olan nanoakışkanların kullanılmasıyla, minimum maliyetlerle ısıl performans artışı sağlanarak, enerji verimliliğinin artırılması beklenmektedir. Böylece yapılacak enerji tasarrufu; hem işletme maliyetleri içerisinde her geçen gün payı artan enerji maliyetlerini, hem de zararlı emisyonların azaltılmasıyla çevresel maliyetleri düşürecektir. Ancak bir arada kullanılan iki pasif yöntemin etkisiyle; ısı geçişinde sağlanan iyileşmeyle birlikte hem hidrolik çaptaki küçülme hem de nanoakışkanların KSTSlara göre değişen termo-fiziksel özeliklerinden, viskozitenin ve yoğunluğun artması nedenleriyle, akış kaynaklı basınç düşümlerindeki yükselmeler de dikkatle değerlendirilmelidir. Çünkü ısı geçişini iyileştirip, enerji tüketimini azaltmak amacıyla yapılan mini kanallı tasarım ve aracı akışkan değişiklikleriyle, pompalama gücündeki olası artışın düşük tutulması önemlidir.

Özetlemek gerekirse, ısıl sistemlerde yüksek verimli ısı dönüşümü (faydalı ısıl güç aktarımı), ısı taşıyıcı aracı akışkana etkin ısı geçişi ile tanımlanır. Fakat etkin ısı geçişi sağlanırken, ısıl sitemlerde enerji kaynaklarının ne kadar verimli kullanıldığını gösteren, işletme maliyetlerinde etkili ve önemli parametrelerden olan aracı akışkanlar için gerekli pompalama gücünün de hesaba katılması önemlidir. Diğer bir ifadeyle, ısıl sistemlerdeki yapısal tasarım değişiklikleri ve üstün özelikli yeni aracı akışkanların, ısıl etkenlik bakımından sağlayacağı faydaların yanında, hidrodinamik bakımdan muhtemel olumsuz etkileri de göz önünde bulundurularak, genel bir enerji verimliliği değerlendirmesi yapılmalıdır.

LİTERATÜR ARAŞTIRMASI VE ÇALIŞMANIN ÖZGÜN DEĞERİ

Literatürde Al_2O_3, SiO_2, ZrO_2, CuO, TiO_2, karbon-nanotüp gibi nanopartiküller ve bunların karışımlarıyla (hibrit) hazırlanan nanoakışkanlarla çok sayıda deneysel çalışma yapılmıştır (Saidur vd., 2011; Sharma vd., 2016). Ancak Al_2O_3 nanopartiküller, diğer nanopartiküllere göre daha düşük maliyetle ve daha kolay temin edildiğinden, literatürdeki deneysel çalışmalarda daha çok tercih edilmiştir (Sergis ve Hardalupas, 2011). Literatür bölümünün çok fazla uzamaması bakımından, çalışmamızın ana teması olan GBIDler ve Al_2O_3 nanopartikülleriyle hazırlanan nanoakışkanlarla yapılan deneysel çalışmalardan, sadece GBIDlerde, Al_2O_3-su nanoakışkanlarının kullanıldığı çalışmalar seçilmiştir. Bu çalışmalar aşağıda kısaca özetlenmiştir.

Barzegarian vd. (Barzegarian vd., 2017), GBIDde (D_i=5 mm ve L/D≅40), 15 nm ortalama çaplı, γ-Al_2O_3 nanopartiküller ile üç farklı konsantrasyonda (hacimsel oranlar: %0.03, %0.14 ve %0.3) hazırlanan nanoakışkanlarla, laminer (Re=250-1200 aralığında) ve zıt akış koşullarında, boru tarafındaki sıcak nanoakışkanlardan (soğuyan akışkan) ısı geçişini ve basınç düşümünü deneysel incelemişlerdir. Araştırmacılar, KSTSyla (su) karşılaştırıldığında; nanoakışkanlarla toplam ısı geçiş katsayısındaki en yüksek iyileşmenin; en yüksek Re sayısında ve %0.3 hacimsel oranda %19.1 olarak elde edildiğini bildirmişlerdir. Bu koşullarda, %0.3 hacimsel oranlı nanoakışkanın basınç düşümünün de, KSTS suya göre ortalama %22 arttığını belirtmişlerdir. Ancak çalışmada, gövde tarafı ısıl ve hidrodinamik koşulları ile boru tarafı ısıl koşulları hakkında bilgi verilmemiştir.

Farajollahi vd. (Farajollahi vd., 2010), GBIDnin (D_i=4.1 mm ve L/D≅160) boru tarafındaki türbülanslı akışta (Pe=20,000-60,000), γ-Al_2O_3-su (ortalama partikül çapı 25 nm) nanoakışkanlarına ısı geçişini, sabit gövde tarafı ısı taşınım katsayısında ve zıt akış koşullarında deneysel incelemişlerdir. Araştırmacılar; %0.3-%2 hacimsel oranlı Al_2O_3-su nanoakışkanları, KSTSyla (su) kıyaslandığında, toplam ısı geçiş katsayısında en yüksek iyileşmenin Pe=50,000'de ve %0.5 hacimsel oranda, %20 olarak elde edildiğini bildirmişlerdir. Ancak çalışmada, gövde tarafı ısıl ve hidrodinamik koşulları, boru tarafı ısıl koşulları ve basınç düşümleri hakkında bilgi verilmemiştir.

Shahrul vd. (Shahrul vd., 2016), boru iç çapı 6.35 mm ve uzunluğu 1220 mm olan (L/D=192) GBIDnin performansını, %0.5 hacimsel oranlı Al_2O_3–su nanoakışkanıyla deneysel incelemişlerdir. Araştırmacılar, sıcak akışkanın giriş sıcaklığını 70°C'de ve nanoakışkanın giriş sıcaklığını da 20°C'de sabit tutukları deneyleri, farklı gövde tarafı ve boru tarafı debilerinde (2-8 *l/dk*.), hem aynı hem de zıt yönlü akış koşullarında gerçekleştirmişlerdir. Bu deneylerden, boru tarafının 4 *l/dk*.'da ve gövde tarafının 8 *l/dk*.'da tutulduğu deneyde, toplam ısı geçiş katsayısında KSTSya (suya) göre %26 iyileşme olduğunu belirtmişlerdir. Ancak çalışmada, akış kaynaklı basınç düşümü sonuçları hakkında bilgiye yer verilmemiştir.

Kabeel ve Abdelgaied (Kabeel ve Abdelgaied, 2016), borularının iç çapı 6.5 mm ve uzunluğu 600 mm (L/D≅92) olan GBIDde, giriş sıcaklığının 60°C sabit tutulduğu üç farklı hacimsel oranlı (%2, %4 ve %6) soğuyan Al_2O_3-su nanoakışkanlarından ısı geçişinde, KSTSya (su) göre iyileşmeyi, Re=9500-56,000 aralığında incelemişlerdir. Araştırmacılar, toplam ısı geçiş katsayısında, KSTS suya göre en yüksek iyileşmenin, %4 hacimsel oranda %29.8 olduğunu ve %4 hacimsel oranlı nanoakışkanla, Re≅56,000'deki basınç düşümünün de KSTS suya göre %28 arttığını bildirmişlerdir. Ancak çalışmada, gövde tarafı ısıl ve hidrodinamik koşulları hakkında bilgi verilmemiştir.

Al_2O_3-su nanoakışkanlarının, boruları 2.4 mm çaplı ve 248 mm uzunluğunda (L/D≅103) olan yatay GBIDde, türbülanslı ($Pe=5x10^5$-$15x10^5$) ve zıt akış koşullarındaki ısıl ve hidrodinamik performansları, Albadr vd. (Albadr vd., 2013) tarafından incelenmiştir. Araştırmacılar

deneylerde, ortalama çapı 30 nm olan Al_2O_3 nanopartiküllerle, %0.3-%2 aralığındaki 5 farklı hacimsel oranda hazırladıkları nanoakışkanları kullanmışlardır. Toplam ısı geçiş katsayısında KSTSya (su) göre en yüksek iyileşmenin, %2 hacimsel oranda ve en yüksek debide, ~%75 olduğunu ve basınç düşümünün, nanoakışkanların artan viskozitesine rağmen çok az yükseldiğini bildirmişlerdir. Ancak çalışmada, gövde tarafı ısıl ve hidrodinamik koşullarıyla, boru tarafı ısıl koşulları hakkında bilgi verilmemiştir.

Kumar vd. (Kumar vd., 2018), tam gelişmiş laminer ve türbülanslı akışta, Re=1000-11,000 aralığında, GBIDde (D_i=10.7 mm ve L/D≅56) boru tarafında ısınan Al_2O_3-su nanoakışkanlarıyla, taşınımla ısı geçiş katsayısının değişimini deneysel incelemişlerdir. Araştırmacılar deneyleri, gövde tarafının ısıl ve hidrodinamik koşullarını sabit tutarak ve zıt akış koşullarında, %0.01-%0.08 hacimsel oranlı nanoakışkanlarla gerçekleştirmişlerdir. En yüksek Re sayısında, %0.02, %0.04, %0.06 ve %0.08 hacimsel oranlarda; ısı taşınım katsayısındaki iyileşmelerin, sırasıyla %13, %18, %23 ve %28 olduğu, KSTS suya göre sürtünme faktöründeki oransal artışın, türbülanslı akışta laminer akıştan daha yüksek olduğu, nanopartiküllerin hacimsel oranı arttıkça, sürtünme faktöründe çok düşük bir artış olduğu, ancak nanoakışkanın debisindeki artıştan dolayı, tam gelişmiş türbülanslı akışta sürtünme faktörünün azaldığı belirtilmiştir.

Mansoury vd. (Mansoury vd., 2020), boruları 7.3 mm iç çaplı ve L/D≅137 olan GBIDde, Re=4200-14,000 aralığında, %0.2, %0.5 ve %1 hacimsel oranlı, giriş sıcaklıkları 45°C'de sabit tutulan (sıcak) Al_2O_3-su nanoakışkanlarından ısı geçişini ve basınç düşümünü deneysel incelemişlerdir. Araştırmacılar, KSTS suya göre %0.2, %0.5 ve %1 hacimsel oranlarda; ısı geçişindeki ortalama iyileşmenin, sırasıyla %12, %20 ve %24 ve basınç düşümündeki artışın da sırasıyla %25, %75 ve %85 olduğunu belirtmişlerdir.

Çalışmamızın özgün yönü, GBIDlerde makro borular (hidrolik çapı 6 mm ve üzerinde) yerine mini kanallar (hidrolik çapı 200 μm-3 mm aralığında) ve Al_2O_3-su nanoakışkanları kullanmanın, ısıl ve hidrodinamik performansa etkilerinin deneysel incelenmesidir. Makro borulara (8-60 mm hidrolik çaplı GBIDler için ortalama kompaktlık 100 m^2/m^3 (Wadekar, 2005)) göre daha küçük hidrolik çaplı boruların (çalışmamızdaki 2 mm hidrolik çaplı GBID için kompaktlık yaklaşık 1100 m^2/m^3) kullanılmasıyla, hem ısı değiştiricinin ısı geçişi alan yoğunluğu (birim hacimdeki ısı geçiş alanı yani kompaktlık) arttırılacak hem de artan kompaktlıkla ısı değiştiricide boyut küçülmesi (çalışmamızdaki MK-GBID toplam uzunluğu 440 mm), dolayısıyla malzeme ve maliyet tasarrufu sağlanacaktır. Bu durum şu örneklerle açıklanabilir: (1) GBIDlerde aynı ısıl güçte ve aynı boru uzunluklarında; 10 mm çaplı boruların yerine 1 mm çaplı boruların kullanılması, ısı değiştirici hacmini %95 küçültecektir (Kandlikar, 2007). (2) Isı değiştiricide mini kanal kullanılması, boyutları %30 ve maliyeti %40 azaltacaktır (Trang vd., 2017). (3) Aynı iç akış hacmindeki; 1 mm çaplı boru, 10 mm çaplı boruya göre 10 kat daha büyük yüzey alanı sağlayacaktır (Kandlikar, 2007). (4) Isı değiştiricide aynı akış kesit alanında kanal çapının %50 azaltılması, yerleştirebilecek kanal sayısını 4 kat artıracaktır. Böylece küçük kanalların toplam çevre uzunluğu, büyük kanalın çevre uzunluğunu 2 katına çıkaracaktır. Kanal uzunluklarının eşit olması durumunda, ısı geçişi yüzey alanı da 2 katına çıkacaktır (Van de Bor, 2014). (5) Aynı akış koşullarında hidrolik çap %50 azaltıldığında, ısı taşınım katsayısı hidrolik çapla ters orantılı artacaktır. Aynı hacimde hem ısı taşınım katsayısının hem de kompaktlığın, azaltılan hidrolik çapla ters orantılı artması nedeniyle, aktarılabilecek toplam ısıl güç, hidrolik çaptaki azalmanın karesiyle orantılı artacaktır (Kakaç vd., 2012). Kompaktlık artışının diğer önemli etkileri de gerekli aracı akışkan miktarlarındaki azalma (çalışmamızdaki MK-GBIDnin; boru tarafı hacmi 9.8 cm^3 ve gövde tarafı hacmi 139.7 cm^3) ve enerjinin daha verimli ve etkin kullanılmasıdır. Böylece, aracı akışkanların kullanım miktarı azaltılarak, ekonomik ve çevresel maliyetlerin azaltılması da hedeflenmiştir. Bu nedenle çalışmamızda, aracı akışkan olarak kullanılan nanoakışkanın maliyeti ve yüksek hacimde/miktarda hazırlama zorlukları göz önüne alındığında, önemli ölçüde tasarruf sağlanmıştır. Bu durum şu örneklerle açıklanabilir: (1) Aynı ısıl güçlerde; iç hacmi 8.4 *l* olan LID ile iç hacmi 2.9 *l* olan GBID (2 mm iç çaplı mini kanallı ve iç hacmi %65 daha az) karşılaştırıldığında, gerekli aracı akışkan şarjı %50 azalacaktır (Del Col vd., 2010). (2) 10 mm çaplı kanallar için 400 m^2/m^3 olan kompaktlık, 1 mm çaplı kanallar için 4000 m^2/m^3 ve 0.5 mm çaplı kanallar için 8000 m^2/m^3'tür (Kandlikar, 2007). Ancak hidrolik çapı küçültmenin ve nanoakışkan kullanmanın taşınımla ısı geçişinde sağladığı iyileşme ve bahsedilen diğer faydalarının yanında, sürtünme basınç kayıplarını artırıcı olumsuz etkileri de çalışmamızda araştırılmıştır. Bu durum şu örnekle açıklanabilir: Aynı gövde iç çapı ve aynı boru demeti tasarım şartlarındaki GBIDde, aynı ısıl gücü aktarmak için 5 mm çaplı borular 2 mm'lik borularla değiştirildiğinde, ısı geçişi alanı %30 artarken boru içi akış kesitinin alanı yaklaşık %53 azalacak, ortalama akış hızının %89 artmasıyla basınç kaybı da yükselecektir (Hejcik ve Jicha, 2014). Ayrıca literatürdeki çalışmalardan farklı olarak, hidrolik çapın küçülmesine ve nanoakışkan kullanımına bağlı olarak ısı geçişindeki iyileşme ve basınç düşümündeki artış arasındaki dengede oluşan değişim de iki farklı termo-hidrodinamik performans ölçütüyle araştırılmıştır. Yani enerjinin daha verimli ve etkin kullanılıp kullanılmadığı, enerji verimliliği ölçütleriyle (ısı geçişi ve basınç düşümü arasındaki etkileşim birlikte değerlendirilerek) irdelenmiştir. Bir başka deyişle de hidrolik çapın küçültülmesinin ve nanoakışkanların kullanılmasının enerji verimliliği bakımından faydalı olup olmadığı gösterilmiştir.

Çalışmanın, literatüre katkısı bakımından önemli yönü; GBIDde (dairesel en-kesitli) mini kanalların ve soğuyan nanoakışkanların birlikte kullanıldığı, ısıl ve hidrodinamik şartların çok iyi tanımlandığı, benzer bir deneysel araştırmanın bulunmamasıdır. Literatürdeki diğer mini kanal uygulamalarından farklı olarak bu çalışmada, sadece GBIDde mini kanal ve boru tarafında soğuyan nanoakışkan uygulamasının, ısıl ve hidrodinamik performansa etkilerine yoğunlaşılmış, deneysel sonuçlar; ısı geçişindeki iyileşme ve basınç düşümündeki artış arasındaki dengenin değişimi gözetilerek değerlendirilmiştir.

PASİF ISI GEÇİŞİ İYİLEŞTİRME YÖNTEMLERİNİN UYGULANMASI, TASARIM VE YAKLAŞIM

Bu çalışmada MK-GBIDde, boru tarafında soğuyan nanoakışkanların kullanılmasının ısı geçişi ve basınç düşümüne etkileri deneysel incelenmiştir. Isı değiştiricide, aynı ısıl ve hidrodinamik koşullarda, sudan-suya ve nanoakışkanlardan-suya ısı geçişi deneyleri yapılmıştır.

Çalışmamızın birinci aşamasında; Kandlikar ve Grande'nin (Kandlikar ve Grande, 2003) mini kanal yaklaşımı dikkate alınarak, Kern (Kern, 1950) yöntemine göre 1.5 kW'lık ortalama ısıl güç için tasarlanan ve imalatı yapılan; E-tipi, tek gövdeli ve tek boru geçişli MK–GBIDde, deneysel ölçümlerin doğruluğu ve güvenilirliği, sıcak sudan-soğuk suya ısı geçişi ve basınç düşümü deneyleriyle kontrol edilmiştir. Boru tarafı doğrulama deneylerinin sonuçları, Ünverdi vd. (Ünverdi vd., 2019) ve gövde tarafı doğrulama deneylerinin sonuçları, Kücük vd. (Kücük vd., 2019) tarafından gerçekleştirilen daha önceki deneysel çalışmalarımızda verilmiştir.

İkinci aşamada, gövde tarafında ısınan akışkan koşullarında, boru tarafında ise soğuyan akışkanlar KSTS (su) ve üç farklı hacimsel oranda (%0.2, %0.4 ve %0.8) hazırlanan Al_2O_3-su nanoakışkanları için MK-GBIDnin, ısıl ve hidrodinamik performansı elde edilmiştir. Bir başka ifadeyle, MK-GBIDde; ısıl güç ve pompalama gücü arasındaki ilişkiyi tanımlayan iki farklı termo-hidrodinamik performans ölçütüyle, boru tarafında soğuyan nanoakışkanların, ısıl ve hidrodinamik performans bakımından genel enerji verimliliğine olumlu ve/veya olumsuz etkileri araştırılmış ve tartışılmıştır.

Çalışmamızın üçüncü ve son aşamasında; literatürde farklı araştırmacıların, farklı ısı değiştiricilerde, farklı KSTSlar ve farklı nanoakışkanlarla elde ettikleri deneysel ısıl güçler ve basınç düşümü sonuçlarıyla, termo-hidrodinamik performans ölçütü sonuçları hesaplanmıştır. Literatürden alınan deneysel verilerle hesaplanan bu sonuçlarla, ısı geçişindeki iyileşmenin ve basınç düşümündeki artışın dengesi gözetilerek, farklı nanoakışkanların ısıl sistemlerin enerji kullanma performanslarına etkileri değerlendirilmiş ve deneysel çalışmamızdan elde edilen genel enerji verimliliği sonuçlarının doğruluğu teyit edilmiştir.

DENEY DÜZENEĞİ

Şekil 1'de akış şeması ve test bölgesinin kesit resimleri verilen deney düzeneği; MK-GBID, üç santrifüj pompa, iki LID, iki şamandıralı debimetre (%4 bağıl hatalı), dijital fark basınçölçer (%0.8 bağıl hatalı), dört sıcaklıkölçer (%1 bağıl hatalı), veri toplama kartı, sıcak akışkan döngüsünün beslenmesini sağlayan termostatik tank (2 kW'lık elektrikli ısıtıcılı), nanoakışkan tankı (mekanik karıştırıcılı), soğuk akışkan döngüsünü besleyen tank, su soğutucusu (4 kW soğutma kapasiteli) ve bilgisayardan oluşmaktadır.

Test bölgesinin dairesel kesitli mini kanallardan üretilen boru tarafı; iç çap/dış çap oranı 2 mm /3 mm ve uzunlukları 240 mm olan 13 bakır borunun, akışa dik doğrultuda 5 boru sırası oluşturacak şekilde ve 60^o döndürülmüş üçgen düzende dizilmesiyle oluşturulan boru demetidir. Gövde tarafı E-tipi tek geçişlidir. İç çapı 30 mm olan gövdedeki akış, yatay-çapraz yönelimli ve %25 kesme oranlı dört şaşırtma levhasıyla düzenlenmiştir. Sıcak nanoakışkanlar, test bölgesinin boru tarafına (60–500 *l/sa.* debi aralığında) 40°C sabit sıcaklıkta pompalanırken, soğuk musluk suyu, test bölgesinin gövde tarafına (sabit 375 *l/sa.*), boru tarafından 20°C daha düşük ve sabit sıcaklıkta pompalanmıştır. Deneyler süresince, her iki akışkanın test bölgesine girişteki sıcaklık değişimleri %2'den azdır. Test bölgesi ısı kaybı ve kazancına karşı iyi yalıtılmıştır.

Deneyler süresince boru tarafı devresinde ve atmosfere açık döngüde dolaştırılan nanoakışkanlar; termostatik tankta ısıtılan (elektrikli ısıtıcıyla) sıcak suyla, lehimli bir LIDde ısıtılmıştır. Gövde tarafı devresinde atmosfere açık döngüde dolaştırılan soğuk musluk suyu ise, diğer lehimli LIDde, su soğutucusundan gelen sabit sıcaklıktaki soğutma suyu ile soğutulmuştur. MK–GBID'nin üretimi ve deneysel çalışmalar, Gerede Meslek Yüksekokulu'ndaki atölyede gerçekleştirilmiştir.

Deneysel araştırmamızdaki; debimetrelerin ölçüm doğrulukları zaman ortalamalı ağırlıklı kap ölçme yöntemiyle, sıcaklıkölçerlerin ölçüm doğrulukları ise hem buzlu-su hem de her seri deneyden önce oda sıcaklığındaki su ile karşılaştırmalı olarak ve dijital fark basınçölçerin ölçüm doğruluğu da cıvalı U-manometre ile kontrol edilmiştir. Rotametrelerden okunan debiler, veri toplama kartıyla aktarılan boru ve gövde tarafındaki giriş-çıkış sıcaklıkları ve boru tarafı basınç düşümleri, bilgisayarda kayıt altına alınmıştır.

NANOAKIŞKANLARIN HAZIRLANMASI

Deneysel araştırmamızdaki su bazlı Al_2O_3 nanoakışkanları, üç farklı hacimsel oranda (%0.2, %0.4 ve %0.8) hazırlanmıştır. Nanopartiküllerin kısa sürede çökelmesini engellemek ve mümkün olduğunca homojen dağılımını sağlamak, kararlı süspansiyonlar hazırlamak ve aynı zamanda hazırlama maliyetlerini düşürmek amacıyla, nanoakışkanların hacimsel oranları %1'den küçük seçilmiştir. Deneysel araştırmamızda daha düşük maliyetli olması, kolay temin edilebilmesi ve diğer (kimyasal kararlılığı ve yüksek ısı iletim katsayısı gibi) üstünlükleri nedeniyle, Al_2O_3 nanopartikülleri tercih edilmiştir. Kullanılan nanopartiküller, neredeyse küresel şekilli ve ortalama partikül çapı 40 nm'dir. Al_2O_3 nanopartiküllerinin yoğunluk, özgül ısı ve ısı iletim katsayısı sırasıyla; 3890 kg/m^3, 880 J/kgK ve 35 W/mK'dir (Somiya, 1989; İnternet, 2023).

Araştırmamızdaki nanoakışkanların hazırlanmasında, iki aşamalı yöntem kullanılmıştır. Bu yöntemde, önceden hazırlanan nanopartiküller, doğrudan KSTSya eklenmektedir. Ancak iki aşamalı yöntemde nanopartiküller; yüksek yüzey alanı/hacim oranı, yüksek yüzey aktivitesi ve Van der Waals kuvvetleri gibi çekici-itici kuvvetlerin etkileriyle, kümelenmeye ve topaklanmaya yatkındır (Das vd., 2007; Hunter, 2002; Russel vd., 1989). Ayrıca topaklanma, nanoakışkanların termo-fiziksel özeliklerini (ısı iletim katsayısı ve viskozite) ve taşınımla ısı geçişi performansını olumsuz etkilemektedir (Anoop vd., 2009; Ghadimi vd., 2011; Prasher vd., 2006). Bu nedenle, endüstriyel ölçekte, kararlı nanoakışkanların hazırlanmasında karşılaşılan zorlukların aşılması amacıyla, bazı fiziksel ve/veya kimyasal teknikler (yüzey aktif maddesi, nanopartikül yüzey kimyasının ve dolayısıyla yüzey yükünün değiştirilmesi ve nanopartiküllerin topaklanmasını önlemek amacıyla nanoakışkana ultrasonik

enerji verilmesi gibi) uygulanmaktadır. Bu tekniklerin yalnızca biri kullanılabileceği gibi ikisi veya daha fazlası da birlikte kullanılarak, daha kararlı nanoakışkanlar üretilebilmektedir (Wang ve Mujumdar, 2007).

Literatürde genel olarak kararlı ve homojen nanoakışkanlar hazırlamak için üç saate kadar karıştırma süresinin yeterli olacağı ifade edilmiştir. Bu nedenle, deneysel araştırmamızda, endüstriyel ölçekteki (20 litre) nanoakışkanların hazırlanması ve yeterince homojen (kolloid) karışımlar elde edebilmek amacıyla, her bir farklı hacimsel oranlı nanoakışkan, ultrasonik titreşim banyosu (daha yaygın ve diğer yöntemlere göre uygulanması daha kolay) kullanılarak, üç saat boyunca karıştırılmıştır. Ayrıca, herhangi bir etken maddenin (katkı maddesinin) eklenmesi, nanoakışkanların özeliklerini değiştirebileceğinden, çalışmamızda seyreltici veya kararlılık artırıcı kimyasal maddeler kullanılmamıştır.

Nanoakışkanların hazırlanması, kullanılan Al_2O_3 nanopartiküller ve nanoakışkanlar hakkındaki daha ayrıntılı bilgiler, Yılmaz vd. (Yılmaz vd., 2022) tarafından yapılan deneysel çalışmamızda verilmiştir.

NANOAKIŞKANLARIN TERMO-FİZİKSEL ÖZELİKLERİNİN BELİRLENMESİ

Deneysel çalışmamızda, nanopartiküllerin ve taşıyıcı sıvı suyun ağırlıkları ve hacmi, hassas ölçek ve terazi kullanılarak belirlenmiştir. Seçilen hacimsel oranlardaki nanoakışkanların (1 litrelik nanoakışkan karışımı için) hazırlanmasında gerekli (taşıyıcı sıvıya eklenecek) nanopartiküllerin kütlesi, Eşitlik 1 ile hesaplanmıştır.

$$m_{np} = \varphi \times 10^{-3} (m^3) \times \rho_{np} \quad (1)$$

Burada, m_{np} (kg); karışıma eklenecek nanopartikül kütlesi, φ (-); karışımın hacimsel oranı, ρ_{np} (kg/m³); nanopartikülün yoğunluğudur. Nanoakışkanın yoğunluğu ve özgül ısısı Eşitlik 2'den ve Eşitlik 3'ten hesaplanmıştır.

$$\rho_{na} = (1-\varphi)\rho_{ts} + \varphi\rho_{np} \quad (2)$$

$$c_{p,na} = [(1-\varphi)\rho_{ts} c_{p,ts} + \varphi\rho_{np} c_{p,np}] / \rho_{na} \quad (3)$$

Eşitlik 2'de ve Eşitlik 3'te ρ (kg/m³) ve c_p (J/kgK) sırasıyla yoğunluğu ve özgül ısıyı, alt indis na, ts ve np sırasıyla nanoakışkanı, taşıyıcı sıvıyı ve nanopartikülü ifade etmektedir. Eşitlik 2'nin geçerliliği, Pak ve Cho (Pak ve Cho, 1998) ve Ho vd. (Ho vd., 2010) tarafından, Al_2O_3-su nanoakışkanları için oda sıcaklığında yapılan deneysel çalışmalarla raporlanmıştır. Eşitlik 3'ün geçerliliği, Zhou ve Ni (Zhou ve Ni, 2008) tarafından, Al_2O_3-su nanoakışkanı için oda sıcaklığında yapılan deneysel çalışmada raporlanmıştır. Taşıyıcı sıvı suyun sıcaklığa bağlı termo-fiziksel özeliklerinin hesaplanmasında, Unverdi ve Islamoğlu, (Unverdi ve Islamoglu, 2017) tarafından önerilen polinomlar kullanılmıştır.

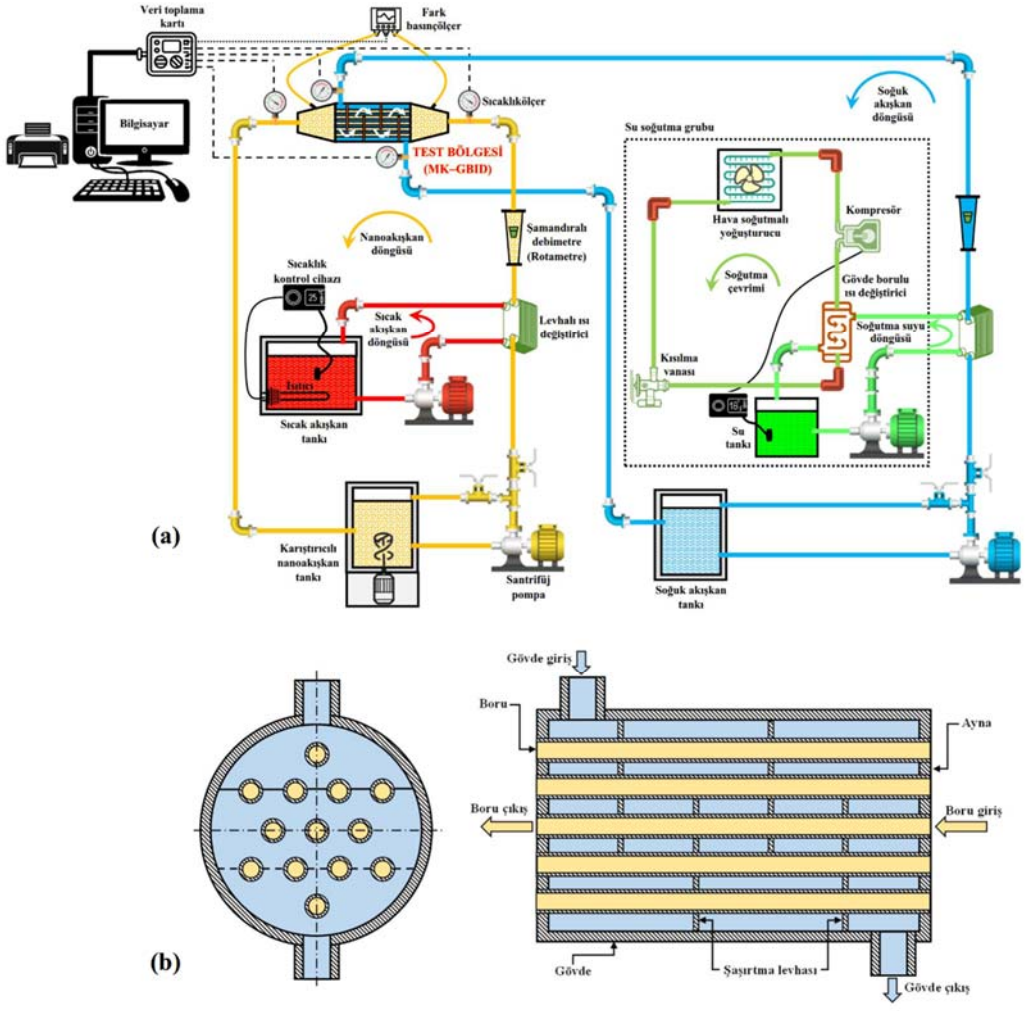

Şekil 1. Deney düzeneğinin (a) akış şeması ve (b) test bölgesinin kesit resimleri.

ISIL VE HİDRODİNAMİK PERFORMANSA DAYALI ENERJİ VERİMLİLİĞİ ÖLÇÜTLERİ

MK-GBIDde boru tarafından gövde tarafına ısı geçişi, sıcak akışkanın verdiği ve soğuk akışkanın aldığı ısıl güçlerle hesaplanmıştır.

$$Q_b = \rho_b \dot{\forall}_b c_{p,b} (T_{b,grş} - T_{b,çkş}) \quad (4)$$

$$Q_g = \rho_g \dot{\forall}_g c_{p,g} (T_{g,çkş} - T_{g,grş}) \quad (5)$$

Burada, Q (W); ısıl güce, ρ (kg/m^3); yoğunluğa, $\dot{\forall}$ (m^3/s); hacimsel debiye, c_p (J/kgK); sabit basınçtaki özgül ısıya, T (K); sıcaklığa karşılık gelmektedir. Alt indisler b ve g, grş ve çkş sırasıyla; boru tarafını ve gövde tarafını, giriş ve çıkış koşullarına göstermektedir. Teorik olarak, adyabatik test bölgesi için bu iki ısıl güç (sıcak ve soğuk akışkanlar) eşit olmalıdır. Ancak, deneysel çalışmamızdaki debi aralığında, taşıyıcı akışkan su, %0.2, %0.4 ve %0.8 hacimsel oranlı nanoakışkanlarla yapılan deneylerde, gövde (soğuk) ve boru (sıcak) tarafında hesaplanan deneysel ısıl güçler arasındaki ortalama farklar, sırasıyla %8, %10.8, %7.4 ve %5.4'den daha azdır.

Isıl sistemlerde kullanılan yeni bir aracı akışkanın ya da bir pasif ısı geçişi iyileştirme yönteminin, genel (ısıl ve hidrodinamik) enerji verimliliği performansına etkilerini belirlemede, ısıl gücün ve pompalama gücünün birlikte dikkate alındığı, aşağıda tanımlanan PDÖ ve VDÖ kullanılmıştır (Ferrouillat vd., 2011; Ma vd., 2014).

Performans Değerlendirme Ölçütü

PDÖ tanımından da görüleceği üzere; ısıl sistemlerde çok fazla akış enerjisi harcanması, akış enerjisinin verimli bir şekilde taşınımla ısı geçişine dönüştürülemediğini göstermektedir. Birbirine alternatif olan aracı akışkanların, aynı ısıl ve hidrodinamik koşullarda, taşıdıkları ısıl güç ve pompalama gücü arasındaki oransal dengenin (enerji performanslarının) karşılaştırılmasında ve değerlendirmesinde kullanılan boyutsuz PDÖnün tanımı şu şekildedir:

$$PDÖ = Q / W_{pg} \quad (6)$$

Burada, PDÖ; performans değerlendirme ölçütünü göstermekte, Q (W); aktarılan (taşınan) ısıl güce ve W_{pg} (W) ise akışın devamı için gerekli olan pompalama gücüne karşılık gelmektedir.

$$Q = \rho \dot{\forall} c_p \Delta T \quad (7)$$

$$W_{pg} = \dot{\forall} \Delta p \quad (8)$$

Burada, ΔT (°C); aracı akışkanın test bölgesindeki sıcaklık farkına ve Δp (Pa); test bölgesindeki akış kaynaklı basınç düşümüne karşılık gelmektedir.

Verimlilik Değerlendirme Ölçütü

VDÖ; ısıl sistemlerin, referans duruma (taşıyıcı sıvı) göre farklı alternatif durumlardaki (nanoakışkanlar), karşılaştırmalı genel performans değişimlerini, PDÖ'ye göre daha açık gösterir. Aynı ısıl ve hidrodinamik koşullarda (aynı giriş sıcaklıkları ve aynı hacimsel debilerde) ve aynı hidrolik çaptaki akış kanallarında, farklı aracı akışkanların genel performanslarını değerlendirmek amacıyla kullanılan boyutsuz VDÖ şu şekildedir:

$$VDÖ = (Q_{na} / Q_{ts}) / (W_{pg,na} / W_{pg,ts}) \quad (9)$$

Burada, VDÖ; verimlilik değerlendirme ölçütünü, Q_{na}/Q_{ts}; nanoakışkanın ısıl gücünün, taşıyıcı sıvının (nanopartiküllerin kullanılmadığı) ısıl gücüne oranını, $W_{pg,na}/W_{pg,ts}$ ise nanoakışkanın pompalama gücünün, taşıyıcı sıvının (nanopartiküllerin kullanılmadığı) pompalama gücüne oranını göstermektedir.

Tanımları verilen iki farklı enerji verimliliği performans ölçütünün temel dayanağı; MK-GBIDnin boru tarafındaki taşıyıcı akışkanın (suyun) ve farklı hacimsel oranlı nanoakışkanların, aynı giriş sıcaklıkları ve aynı debilerde, aktardıkları ısıl gücün, her biri için akışın devamında gerekli pompalama gücüne oranlanmasıdır.

BELİRSİZLİK ANALİZİ

MK-GBID ile yapılan deneylerde kullanılan ölçüm cihazları, özellikleri ve bağıl hataları Tablo 1'de verilmiştir. Ayrıca aynı Tabloda, Kline ve McClintock (Kline ve Mcclintock, 1953) tarafından tanımlanan yöntemle; deneysel çalışılan debi aralığında, gövde ve boru tarafında hesaplanan ısıl güçler ile performans ölçütleri PDÖ ve VDÖ için hesaplanan belirsizlikler de verilmiştir.

Farklı boru tarafı debilerinde gerçekleştirilen deneysel çalışmalarımızda, gövde tarafı debisinin 375 *l/sa.*'te sabit tutulması nedeniyle gövde tarafı belirsizlikleri, boru tarafına göre daha yüksektir. Ayrıca deneysel çalışmalarımızda kullandığımız rotametrelerin ölçme belirsizliklerinin diğer ölçme cihazlarına göre daha yüksek olması ve nanoakışkanların basınç düşümünü ölçmede karşılaşılan zorluklar nedeniyle PDÖnün ve VDÖnün (hesaplamalarda hem ısıl güç hem de basınç düşümü birlikte kullanıldığından) belirsizlikleri yüksektir.

Tablo 1. Ölçüm cihazlarının ölçme hataları ve ortalama belirsizlikler.

Cihazlar	***Tipi***			***Bağıl hata***
Sıcaklık (°C)	K tipi ısıl çift			%1
Hacimsel debi (*l/sa.*)	Rotametre			%4
Basınç düşümü (Pa)	DPC100 dijital fark basınçölçer			%0.8
	Ortalama belirsizlikler (%)			
Akışkanlar	***su***	***Al_2O_3-su***		
Nanoakışkanın hacimsel oranı	***%0.0***	***%0.2***	***%0.4***	***%0.8***
Gövde tarafı ısıl güç (W)*	10.49	15.38	12.98	14.57
Boru tarafı ısıl güç (W)	2.50	3.52	3.14	3.56
PDÖ	10.82	15.28	14.00	15.06
VDÖ	–	18.75	17.71	18.57

* 375 *l/sa.* debi için hesaplanmıştır.

SONUÇLAR VE TARTIŞMA

Isı değiştirici cihazların ısıl performanslarını artırmak amacıyla uygulanan pasif iyileştirme yöntemleriyle birim hacimdeki ısı geçiş alanının (kompaktlık) arttırılması hedeflenmektedir. Kompaktlık artışıyla; aracı akışkan miktarlarında azalma, cihaz boyutlarında küçülme ve ağırlıklarında azalma sağlanarak, yatırım ve işletme maliyetleri düşürülebilmektedir. Kompaktlık artışı sağlanan ısı değiştirici cihazlardaki aracı akışkanların termo-fiziksel özelikleri değiştirilerek/geliştirilerek (örneğin, sıvılar için katı katkılar), ısıl performans daha da iyileştirilebilir. Nanoakışkanlar, KSTSlara düşük konsantrasyonlarda nanopartiküllerin (katı) eklenmesiyle, ısıl performansı iyileştirebileceği düşünülen ve son zamanlarda popülaritesi artan koloit sıvı-partikül süspansiyonlarıdır.

Literatürdeki nanoakışkan çalışmaları hızlıca gözden geçirildiğinde, araştırmacıların üzerinde birleştiği genel sonuçlar; nanoakışkanların ısı iletim katsayısını ve taşınımla ısı geçişini iyileştirdiği, ancak akışkanın akışa karşı direncini temsil eden viskozitenin artışından dolayı akış kaynaklı basınç düşümünü (sürtünme faktörünü) artırma potansiyellerinin yüksek olduğudur. Ayrıca nanoakışkanlarla, ısı iletim katsayısı ve viskoziteye ek olarak, özgül ısı ve yoğunluk da değişmektedir. Ancak literatürdeki çalışmaların büyük çoğunluğunda, nanoakışkanların ısı değiştiricilerin genel enerji performansına etkileri ya hiç tartışılmamıştır ya da nadiren tartışılmıştır.

Viskozitedeki artış, faydalı ısıl güç (aracı akışkana aktarılan ısıl güç) ile akışın devamı için gerekli pompalama gücü arasındaki dengeyi, pompalama gücünün artışı nedeniyle, olumsuz yönde değiştirecektir. Bir başka ifadeyle, ısıl sistemlerde çok fazla akış enerjisinin harcanması, asıl amaç olan basınç düşümünün taşınımla ısı geçişine dönüştürülmesindeki verimsizliği de göstermektedir. Dolayısıyla, ısıl sistemlerde aktif ve/veya pasif ısı geçişi iyileştirme yöntemleri değerlendirilirken ve en uygun aracı akışkan seçilirken, taşınımla ısı geçişindeki iyileşmenin yanında, sistemin genel enerji veriminde etkili, pompalama gücü gibi faktörleri de göz önünde bulunduran yaklaşım/yaklaşımlar izlenmelidir.

Sonuç olarak, nanoakışkanlarla KSTSya göre taşınımla ısı geçişinde bir artış sağlansa da akışın devamı için gerekli pompalama gücü oransal olarak daha fazla artabilir.

Yukarıda özetlenen nedenlerle çalışmamızda, MK-GBIDde, boru tarafında soğuyan nanoakışkanlar kullanılmasının, ısı geçişine ve basınç düşümüne etkileri deneysel incelenmiştir. Çalışmamız üç temel aşamadan oluşmaktadır.

Çalışmamızın ilk aşamasında; GBIDlerin ısıl performansını artırmak amacıyla pasif ısı geçişi iyileştirme yöntemi (hidrolik çapın küçültülmesi) uygulanarak tasarlanan, MK-GBIDden (deney düzeneğinin test bölgesi) elde edilen deneysel ölçümlerin doğruluğu ve güvenilirliği hem boru tarafında hem de gövde tarafında sıcak sudan-soğuk suya ısı geçişi ve basınç düşümü deneyleriyle değerlendirilerek, sonuçların literatürle uyumu referans aracı akışkan su için gösterilmiştir. Boru tarafı ve gövde tarafı deneysel ısı geçişi-basınç düşümü doğrulama sonuçları önceki çalışmalarımızda (Kücük vd., 2019; Ünverdi vd., 2019) ayrıntılı olarak verilmiştir.

Çalışmamızın ikinci aşamasında; doğrulama deneylerinde olduğu gibi, MK–GBIDnin gövde tarafındaki soğuk akışkan (su) debisi 375 *l/sa.*'de ve giriş sıcaklığı 20°C'de sabit tutulmuştur. Boru tarafı devresinde dolaştırılan su ve üç farklı hacimsel oranda (%0.2, %0.4 ve %0.8) hazırlanan Al_2O_3-su nanoakışkanlarının, giriş sıcaklıkları ise gövde tarafından 20°C daha yüksek sıcaklıkta sabit tutulup, debileri de 60-500 *l/sa.* aralığında değiştirilmiştir. Bu işletme koşullarında, ısı değiştiricide hidrolik çapın küçültülmesinin ve aracı akışkanın termo-fiziksel özeliklerinin değiştirilmesinin/iyileştirilmesinin, ısıl ve hidrodinamik performansa birleştirilmiş etkileri değerlendirilmiştir. Başka bir ifadeyle; MK-GBIDde, ısıl güç ve pompalama gücü arasındaki dengeyi tanımlayan iki farklı termo-hidrodinamik performans ölçütüyle (enerji verimliliği ölçütleri PDÖ ve VDÖ ile), boru tarafında soğuyan nanoakışkanların ısıl ve hidrodinamik performansa olumlu/olumsuz etkileri değerlendirilmiştir.

Çalışmamızın üçüncü ve son aşamasında; hesaplanan deneysel PDÖ ve VDÖ sonuçlarının doğruluğu ve güvenilirliği kontrol edilmiştir. Bu amaçla literatürden; farklı araştırmacıların, farklı ısıl sistemlerde, farklı ısıl ve hidrodinamik koşullarda, farklı KSTSlarla ve nanoakışkanlarla elde ettikleri, deneysel ısıl güç ve basınç düşümü sonuçları kullanılarak, PDÖ ve VDÖ hesaplamaları yapılmıştır. Çalışmamızdan elde edilen verilerle ve literatürden alınan verilerle hesaplanan termo-hidrodinamik performans ölçütü sonuçları kullanılarak, nanoakışkanların ısıl sistemlerin genel enerji verimliliğine etkileri değerlendirilmiştir.

Çalışmanın devamında daha kısa olması nedeniyle, geleneksel/bilinen/konvansiyonel saf taşıyıcı sıvılar (KSTS) taşıyıcı sıvı (TS) olarak adlandırılacaktır.

Soğuyan Al_2O_3-su Nanoakışkanlarının Deneysel Performans Sonuçları

Mühendislik sistemleri ve endüstriyel uygulamalarda kullanılması önerilen nanoakışkanların, ısıl ve hidrodinamik performans değerlendirilmesinde izlenecek gerçekçi bir yaklaşım, hedeflenen ısıl güç için gerekli pompalama gücünü, aynı ısıl ve hidrodinamik koşullarda, saf aracı akışkan olan TS ve ikame nanoakışkanlar için karşılaştırmaktır.

Günümüze kadar yapılan deneysel çalışmalarda, nanoakışkanların viskozitesinin ve yoğunluğunun, TSlara (su, yağ, etilen glikol gibi) göre daha yüksek olduğu bilinmektedir. Bu nedenle, nanoakışkanlarla ve suyla elde edilen deneysel sonuçların, eşit (boyutsuz) Re sayılarında karşılaştırılması yanıltıcıdır. Çünkü Re sayısı, tanımı ($Re=\rho u D_h/\mu$) gereği; akış kanalı geometrisinin, akışkanın termo-fiziksel özeliklerinin (yoğunluk ve viskozite) ve akışın hidrodinamik koşullarının (hız-debi) bir kombinasyonunu temsil eder. Aynı akış kanalında ve eşit Re sayılarında, nanoakışkanların ortalama akış hızları, bahsedilen nedenle (yüksek viskozite ve yoğunluk) TSnınkinden daha yüksektir.

Dolayısıyla, eşit Re sayılarında yapılan değerlendirmeler, nanoakışkanlara yanıltıcı bir üstünlük sağlar. Açıklamak gerekirse; TSnın ortalama akış hızı, nanoakışkanların eşit Re sayısındaki ortalama akış hızılarına çıkarılırsa, TSnın ısıl performansı da nanoakışkanlara yaklaşabilir ve/veya nanoakışkanları geçebilir. Ayrıca daha yüksek viskoziteli

nanoakışkanlar için aynı ortalama akış hızında, daha yüksek pompalama gücü gerekecektir. Pompalama gücü de ısıl sistemlerde istenilen ısı geçişine (ısıl güce) ulaşmanın bedelini (enerji ve işletme maliyetini) temsil etmektedir.

Özetlemek gerekirse, deneysel sonuçların eşit Re sayısında karşılaştırılması; yoğunluk, viskozite ve ortalama akış hızındaki farklılıklardan dolayı, nanoakışkanların ısıl iyileştirme oranının, yanıltıcı bir şekilde, gerçekte olduğundan daha büyük gösterilmesine yol açacaktır. Dolayısıyla, nanoakışkanlara taşınımla ısı geçişinde, TS suya göre sağlanan iyileşmenin değerlendirmesi de eşit ortalama akış hızında (aynı hacimsel debide) veya eşit pompalama gücünde yapılmalıdır. Çünkü eşit Re sayılı akışlarda, nanoakışkanlar lehine daha yüksek ortalama akış hızı (debi) gerekeceğinden, TSlara göre ısı geçişindeki iyileşmenin daha yüksek elde edilmesi yanıltıcıdır.

Yukarıda bahsedilen nedenlerle, nanoakışkanların deneysel ısıl-hidrodinamik performanslarının bir arada değerlendirilmesinde, hacimsel debiye bağlı değişimleri kullanmak, daha akılcı ve gerçekçi bir yaklaşımdır.Ancak sonuçların değerlendirilmesinde genel hidrodinamik koşullar hakkında fikir vermesi amacıyla, TS suyun hacimsel debilerine karşılık gelen Re sayıları Şekil 2'deki ve Şekil 3'teki grafiklere eklenmiştir. Ayrıca bu şekillere deneysel belirsizliklerin gösterildiği grafikler de eklenmiştir. Bunun yanı sıra çalışmamızda kullandığımız üç farklı hacimsel oranlardaki nanoakışkanların, deneysel sıcaklık ve basınç farklarının ölçüm veri örnekleri, 60 *l/sa.* ve 100 *l/sa.* debiler için Tablo 2'de verilmiştir.

Tablo 2. 60 *l/sa.* ve 100 *l/sa.* debiler için örnek deneysel veriler.

		Su		***%0.2 Al_2O_3-su***		***%0.4 Al_2O_3-su***		***%0.8 Al_2O_3-su***	
	$\dot{\forall}$ *(l/sa.)*	ΔT (°C)	Δp (Pa)	ΔT (°C)	Δp (Pa)	ΔT (°C)	Δp (Pa)	ΔT (°C)	Δp (Pa)
Boru tarafı	60	6.59	1152	5.98	2198	5.67	2311	5.98	1862
Gövde tarafı	375	0.85	–	0.68	–	0.86	–	0.87	–
Boru tarafı	100	6.97	3982	4.82	4864	5.82	5077	4.32	5872
Gövde tarafı	375	1.66	–	1.22	–	1.44	–	1.06	–

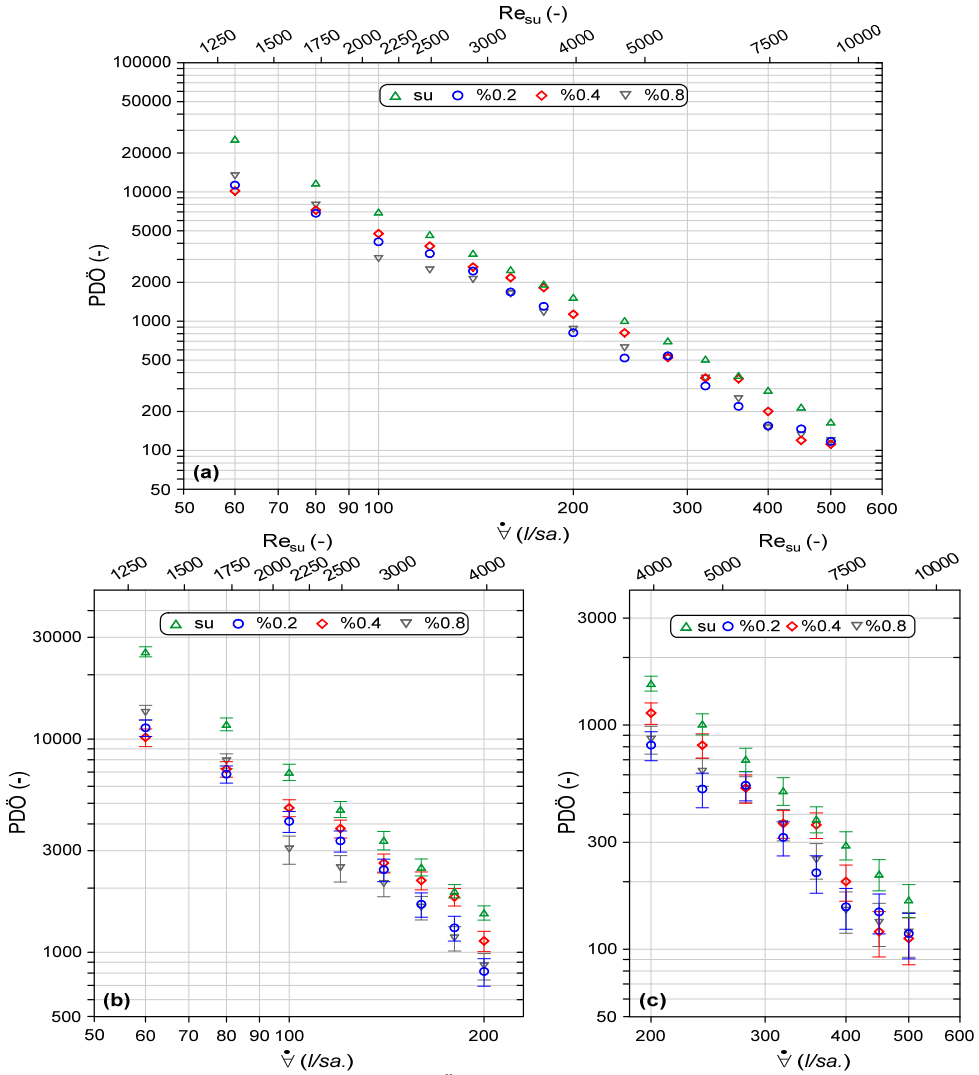

Şekil 2. Taşıyıcı sıvı (su) ve Al_2O_3-su nanoakışkanlarının (a) deneysel PDÖ sonuçlarının ve (b)-(c) deneysel belirsizliklerin hacimsel debiye bağlı değişimleri.

Şekil 2'de, deneysel çalışmadaki TS su ve farklı hacimsel oranlarda hazırlanan Al_2O_3-su nanoakışkanlarıyla elde edilen deneysel verilerle hesaplanan PDÖnün, hacimsel debiye bağlı değişimleri verilmiştir.

Çalışılan debi aralığında, PDÖ sonuçları arasındaki farklar az olsa da TSnın tüm nanoakışkanlardan daha yüksek performanslı olduğu görülmektedir. Bu sonuca göre, aracı akışkan olarak TS su yerine nanoakışkanların kullanılması hem enerji ve hem de ilk yatırım maliyetleri bakımından

uygun değildir. PDÖ sonuçlarına göre, MK-GBIDnin boru tarafında soğuyan nanoakışkanların kullanılması anlamsızdır. Başka bir ifadeyle, PDÖ sonuçları; TS suya göre nanoakışkanlarla artan pompalama gücünün, aynı oranda taşınımla ısı geçişine (ısıl güç aktarımına) dönüştürülemediğini göstermektedir.

Şekil 3'te üç farklı hacimsel oranlı nanoakışkanların VDÖsünün, hacimsel debiye bağlı değişimleri verilmiştir. VDÖye göre yapılan değerlendirmede, 1'in üzerindeki sonuçlar anlamlıdır. Çünkü VDÖnün 1 ya da 1'e yakın olması, iki alternatif durumda ısıl sistemin ısıl güçler oranının (Q_{na}/Q_{ts}) pompalama güçleri oranına ($W_{pg,na}/W_{pg,ts}$) eşit olduğunu göstermektedir. Şekil 3'te VDÖ sonuçlarının debiyle dalgalanarak değişmesinin nedeni, kısa borulardaki iç akışta debiye (ortalama akış hızına) bağlı olarak farklı akış rejimlerinin (laminer akış, geçiş akışı ve türbülanslı akış) baskın olarak görülmesidir. Bunun yanı sıra, nanoakışkanların hacimsel oranına bağlı olarak baskın akış rejimleri arasındaki geçişin görüldüğü debiler de değişmektedir.

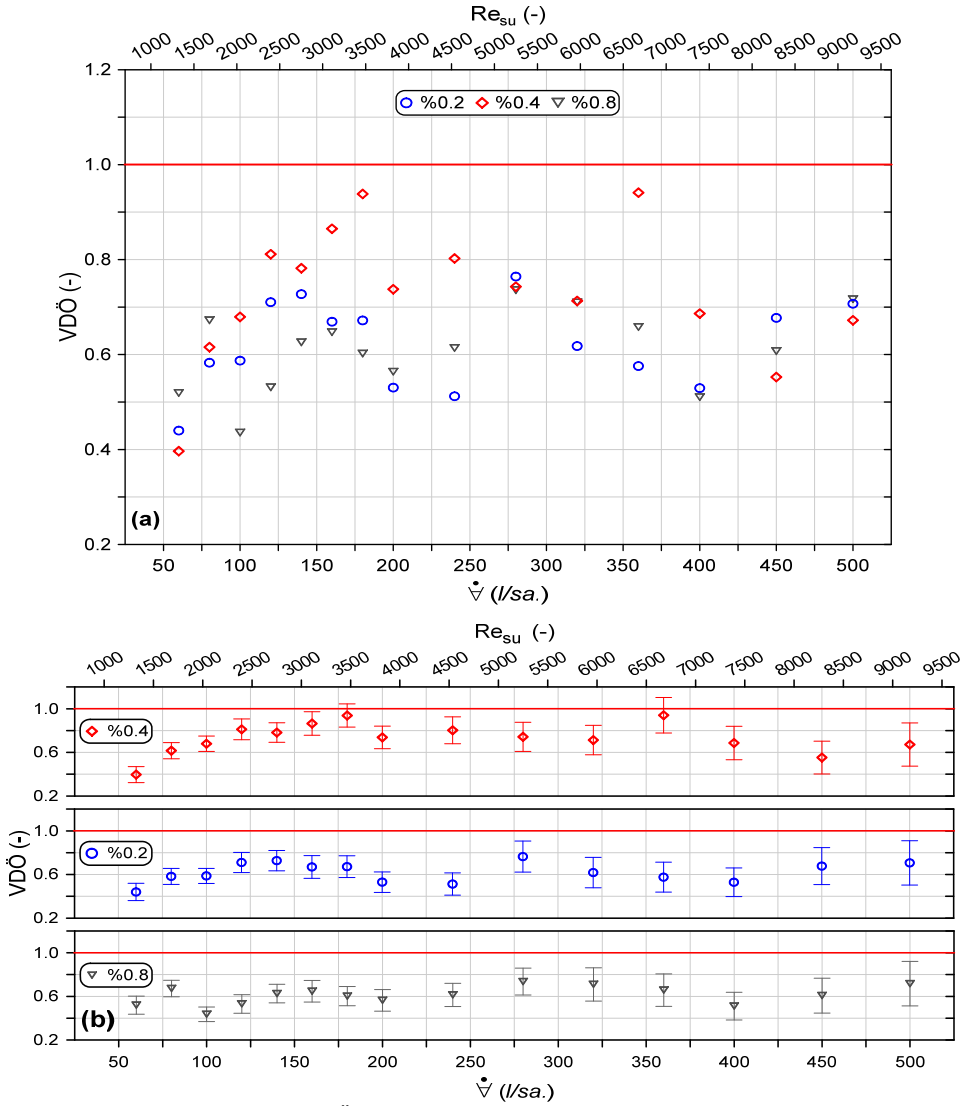

Şekil 3. Al_2O_3-su nanoakışkanlarının (a) deneysel VDÖ sonuçlarının ve (b) deneysel belirsizliklerin hacimsel debiye bağlı değişimleri.

Ayrıca nanoakışkanların basınç düşümünün ölçülmesinde karşılaşılan zorluklardan kaynaklanan yüksek belirsizlikler de VDÖ sonuçlarındaki saçılmada etkilidir.

TS su ile nanoakışkanların hacimsel oranına ve debiye bağlı olarak değişen farklı akış rejimlerinden ve nanoakışkanların basınç düşümünü ölçmede karşılaşılan zorluklardan, önceki çalışmalarımızda detaylı bahsedilmiştir (Ünverdi vd., 2019; Yılmaz vd., 2022).

Deneysel VDÖ sonuçlarımıza göre yapılacak genel değerlendirme, PDÖ sonuçlarımızla benzerdir ve MK-GBIDde nanoakışkanları kullanmak anlamlı değildir.

Hem PDÖye hem de VDÖye göre %0.2, %0.4 ve %0.8 hacimsel oranlı Al_2O_3-su nanoakışkanlarıyla, artacak enerji maliyetleri ve ilave nanoakışkan hazırlama maliyetleri de dikkate alınarak yapılan değerlendirmede, MK-GBIDde soğuyan nanoakışkanları kullanmak uygun değildir.

Nanoakışkan Literatüründen, Deneysel Verilerin Enerji Verimliliği Performans Ölçütleriyle Değerlendirilmesi ve Karşılaştırılması

Çalışmamızdaki deneysel PDÖ ve VDÖ sonuçlarıyla yapılan değerlendirmeye benzer olarak, literatürden farklı araştırmacıların, farklı ısı değiştiricilerle, farklı nanopartikül türleriyle, farklı nanopartikül boyutları ve hacimsel oranlarıyla, farklı işletme koşullarında yaptıkları deneysel çalışmaların sonuçları kullanılarak, nanoakışkanların ısıl ve hidrodinamik performansa etkileri değerlendirilmiştir.

Tablo 3'te LIDlerde ve Tablo 4'te GBIDlerde, ısıl güç ve hidrodinamik performansla ilgili yeterli veriye ulaşılabilen, literatürden; farklı nanoakışkanların kullanıldığı deneysel

çalışmalara ait test bölgelerinin geometrik boyutları ve özellikleri, nanopartikül özellikleri ve hacimsel/kütlesel oranları, ısıl ve hidrodinamik koşullar ile elde edilen önemli sonuçlar özetlenmiştir.

Deneysel çalışmamızda elde edilen PDÖ ve VDÖ sonuçlarının doğruluğunu ve güvenilirliğini desteklemek amacıyla, literatürden seçilen deneysel çalışmaların verileriyle hesaplanan PDÖ ve VDÖ sonuçları Şekil 4'te ve Şekil 5'te verilmiştir. Ayrıca literatürde yayımlanmış her bir deneysel çalışma için TSların ve nanoakışkanların enerji verimliliği performans sonuçlarını ayrı ayrı grafiklerde göstermek yerine Şekil 4'te ve Şekil 5'te deneysel çalışmaların TSları ve nanoakışkanları kendi içerisinde karşılaştırmalı olarak gösterilmiştir. PDÖ ve VDÖ sonuçlarının tanımı gereği her bir çalışmanın TSları ve nanoakışkanlarının kendi içerisinde birbirileriyle karşılaştırılması anlamlıdır. Bu nedenle Şekil 4'te ve Şekil 5'te grafiklerin anlaşılmasının kolaylaştırılması amacıyla her bir çalışmaya ait eksenlerde ve simgelerde farklı renkler kullanılmıştır.

Şekil 4a'da görülen PDÖ sonuçları incelendiğinde; LID-1'de hesaplanan PDÖ sonuçlarından, en yüksek performanslı nanoakışkanın (%0.6 hacimsel oranda) TS suya göre daha düşük (ortalama -%16) performanslı olduğu görülmektedir.

LID-2'de, deneylerde kullanılan nanoakışkanların (iki farklı nanopartikül malzemesiyle ve tümü %1 kütlesel oranlı hazırlanan), aynı Re sayılarındaki performanslarının, TS suya göre sırasıyla; Al_2O_3-su nanoakışkanında ortalama -%5.3 daha düşük, CuO-su nanoakışkanında nerdeyse TS suyla aynı ve Al_2O_3+CuO-su hibrit nanoakışkanında ise ortalama +%4.8 daha yüksek olduğu görülmektedir. Ancak, LID-2'in kullanıldığı deneysel çalışmada araştırmacılar, TS su ve nanoakışkanlar için basınç düşümlerini ölçmek yerine, literatürden bir bağıntıyla (Pandey ve Nema, 2012) basınç düşümlerini hesaplayarak ortalama sonuçları vermişlerdir. Nanoakışkanların TS suya göre daha düşük ya da neredeyse aynı olan performansları, eşit Re sayılarında yapılan karşılaştırmanın nanoakışkanlara yanıltıcı bir üstünlük sağladığı da (Soğuyan Al_2O_3-su Nanoakışkanlarının Deneysel Performans Sonuçları bölümü) hatırlanarak değerlendirilmelidir.

LID-3'te hesaplanan PDÖ sonuçlarında, en yüksek performanslı nanoakışkanın (%0.75 hacimsel oranda) TS suya göre daha düşük (ortalama -%10) performanslı olduğu görülmektedir ve bu sonuçlar LID-1 ile benzerdir.

Nanoakışkanların kullanılması yerine; TS suyla daha yüksek Re sayılarına (debilere) çıkılarak, aynı/yakın performans (ısıl güç) artışlarının elde edilebileceği açıktır. Aslında bu sonuçlar; nanoakışkanların tek fazlı ısı geçişi uygulamalarında kullanılmasıyla, TSya göre gerekli akış enerjisinde görülen artışın, yeterince ısıl güç artışına dönüştürülemediğini göstermektedir. Ayrıca bu sonuçlar, deneysel çalışmamızdaki sonuçları desteklemekte ve TSların yerine nanoakışkanların kullanılmasının uygun olmadığını doğrulamaktadır.

Şekil 4b'de VDÖ ile yapılan değerlendirmelerde (TS suya göre); LID-1, LID-2 ve LID-3'ün sonuçlarının 1'e yakın ve çoğunlukla 1'in oldukça altında kaldığı açıkça görülmektedir. VDÖye göre en yüksek sonuçlar; LID-1'de %0.1 hacimsel oranlı Ni-su nanoakışkanında 1.01 (%1 iyileşme), LID-2'de Al_2O_3-CuO-su hibrit nanoakışkanında 1.07 (%7 iyileşme) ve LID-3'te %0.5 hacimsel oranlı CeO_2-su nanoakışkanında 1.03 (%3 iyileşme)'dür.

PDÖ sonuçlarına benzer olarak VDÖ sonuçları da nanoakışkanları LIDlerdeki tek fazlı ısı geçişi uygulamalarında kullanmanın uygun olmadığını ve nanoakışkanlar yerine, TS suyla daha yüksek Re sayılarına (debilerde) çıkılarak aynı/yakın performansların (ısıl güçlerin) elde edilebileceğini göstermektedir.

Enerji verimliliği performans ölçütleriyle LIDler için yapılan karşılaştırmanın benzeri, GBIDler için de yapılmıştır. Şekil 5a'da GBIDlerde PDÖ ile yapılan değerlendirmelerden; nanoakışkanların GBID-1'de (%1 hacimsel oranlı TDKNT-su için ortalama %32 daha düşük), GBID-2'de (%0.2 hacimsel oranlı Al_2O_3-su için ortalama %6 daha düşük) ve GBID-3'te (%0.25 hacimsel oranlı SiC-su için ortalama %7.7 daha düşük) TS suya göre daha düşük performanslı oldukları görülmektedir. Şekil 5b'de VDÖ ile yapılan değerlendirmelerde; GBID-1 ve GBID-3'ün tüm sonuçları 1'in altında iken, GBID-2'de ise en yüksek Re sayısında (%0.2 hacimsel oranlı Al_2O_3-su için) en fazla %9'luk (1.09) bir iyileşme olduğu görülmüştür.

Ancak "Soğuyan Al_2O_3-su Nanoakışkanlarının Deneysel Performans Sonuçları" bölümünde bahsedildiği gibi aynı Re sayılarında yapılan değerlendirmede, nanoakışkanların yanıltıcı üstünlüğü de göz önüne alınırsa, LID-1'de %1 kütlesel oranlı Al_2O_3+CuO-su nanoakışkanı için yapılan değerlendirmeyle benzer olarak, GBIDlerde de TS suyla daha yüksek Re sayılarında (debilerde) çalışılarak aynı/yakın performanslar elde edilebilir.

Çalışmamızdaki MK-GBIDde (Şekil 2'deki ve Şekil 3'teki) ve literatürden seçilen ısı değiştiricilerde (Şekil 4'teki ve Şekil 5'teki) TSlara göre en düşük ve en yüksek farkla PDÖ sonuçlarını veren hacimsel/kütlesel oranlı nanoakışkanların PDÖ sonuçlarının nicel karşılaştırması, Tablo 5'te ve Tablo 6'da verilmiştir. Ayrıca Tablo 5'te ve Tablo 6'da aynı nanoakışkanlar için hesaplanan VDÖ sonuçları da karşılaştırmalı verilmiştir. Bunun yanı sıra Tablo 7'de bu nanoakışkanlarla TSlara göre ısıl güçte ve pompalama gücünde oluşan değişimler ile pompalama gücündeki değişimlerin ısıl güçteki değişimlere oranları da karşılaştırmalı verilmiştir.

Şekil 4'te ve Şekil 5'te hacimsel debi arttıkça, nanoakışkanların basınç düşümü ve pompalama gücünde görülen artışlar, nanoakışkanların hacimsel/kütlesel oranları (nanopartiküllerin) artıkça daha belirgin hale gelmiştir. Bu ise değerlendirmede kullanılan enerji verimliliği performans ölçütlerinin sonuçlarındaki düşmenin, hacimsel orana bağlı değişen nanoakışkanların viskozitelerinin ve yoğunluklarının, TSlara göre artmasından kaynaklandığını göstermektedir.

Ayrıca Tablo 5'te ve Tablo 6'da verilen sayısal sonuçlara göre MK-GBIDde TS suyla karşılaştırıldığında, %0.4 ve %0.8 hacimsel oranlı Al_2O_3-su nanoakışkanlarının PDÖ sonuçları sırasıyla; en az -%5.9 ve -%26.4; en fazla -%60.3 ve -%56.5; ortalama -%27.1 ve -%39 daha düşük iken, bu hacimsel oranlı nanoakışkanların VDÖ sonuçları ise sırasıyla; en düşük 0.40 ve 0.44; en yüksek 0.94 ve 0.74; ortalama 0.73 ve 0.61'dir.

Tablo 3. Levhalı ısı değiştiricilerde nanoakışkanların kullanıldığı deneysel çalışmalar ve önemli sonuçları.

Deney No	*Test bölgesi ve önemli değişkenleri*	*Nanoakışkan (partikül boyutu) Hacimsel/kütlesel oran*	*İşletme koşulları*					*Önemli sonuçlar*
			Isıl koşullar	*Re sayısı*	*Debi*	*Isıl güç (W)*	*Basınç düşümü (Pa)*	
LID-1 (Saleh ve Sundar, 2021)	6 levhalı Balıksırtı açısı: 30° Levha uzunluğu: 480 mm Levha genişliği: 180 mm Levhalar arası mesafe: 2.4 mm	Ni–su (72 nm) Hacimsel: %0.1, %0.3, %0.6	80°C (Sıcak su) 30°C (Nanoakışkan)	300–1000	Sıcak su 3 *l/dk.* Soğuk su 3–7 *l/dk.*	3800–6200	İki fark basınçölçer kullanarak: 50–200	• Sudan-suya deneysel sonuçlar bağıntılarla karşılaştırılmıştır. • Suya göre; hacimsel oran artıkça ısı geçişi iyileşmiştir. • Suya göre; artan hacimsel oran ve Re sayısıyla basınç düşümünün arttığı belirtilmiştir.
LID-2 (Gürbüz vd., 2020)	12 levhalı Balıksırtı açısı: 60° Levha uzunluğu: 208 mm Levha genişliği: 76 mm Levha kalınlığı: 0.4 mm Paslanmaz çelik	Al_2O_3–su (77 nm) CuO–su (78 nm) Al_2O_3+CuO–su (–) Kütlesel: %1 (50:50)	–	1500–4000	3–7 *l/dk.*	7102–19532	Deneysel ölçüm yapılmamış, bağıntılardan hesaplanmış: ~500–1700	• Sudan-suya deneysel sonuçlar bağıntılarla karşılaştırılmamıştır. • Suya göre; Al_2O_3–su, CuO–su ve Al_2O_3+CuO-su için ısı geçişinde ortalama iyileşmeler sırasıyla; %4.6, %8.9 ve %9.5'dir. • Suya göre; nanoakışkanların daha fazla basınç düşümüne neden olduğu ancak, su ve nanoakışkanların basınç düşümleri arasındaki farkın az olduğu belirtilmiştir.
LID-3 (Tiwari vd., 2013)	10 levhalı Balıksırtı açısı: 30° Levha uzunluğu: 355 mm Levha genişliği: 60 mm Levhalar arası mesafe: 2.4 mm Levha kalınlığı: 0.5 mm	CeO_2–su (30 nm) Hacimsel: %0.5, %0.75, %1, %1.5, %3	70°C (Sıcak su) 25–30°C (Nanoakışkan)	–	Sıcak su 1–4 *l/dk.* Soğuk su 1–4 *l/dk.*	2250–4500	Basınçölçer kullanarak: 37–910	• Sudan-suya deneysel sonuçlar bağıntılarla karşılaştırılmamıştır. • Suya göre; ısı geçişinde en yüksek iyileşme %0.75 hacimsel konsantrasyonda %15'dir. • Suya göre; artan konsantrasyonla ve debiyle, basınç düşümünün arttığı belirtilmiştir.

Tablo 4. Gövde borulu ısı değiştiricilerde nanoakışkanların kullanıldığı deneysel çalışmalar ve önemli sonuçları.

Deney No	*Test bölgesi ve önemli değişkenleri*		*Nanoakışkan (partikül boyutu) Hacimsel/kütlesel oran*	*İşletme koşulları*					*Önemli sonuçlar*
				Isıl koşullar	*Re sayısı*	*Debi*	*Isıl güç (W)*	*Basınç düşümü (Pa)*	
GBID-1 (Rostami vd., 2020)	Boru tarafı	21 kanatlı borulu (30^o ve 45^o açılı) Dış çapı: 10 mm Et kalınlığı: 1 mm Uzunluk: 400 mm Kare dizilmiş borular Bakır	Tek duvarlı karbon nanotüp (TDKNT)–su Hacimsel: %1, %5	Gövde tarafı Soğuk (20^oC) Boru tarafı Sıcak (80^oC)	Gövde tarafı – Boru tarafı 850–3300	Gövde tarafı 2.5 *l/dk.* Boru tarafı 2.5–10 *l/dk.*	2250–30000	Deneysel ölçüm yapılmamış, bağıntılardan hesaplanmış: 3–43	• Sudan-suya deneysel sonuçlar bağıntılarla karşılaştırılmamıştır. • Suya göre; kütlesel oranın %1'den %5'e artırılmasının ısı geçişinde önemli bir iyileşmeye sağlamadığı, ancak basınç düşümünü arttırdığı belirtilmiştir.
	Gövde tarafı	İç çap: 150 mm Et kalınlığı: 2 mm Uzunluk: 400 mm Şaşırtma levhasız Paslanmaz çelik							
GBID-2 (Mansoury vd., 2020)	Boru tarafı	15 borulu Dış çapı: 9.5 mm Et kalınlığı: 1.1 mm Uzunluk: 1000 mm Kare dizilmiş borular Paslanmaz çelik	Al_2O_3–su (20 nm) Hacimsel: %0.2, %0.5, %1	Gövde tarafı Soğuk (–) Boru tarafı Sıcak (45^oC)	Gövde tarafı – Boru tarafı 4200–14000	–	5600–8300	Fark basınçölçer kullanarak: 330–6750	• Sudan-suya deneysel ısı geçişi sonuçları bağıntılarla karşılaştırılmıştır. • Suya göre; hacimsel oran %0.2, %0.5 ve %1 için ısı geçişinde ortalama iyileşme sırasıyla %12, %3–%20 ve %4–%24'dür. • Suya göre; hacimsel oran %0.2, %0.5 ve %1 için basınç düşümündeki artış %25, %75 ve %85'dir.
	Gövde tarafı	Dış çap: 114.3 m Et kalınlığı: 3 mm %25 kesme oranlı şaşırtma levhası Boru eksenleri arası mesafe: 18 mm Paslanmaz çelik							
GBID-3 (Karimi vd., 2020)	Boru tarafı	28 borulu Dış çapı: 6.25 mm Et kalınlığı: 0.508 mm Uzunluk: 354 mm Boru eksenleri arası mesafe: 8 mm Bakır	SiC–su (50 nm) Hacimsel: %0.25–%1	Gövde tarafı Sıcak (35,45, 55^oC) Boru tarafı Soğuk (35, 50^oC)	Gövde tarafı – Boru tarafı 350–1100	Gövde tarafı 180 *l/sa.* Boru tarafı 100–300 *l/sa.*	250–750	Fark basınçölçer kullanarak: 440–1620	• Sudan-suya deneysel sonuçlar teorik bağıntılarla karşılaştırılmıştır. • Gövde tarafı 55^oC'de tutulduğunda suya göre; hacimsel oran %0.25, %0.5, %0.75 ve %1 için ısı geçişinde yaklaşık iyileşme sırasıyla %3.2, %6.7, %10.1 ve %19.8'dir. • Artan hacimsel oran ve Re sayısıyla basınç düşümünün de arttığı belirtilmiştir.
	Gövde tarafı	İç çap: 78 mm Et kalınlığı: 3 mm Şaşırtma levhası kesme oranı: %25 Şaşırtma levhalar arası mesafe: 43.75 mm Paslanmaz çelik							

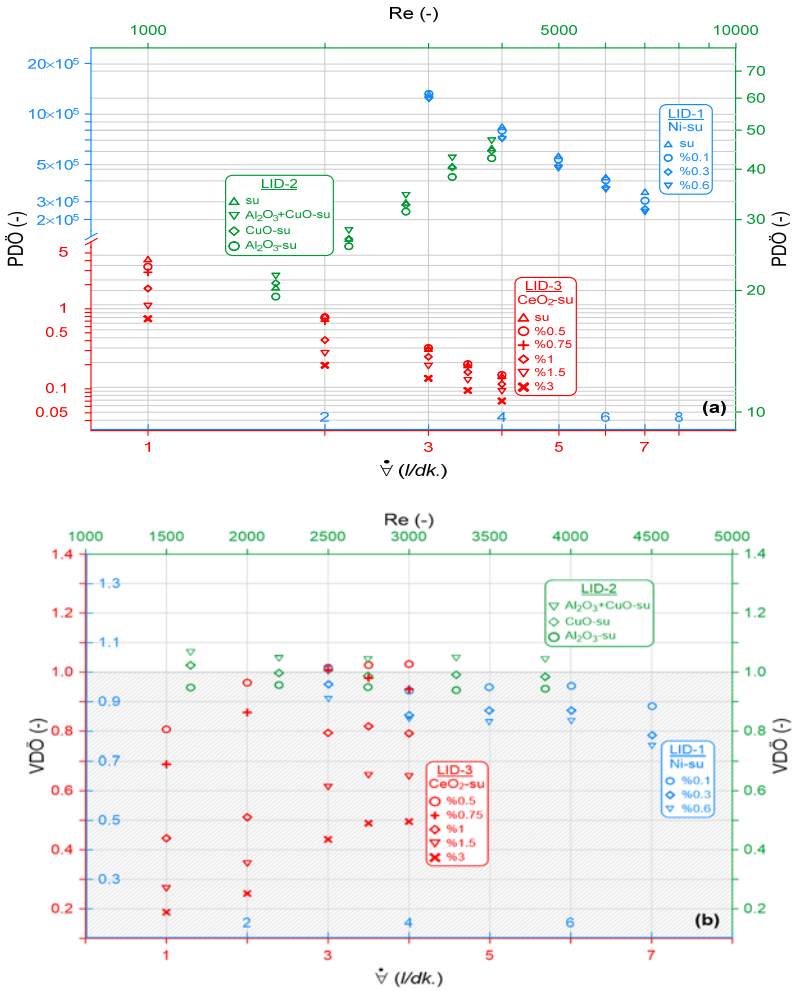

Şekil 4. LIDlerde (a) PDÖnün ve (b) VDÖnün hacimsel debi ve Re sayısına bağlı değişimleri.

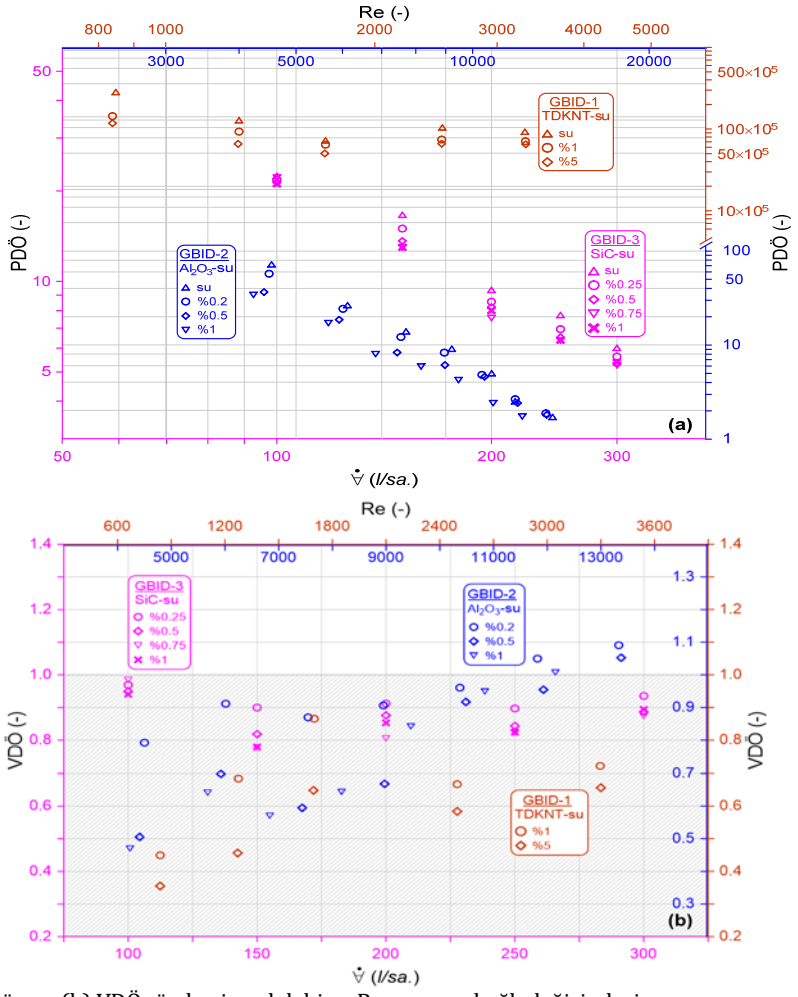

Şekil 5. GBIDlerde (a) PDÖnün ve (b) VDÖnün hacimsel debi ve Re sayısına bağlı değişimleri.

Tablo 5. Mini kanallı gövde borulu ısı değiştirici ile literatürdeki levhalı ısı değiştiricilerin PDÖ ve VDÖ sonuçlarının karşılaştırılması.

MK-GBID (Bu çalışma)						LID-1 (Saleh ve Sundar, 2021)						LID-2 (Gürbüz vd., 2020)						LID-3 (Tiwari vd., 2013)					
	PDÖ			***VDÖ***			***PDÖ***			***VDÖ***			***PDÖ***			***VDÖ***			***PDÖ***			***VDÖ***	
	Su	Al_2O_3-su		Al_2O_3-su			Su	Ni-su		Ni-su			Su	Al_2O_3-su	CuO-su	Al_2O_3-su	CuO-su		Su	CeO_2-su		CeO_2-su	
$\dot{\forall}$ (*l/sa.*)	%0	%0.4	%0.8	%0.4	%0.8	$\dot{\forall}$ (*l/dk.*)	%0	%0.1	%0.6	%0.1	%0.6	Re	%0	%1	%1	%1	%1	$\dot{\forall}$ (*l/dk.*)	%0	%0.5	%3	%0.5	%3
60	25666.06	10179.37	13317.46	0.40	0.52	3	1321260.8	1325428.1	1236802.0	1.01	0.91	1650	20.40	19.33	20.86	0.95	1.02	1	3.59	2.90	0.68	0.81	0.19
		(–%60.3)	**(–%48.1)**					**(+%0.3)**	**(–%6.4)**					**(–%5.2)**	**(+%2.3)**					**(–%19.2)**	**(–%81.1)**		
80	11741.28	7229.00	7890.44	0.62	0.67	4	846363.3	798839.3	710974.6	0.94	0.84	2200	26.95	25.76	26.86	0.96	1.00	2	0.73	0.71	0.19	0.96	0.25
		(–%38.4)	**(–%32.8)**					**(–%5.6)**	**(–%16.0)**					**(–%4.4)**	**(–%0.3)**					**(–%2.7)**	**(–%74.0)**		
100	7002.02	4756.89	3049.32	0.68	0.44	5	565293.8	536596.9	474332.3	0.95	0.83	2750	33.09	31.39	32.64	0.95	0.99	3	0.30	0.30	0.13	1.01	0.44
		(–%32.1)	**(–%56.5)**					**(–%5.1)**	**(–%16.1)**					**(–%5.1)**	**(–%1.4)**					**(%0)**	**(–%56.7)**		
120	4688.87	3804.29	2489.56	0.81	0.53	6	422005.9	403300.3	354556.1	0.95	0.83	3290	40.77	38.27	40.39	0.94	0.99	3.5	0.19	0.19	0.09	1.02	0.49
		(–%18.9)	**(–%46.9)**					**(–%4.4)**	**(–%16.0)**					**(–%6.1)**	**(–%0.9)**					**(%0)**	**(–%52.6)**		
140	3356.62	2624.42	2100.15	0.78	0.63	7	345283.7	304249.3	260132.7	0.88	0.75	3840	45.14	42.59	44.42	0.94	0.98	4	0.14	0.14	0.07	1.03	0.50
		(–%21.8)	**(–%37.4)**					**(–%11.9)**	**(–%24.7)**					**(–%5.6)**	**(–%1.6)**					**(%0)**	**(–%50.0)**		
160	2511.25	2172.17	1624.75	0.86	0.65																		
		(–%13.5)	**(–%35.3)**																				
180	1939.25	1819.72	1167.21	0.94	0.60																		
		(–%6.2)	**(–%39.8)**																				
200	1534.00	1131.35	864.69	0.74	0.56																		
		(–%26.2)	**(–%43.6)**																				
240	1012.74	812.68	621.40	0.80	0.61																		
		(–%19.8)	**(–%38.6)**																				
280	704.83	523.62	518.42	0.74	0.74																		
		(–%25.7)	**(–%26.4)**																				
320	510.17	363.71	362.06	0.71	0.71																		
		(–%28.7)	**(–%29.0)**																				
360	381.00	358.54	250.62	0.94	0.66																		
		(–%5.9)	**(–%34.2)**																				
400	292.17	200.54	149.05	0.69	0.51																		
		(–%31.4)	**(–%49.0)**																				
450	216.67	119.75	131.53	0.55	0.61																		
		(–%44.7)	**(–%39.3)**																				
500	166.20	111.71	119.07	0.67	0.72																		
		(–%32.8)	**(–%28.4)**																				

Not: Parantez içerisindeki sonuçlar nanoakışkanların PDÖlerinin taşıyıcı sıvılara göre iyileşmelerini/kötüleşmelerini göstermektedir.

Tablo 6. Mini kanallı gövde borulu ısı değiştirici ile literatürdeki gövde borulu ısı değiştiricilerin PDÖ ve VDÖ sonuçlarının karşılaştırılması.

MK-GBID (Bu çalışma)						GBID-1 (Rostami vd., 2020)						GBID-2 (Mansoury vd., 2020)						GBID-3 (Karimi vd., 2020)					
	PDÖ			***VDÖ***			***PDÖ***			***VDÖ***			***PDÖ***			***VDÖ***			***PDÖ***			***VDÖ***	
	Su	Al_2O_3-su		Al_2O_3-su			Su	TDKNT-su		TDKNT-su			Su	Al_2O_3-su		Al_2O_3-su			Su	SiC-su		SiC-su	
$\dot{\forall}$ (*l/sa.*)	%0	%0.4	%0.8	%0.4	%0.8	Re	%0	%1	%5	%1	%5	Re	%0	%0.2	%1	%0.2	%1	$\dot{\forall}$ (*l/sa.*)	%0	%0.25	%1	%0.25	%1
60	25666.06	10179.37 **(–%60.3)**	13317.46 **(–%48.1)**	0.40	0.52	850	22798140.3	10242124.3 **(–%55.1)**	8091183.0 **(–%64.5)**	0.45	0.35	4545	72.5	57.4 **(–%20.8)**	34.06 **(–%53.0)**	0.79	0.47	100	22.46	21.77 **(–%3.1)**	21.13 **(–%5.9)**	0.97	0.94
80	11741.28	7229.00 **(–%38.4)**	7890.44 **(–%32.8)**	0.62	0.67	1275	8956140.2	6124806.0 **(–%31.6)**	4085005.1 **(–%54.4)**	0.68	0.46	6125	26.6	24.3 **(–%8.6)**	17.05 **(–%35.9)**	0.91	0.64	150	16.66	14.99 **(–%10.0)**	12.99 **(–%22.0)**	0.90	0.78
100	7002.02	4756.89 **(–%32.1)**	3049.32 **(–%56.5)**	0.68	0.44	1700	4590919.6	3973208.0 **(–%13.5)**	2974861.5 **(–%35.2)**	0.87	0.65	7700	14.0	12.1 **(–%13.6)**	7.96 **(–%43.1)**	0.87	0.57	200	9.38	8.56 **(–%8.7)**	8.01 **(–%14.6)**	0.91	0.85
120	4688.87	3804.29 **(–%18.9)**	2489.56 **(–%46.9)**	0.81	0.53	2500	7061295.5	4708879.4 **(–%33.3)**	4121233.5 **(–%41.6)**	0.67	0.58	9215	9.1	8.3 **(–%8.8)**	5.87 **(–%35.5)**	0.91	0.64	250	7.74	6.94 **(–%10.3)**	6.38 **(–%17.6)**	0.90	0.82
140	3356.62	2624.42 **(–%21.8)**	2100.15 **(–%37.4)**	0.78	0.63	3290	6142507.6	4440298.9 **(–%27.7)**	4029409.5 **(–%34.4)**	0.72	0.66	10775	5.0	4.8 **(–%4.0)**	4.20 **(–%16.0)**	0.96	0.84	300	6.02	5.63 **(–%6.5)**	5.38 **(–%10.6)**	0.94	0.89
160	2511.25	2172.17 **(–%13.5)**	1624.75 **(–%35.3)**	0.86	0.65							11820	2.5	2.6 **(+%4.0)**	2.38 **(–%4.8)**	1.05	0.95						
180	1939.25	1819.72 **(–%6.2)**	1167.21 **(–%39.8)**	0.94	0.60							13690	1.7	1.9 **(+%11.8)**	1.72 **(+%1.2)**	1.09	1.01						
200	1534.00	1131.35 **(–%26.2)**	864.69 **(–%43.6)**	0.74	0.56																		
240	1012.74	812.68 **(–%19.8)**	621.40 **(–%38.6)**	0.80	0.61																		
280	704.83	523.62 **(–%25.7)**	518.42 **(–%26.4)**	0.74	0.74																		
320	510.17	363.71 **(–%28.7)**	362.06 **(–%29.0)**	0.71	0.71																		
360	381.00	358.54 **(–%5.9)**	250.62 **(–%34.2)**	0.94	0.66																		
400	292.17	200.54 **(–%31.4)**	149.05 **(–%49.0)**	0.69	0.51																		
450	216.67	119.75 **(–%44.7)**	131.53 **(–%39.3)**	0.55	0.61																		
500	166.20	111.71 **(–%32.8)**	119.07 **(–%28.4)**	0.67	0.72																		

Not: Parantez içerisindeki sonuçlar nanoakışkanların PDÖlerinin taşıyıcı sıvılara göre iyileşmelerini/kötüleşmelerini göstermektedir.

Tablo 7. Mini kanallı gövde borulu ısı değiştirici ile literatürdeki ısı değiştiricilerin ısıl güçteki ve pompalama gücündeki değişimlerinin karşılaştırılması.

MK-GBID (Bu çalışma)

Al_2O_3-su

	%0.4			***%0.8***		
$\dot{\forall}$ (*l/sa.*)	ΔQ (%)	ΔW_{pg} (%)	$\Delta W_{pg}/\Delta Q$	ΔQ (%)	ΔW_{pg} (%)	$\Delta W_{pg}/\Delta Q$
60	-11.9	122.1	10.3	-11.6	91.3	7.9
80	-18.9	61.7	3.3	-24.0	51.7	2.2
100	-7.7	35.9	4.7	-34.6	24.6	0.7
120	-12.4	8.0	0.6	-27.1	14.2	0.5
140	-11.2	13.6	1.2	-31.9	8.8	0.3
160	-11.8	10.8	0.9	-26.2	14.1	0.5
180	-15.4	3.6	0.2	-25.9	23.1	0.9
200	-16.1	28.5	1.8	-28.1	20.9	0.7
240	-16.1	12.2	0.8	-27.5	18.2	0.7
280	-22.1	9.5	0.4	-24.5	15.3	0.6
320	-18.8	31.6	1.7	-24.1	7.0	0.3
360	-13.9	14.2	1.0	-26.8	16.5	0.6
400	-22.7	21.1	0.9	-26.4	44.3	1.7
450	-24.2	37.1	1.5	-25.5	22.7	0.9
500	-24.0	13.1	0.5	-25.4	4.1	0.2
Ortalama	-16.5	28.2	2.0	-26.0	25.1	1.25

* Basınç düşümleri deneysel ölçülmemiştir. Tüm nanoakışkanlar için bağıntıdan hesaplanan ortalama pompalama gücü kullanılmıştır.

$$\Delta Q = \frac{Q_{na} - Q_{ts}}{Q_{ts}} \times 100, \quad \Delta W_{pg} = \frac{W_{pg,na} - W_{pg,ts}}{W_{pg,ts}} \times 100$$

LID-1 (Saleh ve Sundar, 2021)

Ni-su

	%0.1			***%0.6***		
$\dot{\forall}$ (*l/dk.*)	ΔQ (%)	ΔW_{pg} (%)	$\Delta W_{pg}/\Delta Q$	ΔQ (%)	ΔW_{pg} (%)	$\Delta W_{pg}/\Delta Q$
3	4.8	4.5	0.9	18.1	26.1	1.4
4	3.5	9.6	2.7	13.6	35.3	2.6
5	5.9	11.6	2.0	16.2	38.4	2.4
6	4.9	9.8	2.0	20.5	43.4	2.1
7	7.0	21.5	3.1	21.2	60.8	2.9
Ortalama	5.2	11.4	2.1	17.9	40.8	2.3

LID-2 (Gürbüz vd., 2020)*

	Al_2O_3-su			CuO-su		
	%1			***%1***		
Re	ΔQ (%)	ΔW_{pg} (%)	$\Delta W_{pg}/\Delta Q$	ΔQ (%)	ΔW_{pg} (%)	$\Delta W_{pg}/\Delta Q$
1650	4.7	10.5	2.2	13.1	10.5	0.8
2200	5.7	10.5	1.8	10.2	10.5	1.0
2750	4.9	10.5	2.1	9.1	10.5	1.2
3290	3.8	10.5	2.8	9.5	10.5	1.1
3840	4.3	10.5	2.4	8.8	10.5	1.2
Ortalama	4.7	10.5	2.3	10.1	10.5	1.1

LID-3 (Tiwari vd., 2013)

CeO_2-su

	%0.5			***%3***		
$\dot{\forall}$ (*l/dk.*)	ΔQ (%)	ΔW_{pg} (%)	$\Delta W_{pg}/\Delta Q$	ΔQ (%)	ΔW_{pg} (%)	$\Delta W_{pg}/\Delta Q$
1	3.9	28.9	7.4	2.2	442.0	200.9
2	4.5	8.4	1.9	2.9	307.9	106.2
3	9.4	7.8	0.8	7.3	146.6	20.1
3.5	7.9	5.4	0.7	5.9	116.1	19.7
4	7.9	5.1	0.6	5.4	112.5	20.8
Ortalama	6.7	11.1	2.3	4.7	225.0	73.5

GBID-1 (Rostami vd., 2020)

TDKNT-su

	%1			***%5***		
Re	ΔQ (%)	ΔW_{pg} (%)	$\Delta W_{pg}/\Delta Q$	ΔQ (%)	ΔW_{pg} (%)	$\Delta W_{pg}/\Delta Q$
850	176.1	514.6	2.9	138.4	571.8	4.1
1275	227.7	379.3	1.7	164.3	479.4	2.9
1700	248.5	302.7	1.2	173.1	321.5	1.9
2500	42.8	114.2	2.7	30.5	123.6	4.1
3290	23.2	70.5	3.0	16.6	77.7	4.7
Ortalama	143.7	276.3	2.3	104.6	314.8	3.5

GBID-2 (Mansoury vd., 2020)

Al_2O_3-su

	%0.2			***%1***		
Re	ΔQ (%)	ΔW_{pg} (%)	$\Delta W_{pg}/\Delta Q$	ΔQ (%)	ΔW_{pg} (%)	$\Delta W_{pg}/\Delta Q$
4545	9.9	38.7	3.9	23.1	162.0	7.0
6125	9.5	20.1	2.1	23.8	93.1	3.9
7700	7.4	23.5	3.2	3.5	81.6	23.3
9215	2.0	12.6	6.3	4.1	61.8	15.1
10775	0.1	4.1	41.0	1.6	20.7	12.9
11820	12.2	6.9	0.6	17.7	24.0	1.4
13690	5.8	-3.0	0.5	4.6	3.8	0.8
Ortalama	6.7	14.7	8.2	11.2	63.9	9.2

GBID-3 (Karimi vd., 2020)

SiC-su

	%0.25			***%1***		
$\dot{\forall}$ (*l/sa.*)	ΔQ (%)	ΔW_{pg} (%)	$\Delta W_{pg}/\Delta Q$	ΔQ (%)	ΔW_{pg} (%)	$\Delta W_{pg}/\Delta Q$
100	2.0	5.2	2.6	10.8	17.8	1.6
150	2.3	13.7	6.0	12.6	44.5	3.5
200	2.4	12.3	5.1	19.3	39.9	2.1
250	1.8	13.5	7.5	10.5	34.0	3.2
300	2.9	10.1	3.5	16.4	30.2	1.8
Ortalama	2.3	11.0	4.9	13.9	33.3	2.4

Benzer şekilde, LID-1 için %0.1 ve %0.6 hacimsel oranlı Ni-su nanoakışkanlarının PDÖ sonuçları sırasıyla; en az %0.3 ve -%6.4; en fazla -%11.9 ve -%24.7; ortalama -%5.3 ve -%15.8 farklı/daha düşük iken, bu hacimsel oranlı nanoakışkanların VDÖ sonuçları ise sırasıyla; en düşük 0.88 ve 0.75; en yüksek 1.01 ve 0.91; ortalama 0.95 ve 0.83, LID-2 için %1 hacimsel oranlı Al_2O_3-su ve CuO-su nanoakışkanlarının PDÖ sonuçları sırasıyla; en az -%4.4 ve %2.3; en fazla -%6.1 ve -%1.6; ortalama -%5.3 ve -%0.4 farklı/daha düşük iken, bu nanoakışkanların VDÖ sonuçları ise sırasıyla; en düşük 0.94 ve 0.98; en yüksek 0.96 ve 1.02 ; ortalama 0.95 ve 1.00, LID-3 için %0.5 ve %3 hacimsel oranlı CeO_2-su nanoakışkanlarının PDÖ sonuçları sırasıyla; en az %0.0 ve -%50; en fazla -%19.2 ve -%81.1; ortalama -%4.4 ve -%62.9 farklı/daha düşük iken, bu hacimsel oranlı nanoakışkanların VDÖ sonuçları ise sırasıyla; en düşük 0.81 ve 0.19; en yüksek 1.03 ve 0.50; ortalama 0.97 ve 0.37'dir.

GBID-1 için %1 ve %5 hacimsel oranlı TDKNT-su nanoakışkanlarının PDÖ sonuçları sırasıyla; en az -%13.5 ve -%34.4; en fazla -%55.1 ve -%64.5; ortalama -%32.2 ve -%46.0 daha düşük iken, bu hacimsel oranlı nanoakışkanların VDÖ sonuçları ise sırasıyla; en düşük 0.45 ve 0.35; en yüksek 0.87 ve 0.66; ortalama 0.68 ve 0.54, GBID-2 için %0.2 ve %1 hacimsel oranlı Al_2O_3-su nanoakışkanlarının PDÖ sonuçları sırasıyla; en az %11.8 ve %1.2; en fazla -%20.8 ve -%53; ortalama -%5.7 ve -%26.7 farklı/daha düşük iken, bu hacimsel oranlı nanoakışkanların VDÖ sonuçları ise sırasıyla; en düşük 0.79 ve 0.47; en yüksek 1.09 ve 1.01; ortalama 0.94 ve 0.73, GBID-3 için %0.25 ve %1 hacimsel oranlı SiC-su nanoakışkanlarının PDÖ sonuçları sırasıyla; en az -%3.1 ve -%5.9; en fazla -%10.3 ve -%22; ortalama -%7.7 ve -%14.2 daha düşük iken, bu hacimsel oranlı nanoakışkanların VDÖ sonuçları ise sırasıyla; en düşük 0.90 ve 0.78; en yüksek 0.97 ve 0.94; ortalama 0.92 ve 0.86'dır.

Tablo 7'deki sayısal sonuçlara göre de MK-GBIDde TS su ile karşılaştırıldığında Al_2O_3-su nanoakışkanlarıyla ısıl güçteki değişimler (ΔQ), pompalama gücündeki değişimler (ΔW_{pg}) ve pompalama gücündeki değişimlerin ısıl güçteki değişimlere oranları ($\Delta W_{pg}/\Delta Q$) sırasıyla; %0.4 hacimsel oranda en fazla -%24.2 ve en az -%7.7, en az %3.6 ve en fazla %122.1 ve en düşük 0.2 kat ve en yüksek 10.3 kat iken; %0.8 hacimsel oranda ise en fazla -%34.6 ve en az -%11.6, en az %4.1 ve en fazla %91.3 ve en düşük 0.2 kat ve en yüksek 7.9 kattır.

Benzer şekilde LID-1'de %0.1 hacimsel oranlı Ni-su nanoakışkanı için sırasıyla; en fazla %7.0 ve en az %3.5, en az %4.5 ve en fazla %21.5 ve en düşük 0.9 kat ve en yüksek 3.1 kat iken; %0.6 hacimsel oranlı Ni-su nanoakışkanı için sırasıyla; en fazla %21.2 ve en az %13.6, en az %26.1 ve en fazla %60.8 ve en düşük 1.4 kat ve en yüksek 2.9 kattır. LID-2'de %1 hacimsel oranlı Al_2O_3-su nanoakışkanı için sırasıyla; en fazla %5.7 ve en az %3.8, ortalama %10.5 ve en düşük 1.8 kat ve en yüksek 2.8 kat iken; %1 hacimsel oranlı CuO-su nanoakışkanı için sırasıyla; en fazla %13.1 ve en az %8.8, ortalama %10.5 ve en düşük 0.8 kat ve en yüksek 1.2 kattır. LID-3'te %0.5 hacimsel oranlı CeO_2-su nanoakışkanı için sırasıyla; en fazla %9.4 ve en az %3.9, en az %5.1 ve en fazla %28.9 ve en düşük 0.6 kat ve en yüksek 7.4 kat iken; %3 hacimsel oranlı CeO_2-su nanoakışkanı için sırasıyla; en fazla %7.3 ve en az %2.2, en az %112.5 ve en fazla %442 ve en düşük 19.7 kat ve en yüksek 200.9 kattır.

GBID-1'de %1 hacimsel oranlı TDKNT-su nanoakışkanı için sırasıyla; en fazla %248.5 ve en az %23.2, en az %70.5 ve en fazla %514.6 ve en düşük 1.2 kat ve en yüksek 3 kat iken; %5 hacimsel oranlı TDKNT-su nanoakışkanı için sırasıyla; en fazla %173.1 ve en az %16.6, en az %77.7 ve en fazla %571.8 ve en düşük 1.9 kat ve en yüksek 4.7 kattır. GBID-2'de %0.2 hacimsel oranlı Al_2O_3-su nanoakışkanı için sırasıyla; en fazla %12.2 ve en az %0.1, en az -%3 ve en fazla %38.7 ve en düşük 0.5 kat ve en yüksek 41 kat iken; %1 hacimsel oranlı Al_2O_3-su nanoakışkanı için sırasıyla; en fazla %23.8 ve en az %1.6, en az %3.8 ve en fazla %162 ve en düşük 0.8 kat ve en yüksek 23.3 kattır. GBID-3'te %0.25 hacimsel oranlı SiC-su nanoakışkanı için sırasıyla; en fazla %2.9 ve en az %1.8, en az %5.2 ve en fazla %13.7 ve en düşük 2.6 kat ve en yüksek 7.5 kat iken; %1 hacimsel oranlı SiC-su nanoakışkanı için sırasıyla; en fazla %19.3 ve en az %10.5, en az %17.8 ve en fazla %44.5 ve en düşük 1.6 kat ve en yüksek 3.5 kattır.

Tablo 5-7'de verilen ve yukarıda özetlenen sonuçlara göre nanopartikül oranı yüksek nanoakışkanların, PDÖ ve VDÖ sonuçları, düşük nanopartikül oranlı nanoakışkanların sonuçlarından daha kötüdür. Ayrıca nanoakışkanların nanopartikül oranı artıkça, yoğunlukları da artmakla birlikte, nanoakışkanların özgül ısıları da azalmaktadır. Başka bir ifadeyle aynı hacimsel debide TS suya göre yüksek nanopartikül oranlı nanoakışkanların yoğunluğundaki artışla, kütlesel debileri artarken, nanoakışkanların özgül ısısındaki azalma nedeniyle ısı taşıma kapasiteleri aynı oranda artmamaktadır. Yani nanopartikül oranındaki artış, TS suya göre nanoakışkanın ısı taşıma kapasitesi bakımından yoğunluktaki artışla olumlu etki yaparken, özgül ısısındaki azalma bu olumlu etkiyi kısmen kötüleştirmektedir.

Çalışmamızdan elde ettiğimiz PDÖ ve VDÖ sonuçları (Şekil 2, Şekil 3, Tablo 5-7), Tablo 3'te ve Tablo 4'te verilen literatürdeki deneysel çalışmaların hesaplanan PDÖ ve VDÖ sonuçlarıyla (Şekil 4, Şekil 5, Tablo 5-7) uyumlu olarak, tek fazlı ısı geçişi uygulamalarında nanoakışkanları kullanmanın enerji verimliliği bakımından anlamlı olmadığını göstermektedir. Yani ısıl güç ve pompalama gücü, ilk yatırım ve işletme (enerji) maliyetleri bir arada dikkate alındığında, deneysel çalışmamızın sonuçları ve literatürdeki diğer deneysel çalışmaların sonuçları, mühendislik sistemleri olan endüstriyel uygulamalarda, nanoakışkanları kullanmanın uygun olmadığını söylemektedir. Bu nedenle, ısıl sistemlerde aracı akışkana aktarılan ısıl güç ve akışın devamı için gerekli pompalama gücü arasındaki ilişkiyi birlikte değerlendirmek, taşınımla ısı geçişindeki iyileşmenin enerji maliyetlerine etkisini daha açık temsil edecektir. Bu sonuçlar, diğer dezavantajları (hazırlama maliyeti, birikme, çökelme ve kanalların tıkanması gibi) da göz önüne alındığında, iddia edilenin aksine, ısıl sistemlerde ve endüstriyel tek fazlı ısı geçişi uygulamalarında TSların yerine nanoakışkanların kullanılmaması gerektiğini göstermektedir.

DEĞERLENDİRME

Bu çalışmada, MK-GBIDde, boru tarafındaki soğuyan Al_2O_3-su nanoakışkanlarının ısı geçişi (ısıl güç) ve basınç düşümü (pompalama gücü) sonuçları deneysel incelenmiştir. Enerji verimliliği bakımından ısı geçişi ve pompalama gücü arasındaki ilişkiyi/dengeyi tanımlayan iki farklı termo-hidrodinamik performans ölçütüyle (PDÖ ve VDÖ), nanoakışkanların ısıl ve hidrodinamik bakımdan KSTSlara göre olumlu ve olumsuz etkileri değerlendirilmiştir. Ayrıca nanoakışkanlarla ilgili literatürden, ısıl güç ve hidrodinamik performansla ilgi yeterli deneysel veriye ulaşılabilen çalışmalar gözden geçirilerek, deneysel çalışmamızdaki

termo-hidrodinamik enerji verimliliği performans ölçütü sonuçları desteklenmiştir.

Çalışmamızdaki MK-GBIDde deneysel performansları incelenen %0.2, %0.4 ve %0.8 hacimsel oranlı Al_2O_3-su nanoakışkanlarından TS suya en yakın performans sonuçlarını, %0.4 hacimsel oranlı nanoakışkan göstermiştir. TS suyla karşılaştırıldığında, %0.4 hacimsel oranlı nanoakışkanının PDÖ sonuçları en az -%5.9, en fazla -%60.3 ve ortalama -%27.1 farklıdır. Bu hacimsel oranlı nanoakışkanın VDÖ sonuçları ise en düşük 0.40, en yüksek 0.94 ve ortalama 0.73'tür.

Ayrıca %0.4 hacimsel oranlı Al_2O_3-su nanoakışkanı TS suyla karşılaştırıldığında ısıl güçteki ortalama değişim ΔQ= -%16.5, pompalama gücündeki ortalama değişim ΔW_{pg}= +%28.2 ve pompalama gücündeki değişimin ısıl güçteki değişime oranlarının ortalaması ise $\Delta W_{pg}/\Delta Q$ = 2.0'dır. Yani %0.4 hacimsel oranlı Al_2O_3-su nanoakışkanı için TS suya göre ısıl güçlerin ortalaması %16.5 azalırken, pompalama güçlerinin ortalaması %28.2 artmaktadır. Dolayısıyla pompalama güçlerindeki artışların ısıl güçlerdeki artışlara oranlarının ortalaması da TS suya göre 2 kat artmıştır.

Aynı hacimsel debide (ortalama akış hızında); nanoakışkanların KSTSlara göre daha büyük pompalama gücü gereksinimleri, nanoakışkanların artan nanopartikül oranıyla, viskozitenin ve yoğunluğun artmasıyla ve özgül ısının azalmasıyla açıklanmıştır. Yani nanoakışkanlarla artan viskoziteye bağlı olarak, yükselen akış kaynaklı basınç düşümleri nedeniyle, aynı hacimsel debideki pompalama gücü gereksinimi KSTSdan daha büyüktür. Tam tersine aynı hacimsel debide, yoğunluktaki artışa bağlı olarak nanoakışkanlarla artan kütlesel debilere rağmen, özgül ısılardaki azalma nedeniyle nanoakışkanların ısı taşıma kapasiteleri aynı oranda artmamaktadır.

Hem deneysel çalışmamızdaki Al_2O_3-su nanoakışkanları hem de literatürden seçilen diğer deneysel çalışmalardaki Ni-su, Al_2O_3-su, CuO-su, Al_2O_3+CuO-su, CeO_2-su, TDKNT-su ve SiC-su nanoakışkanlarının ısı geçişi ve basınç düşümü verileri kullanılarak, aynı hacimsel debilerde/Re sayılarında hesaplanan PDÖ ve VDÖ sonuçları, nanoakışkanların performanslarının KSTSlara göre daha düşük olduğunu göstermektedir. Bu sonuç, endüstriyel tesislerin enerji bütçesi bakımından, nanoakışkanların dezavantajlı olduğu anlamına gelmektedir. Dolayısıyla nanoakışkanların kullanılması, enerji verimliliği bakımından bu dezavantajlarının önemsiz olduğu özel uygulamalarda (enerji maliyetlerinin önemsiz, yüksek ısı akılarının öncelikli olduğu gibi) söz konusu olabilir.

Sonuç olarak, belirli bir ısıl görevin yerine getirilmesinde, KSTSların yerine nanoakışkanların kullanılması amacıyla yapılacak değerlendirmelerde, her iki durumda akışın devamı için gerekli pompalama gücü göz önünde bulundurulmalıdır. Isıl sistemlerde kullanılacak nanoakışkanlar gibi yeni aracı akışkanlar ya da farklı iyileştirme yöntemleri değerlendirilirken, sistemin genel enerji veriminde etkili, pompalama gücü gibi faktörleri de göz önünde bulunduran bir yaklaşım izlenmelidir. Ayrıca, tüm ısıl sistem ve borulama devresi dikkate alındığında (yani tüm borular, vanalar, ısı değiştiriciler gibi) bu etkinin daha da önem kazanacağına dikkat edilmelidir.

BİLGİLENDİRME

Çalışmadaki deneysel veriler, yazarların yazılı onayı olmadan kullanılamaz.

KAYNAKLAR

Albadr, J., Tayal, S., & Alasadi, M. (2013). Heat transfer through heat exchanger using Al_2O_3 nanofluid at different concentrations. *Case Studies in Thermal Engineering*, 1(1), 38–44.

Anoop, K. B., Kabelac, S., Sundararajan, T., & Das, S. K. (2009). Rheological and flow characteristics of nanofluids: Influence of electroviscous effects and particle agglomeration. *Journal of Applied Physics*, 106(3), 034909.

Barzegarian, R., Aloueyan, A., & Yousefi, T. (2017). Thermal performance augmentation using water based Al_2O_3-gamma nanofluid in a horizontal shell and tube heat exchanger under forced circulation. *International Communications in Heat and Mass Transfer*, 86, 52–59.

Bianco, V., Manca, O., & Nardini, S. (2011). Numerical investigation on nanofluids turbulent convection heat transfer inside a circular tube. *International Journal of Thermal Sciences*, 50(3), 341–349.

Chand, R. (2017). *Nanofluid Technologies and Thermal Convection Techniques*. IGI Global, USA.

Choi, S. U. S. (2009). Nanofluids: From Vision to Reality Through Research. *Journal of Heat Transfer*, 131(3), 03310.

Das, S. K., Choi, S. U. S., & Patel, H. E. (2006). Heat Transfer in Nanofluids-A Review. *Heat Transfer Engineering*, 27(10), 3–19.

Das, S. K., Choi, S. U. S., Yu, W., & Pradeep, T. (2007). *Nanofluids*. John Wiley & Sons, Inc., Hoboken.

Del Col, D., Cavallini, A., Da Riva, E., Mancin, S., & Censi, G. (2010). Shell-and-tube minichannel condenser for low refrigerant charge. *Heat Transfer Engineering*, 31(6), 509–517.

Farajollahi, B., Etemad, S. G., & Hojjat, M. (2010). Heat transfer of nanofluids in a shell and tube heat exchanger. *International Journal of Heat and Mass Transfer*, 53(1–3), 12–17.

Ferrouillat, S., Bontemps, A., Ribeiro, J.-P., Gruss, J.-A., & Soriano, O. (2011). Hydraulic and heat transfer study of SiO_2/water nanofluids in horizontal tubes with imposed wall temperature boundary conditions. *International Journal of Heat and Fluid Flow*, 32(2), 424–439.

Ghadimi, A., Saidur, R., & Metselaar, H. S. C. (2011). A review of nanofluid stability properties and characterization in stationary conditions. *International Journal of Heat and Mass Transfer*, 54(17–18), 4051–4068.

Gonçalves, I., Souza, R., Coutinho, G., Miranda, J., Moita, A., Pereira, J. E., Moreira, A., & Lima, R. (2021). Thermal conductivity of nanofluids: A Review on prediction models, controversies and challenges. *Applied Sciences*, 11(6), 2525.

Gupta, S. K., Verma, H., & Yadav, N. (2022). A review on recent development of nanofluid utilization in shell & tube heat

exchanger for saving of energy. *Materials Today: Proceedings*, 54, 579–589.

Gürbüz, E. Y., Sözen, A., Variyenli, H. İ., Khanlari, A., & Tuncer A. D. (2020). A comparative study on utilizing hybrid-type nanofluid in plate heat exchangers with different number of plates. *Journal of the Brazilian Society of Mechanical Sciences and Engineering*, 42(10), 524.

Hejcik J., & Jicha M. (2014). Single phase heat transfer in minichannels. *EPJ Web of Conferences*, 67, 02034.

Ho, C. J., Liu, W. K., Chang, Y. S., & Lin, C. C. (2010). Natural convection heat transfer of alumina-water nanofluid in vertical square enclosures: An experimental study. *International Journal of Thermal Sciences*, 49(8), 1345–1353.

Hunter, R. J. (2002). *Foundations of Colloid Science*, Oxford University Press, New York.

İnternet, (2023). Accuratus Corporation, Alumox, https://www.accuratus.com/pdf/995aluminaprops.pdf.

Kabeel, A. E., & Abdelgaied M. (2016). Overall heat transfer coefficient and pressure drop in a typical tubular exchanger employing alumina nano-fluid as the tube side hot fluid. *Heat and Mass Transfer*, 52(8), 1417–1424.

Kakaç, S., Liu, H., & Pramuanjaroenkij, A. (2012). *Heat Exchangers: Selection, Rating, and Thermal Design* (Third Ed.). CRC Press, New York.

Kandlikar, S. G. (2007). A roadmap for implementing minichannels in refrigeration and air-conditioning systems-Current status and future directions. *Heat Transfer Engineering*, 28(12), 973–985.

Kandlikar, S. G., & Grande, W. J. (2003). Evolution of microchannel flow passages-thermohydraulic performance and fabrication technology. *Heat Transfer Engineering*, 24(1), 3–17.

Karimi, S., Heyhat, M. M., Isfahani, A. H. M., & Hosseinian, A. (2020). Experimental investigation of convective heat transfer and pressure drop of SiC/water nanofluid in a shell and tube heat exchanger. *Heat and Mass Transfer*, 56(8), 2325–2331.

Kern, D. Q. (1950). *Process Heat Transfer*, McGraw-Hill, New York.

Kline, S. J., & Mcclintock, F. A. (1953). Describing uncertainties in single sample experiments. *Mechanical Engineering*, 75(1), 3–8.

Kücük, H., Ünverdi, M., & Senan, Yılmaz, M. (2019). Experimental investigation of shell side heat transfer and pressure drop in a mini-channel shell and tube heat exchanger. *International Journal of Heat and Mass Transfer*, 143, 118493.

Kumar, N., Sonawane, S. S., & Sonawane, S. H. (2018). Experimental study of thermal conductivity, heat transfer and friction factor of Al_2O_3 based nanofluid. *International Communications in Heat and Mass Transfer*, 90, 1–10.

Ma, L., Yang, J., Liu, W., & Zhang, X. (2014). Physical quantity synergy analysis and efficiency evaluation criterion of heat transfer enhancement. *International Journal of Thermal Sciences*, 80, 23–32.

Mansoury, D., Doshmanziari, F. I., Kiani, A., Chamkha, A. J., & Sharifpur, M. (2020). Heat Transfer and Flow Characteristics of Al_2O_3/Water Nanofluid in Various Heat Exchangers: Experiments on Counter Flow. *Heat Transfer Engineering*, 41(3), 220–234.

Minkowycz, W. J., Sparrow, E., & Abraham, J. P. (2013). *Nanoparticle Heat Transfer and Fluid Flow*. CRC Press, New York.

Pak, B. C., & Cho Y. I. (1998). Hydrodynamic and Heat Transfer Study of Dispersed Fluids with Submicron Metallic Oxide Particles. *Experimental Heat Transfer*, 11(2), 151–170.

Pandey, S. D., & Nema V. K. (2012). Experimental analysis of heat transfer and friction factor of nanofluid as a coolant in a corrugated plate heat exchanger. *Experimental Thermal and Fluid Science*, 38, 248–256.

Prasher, R., Phelan, P. E., & Bhattacharya, P. (2006). Effect of Aggregation Kinetics on the Thermal Conductivity of Nanoscale Colloidal Solutions (Nanofluid). *Nano Letters*, 6(7), 1529–1534.

Rostami, M. H., Najafi, G., Ghobadin, B., & Motevali, A. (2020). Thermal performance investigation of SWCNT and graphene quantum dots nanofluids in a shell and tube heat exchanger by using fin blade tubes. *Heat Transfer*, 49(8), 4783–4800.

Russel, W. B., Saville, D. A., & Schowalter, W. R. (1989). *Colloidal Dispersions*. Cambridge University Press, New York.

Saidur, R., Leong, K. Y., & Mohammed, H. A. (2011). A review on applications and challenges of nanofluids. *Renewable and Sustainable Energy Reviews*, 15(3), 1646–1668.

Saleh, B., & Sundar, L. S. (2021). Experimental study on heat transfer, friction factor, entropy and exergy efficiency analyses of a corrugated plate heat exchanger using Ni/water nanofluids. *International Journal of Thermal Sciences*, 165, 106935.

Sekhar, Y. R., & Sharma, K. V. (2015). Study of viscosity and specific heat capacity characteristics of water-based Al_2O_3 nanofluids at low particle concentrations. *Journal of Experimental Nanoscience*, 10(2), 86–102.

Sergis, A., & Hardalupas, Y. (2011). Anomalous heat transfer modes of nanofluids: a review based on statistical analysis. *Nanoscale Research Letters*, 6(1), 391.

Shahrul, I. M., Mahbubul, I. M., Saidur, R., & Sabri, M. F. M. (2016). Experimental investigation on Al_2O_3-W, SiO_2-W and ZnO-W nanofluids and their application in a shell and tube heat exchanger. *International Journal of Heat and Mass Transfer*, 97, 547–558.

Sharma, A. K., Tiwari, A. K., & Dixit, A. R. (2016). Rheological behavior of nanofluids: A review. *Renewable and Sustainable Energy Reviews*, 53, 779–791.

Somiya, S. (1989). *Advanced Technical Ceramics*. Academic Press, California.

Tiwari, A. K., Ghosh, P., & Sarkar, J. (2013). Heat transfer and pressure drop characteristics of CeO_2/water nanofluid in plate heat exchanger. *Applied Thermal Engineering*, 57(1–2), 24–32.

Trang, N. V., Trung, D. T., & Dzung, D. V. (2017). Experimental Study of Alternative Minichannel Heat Exchanger for Scooter Radiator. *International Journal of Emerging Research in Management and Technology*, 6(4), 46–50.

Unverdi, M., & Islamoglu, Y. (2017). Characteristics of heat transfer and pressure drop in a chevron-type plate heat exchanger with Al_2O_3/water nanofluids. *Thermal Science*, 21(6 Part A), 2379–2391.

Ünverdi, M., Kücük, H., & Yılmaz, M. S. (2019). Experimental investigation of heat transfer and pressure drop in a mini-channel shell and tube heat exchanger. *Heat and Mass Transfer*, 55, 1271–1286.

Van de Bor, D. M. (2014). *Mini-channel heat exchangers for industrial distillation processes*. Ph.D. Thesis, Delft University of Technology, Delft.

Wadekar, V. V. (2005). Heat Exchangers in Process Industry and Mini- and Microscale Heat Transfer. *Proceedings of Fifth International Conference on Enhanced, Compact and Ultra-Compact Heat Exchangers: Science, Engineering and Technology*, USA, 318–322.

Wang, X.-Q., & Mujumdar, A. S. (2007). Heat transfer characteristics of nanofluids: a review. *International Journal of Thermal Sciences*, 46(1), 1–19.

Webb, R. L., & Kim, N. H. (2005). *Principles of Enhanced Heat Transfer* (2nd Ed.), Taylor and Francis, New York.

Yılmaz, M. S., Ünverdi, M., Kücük, H., Akcakale, N., & Halıcı, F. (2022). Enhancement of heat transfer in shell and tube heat exchanger using mini-channels and nanofluids: An experimental study. *International Journal of Thermal Sciences*, 179, 107664.

Zhang, J., Zhu, X., Mondejar, M. E., & Haglind F. (2019). A review of heat transfer enhancement techniques in plate heat exchangers. *Renewable and Sustainable Energy Reviews*, 101, 305–328.

Zhou, S.-Q., & Ni, R. (2008). Measurement of the specific heat capacity of water-based Al_2O_3 nanofluid. *Applied Physics Letters*, 92(9), 093123.

Journal Homepage: https://dergipark.org.tr/tr/pub/isibted

Isı Bilimi ve Tekniği Dergisi

Archive: https://tibtd.org.tr/dergi

Experimental Investigation of Effects of Nanorefrigerants on Vapor Compression Refrigeration System Using R1234yf Instead of R134a

Kemal BİLEN [1, *], Kayhan DAĞIDIR [2], Erol ARCAKLIOĞLU [1]

[1] *Ankara Yıldırım Beyazıt Üniversitesi, Mühendislik ve Doğa Bilimleri Fakültesi, Makine Mühendisliği Bölümü, Keçiören, 06010, Ankara, Türkiye*
[2] *Tarsus Üniversitesi, Mühendislik Fakültesi, Makine Mühendisliği Bölümü, Tarsus, 33400, Mersin, Türkiye*

A R T I C L E I N F O

2024, vol. 44, no.2, pp. 280-293

doi: 10.47480/isibted.1563896

Research Article
Received: 17 July 2023
Accepted: 07 September 2024

* *Corresponding Author*
e-mail: kemal.bilen@aybu.edu.tr

Keywords:
R134a and R1234yf
Al_2O_3
Graphene
CNT
VCRS

ORCID Numbers in author order:
0000-0003-1775-7977
0000-0003-0499-1764
0000-0001-8073-5207

A B S T R A C T

In this study, the refrigerant R1234yf was subjected to experimental investigation in conjunction with a variety of nanoparticles as a potential alternative to R134a in a vapor compression refrigeration system. Initially, the performance of pure R1234yf was evaluated in the absence of modifications to the VCRS, employing energy and exergy analyses. The results demonstrated that R1234yf resulted in a 9% increase in compressor power input, an 8% reduction in cooling capacity, and a 17% decrease in EER in comparison to R134a. Furthermore, the second law efficiency exhibited a decline of 8%. In order to address these declines, Al_2O_3, graphene, and CNT nanoparticles were introduced to the VCRS with R1234yf via compressor oil at varying mass fractions. The greatest improvement in system performance was observed with the addition of 0.250% graphene by mass. This resulted in a 24% and 14% enhancement in cooling capacity and an increase in EER by 32% and 13%, respectively, when compared to pure R1234yf and R134a. The second law efficiency exhibited a slight improvement with the addition of graphene.

R134a Yerine R1234yf Kullanılan Buhar Sıkıştırmalı Soğutma Sisteminde Nanosoğutucu Akışkanların Etkilerinin Deneysel Olarak İncelenmesi

M A K A L E B İ L G İ S İ

Anahtar Kelimeler:
R134a ve R1234yf
Al_2O_3
Grafen
CNT
BSSS

Ö Z E T

Bu çalışmada, soğutucu akışkan R1234yf, buhar sıkıştırmalı bir soğutma sisteminde (BSSS'nde) R134a'ya potansiyel bir alternatif olarak çeşitli nanopartiküllerle birlikte deneysel olarak incelemeye tabi tutulmuştur. Başlangıçta, saf R1234yf'nin performansı, enerji ve ekserji analizleri kullanılarak BSSS'de değişiklik yapılmadan değerlendirilmiştir. Sonuçlar, R1234yf'nin R134a'ya kıyasla kompresör güç girişinde %9 artışa, soğutma kapasitesinde %8 azalmaya ve EER'de %17 düşüşe neden olduğunu göstermiştir. Ayrıca, ikinci yasa verimliliği %8'lik bir düşüş sergilemiştir. Bu düşüşleri gidermek için, Al_2O_3, grafen ve CNT nanopartikülleri, değişen kütlesel karışım oranlarında kompresör yağı aracılığıyla R1234yf içeren BSSS'ye eklenmiştir. Sistem performansındaki en iyi iyileşme kütlece %0,250 grafen ilavesinde gözlenmiştir. Kütlece %0,250 grafen ilave edilen sistem, saf R1234yf ve R134a'lı durumlarla karşılaştırıldığında soğutma kapasitesinde sırasıyla %24 ve %14'lük ve EER'de %32 ve %13'lük bir artış göstermiştir. İkinci yasa verimliliğinde ise grafen ilavesi ile küçük miktarda bir iyileşme gözlenmiştir.

NOMENCLATURE

CFC	Clorofluorocarbon
EER	Energy Efficiency Ratio
EEV	Electronic Expansion Valve
Ex	Exergy (kJ)
η	Efficiency
GWP	Global Warming Potential
h	Specific enthalpy (kJ/kg)
HCFC	Hydrocloroflorocarbon
HCFCs	Hydrocloroflorocarbons
HFC	Hydroflorocarbon
HFCs	Hydroflorocarbons
$\dot{m}$	Mass (kg/s)
ODP	Ozone Depletion Potential
P	Pressure (Pa)
POE	Polyolester
$\dot{Q}$	Heat transfer rate (kW)
R	Magnitude of any calculated dependent variables
S	Specific entropy [kJ/(kg·K)]
T	Temperature (K or °C)
u	Uncertainty
UNEP	United Nations Environment Programme
VCRC	Vapor Compression Refrigeration Cycle
VCRCs	Vapor Compression Refrigeration Cycles
VCRS	Vapor Compression Refrigeration System
VCRSs	Vapor Compression Refrigeration Systems
$\dot{W}$	Work (kW)
x	Independent variable

Subscripts

0	Medium
c	Condensation process
e	Evaporation process
in	Inlet
isen	Isentropic
out	Outlet
R	Refrigerant
s	Constant entropy process
VCRS	Experimental setup
w	Water

INTRODUCTION

Under the guidance of the United Nations (UN), numerous countries have made decisions at different times within the negotiations of climate change, impacting the choice of refrigerants utilized as the working fluid in Vapor Compression Refrigeration Systems (VCRSs). Accordingly, the use of Chlorofluorocarbons (CFCs) was restricted due to the high Ozone Depletion Potential (ODP) with the Montreal Protocol signed in 1987 (UNEP, 1987). Later, use of the Hydrochlorofluorocarbons (HCFCs) and Hydrofluorocarbons (HFCs) was also restricted due to the high Global Warming Potential (GWP) with the Kyoto Protocol signed in 1997 (1997, GCRP). Recently, a reduction schedule of usage of HFCs was prepared to prevent harmful effects of refrigerants on the environment based on GWP value of HFCs in heat pump and air conditioning systems. Accordingly, commercial refrigerators involving HFC with a GWP value of bigger than 150 have been banned as of January 1, 2029 (UNEP, 2016). The primary objective of these protocols is to eliminate the use of refrigerants that are environmentally harmful in terms of ODP and GWP. A summary of impacts of decisions made in various climate change negotiations on refrigerants are shown in Figure 1 (Mota-Babiloni and Makhnatch, 2021; Yang et al., 2021).

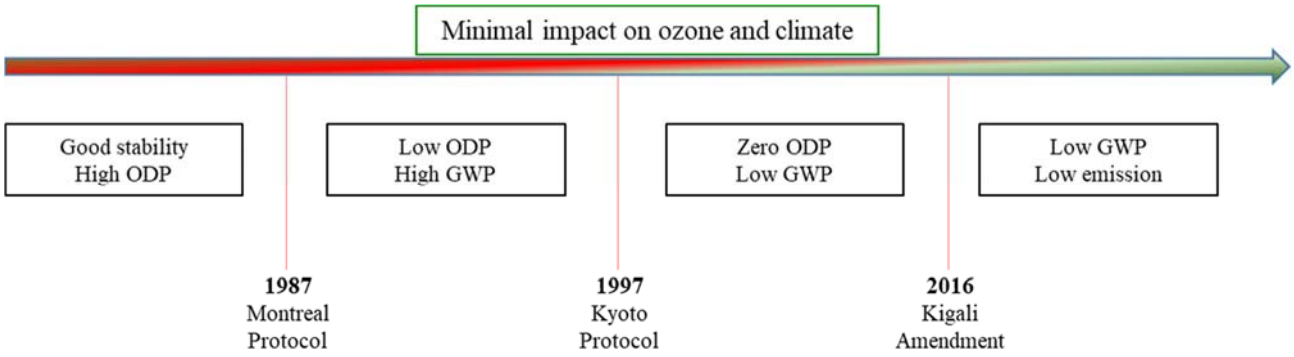

Figure 1. The effects of decisions within the various climate change negotiations on refrigerants.

In the fifth Assessment Report (AR5) by the Intergovernmental Panel on Climate Change (IPCC), R134a, widely favored in refrigeration, air conditioning, and heat pump applications, is noted with a 100-year GWP value of 1 300 (IPCC, 2013). The GWP of R134a is well above the specified limit. Therefore, in the last decade, various alternative refrigerants have been tried instead of R134a (Bilen et al., 2024; Dağıdır and Bilen, 2024). Lately, Hydrofluroolefins (HFOs) have been used as alternative refrigerants in refrigeration applications (Bilen et al., 2023). Recommended as an alternative to R134a, R1234yf is a HFO with a GWP of less than 1 (Arora et al., 2018; Yadav et al., 2022; Li and Tang, 2022). The first studies on R1234yf were related to the replacement of R134a in mechanical VCRSs (Navarro-Esbri et al., 2013). However, it was observed that research involving various system modifications began after it was found that using R1234yf in place of R134a in VCRSs without any modifications led to a decline in performance. (Moles et al., 2014; Li et al., 2014). It has been suggested that various modifications in the system compensate for the drops in system performance (Al-Sayyab et al., 2022; Mishra and Sarkar, 2016). One of the most common modification proposals was to add an internal heat exchanger to the system. Although the use of the internal heat exchanger

provided some improvements in system performance, it was not at the desired level. The use of the ejector was another proposed method to compensate for the performance drops in the system. It is possible to state that the usage of the ejector gives better results compared to the usage of internal heat exchangers (Moles et al. 2014). Therefore, studies that require modification to the system, which started with the usage of both an internal heat exchanger and ejector, have become increasingly common. Newly, hybrid studies have been commonly conducted to enhance system performance by implementing multiple modifications simultaneously in VCRSs (Malwe et al., 2022; Khatoon and Karimi, 2023; Erdinc, 2023). However, all these suggested methods require modification in the system and modifying VCRSs may be cause a change in almost all system equipment. It is a more rational approach to turn to methods that do not require modification in the system. Thus, addition of nanoparticles to the refrigerant used in the system can be tried to enhance performance of the VCRSs. It is known that the usage of nanoparticles influences the refrigerants thermal and physical properties such as specific heat capacity, viscosity, density, and thermal conductivity (Sanukrishna et al., 2018; Bhattad et al., 2018; Bilen et al., 2023). Therefore, it is considered that the use of nanoparticles can be accepted as a good alternative method to improve refrigerant thermophysical properties in VCRSs. Refrigerants in VCRSs with nanoparticles are called nanorefrigerants. The term nanorefrigerant refers to the mixture of nanoparticles and refrigerant in VCRSs. However, nanoparticles and refrigerants do not mix easily. It is known that the lubricant of a compressor meets the refrigerant under operating conditions in VCRS. Therefore, the lubricant of the compressor is generally used to mix the nanoparticles with the refrigerant. The working fluid of the systems in which the interactions between the refrigerant and the nanoparticles are provided indirectly is called nanorefrigerant. Soliman et al. (2019) experimentally studied the addition of nanoparticles to the VCRS. It was used as nanoparticles of Al_2O_3 and working fluid of R134a. Results showed that the energy consumption of the system decreased by 10% and actual Coefficient of Performance (COP) increased by 19.5% with the addition of nanoparticles to the system compared to the base system. Salem (2020) experimentally examined the performance of a VCRS using nanoparticles of Carbon Nanotube (CNT) and working fluid of R134a. Results showed that the COP value enhanced up to 37.3% with the addition of nanoparticles to the system compared to the base system. Nair et al. (2020) conducted an experimental study to investigate the effects of adding Al_2O_3 nanoparticles at mass fractions ranging from 0.1% to 0.5% to the VCRS using R134a refrigerant. The study highlighted that the COP of the system increased by 6.5% with the addition of Al_2O_3 nanoparticles. Choi et al. (2021) conducted an experimental investigation into the effects of adding CNT nanoparticles to the VCRS utilizing R134a refrigerant. The study indicated that the COP increased with the increasing volume fraction of the nanoparticles. Subhedar et al. (2022) experimentally examined energy efficiency of the VCRS with the use of nanorefrigerant including Al_2O_3 nanoparticles and R134a refrigerant. The results indicated that the COP increased by up to 85%, while the compressor power input decreased by up to 27% with the addition of 0.075% volume of Al_2O_3 to the system, compared to the baseline system. Akkaya et al. (2023) experimentally investigated the lubrication properties of carbon composites, including Carbon Black (CB), sepiolite (SP), reduced Graphene Oxide (rGO), and CNT in the VCRS. According to the result of the study, usage of nanoparticles SP-rGO provided the best enhancement in COP. In recent years, nanorefrigerants continue to be used in VCRSs with different refrigerants and nanoparticles (Sharif et al., 2022; Ismail et al., 2023; Ogbonnaya et al., 2023).

Nowadays, energy efficiency is becoming more important day by day. However, the performance decrease in alternative refrigerant applications is remarkable. Since the usage of refrigeration, air conditioning, and heat pump systems containing fluorinated greenhouse gases is restricted, the systems currently used must obey the conditions specified in the regulations. However, modification of these VCRSs is both costly and very laborious. It can take a very long time to develop all this system equipment for a new working fluid. In such circumstances, the most rational approach is to investigate methods for effectively utilizing alternative refrigerants without requiring modifications to existing systems. The system performance decreases due to the usage of R1234yf instead of R134a at the same conditions without any modification in the system. Therefore, in this study, R1234yf, R1234yf+Al_2O_3, R1234yf+graphene, and R1234yf+CNTs have been used as alternative working fluid to R134a in VCRSs. It is predicted that the performance drops due to the use of alternative refrigerant R1234yf instead of R134a in the same system without any modification can be compensated with the use of nanorefrigerants. It is considered that the use of nanorefrigerants examined in this study in alternative refrigerant applications will contribute to the literature.

MATERIAL AND METHODS

Test facility

Experimental setup comprises circuits for refrigeration (cooling), condenser and evaporator with water and water including ethylene glycol (EG), respectively. Pivotal equipment of the Vapor Compression Refrigeration Cycle (VCRC) is situated within the circuit of refrigeration, encompassing four primary operations. These operations are delineated as given a) compression, executed by a compressor of reciprocating; b) condensation, transpiring in a plate type heat exchanger with water-cooled; c) expansion, regulated by an Electronic Expansion Valve (EEV); and d) evaporation, transpiring in a plate heat exchanger with water-heated. The EG water mixture (60% water and 40% EG by volume) serves as cooling medium. The evaporation and condensation transpire within dedicated lines, comprising the evaporator EG water mixture line and the condenser water line, respectively. It employs circulation pumps to propel the EG water mixture and water within the evaporator and condenser lines in the closed flow circuits. Heat transfer (cooling) occurs between the EG water mixture and refrigerant in the evaporator, whereas heat transfer (heating) transpires between the refrigerant and water in the condenser. A heat recovery system and a chiller uphold constant temperatures within the EG water mixture and water tanks. Detailed insights into the refrigeration and auxiliary circuits, including a schematic depiction (Figure 2a) and various photographs of the system (Figure 2b), are provided in Figure 2. Furthermore, Table 1 elucidates the components of the system.

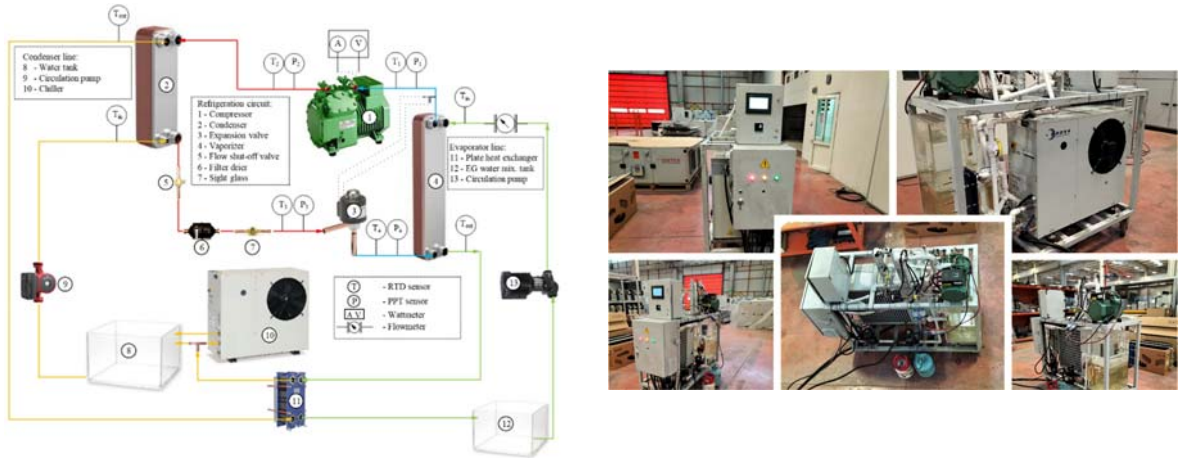

(a) (b)

Figure 2. a) Schematic representation and b) some photos of the test installation.

Table 1. Experimental setup equipment.

Equipment	Specification
1) Compressor	Semi-hermetic BITZER compressor of reciprocating, 4CES-6Y-40S model.
2) Condenser	Plate ALFA LAVAL heat exchanger, AC-30EQ-20H-F model.
3) Throttling device	DANFOSS EEV, model of ETS 6.
4) Evaporator	Plate ALFA LAVAL heat exchanger, AC-70X-20M-F model.
5) Shut-off valve	DANFOSS shut-off valve, GBC model.
6) Filter-drier	DANFOSS filter-dryer, DML model.
7) Sight glass	DANFOSS sight-glass, SGP model.
8) Condenser line tank	64 L capacity.
9) Circulation pump	GRUNDFOS pump for water, UPS2 25-80 model.
10) Chiller	RHOSS chiller, model of THAEY 105.
11) Heat exchanger	Plate ALFA LAVAL heat exchanger, model of T2-BFG.
12) Evaporator line tank	48 L capacity.
13) Circulation pump	GRUNDFOS pump for EG water mixture, TP 25/2 A-O-A-BQQE-AX1 model.

Specific measurement points and strategically positioned measurement devices were carefully selected to perform a comprehensive thermodynamic analysis of the test facility. Temperature and pressure measuring were carried out at these identified points to execute the refrigeration circuit analysis. The Resistance Temperature Detectors (RTDs) were utilized as the temperature measuring device. Also, the Piezoresistive Pressure Transmitters (PPTs) were used as the pressure measuring device. The RTD sensors were utilized to measure not only the refrigerant temperature, but also the water and water including EG temperature at the entrance and exit of both condenser and evaporator. Additionally, ambient temperature was measured using the thermistor named Negative Temperature Coefficient (NTC). Besides, the digital wattmeter was employed in order to monitor the electrical power consumption of the compressor throughout the experiments. Furthermore, the digital turbine-type flowmeter was utilized to determine the volume flow rate for the evaporator EG water mixture line. It can be stated that the measuring range and uncertainty of these measurement devices are matched with those reported in similar studies in the literature (Singh et al., 2021). For more technical details regarding all measurement devices utilized in the experiments, please refer to Table 2.

Table 2. The measurement devices specifications.

Equipment	Measuring range	Uncertainty
Wattmeter	0 ~ 10 kW	±1%
Flowmeter	5 ~ 60 L/min	±1%
RTD sensor	–70 ~ 200 °C	±0.5 °C
PPT sensor	0 ~ 25 bar	±0.25%
NTC sensor	–20 ~ 60 °C	±0.5 °C

In the described test facility, average superheating of 6 °C is consistently maintained using an EEV, a parameter held constant across all tests. Similarly, the setup is configured to achieve the subcooling of 5 °C at the outlet of condenser for R134a. The data collected during the experimental trials are meticulously recorded and monitored by a Programmable Logic Controller (PLC) of the DELTA model. The data logger with sixteen-inputs is utilized to store the measurement data used in analyses. Electrical power, temperature, and pressure measuring could be easily monitored with the help of 7-inch screen of the Delta throughout the tests. Moreover, a separate small screen was allocated for monitoring the volume flow rate. By this way, it was enabled real-time monitoring of all measuring data in experiments.

Refrigerants (working fluids)

In the research, R1234yf was alternatively employed as a refrigerant to commonly used R134a in VCRSs, involving applications in household air conditioners and refrigerators. Diverse properties of R1234yf and R134a are similar such as critical pressure, critical temperature, and molecular weight. The molecular weight of R134a is 102.03 and the molecular weight of R1234yf is 114.04 g/mol. The critical pressure of R134a is 40.59 bar and the critical pressure of R1234yf is 33.42 bar. The critical temperature of R134a is 101.06 and the critical temperature of R1234yf is 94.70 °C. R1234yf is distinguished from other refrigerants by a notably lower GWP value of ~1, in comparison to R134a's value of 1300. This makes it a more environmentally friendly refrigerant. Furthermore, the atmospheric lifetime of R1234yf is considerably shorter, with a duration of

approximately 11 days, in comparison to R134a, which remains in the atmosphere for 13 years. Attributes render R1234yf a compelling alternative to refrigerant R134a. For a detailed comparison of the important properties of the refrigerants, please refer to Table 3. Also, latent heat of condensation and evaporation both R134a and R1234yf are assessable with the help of pressure-enthalpy (*P-h*) and temperature-entropy (*T-s*) diagrams. These diagrams for both R134a and R1234yf are illustrated in Figure 3. Thus, it could be observed that latent heat of both refrigerants is close to each other under the same conditions.

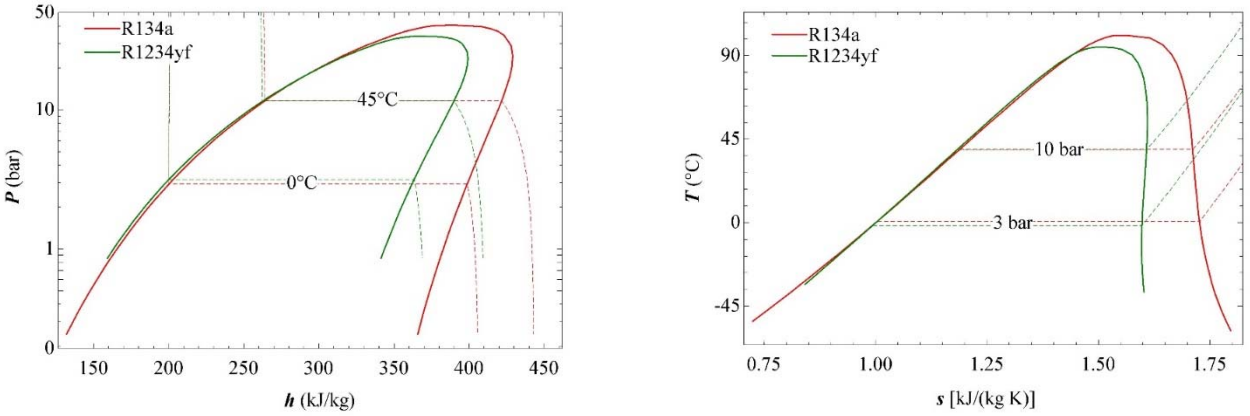

(a) (b)

Figure 3. a) *P-h* chart and b) *T-s* chart for R134a and R1234yf.

Table 3. Refrigerant properties using this study (Colombo et al., 2020).

Property	R134a	R1234yf
Chemical name	1,1,1,2 Tetrafluoroethane	2,3,3,3 Tetrafluoropropene
Molecular formula	CH_2FCF_3	CH_2-CF=CF_3
Molecular mass (g/mol)	102.03	114.04
Boiling point (°C) at 1 atm	–25.90	–29.50
Critic temperature (°C)	101.06	94.70
Critic pressure (kPa)	4059	3342.20
GWP_{100} (IPCC, 2013)	1300	<1
ODP	0	0
Atmospheric lifetime	13 years	11 days
Flammability	A1	A2L

Nanorefrigerants preparation

In this study, nanoparticles were introduced into the VCRS through the compressor lubricant, which is Polyolester (POE) oil. The POE oil in the experimental setup is EMKARATE RL 32H matched with both refrigerants. Technical specification of this lubricant is presented in Table 4. It is known that the lubricant of a compressor meets the refrigerant under operating conditions in VCRSs. Therefore, it is important to emphasize that the nanoparticles added to the lubricant also interact with the refrigerant when mixed with the compressor lubricant. Additionally, it can be stated that this contact of the nanoparticles affects the refrigerant. Therefore, the working fluid of such systems is called nanorefrigerant and compressor lubricant including nanoparticle is also called nanolubricant. In scope of this study, R1234yf+Al_2O_3, R1234yf+graphene, and R1234yf+CNTs nanorefrigerants were utilized as the working fluid in the VCRS in place of R134a. Technical specification of nanoparticles used nanorefrigerants is presented in Table 5. Previous studies were also used the same nanoparticles for different purposes (Dağıdır and Bilen, 2023a; Dağıdır and Bilen 2023b). EDS and XRD analyses were performed for each nanoparticle type, and FE-SEM images were given. Thus, it could be stated that characteristics of Al_2O_3 (Prins, 2020), graphene (Dang et al., 2020), and CNTs (He et al., 2020) nanoparticles are compatible with the literature. Given that both graphene and CNTs are carbon-based nanomaterials, while Al_2O_3 is a metal-based nanomaterial, the mass fractions in the lubricant differ from each other. Mass fraction of nanoparticles was determined according to similar studies in literature. Accordingly, minimum mass fraction of Al_2O_3 (Akkaya et al., 2021), graphene and CNTs (Salem, 2020) were selected as 0.250%, 0.125%, and 0.125%, respectively.

Nanoparticles was added step by step to the system using R1234yf starting from the minimum mass fraction. Compressor power input in the system was checked during experiments, thus mass fraction of nanoparticles was raised as compressor power input decrement continued. Experiment for relevant nanorefrigerant type was stopped when the compressor electrical power increased again. Then other nanorefrigerant type was tried similarly. In this way, it was purposed to find the ideal nanoparticles mass fraction.

Table 4. Specifications of the POE oil (Emkarate, 2015).

Feature	ASTM standard	Result
Kinematic viscosity	D445	32.5 cSt (at 40 °C)
Kinematic viscosity	D445	5.8 cSt (at 100 °C)
Index of viscosity	D2270	121
Density	D1298	0.98 g/mL (at 20 °C)
Flash point	D92	264 °C
Pour point	D97	–55 °C

In this study, a two-step method, commonly employed in similar studies in the literature, was utilized to mix the POE

lubricant with nanoparticles (Senthilkumar and Anderson, 2021; Sharif et al., 2022). Mass measuring of the lubricant and nanoparticle is performed with the precision balance with brand named RADWAG PS1000.R2. Initially, nanoparticles and this lubricant were stirred by the mechanical mixer with brand named TOPTION MX-S, later they were mixed by the ultrasonic mixer with brand named TOPTION TU-900E4 again. These mixtures were maintained in an ultrasonic mixer for at least 90 minutes before being charged into the compressor through the lubricating chamber for experiments. This method has been successfully applied in previous studies (Dağıdır and Bilen, 2023a). The devices employed in the two-step method are depicted in Figure 4.

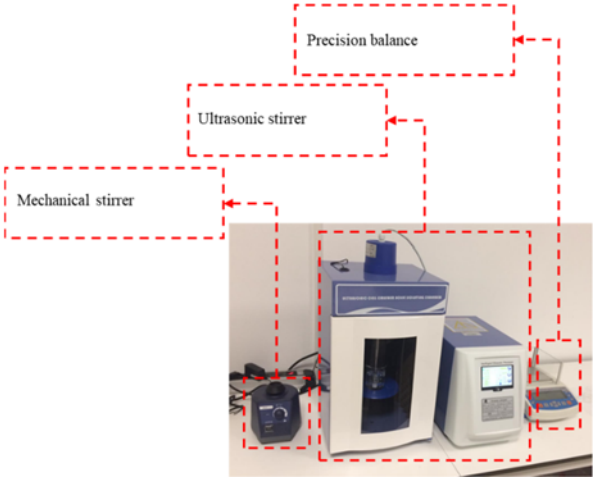

Figure 4. Apparatus utilized in the two-step method.

Nanolubricants stability

During the preparation step, the ultrasonic mixing time is conducted as 90 minutes to provide stability as recommended in the similar research in the literature (Redhwan et al., 2019). Measured zeta potential values for nanolubricants involving Al_2O_3 nanoparticles were compared to a previous study (Zawawi et al., 2022) in literature in Figure 5. According to these values, stability of nanolubricants involving Al_2O_3 nanoparticles is normal at the mass fraction of $\omega = 1.00\%$ (the highest) and excellent at the mass fraction of $\omega = 0.25\%$ (the lowest). Stability of all nanolubricants was also considered to be stable since all nanolubricant samples were prepared with the two-step method.

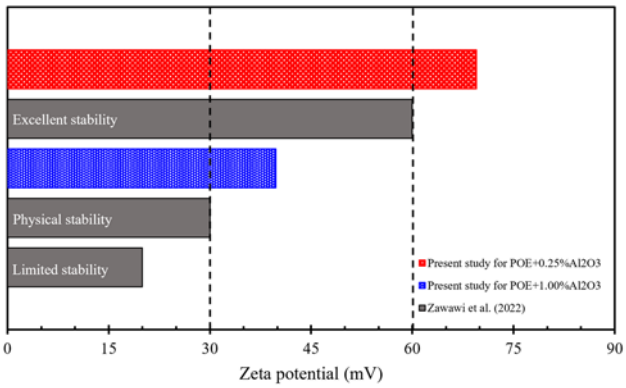

Figure 5. Zeta potential values of nanolubricant samples involving Al_2O_3 nanoparticles.

Table 5. Technical specifications of the nanoparticles (Dağıdır and Bilen, 2023a).

	Al_2O_3	Graphene	CNTs
Properties	Purity: 99.5% Type: Gamma nanoparticles Average particle size: 18 nm Morphology: Nearly spherical Specific surface area:140 m^2/g Color: White	Purity: 99.9% Type: Graphene Nanoplatelets Diameter: 18 µm Thickness: 5 nm Specific surface area: 170 m^2/g Color: Gray	Purity: 96% Type: Multi-Walled Carbon Nanotube (MWCNT) Inside diameter: 5-10 nm Outside diameter: 8-18 nm Length: 10-30 µm Specific surface area: 220 m^2/g Color: Black
FE-SEM images	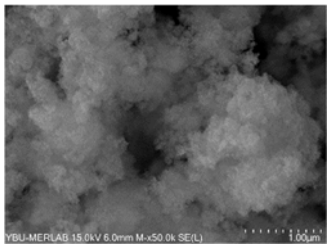	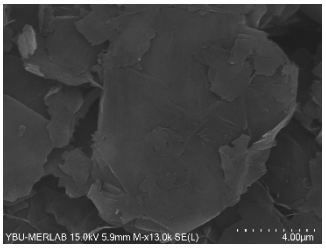	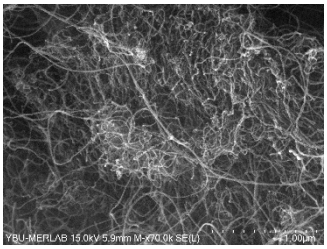
XRD analysis	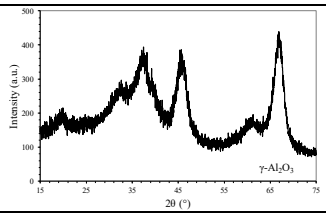	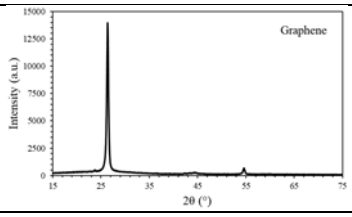	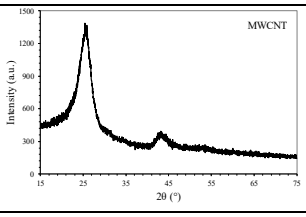

Thermodynamic analyses of the test facility

In this investigation, tests were performed on the VCRS at steady-state steady-flow conditions. Equations were individually obtained for the primary equipment of the system which are the compressor for compression, condenser for condensation, EEV for throttling, and evaporator for evaporation. Thermodynamic assessments of the refrigeration circuit were conducted based on the following assumptions: 1) VCRS equipment operates under steady-state, steady-flow conditions. 2) Heat transfer between the VCRS equipment and the environment is considered negligible. 3) Changes in potential and kinetic energy are disregarded.

Compression in compressor

The requirement compressor energy input per unit time $\dot{W}_{in}$ is specified with the electrical power directly measured using wattmeter throughout experiments. Compression Ratio (CR) in compressor is the ratio of state 2 (discharge) absolute pressure to state 1 (suction) absolute pressure. The isentropic efficiency, η_{isen} is calculated with Eq. (1).

$$\eta_{isen} = \frac{h_{2,s} - h_1}{h_2 - h_1} \quad (1)$$

where h is specific enthalpy (kJ/kg). Subscripts numbered 1 and 2 refer to state and s refers to the isentropic compression process.

The compressor exergy destruction rate, $\dot{E}x_{dest,comp}$ is calculated with Eq. (2).

$$\dot{E}x_{dest,comp} = \dot{m}_R T_o (s_2 - s_1) \quad (2)$$

where $\dot{m}$ is the mass flow rate (kg/s), T_0 is ambient temperature, and s is specific entropy [kJ/(kg·K)]. Additionally, subscript R refers to the refrigerant.

Condensation in condenser

Heat rejection rate of the condenser, $\dot{Q}_H$, is determined as the sum of cooling capacity and compressor electrical power input. Exergy destruction rate in the condenser, $\dot{E}x_{dest,cond}$ is calculated by using Eq. (3).

$$\dot{E}x_{dest,cond} = \dot{m}_R(ex_2 - ex_3) + \dot{m}_w(ex_{w,in} - ex_{w,out}) \quad (3)$$

where subscripts *in* and *out* refer to the *inlet* and *outlet*, respectively, and *ex* is the specific exergy (kJ/kg).

Throttling in EEV

EEV exergy destruction rate, $\dot{E}x_{dest,exp}$ is calculated with Eq. (4).

$$\dot{E}x_{dest,exp} = \dot{m}_R(ex_3 - ex_4) \quad (4)$$

where the expansion valve is represented by the subscript *exp*.

Evaporation in evaporator

VCRS's cooling capacity, $\dot{Q}_L$, is determined using Eq. (5).

$$\dot{Q}_L = \dot{m}_{ew}\left(h_{ew,in} - h_{ew,out}\right) \quad (5)$$

where subscript *ew* indicates water including EG in the evaporator.
Evaporator exergy destruction rate, $\dot{E}x_{dest,evap}$ is calculated with Eq. (6).

$$\dot{E}x_{dest,evap} = \dot{m}_R(ex_4 - ex_1) + \dot{m}_{ew}(ex_{ew,in} - ex_{ew,out}) \quad (6)$$

where the evaporator is represented by subscript *evap*.

General system performance parameters

The overall performance parameters of the VCRS are represented by the Energy Efficiency Ratio (EER) as energetic performance indicator and second law efficiency as exergetic performance indicator.

EER of the VCRS, EER_{VCRS}, is determined as the heat transfer rate in the evaporator (cooling capacity) per the compressor electrical power input as represented in Eq. (7).

$$EER_{VCRS} = \frac{\dot{Q}_L}{\dot{W}_{in}} \quad (7)$$

VCRS's exergy efficiency, $\eta_{ex,VCRS}$, is determined as in Eq. (8). VCRS's total exergy destruction rate, $\dot{E}x_{dest,total}$ is the sum of the exergy destruction rate obtained for each equipment (De Paula et al., 2020).

$$\eta_{ex,VCRS} = 1 - \frac{\dot{E}x_{dest,total}}{\dot{W}_{in}} \quad (8)$$

Additionally, refrigerant mass flow rate, $\dot{m}_R$ is determined with the standard named American Society of Heating, Refrigerating and Air-Conditioning Engineers: Standard 41.1-1986 (Sharif et al., 2022) as represented in Eq. (9).

$$\dot{m}_R = \frac{\dot{Q}_L}{h_1 - h_4} \quad (9)$$

The measured temperature and pressure values are used to determine the thermophysical properties in the thermodynamic analysis of the system. The thermophysical properties were determined using the Engineering Equation Solver (EES) software. In the exergy analysis, the ambient temperature was measured and taken as the dead state temperature (T_0). The standard atmospheric pressure was also taken as the dead state pressure (P_0). Other dead state properties such as enthalpy (h_0) and entropy (s_0) were determined depending on the dead state temperature and pressure.

Operating conditions

The experimental setup utilized in this study was designed to operate with R134a as the working fluid. At the same time, in the test facility of this study, an EEV was utilized. This valve adjusts its opening automatically, responding to the refrigerant pressure and temperature at the outlet of evaporator. Supported by electronic control equipment, the EEV plays a crucial mission in maintaining stability of the VCRS by promptly reacting in order to change in system variables. Throughout the experiments, superheating at the evaporator outlet was maintained at approximately 6 °C thanks to the EEV. Refrigerants were incrementally charged into the VCRS until reaching the target superheating value, at which point the tests were conducted. The EEV also provided a standardized approach to refrigerant charging. Thus, the charge amount of R134a refrigerant was approximately 700 g and the charge amount of R1234yf refrigerant was approximately 780 g. The comparison of results was based on constant evaporation and condensation temperatures. Experiments were conducted at approximately 0 °C and 45 °C temperatures for evaporation and condensation, respectively. Firstly, R134a was tested under these test conditions, then R1234yf was used instead of R134a without any modification in the system and pure refrigerant tests were completed. After this stage, nanoparticles were added by means of compressor oil to the system using R1234yf. Also, the filter-drier in the system was replaced with a new one for each type of nanoparticle. It was observed that the addition of nanoparticles has both positive and negative effects, as in similar studies in the literature (Pawale et al., 2017). Thus, it was understood that there was an upper limit to the mass fraction of nanoparticles added to the system. Mass fractions

of 0.75% for Al_2O_3 and 0.250% for graphene and CNTs yielded the most significant improvements in system performance parameters under the operating conditions evaluated in this study.

ERROR ANALYSIS

Error analysis is a crucial aspect of validating experimental examination. In practical terms, various approaches are devised to pinpoint errors in obtained parameters with the help of data gathered from tests. Among the approaches, uncertainty analysis stands out as one of the most employed approaches. Thus, the uncertainty of any magnitude, contingent upon measuring data, is given as shown in Eq. (10).

$$u_R = \pm\left[\left(\frac{\partial R}{\partial x_1}u_{x_1}\right)^2 + \left(\frac{\partial R}{\partial x_2}u_{x_2}\right)^2 + \left(\frac{\partial R}{\partial x_3}u_{x_3}\right)^2 + \cdots + \left(\frac{\partial R}{\partial x_n}u_{x_n}\right)^2\right]^{1/2} \quad (10)$$

where x is independent variable, R is any measured magnitude, u is uncertainty.

The EES software was employed for calculating uncertainties. The uncertainty determined for the EER, indicating the energetic performance of the VCRS, is between 5.74%-6.75%. Likewise, the uncertainty obtained for the exergy efficiency, reflecting the exergetic performance of the VCRS, is between 7.24%-8.10%. It was observed that the obtained uncertainty values were consistent with findings in the literature (Al-Sayyab et al., 2022).

RESULTS AND DISCUSSIONS

In this experimental research, R1234yf, R1234yf+Al_2O_3, R1234yf+graphene, and R1234yf+CNTs were investigated as alternative refrigerants to R134a concerning their thermodynamic properties, without any modifications to the system. Accordingly, the results related to effects of the usage of R1234yf+Al_2O_3, R1234yf+graphene, and R1234yf+CNTs nanorefrigerants in the system were shared. An EEV was employed in the test facility of this study. Throughout the experiments, superheating at the evaporator outlet was maintained at approximately 6 °C thanks to throttling device. Working fluids were charged gradually into the VCRS up to desired value of superheating and experiments were performed at this value. The comparison of the results was based on approximately 0 °C and 45 °C temperatures for evaporation and condensation, respectively.

Validation of the study

Initially, the test results were validated by comparing the actual and ideal pressure-specific enthalpy (*P-h*) and temperature-specific entropy (*T-s*) diagrams of the system using R134a with previous studies found in the literature (Morales-Fuentes, 2021; Al-Sayyab et al., 2022). Moreover, the reciprocating compressor compatible with R134a is certified by a respected organization named Association of European Refrigeration Component Manufacturers (ASERCOM). Thus, validation experiments were carried out in the test installation using R134a at the same conditions. Results of the validation experiments were compared with the results of the ASERCOM data, focusing on *P-h* and *T-s* charts as given in Figure 6a and Figure 6b, respectively. Accordingly, it could be stated that results of these verification tests align well with both the ASERCOM data and ideal cycle data. Subsequently, EER values calculated in the validation study were compared to the ASERCOM results and this comparison is depicted in Figure 6c. It could be concluded that these EER values fall within reasonable limits, consistent with the certified data. Finally, R1234yf was used as the working fluid instead of R134a in this study. The EER value declined when R1234yf was used in place of R134a under the same conditions in the VCRS. This EER decrease was compared to the previous studies (Sanchez et al., 2017; Li et al., 2019; Chen et al., 2020; Alkan et al., 2021) in literature. Results obtained are given in Figure 6d. Consequently, the EER decreases in previous studies in the literature and the EER decrease in this study are at similar levels. Accordingly, it is considered that the experiments are reliable.

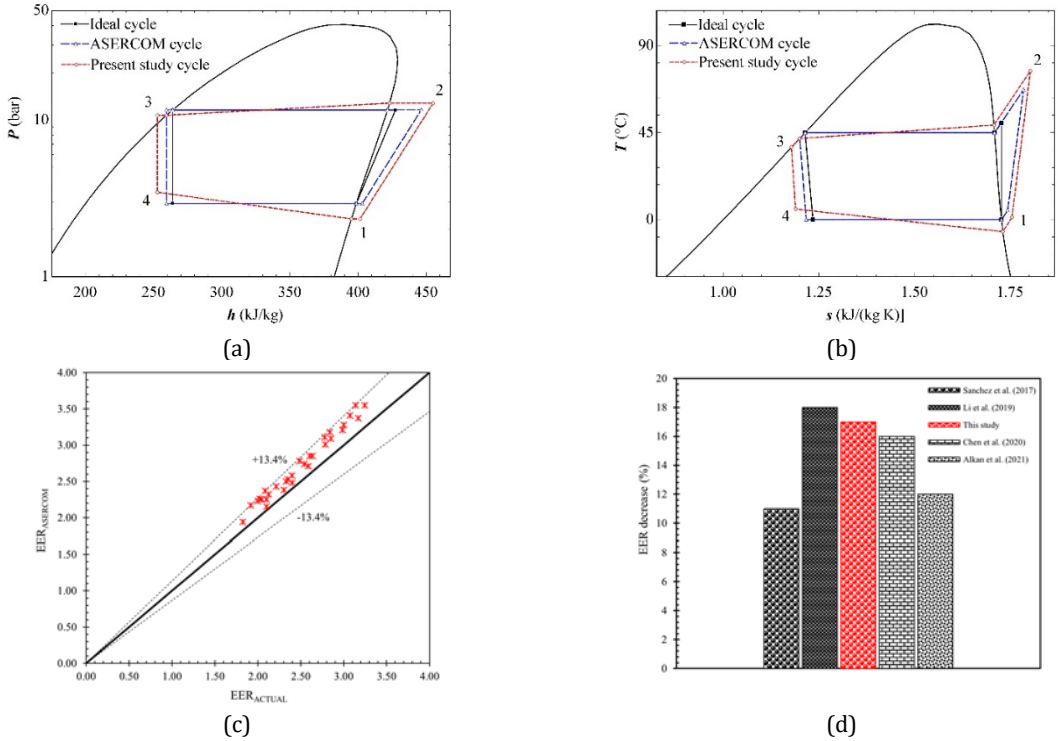

Figure 6 The a) *P-h* diagram and b) *T-s* diagram of ideal, actual, and ASERCOM cycles, c) comparison of actual and ASERCOM systems in view of EER values, d) comparison of this study and previous studies in terms of decrease in EER.

Discussions on the experimental results

In this study, it was predicted that the performance decrease caused by the usage of an alternative refrigerant R1234yf instead of R134a in the VCRS could be compensated by adding nanoparticles to the system without any modifications. The results of the study showed that the nanoparticles added to the VCRS improved the system performance parameters. It was observed that the addition of nanoparticles has both positive and negative effects, as in the similar studies in the literature (Pawale et al., 2017). While the positive effects prevail due to the favorable thermal and tribological properties of the compressor oil and refrigerant up to a certain mass ratio, the negative effects become predominant beyond that ratio due to the instability of the mixture and increased friction (Kaushik et al., 2021). Thus, there is a limit for mass fraction of nanoparticles added to the system. For the operating conditions of this study, these limits are 0.75% for Al_2O_3, and 0.250% for both graphene and CNTs. Since CNTs and graphene are carbon-based nanomaterials, their optimum mass fractions are similar. However, since Al_2O_3 is a metal-based nanomaterial, it has an optimum mass fraction different from graphene and CNTs. The results have shown that the system performance starts to deteriorate in case of exceeding these optimum mass fractions of nanoparticles. Performance parameters of the system containing pure refrigerants and nanorefrigerants are discussed in the following section.

Results about compressor performance parameters

The variation of compressor power input for pure refrigerants and nanorefrigerants is seen in Figure 7. Therefore, it was observed that the increase in compressor power input resulting from the use of R1234yf instead of R134a in the VCRS was nearly offset by the addition of nanoparticles. The variation of the compression ratio for pure refrigerants and nanorefrigerants is shown in Figure 8. Thus, it was seen that the compression ratio increased with the usage of nanorefrigerant in the system. The variation of the compressor isentropic efficiency for pure refrigerants and nanorefrigerants is given in Figure 9. Thus, it was seen an increase in the compressor isentropic efficiency at similar operating conditions with the use of carbon-based nanorefrigerant compared to R134a. Maximum increment in isentropic efficiency was obtained by around 16% at graphene mass fraction of 0.250% compared to R134a. The variation of compressor exergy destruction rate for pure refrigerants and nanorefrigerants is seen in Figure 10. Hence, it was observed a decrease in compressor destruction rate at similar operating conditions with the usage of nanorefrigerant up to 29% at a graphene mass fraction of 0.250% compared to R134a.

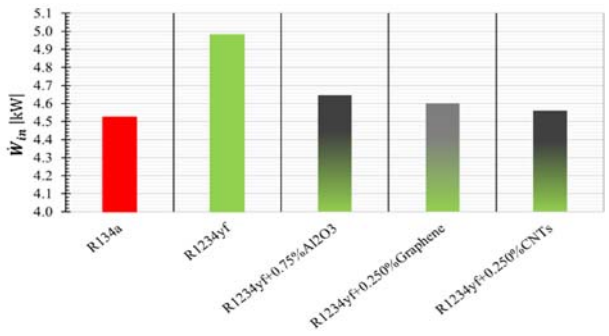

Figure 7. Variation in the compressor power input based on the working fluid.

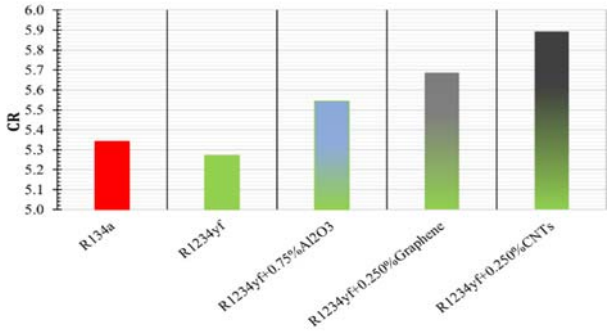

Figure 8. Variation of the compression ratio with the working fluid.

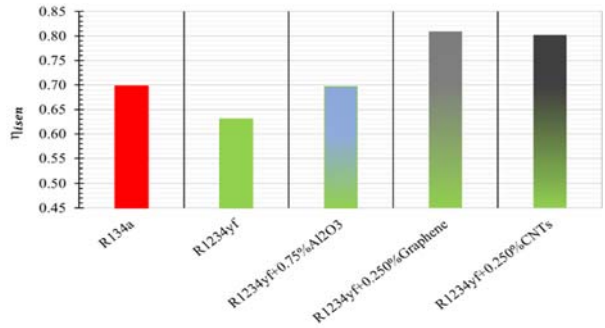

Figure 9. Variation of the compressor isentropic efficiency with the working fluid.

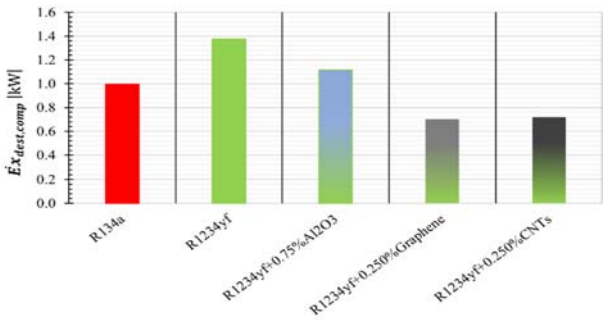

Figure 10. Variation of the compressor exergy destruction rate with the working fluid.

Results about condenser performance parameters

The changing of heat rejection rate for pure refrigerants and nanorefrigerants in the condenser is given in Figure 11. It was seen that the condenser heat rejection rate increased with the usage of nanorefrigerant. This maximum increment rate was approximately 11% at graphene mass fraction of 0.250% compared to R134a. The variation of the condenser exergy destruction rate for pure refrigerants and nanorefrigerant is shown in Figure 12. Accordingly, it was observed that the exergy destruction rate of the condenser increased with the use of nanorefrigerant. This maximum increment rate was nearly 9%.

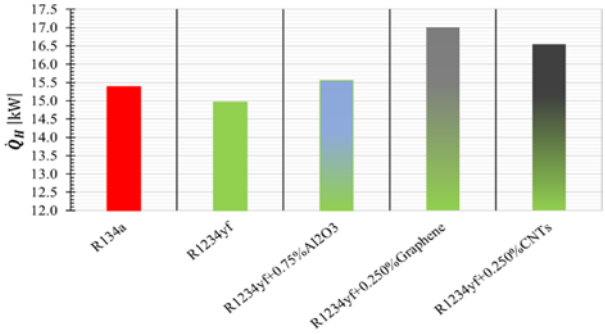

Figure 11. Variation in heat rejection rate within the condenser based on the working fluid.

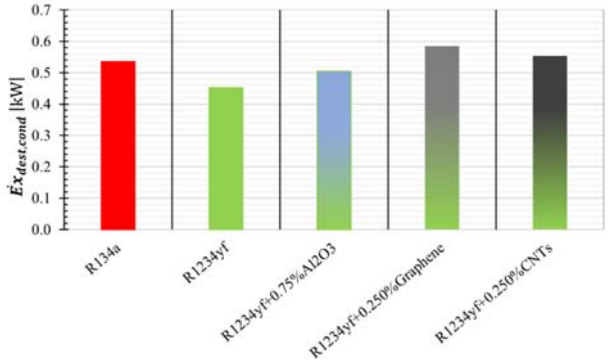

Figure 12. Variation of the condenser exergy destruction rate with the working fluid.

Results about EEV performance parameters

The variation of EEV exergy destruction rate for pure refrigerants and nanorefrigerants is given in Figure 13. It was seen that the EEV exergy destruction rate reduced up to 23% by using nanorefrigerant at the CNTs mass fraction of 0.250%.

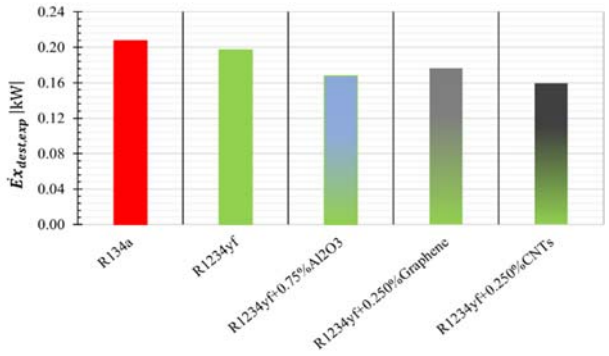

Figure 13. Variation of exergy destruction rate in the EEV with the working fluid.

Results about evaporator performance parameters

The variation of cooling capacity for pure refrigerants and nanorefrigerants is given in Figure 14. Accordingly, the cooling capacity increased up to 14% with the addition of graphene to the system with R1234yf compared to the usage of R134a. The variation of the evaporator exergy destruction rate for pure refrigerants and nanorefrigerant is given in Figure 15. It was noted that the exergy destruction rate in the evaporator increased with the use of nanorefrigerant. The maximum increment in the evaporator exergy destruction rate was by around 68% at the usage of R1234yf+0.250% graphene nanorefrigerant.

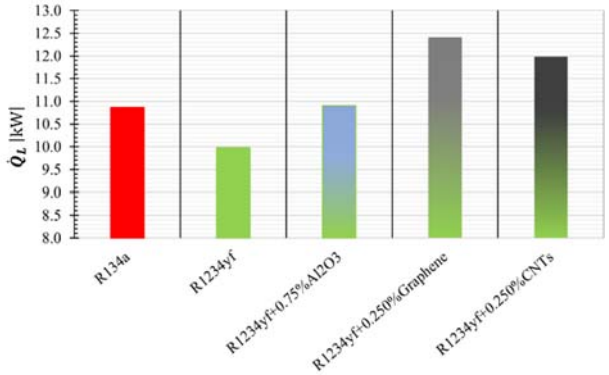

Figure 14. Variation of the cooling capacity in the system with the working fluid.

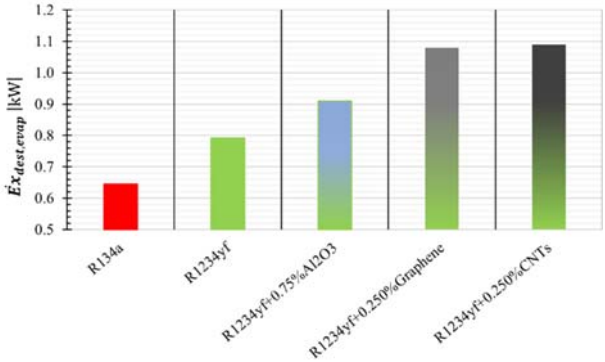

Figure 15. Variation of the evaporator exergy destruction rate with the working fluid.

Results about overall system performance parameters

The usage of carbon-based nanoparticles was better than Al_2O_3 in increasing the system performance. On the other hand, the usage of graphene nanoparticles is better than CNTs in terms of system performance parameters. The EER value of the system increased because of the increase in the cooling capacity. The cooling capacity increased up to 14% with the addition of graphene to the system with R1234yf compared to the usage of R134a. The variation of EER for pure refrigerants and nanorefrigerants is given in Figure 16. Accordingly, it revealed that EER, which was an expression of overall system energetic performance, increased up to 13% with the usage of R1234yf+graphene nanorefrigerants in the system compared to the usage of R134a. Besides, the VCRS's total exergy destruction rate for both pure refrigerants and nanorefrigerants is given in Figure 17. It was observed that total exergy destruction rate slightly increased in respect to the VCRS including R134a. Additionally, the VCRS's exergetic efficiency is shown in Figure 18. It was also seen that there was no significant change in exergy efficiency in all cases. Consequently, it was emphasized that the VCRS with R1234yf containing graphene nanoparticles at the mass fraction of 0.250% had the best system performance among all cases.

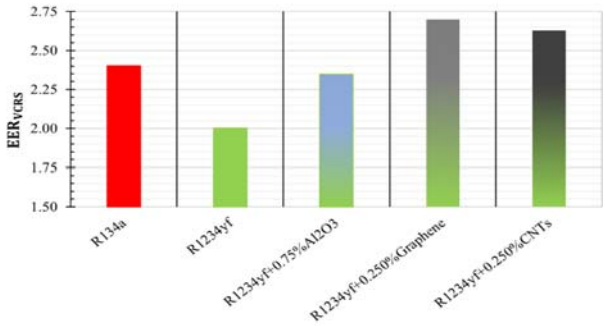

Figure 16. Variation of the EER value of the system with the working fluid.

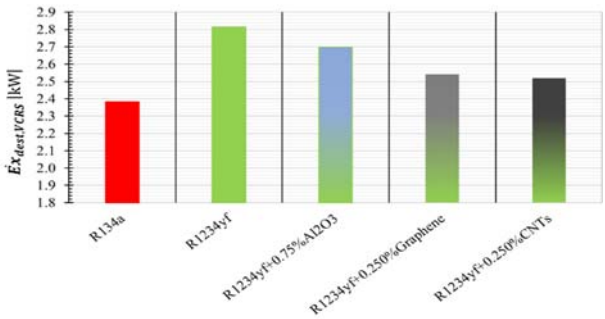

Figure 17. Variation of the total exergy destruction rate of the system with the working fluid.

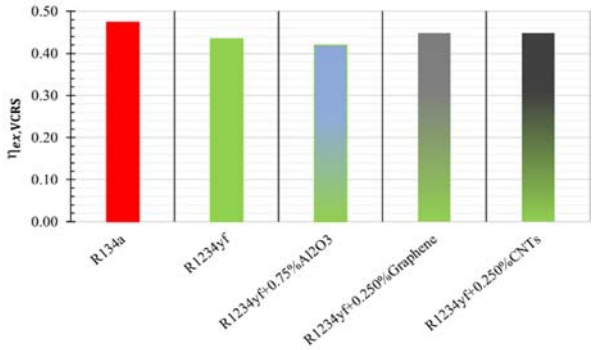

Figure 18. Variation in the second law efficiency of the system as a function of the working fluid.

As a result of this study, it was found that the energetic performance parameter, EER, increased by approximately 13% when using R1234yf with nanoparticles compared to using pure R134a in the VCRS. This increase cannot be directly compared with previous studies in the literature because no study has been identified in the literature testing R1234yf with nanoparticles instead of R134a in the system. Therefore, this study can be indirectly compared to previous studies. For example, previous studies in the literature on the use of R134a with nanoparticles in VCRS are summarized in Table 6. It is considered as an important advantage that this study obtained an increase close to the EER increment obtained by using R134a with nanoparticles compared to the use of pure R134a as shown in Table 6. This is because of the increase in EER obtained in this study by using the alternative refrigerant R1234yf with nanoparticles instead of pure R134a.

Table 6. Energetic performance increases obtained in previous studies in literature.

Reference	Nanoparticle(s)	Finding
Saravanan and Vijayan (2018)	Al_2O_3 and TiO_2	EER raised up to 10.6%
Soliman et al. (2019)	Al_2O_3	EER increased up to 19.5%
Chauhan et al. (2019)	TiO_2	EER increased up to 29.1%
Salem (2020)	CNTs	EER value enhanced up to 37.3%.
Yilmaz (2020)	CuO and Cu/Ag	EER value improved op to 20.88%.
Nair et al. (2020)	Al_2O_3	EER increased up to 6.5%.
Raghavulu and Rasu (2021)	Graphene	EER increased up to 29%.
Afolalu et al. (2021)	ZnO	EER increased up to 15%.
Akkaya et al. (2021)	Al_2O_3	EER increased up to 18.27%.
Arumuganainar et al. (2022)	CeO_2	EER increased up to 7.6%.
Mohamed et al. (2022)	CuO and CeO_2	EER increased up to 25%
Farahani et al. (2022)	SiO_2 and TiO_2	EER increased up to 16.4%.

CONCLUSIONS

In conclusion, the experimental investigation of R1234yf, an environmentally friendly refrigerant, as a working fluid in a VCRS revealed that the system can safely operate with R1234yf without modifications. However, the use of pure R1234yf results in some drops in the system performance parameters compared to R134a. Therefore, Al_2O_3, graphene, and CNTs nanoparticles were introduced into the VCRS using pure R1234yf through the compressor oil to mitigate the performance losses associated with replacing R134a with R1234yf.

The system performance parameters increased with adding nanoparticles up to the optimum mass fraction. Accordingly, in this study, the optimal mass fractions were identified as 0.75% for Al_2O_3, 0.250% for graphene, and 0.250% for CNTs under the same operating conditions. The most significant enhancement in system performance parameters was achieved with the addition of graphene at its optimal mass fraction of 0.250%.

This study examined the use of R1234yf together with nanoparticles as an alternative to R134a in VCRSs experimentally. Similarly, various studies can also be carried out for different alternative refrigerants and nanoparticles in VCRSs. Nevertheless, it is recommended that future studies should compare the service life of system components in VCRSs with and without nanoparticles by means of life cycle testing. In this way, it can be reported whether the lifetime of systems with nanoparticles is shorter than that of systems without nanoparticles. In addition, it can be proposed to investigate whether the addition of nanoparticles has any negative effects on the main and auxiliary elements of the system over time. This is because VCRSs are formed by the combination of many components. Additionally, the typical types of failure to which VCRSs are exposed under operating conditions are known, so that solutions to possible failures can be proposed to final users in advance. In this context, it can be recommended to carry out studies to determine the typical failures of systems with nanoparticles compared to the systems without nanoparticles. Finally, it can be suggested to perform studies on the thermoeconomic analysis of the system with nanorefrigerants. It is believed that reporting the cost of adding nanoparticles to the system under different operating conditions will contribute to developments in this area.

ACKNOWLEDGEMENT

The authors are grateful to TUBITAK (The Scientific and Technological Research Council of TURKEY) for their valuable support to this research with the 1001 project numbered 119M074. Besides, the authors express their gratitude to UNTES Air Conditioning Systems Incorporation for their precious support.

REFERENCES

Afolalu S. A., Ikumapayi O. M., Ogundipe A. T., Yusuf O. O., & Oloyede O. R. (2021). Development of nanolubricant using Aloe Vera plant to enhance the thermal performance of a domestic refrigeration system. *International Journal of Heat and Technology*, 39(6), 1904-1908. https://doi.org/10.18280/ijht.390626

Akkaya M., Menlik T., & Sozen A. (2021). Performance enhancement of a vapor compression cooling system: An application of POE/Al_2O_3. *Journal of Polytechnic-Politeknik Dergisi*, 24(3), 755-761. https://doi.org/10.2339/politeknik.679563

Akkaya M., Sarilmaz A., Balci S., & Ozel F. (2023). Numerical and experimental analysis of refrigerating performance for hybrid nanolubricants with sepiolite additives. *Thermal Science and Engineering Progress*, 37, 101576. https://doi.org/10.1016/j.tsep.2022.101576

Alkan A., Kolip A., & Hosoz M. (2021). Energetic and exergetic performance comparison of an experimental automotive air conditioning system using refrigerants R1234yf and R134a. *Journal of Thermal Engineering*, 7, 1163-1173. https://doi.org/10.18186/thermal.978014

Al-Sayyab A. K. S., Navarro-Esbri J., Barragan-Cervera A., Kim S., & Mota-Babiloni A. (2022). Comprehensive experimental evaluation of R1234yf-based low GWP working fluids for refrigeration and heat pumps. *Energy Conversion and Management*, 258, 115378. https://doi.org/10.1016/j.enconman.2022.115378

Arora P., Seshadri G., & Tyagi A. K. (2018). Fourth-generation refrigerant: HFO 1234yf. *Current Science*, 115(8), 1497-1503. https://doi.org/10.18520/cs/v115/i8/1497-1503

Arumuganainar K., Edwin M., & Raj J. B. (2022). Investigation on the performance improvement of household refrigeration system using R-134a refrigerant blended with ceria nano additives. *Applied Nanoscience*, 12(5), 1753-1761. https://doi.org/10.1007/s13204-022-02365-1

Bhattad A., Sarkar J., & Ghosh P. (2018). Improving the performance of refrigeration systems by using nanofluids: A comprehensive review. *Renewable and Sustainable Energy Reviews*, 82, 3656-3669. https://doi.org/10.1016/j.rser.2017.10.097

Bilen K., Dağidir K., & Arcaklioğlu E. (2022). The effect of nanorefrigerants on performance of the vapor compression refrigeration system: A comprehensive review. *Energy Sources, Part A: Recovery, Utilization, and Environmental Effects*, 44(2), 3178-3204. https://doi.org/10.1080/15567036.2022.2062071

Bilen K., Dağıdır K., Arcaklıoğlu E., & Cansevdi B. (2023). Energy and exergy analysis of R1234yf using instead of R134a in a vapour compression refrigeration system: An experimental study. *International Journal of Exergy*, 42(3), 315-336. https://doi.org/10.1504/IJEX.2023.135517

Bilen K., Işık B., Dağıdır K., & Arcaklıoğlu E. (2024). Thermodynamic analysis of usage of R134a, R1234yf, R450A, R513A, and R515B in the mechanical vapor compression refrigeration system. *Journal of the Faculty of Engineering and Architecture of Gazi University*, 39(1), 161-175. https://doi.org/10.17341/gazimmfd.1203826

Chauhan S. S., Kumar R., & Rajput S. P. S. (2019). Performance investigation of ice plant working with R134a and different concentrations of POE/TiO_2 nanolubricant using experimental method. *Journal of the Brazilian Society of Mechanical Sciences and Engineering*, 41, 163. https://doi.org/10.1007/s40430-019-1657-3

Chen X., Liang K., Li Z., Zhao Y., Xu J., & Jiang H. (2020). Experimental assessment of alternative low global warming potential refrigerants for automotive air conditioners application. *Case Studies in Thermal Engineering*, 22, 100800. https://doi.org/10.1016/j.csite.2020.100800

Choi T. J., Kim D. J., Jang S. P., Park S., & Ko S. (2021). Effect of polyolester oil-based multiwalled carbon-nanotube nanolubricant on the coefficient of performance of refrigeration systems. *Applied Thermal Engineering*, 192, 116941. https://doi.org/10.1016/j.applthermaleng.2021.116941

Colombo L. P. M., Lucchini A., & Molinaroli L. (2020). Experimental analysis of the use of R1234yf and R1234ze(E) as drop-in alternatives of R134a in a water-to-water heat pump. *International Journal of Refrigeration*, 115, 18-27. https://doi.org/10.1016/j.ijrefrig.2020.03.004

Dağıdır K. & Bilen K. (2023a). Experimental investigation of usage of POE lubricants with Al_2O_3, graphene or CNT nanoparticles in a refrigeration compressor. *Beilstein Journal of Nanotechnology*, 14(1), 1041-1058. https://doi.org/10.3762/bjnano.14.86

Dağıdır K. & Bilen K. (2023b). Principles of using nanorefrigerant in a VCRS: An experimental application. *International Journal of Advanced Natural Sciences and Engineering Researches*, 7(3), 38-43. https://as-proceeding.com/index.php/ijanser

Dağıdır K. & Bilen K. (2024). Usage of R513A as an alternative to R134a in a refrigeration system: An experimental investigation based on the Kigali amendment. *International Journal of Thermofluids*, 21, 100582. https://doi.org/10.1016/j.ijft.2024.100582

Dang M. N., Nguyen T. H., Nguyen V., Thu T. V., Le H., Akabori M., Ito N., Nguyen H. Y., Le T. L., & Nguyen T. H. (2020). One-pot synthesis of manganese oxide/graphene composites via a plasma-enhanced electrochemical exfoliation process for supercapacitors. *Nanotechnology*, 31, 345401. https://doi.org/10.1088/1361-6528/ab8fe5

De Paula C. H., Duarte W. M., Rocha T. T. M., De Oliveira R. N., & Maia A. A. T. (2020). Optimal design and environmental, energy and exergy analysis of a vapor compression refrigeration system using R290, R1234yf, and R744 as alternatives to replace R134a. *International Journal of Refrigeration*, 113, 10-20. https://doi.org/10.1016/j.ijrefrig.2020.01.012

Emkarate RL 32H Typical Properties Data Sheet. (2015). The Lubrizol Corporation, USA.

Erdinc M. T. (2023). Performance simulation of expander-compressor boosted subcooling refrigeration system. *International Journal of Refrigeration*, 149, 237-247. https://doi.org/10.1016/j.ijrefrig.2022.12.013

Farahani S. D., Farahani M., & Ghanbari D. (2022). Experimental study of the effect of spiral-star fins and nano-oil-refrigerant mixture on refrigeration cycle characteristics. J*ournal of Thermal Analysis and Calorimetry*, 147(11), 6469-6480. https://doi.org/10.1007/s10973-021-10921-0

Global Environmental Change Report GCRP. (1997). A Brief Analysis Kyoto Protocol, vol. IX, p. 24.

He X., Xu X., Bo G., & Yan Y. (2020). Studies on the effects of different multiwalled carbon nanotube functionalization techniques on the properties of bio-based hybrid non-isocyanate polyurethane. *The Royal Society of Chemistry Advances*, 10, 2180-2190. https://doi.org/10.1039/c9ra08695a

Intergovernmental Panel on Climate Change (IPCC), The Physical Science Basis. Contribution of Working Group I to the Fifth Assessment Report of the Intergovernmental Panel on Climate Change. In: Stocker T. F., Qin D., Plattner G.-K., Tignor M. M. B., Allen S. K., Boschung J., Nauels A., Xia Y., Bex V., & Midgley P. M. (2013). Cambridge University Press, Cambridge, United Kingdom, and New York, NY, USA. https://doi.org/10.1017/CBO9781107415324

Ismail M. F., Azmi W. H., Mamat R., Sharma K. V., & Zawawi N. N. M. (2023). Stability assessment of polyvinyl-ether-based TiO_2, SiO_2, and their hybrid nanolubricants. *Lubricants*, 11, 23. https://doi.org/10.3390/lubricants11010023

Kaushik R., Kundan L., & Sharma R. K. (2021). Investigating the performance of nanorefrigerant (R134a+CuO)-based vapor compression cycle: A new scope. *Heat Transfer Research*, 52(13), 33-53. https://doi.org/10.1615/HeatTransRes.2021036516

Khatoon S. & Karimi M. N. (2023). Thermodynamic analysis of two evaporator vapor compression refrigeration system with low GWP refrigerants in automobiles. *International Journal of Air-Conditioning and Refrigeration*, 31(1), 2. https://doi.org/10.1007/s44189-022-00017-1

Li H. & Tang K. (2022). A comprehensive study of drop-in alternative mixtures for R134a in a mobile air-conditioning system. *Applied Thermal Engineering*, 203, 117914. https://doi.org/10.1016/j.applthermaleng.2021.117914

Li H. S., Cao F., Bu X. B., Wang L. B., & Wang X. L. (2014). Performance characteristics of R1234yf ejector-expansion refrigeration cycle. *Applied Energy*, 121, 96-103. https://doi.org/10.1016/j.apenergy.2014.01.079

Li Z. H., Liang K., & Jiang H. Y. (2019). Experimental study of R1234yf as a drop-in replacement for R134a in an oil-free refrigeration system. *Applied Thermal Engineering*, 153, 646-654. https://doi.org/10.1016/j.applthermaleng.2019.03.050

Malwe P. D., Shaikh J., & Gawali B. S. (2022). Exergy assessment of a multistage multi-evaporator vapor compression refrigeration system using eighteen refrigerants. *Energy Reports*, 8, 153-162. https://doi.org/10.1016/j.egyr.2021.11.072.

Mishra S. & Sarkar J. (2016). Performance characteristics of low global warming potential R134a alternative refrigerants in ejector-expansion refrigeration system. *Archives of Thermodynamics*, 37(4), 55-72. https://doi.org/10.1515/aoter-2016-0027.

Mohamed H. A., Camdali U., Biyikoglu A., & Aktas M. (2022). Performance analysis of R134a vapor compression refrigeration system based on CuO/CeO_2 mixture nanorefrigerant. *Journal of the Brazilian Society of Mechanical Sciences and Engineering*, 44(5), 220. https://doi.org/10.1007/s40430-022-03522-x.

Moles F., Navarro-Esbri J., Peris B., Mota-Babiloni A., & Barragan-Cervera A. (2014). Theoretical energy performance evaluation of different single stage vapour compression refrigeration configurations using R1234yf and R1234ze(E) as working fluids. *International Journal of Refrigeration-Revue Internationale Du Froid*, 44, 141-150. https://doi.org/10.1016/j.ijrefrig.2014.04.025.

Morales-Fuentes A., Ramirez-Hernandez H. G., Mendez-Diaz S., Martinez-Martinez S., Sanchez-Cruz F. A., Silva-Romero J. C., and Garcia-Lara H. D. (2021). Experimental study on the operating characteristics of a display refrigerator phasing out R134a to R1234yf. *International Journal of Refrigeration*, 130, 317-329. https://doi.org/10.1016/j.ijrefrig.2021.05.032.

Mota-Babiloni A. & Makhnatch P. (2021). Predictions of European refrigerants place on the market following F-gas regulation restrictions. *International Journal of Refrigeration*, 127, 101-110. https://doi.org/10.1016/j.ijrefrig.2021.03.005.

Nair V., Parekh A. D., & Tailor P. R. (2020). Experimental investigation of a vapour compression refrigeration system using R134a/nano-oil mixture. *International Journal of Refrigeration*, 112, 21-36. https://doi.org/10.1016/j.ijrefrig.2019.12.009.

Navarro-Esbri J., Mendoza-Miranda J. M., Mota-Babiloni A., Barragan-Cervera A., & Belman-Flores J. M. (2013). Experimental analysis of R1234yf as a drop-in replacement for R134a in a vapor compression system. *International Journal of Refrigeration-Revue Internationale Du Froid*, 36(3), 870-880. https://doi.org/10.1016/j.ijrefrig.2012.12.014.

Ogbonnaya M., Ajayi O. O., & Waheed M. A. (2023). Influence of refrigerant type, nanoparticles concentration and size on the performance and exergy efficiency of the vapour compression refrigeration system using Al_2O_3 based nanolubricant. *Journal of Nanofluids*, 12(3), 712-722. https://doi.org/10.1166/jon.2023.1953.

Pawale K. T., Dhumal A. H., & Kerkal G. M. (2017). Performance analysis of VCRS with nano-refrigerant. *International Research Journal of Engineering and Technology*, 4(4), 1031-1037. https://www.irjet.net/archives/V4/i5/IRJET-V4I5201.pdf

Prins R. (2020). Mini-review on the structure of γ-Al_2O_3. *Journal of Catalysis*, 392, 336-346. https://doi.org/10.1016/j.jcat.2020.10.01

Raghavulu K. V. & Rasu N. G. (2021). An experimental study on the improvement of coefficient of performance in vapor compression refrigeration system using graphene lubricant additives. *Energy Sources, Part A: Recovery, Utilization, and Environmental Effects*. https://doi.org/10.1080/15567036.2021.1909186

Redhwan A. A. M., Azmi W. H., Sharif M. Z., Mamat R., Samykano M., & Najafi G. (2019). Performance improvement in mobile air conditioning system using Al_2O_3/PAG nanolubricant. *Journal of Thermal Analysis and Calorimetry*, 135, 1299-1310. https://doi.org/10.1007/s10973-018-7656-2

Salem M. R. (2020). Performance enhancement of a vapor compression refrigeration system using R134a/MWCNT-oil mixture and liquid-suction heat exchanger equipped with

twisted tape turbulator. *International Journal of Refrigeration*, 120, 357-369. https://doi.org/10.1016/j.ijrefrig.2020.09.009

Sanchez D., Cabello R., Llopis R., Arauzo I., Catalan-Gil J., & Torrella E. (2017). Energy performance evaluation of R1234yf, R1234ze(E), R600a, R290 and R152a as low-GWP R134a alternatives. *International Journal of Refrigeration*, 74, 269-282. https://doi.org/10.1016/j.ijrefrig.2016.09.020

Sanukrishna S. S., Murukan M., & Jose P. M. (2018). An overview of experimental studies on nanorefrigerants: Recent research, development and applications. *International Journal of Refrigeration*, 88, 552-577. https://doi.org/10.1016/j.ijrefrig.2018.03.013

Saravanan K. & Vijayan R. (2018). First law and second law analysis of Al_2O_3/TiO_2 nano composite lubricant in domestic refrigerator at different evaporator temperature. *Materials Research Express*, 5, 095015. https://doi.org/10.1088/2053-1591/aad72d

Sharif M. Z., Azmi W. H., Zawawi N. N. M., & Ghazali M. F. (2022). Comparative air conditioning performance using SiO_2 and Al_2O_3 nanolubricants operating with Hydrofluoroolefin-1234yf refrigerant. *Applied Thermal Engineering*, 205, 118053. https://doi.org/10.1016/j.applthermaleng.2022.118053

Singh D. K., Kumar S., Kumar S., & Kumar R. (2021). Potential of MWCNT/R134a nanorefrigerant on performance and energy consumption of vapor compression cycle: A domestic application. *Journal of the Brazilian Society of Mechanical Sciences and Engineering*, 43(12), 540. https://doi.org/10.1007/s40430-021-03240-w

Soliman A. M. A., Rahman A. K. A., & Ookawara S. (2019). Enhancement of vapor compression cycle performance using nanofluids: Experimental results. *Journal of Thermal Analysis and Calorimetry*, 135(2), 1507-1520. https://doi.org/10.1007/s10973-018-7623-y

Subhedar D. G., Patel J. Z., & Ramani B. M. (2022). Experimental studies on vapour compression refrigeration system using Al_2O_3/mineral oil nano-lubricant. *Australian Journal of Mechanical Engineering*, 20(4), 1136-1141. https://doi.org/10.1080/14484846.2020.1784558

United Nations Environment Programme (UNEP). (1987). Montreal Protocol on Substances that Deplete the Ozone Layer, Final Act, United Nations, New York.

United Nations Environment Programme (UNEP). (2016) Twenty-eighth Meeting of the Parties to the Montreal Protocol on Substances that Deplete the Ozone Layer, Decision XXVIII/Further Amendment of the Montreal Protocol, 2016:1-9.

Yadav S., Liu J., & Kim S. C. (2022). A comprehensive study on 21st century refrigerants - R290 and R1234yf: A review. *International Journal of Heat and Mass Transfer*, 182, 121947. https://doi.org/10.1016/j.ijheatmasstransfer.2021.121947

Yang Z., Feng B., Ma H., Zhang L., Duan C., Liu B., Zhang Y., Chen S., & Yang Z. (2021). Analysis of lower GWP and flammable alternative refrigerants. *International Journal of Refrigeration*, 126, 12-22. https://doi.org/10.1016/j.ijrefrig.2021.01.022

Yilmaz A. C. (2020). Performance evaluation of a refrigeration system using nanolubricant. *Applied Nanoscience*, 10(5), 1667-1678. https://doi.org/10.1007/s13204-020-01258-5

Zawawi N. N. M., Azmi W. H., Redhwan A. A. M., Ramadhan A. I., & Ali H. M. (2022). Optimization of air conditioning performance with Al_2O_3-SiO_2/PAG composite nanolubricants using the response surface method. *Lubricants*, 10, 243. https://doi.org/10.3390/lubricants10100243

Journal Homepage: https://dergipark.org.tr/tr/pub/isibted

Isı Bilimi ve Tekniği Dergisi

Archive: https://tibtd.org.tr/dergi

Investigations on Thermal Performance of an Electronic Board using Conduction-Based Finite Element Method with a New Modeling Approach

Yener USUL [1], Şenol BAŞKAYA [2], Bülent ACAR [1], Tamer ÇALIŞIR [3,*]

[1] *Roketsan Inc. Ankara, Türkiye*
[2] *University of Kyrenia Faculty of Aviation and Space Sciences Dept. of Aeronautical Engineering, Girne, North Cyprus*
[3] *Gazi Üniversitesi Mühendislik Fakültesi Makina Mühendisliği Bölümü 06570 Maltepe, Ankara, Türkiye*

A R T I C L E I N F O

2024, vol. 44, no.2, pp. 294-307

doi: 10.47480/isibted.1563932

Research Article
Received: 18 September 2023
Accepted: 22 August 2024

* *Corresponding Author*
e-mail: tamercalisir@gazi.edu.tr

Keywords:
Conduction-based finite element method (FEM)
Experiment
Natural Convection
Thermal Management

ORCID Numbers in author order:
0000-0002-1087-4743
0000-0001-9676-4387
0000-0002-0721-0444

A B S T R A C T

Electronic systems are used in almost all areas of industry, with an increasing power consumption rate. This trend makes thermal management of electronics compulsory in order for proper operation. Several methods can be employed to examine electronics' thermal behavior. Conduction-based Finite Element Method (FEM) for heat transfer analysis is one of them; providing accurate solutions within short solution times is one of its outstanding advantages. Nevertheless, the fluid inside or around the system, usually air for electronic systems, is not included directly in the conduction-based FEM analysis model. This is an essential deficiency in terms of solution accuracy. If this drawback is overcome, conduction-based FEM will become a preferred analysis method, especially for transient problems under natural convection. In this study, a conduction-based FEM analysis model of an electronic board with two heat-dissipating components inside an enclosure under transient natural convection was developed. The procedure of the model involves the correction of unknown input parameters. An experimental investigation was performed, the results of which were used as reference values for the correction process. These unknown parameters were determined iteratively. The iteration was continued until the results of the analysis and those of the experiment matched. The difference between the results of the analysis and those of the experiment was less than 2-3°C. Some parametrical thermal investigations were performed on the electronic board using the final analysis model.

İletim Tabanlı Sonlu Elemanlar Yöntemi Kullanılarak Yeni bir Modelleme Yaklaşımı ile bir Elektronik Kartın Isıl Performansının İncelenmesi

M A K A L E B İ L G İ S İ

Anahtar Kelimeler:
İletim Tabanlı sonlu eleman yöntemi
Deney
Doğal Konveksiyon
Isıl Yönetim

Ö Z E T

Elektronik sistemler, artan güç tüketimiyle birlikte sanayinin hemen her alanında kullanılmaktadır. Bu eğilim, elektronik elemanların düzgün çalışması için termal yönetimini zorunlu kılmaktadır. Elektronik elemanların termal davranışını incelemek için çeşitli yöntemler kullanılmaktadır. Isı transferi analizi için İletim Tabanlı Sonlu Elemanlar Yöntemi (SEY) bunlardan biridir; Kısa çözüm sürelerinde doğru çözümler sunması öne çıkan avantajlarından biridir. Bununla birlikte, sistemin içindeki veya etrafındaki akışkan (elektronik sistemler için genellikle hava), doğrudan iletim tabanlı SEY analiz modeline dahil edilmez. Bu çözüm doğruluğu açısından önemli bir eksikliktir. Bu dezavantajın aşılması durumunda, iletim tabanlı SEY, özellikle doğal taşınım altındaki geçici problemler için tercih edilen bir analiz yöntemi haline gelecektir. Bu çalışmada, zamana bağlı doğal konveksiyon altında bir kapalı ortam içinde iki ısı kaynağına sahip bir elektronik kartın iletim tabanlı SEY analiz modeli geliştirilmiştir. Modelin prosedürü bilinmeyen parametrelerinin düzeltilmesini içermektedir. Sonuçları düzeltme işlemi için referans değerleri olarak kullanılan deneysel bir araştırma gerçekleştirilmiştir. Bu bilinmeyen parametreler iteratif olarak belirlenmiştir. Analiz sonuçları ile deneyin sonuçları eşleşene kadar iterasyona devam edildi. Analiz sonuçları ile deneysel sonuçlar arasındaki fark 2-3°C'nin altında olduğu tespit edilmiştir. Son analiz modeli kullanılarak elektronik kart üzerinde bazı parametrik termal incelemeler gerçekleştirilmiştir.

NOMENCLATURE

α	Thermal diffusivity (m^2/s)
C	Coefficient (-)
c_p	Specific Heat (J/kg.K)
ε	Emissivity (-)
h	Heat Transfer Coefficient ($W/m^2.K$)
k	Thermal conductivity (W/m.K)
L	Characteristic lenght (m)
Nu	Nusselt number (-)
q	Heat flux (W/m^2)
Q	Thermal power (W)
R	Thermal resistance ($m^2.k/W$)
Ra	Rayleigh number (-)
T	Temperature (°C)
$T_{heater\ plate}$	Heater plate temperature (°C)
$T_{initial}$	Initial temperature (°C)

INTRODUCTION

Electronic systems are excessively used in almost all areas of industry. Moreover, the demand for the usage of electronic systems is increasing continuously. This demand makes the macro level packaging of the electronics more compact, which causes a higher rate of heating with a lower cooling capacity. Because of this, thermal management is vital for electronic systems, especially for those placed in narrow enclosures with a high heat dissipating rate. Automobiles, airplanes, missiles, and informatics can be seen as the areas of application, where the thermal management of electronics is important.

There are two main stages in the thermal management of electronics. The first one is to take precautions during the design phase, in order to minimize the internal and external heating and to let the heat be released from the system. The second stage of thermal management is finding a solution for cooling the system. If the first stage is applied properly, the need for the second step is minimized. In this way, additional costs, weight, maintenance, etc., that come from the use of extra equipment for thermal management are minimized. Therefore, great attention should be paid to the precaution step of the electronics during the design phase, to get more economical and robust systems.

An electronic system can be analyzed experimentally and numerically in practical applications, in terms of thermal considerations. The experimental method is usually the most accurate. Nevertheless, some factors, such as cost, repeatability, accessibility, are disadvantages to experimental methods. Considering the combined effect of cost, accuracy, repeatability, etc., numerical methods are the best choice. There are different numerical methods. The most commonly used ones are CFD (Computational Fluid Dynamics) and conduction-based FEM (Finite Element Method) for the analyses of electronic systems used in practice. Since fluid inside or around the system is modeled in the CFD method, computation time can be long, especially for time-dependent conjugate heat transfer problems with natural convection behavior. On the other hand, for the conduction-based FEM, the fluid inside the computational domain is not directly included in the model. Instead, the heat transfer between the solid and the fluid part inside the computational domain is accounted for by applying a proper boundary condition. Once the conduction-based FEM model and the convective heat transfer boundary conditions are set up properly and correctly, accurate results can be obtained by solving the main disadvantage of the CFD approach, which is the long solution time for time-dependent conjugate heat transfer problems, including natural convection.

Some studies have conducted on the thermal analysis of electronic systems at different levels, such as the component level, the board level, and the system level, using different methods in the literature. Ocak (2010) studied the thermal behavior of an electronic board experimentally and numerically at different configurations. CFD analyses were performed by the author. The board and the components were modeled according to conduction-based compact thermal modeling, at five different levels. The problem includes natural convection for one configuration and forced convection for another. Eveloy and Rodgers (2005) performed a numerical and experimental study of an electronic board carrying a 160-lead PQFP (Plastic Quad Flat Pack) component. The effects of the ambient velocity, and an increasing rate of the ambient temperature were researched. The CFD analyses were performed as conjugate and segregated, and the results were compared with experimental results. Byon et al. (2011) studied the variation of the thermal performance of a chip for different chip thickness and power values. Since geometry is not complicated, the results of the experiment and the analytical solutions matched well. Lira and Greenlee (2007) performed detailed and simplified numerical thermal analyses of an electronic board. The convective heat transfer coefficients were obtained using the empirical relations in the literature. The results of the analyses were compared. The simplified model is said to be enough for data that are relatively more general. However, for the results that are more specific, such as, the temperature values of the components, a detailed modeling technique is preferred. Joshy et al. (2017) examined the thermal behavior of electronic boards placed in a parallel configuration. The examination was carried out for both steady and transient state and both experimental and numerical methods were employed. Resistor-capacitor method was used as the numerical method. Lim et al. (2021) investigated the effect of independent variables on the thermal behavior of flexible printed circuit boards in order to obtain optimum cooling performance with least deflection and stress. The optimized Reynolds number has been identified in the range of 21364-29367 for various packages. Otaki et al. (2022) described a method where they combined the Bayesian optimization and lumped-capacitance thermal network model for speeding up of the thermal design optimization of electronic circuit board layouts. Wang et al. (2024) investigated the thermal design of a PCB by using micro-pin fin array heat sinks. They investigated four different types of micro-pin fin arrays. Rakshith et al. (2022) showed an overview about the design and operation of thermal ground planes and their applications to various fields.

Thermal performance of electronics at the component level, the board level, and the system level was analyzed by conduction-based methods (Devellioğlu, 2008; Cheng et al., 2013; Cheng et al., 2008; Chen et al., 2003; Zahn and Stout, 2002), for different geometrical and boundary conditions for

steady-state problems. The convective HTCs (Heat Transfer Coefficients) for those studies were calculated using empirical relations obtained from the literature.

CFD analyses were performed for electronic systems in an enclosure under natural convection to examine the effects of different geometries and boundary conditions at different levels, such as the component level, the board level, the and system level (Xu, 2017; Stancato et al., 2017; Eveloy et al., 2002). All of them were conducted for steady-state conditions, because the solution of conjugate CFD problems for heat transfer problems under transient natural convection takes long time. In the studies of Han and Jung (2017) and Rodgers et al. (1999) similar studies were carried out, by modeling some extra geometrical details.

CFD analyses, together with experimental studies, were performed for the purpose of comparison of the system level and component level electronic units (Taliyan et al., 2010; Chavan and Sathe, 2016; Pang, 2005; Rosten et al., 1995). The systems and components were inside an enclosure in the above mentioned studies. Parametric studies were performed under steady-state conditions for different values of the geometrical and boundary conditions.

There are also studies in which the thermal behavior of the air inside an enclosure was examined, with heat sources at the walls of the enclosure instead of electronic components or systems (Deng, 2008; Khatamifar et al., 2017; Zaman et al., 2013; Nogueira et al., 2011). The results of those studies can be utilized to determine the way to examine the thermal performance of electronics, since the geometry and boundary conditions resemble electronic systems.

Battula et al. (2024) investigated numerically the combined effect of conduction, convection and radiation from a heated vertical electronic board. They obtained the optimum values of surface emissivity, thermal conductivity and modified Richardson number.

Some studies mentioned above examined the thermal performance of electronic components under different geometrical and boundary conditions, by utilizing experimental or numerical methods that include CFD, conduction-based FEM, or resistor-capacitor methods. Other studies evaluated and compared the analysis methods among each other or with the experimental method. However, no study is about tuning the conduction-based FEM model parameters by using experimental data in order to improve the accuracy of the FEM without making any concessions on short solution time, by virtue of the conduction-based FEM.

This study examined the thermal performance of an electronic board with two heat-dissipating components for different boundary conditions, parametrically. Conduction-based FEM was used to examine the thermal performance of the board. Before the parametric analyses, a proper analysis model was set up. The set up process included the determination of the analysis model input parameters that were unknown or uncertain. These were: thermal contact resistance values between the components and the PCB (Printed Circuit Board), component power deration rate, which is the deration of the power of the resistor-type components after they exceeded a certain temperature, generally 75°C, and coefficients for calculating the natural convective HTCs at PCB and component surfaces. The determination of the coefficients for calculating the natural convective HTCs was the key in eliminating the main disadvantages to the conduction-based FEM.

The aims of the present study were to show a comparison of the thermal behavior of the system under various boundary conditions, and to obtain the most suitable analysis method.

PROBLEM DESCRIPTION

In this part of the study, the applied experimental and numerical model has been described. The used experimental setup and experimental procedure has been introduced. Afterwards, the numerical model has been given.

The determination of the input parameters were achieved by performing an experiment and corresponding analyses, iteratively. The results of the experiments were used as reference values. The initial analyses were performed with initial values of the input parameters. The initial values were guessed within a physically sensible range. Then, the results of the experiments and the initial analyses were compared. According to the difference between the results, the initially guessed values of the input parameters were tuned. Analyses were repeated with those tuned values, and the results were compared again with the experimental results. Parameters were updated, within a physically acceptable range. This iterative process continued until the results of the experiments and the analysis matched within an acceptable error range.

The iterative comparison was made for thermal contact resistance between the components and the PCB, component power deration rate, and the coefficient used to calculate the natural convective HTCs on the surfaces in a certain order, in order to minimize the number of unknowns. First, the thermal contact resistance values were determined. Then, the power deration rate and coefficients for calculating the convective HTC on the surfaces have been obtained. A representative flow diagram of the whole process is shown in Fig. 1.

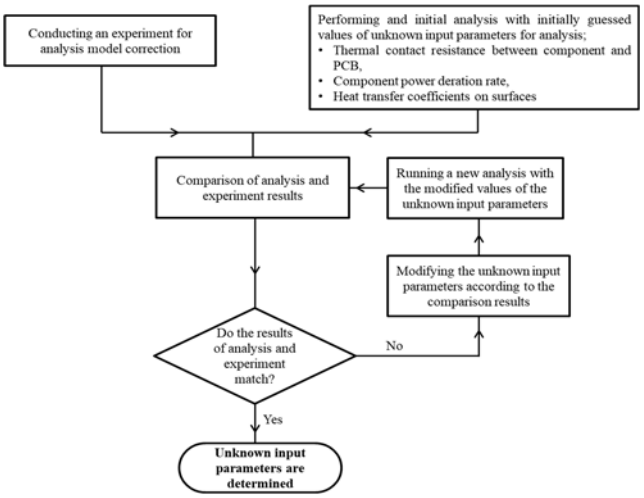

Figure 1. The flow diagram of the proposed thermal analysis model.

Experimental Setup

The experiments were conducted inside an enclosure of a size of 300 mm × 300 mm × 300 mm. The main body of the enclosure was made of aluminum. To prevent heat loss as much as possible, thermal insulation was applied outside of

the main body. There was a 290 mm × 290 mm heater plate at the bottom of the enclosure, which covers almost the whole bottom area. The purpose of the heater plate is to provide a desired temperature profile to the sample from the bottom side. There were heater resistors under the plate to supply heat to the plate. The resistors were controlled by a manual type of variac, in order to control the power supplied to the heater resistors. The input voltage to the resistors can be adjusted to any value within a continuous range of 0–220 V using the variac. A photograph of the experimental setup, the power supply, and the placement of the PCB inside the enclosure is presented in Fig 2.

Figure 2. A general view of the experimental setup.

There were thermocouples inside the heater plate to measure its temperature, in order to adjust the variac at the correct value. In addition to the embedded thermocouples, there were 10 more thermocouples for the temperature measurement of the air inside the enclosure.

Experimental Procedure

The purpose of the experiments was to obtain reference results for correction of the analysis model. The experiments were performed in a certain sequence, according to the model's correction sequence. The experiments were composed of two parts. In the first part, the heater plate was heated from room temperature to 60°C, with a heating rate of 2.8°C/min for approximately 650 seconds and then maintained at 60°C for 350 seconds. The components of the PCB were powered off during the first session of the experiments. The second part of the experiments was conducted by maintaining the heater plate at a constant temperature of 60 °C, while the components were powered on. The first part persisted for 1000 seconds, while the second part lasted for 600 seconds.

During the whole experiment, the temperature of the components and the PCB was measured via thermocouples in certain locations (S-1, S-2, and S-3), which are shown in Fig. 3.

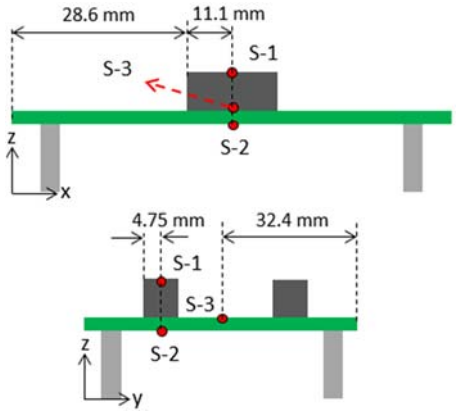

Figure 3. Locations on electronic board where temperature changes with time.

Uncertainty Analysis

An uncertainty analysis was performed to determine the accuracy of the experimental measurements. The uncertainty has been obtained according to the procedure of Holman (1994). The uncertainty of variables have been obtained by using the root-sum-square formulation:

$$W_R = \left[\left(\frac{\partial R}{\partial x_1} W_1 \right)^2 + \left(\frac{\partial R}{\partial x_2} W_2 \right)^2 + \left(\frac{\partial R}{\partial x_3} W_3 \right)^2 + \ldots\ldots\ldots + \left(\frac{\partial R}{\partial x_n} W_n \right)^2 \right]^{1/2} \quad (1)$$

where R is the result of a given function of the independent variables x_1, x_2, x_3,...,x_n. W_R shows the uncertainty of the variable R, and $W_i(W_1, W_2,...,W_n)$ represents the uncertainty of the independent variable. The uncertainties obtained for calculated variables have been given in Table 1.

Table 1. Measurement Uncertainties.

Variable	Value	Uncertainty	Percentage Uncertainty (%)
Heat Transfer in the component	Q_{comp}=793 W	W_{Qcomp} = 0.0143	1.80
Thermal resistance along electronic board	R_{board}=0.00483 m²K/W	W_{Rboard} = 0.000167	3.45
Heat flux from the component to the electronic board by conduction	q_{cond}=627.28 W/m²	W_{qcond} = 77.04	12.30
Heat stored in the component	Q_{st}=0.49254 W	W_{Qst} = 0.0161	3.27
Heat transfer by convection and radiation from the component	$Q_{conv+Qrad}$ = 0.1681 W	$W_{Qconv+Qrad}$ = 0.0217	12.90
Experimentally obtained heat transfer coefficient	h=13.2 W/m²K	W_h = 1.756	13.30
Rayleigh number	Ra=8630	W_{Ra} = 474.7	5.50
Nusselt number	Nu=5.2	W_{Nu} = 0.0715	1.38

Numerical Model

ABAQUS, a commercial conduction-based FEM software, was used in the numerical study. The enclosure was excluded from the analysis model. In order to represent the heat transfer effects of the air on the solid parts, convective heat transfer boundary conditions were defined on the surface of the components and the PCB.

Mathematical Formulation

The numerical method used in this study contains no fluid motion. Therefore, only conduction through solid parts was

considered. The fundamental equation used for conduction-based FEM heat transfer analysis is the general heat conduction equation for three-dimensional space, given in Eq. (2):

$$\frac{\partial^2 T}{\partial x^2}+\frac{\partial^2 T}{\partial y^2}+\frac{\partial^2 T}{\partial z^2}+\frac{\dot{q}}{k}=\frac{1}{\alpha}\frac{\partial T}{\partial t} \quad (2)$$

where, T is temperature, x, y, and z are coordinate axes, is the internal heat generation, k is the thermal conductivity, α is the thermal diffusivity and t is time.

In the first part of the analysis, where the components were powered off, the heater plate was the only heat source, and it was heated from room temperature to 60°C. Convective heat transfer boundary conditions were applied on the surface of the electronic board and the components. The convective heat transfer boundary condition was defined to take the combined effects of convective and radiative heat transfer between the heater plate and the electronic board. The temperature range and temperature differences between the plate and the board were appropriate for accepting this combined boundary condition assumption. The ambient temperature was taken from the experimental data, to define the convective heat transfer boundary condition. The following equations were used for the calculation of the combined convective radiative heat transfer coefficient:

$$q_{radiative}=\varepsilon\sigma\left(T_1^4-T_2^4\right) \quad (3)$$

$$q_{radiative}=\varepsilon\sigma\left(T_1+T_2\right)\left(T_1^2+T_2^2\right)\left(T_1-T_2\right) \quad (4)$$

$$q_{radiative}=h_{equivalent}\left(T_1-T_2\right) \quad (5)$$

$$h_{equivalent}=\varepsilon\sigma\left(T_1+T_2\right)\left(T_1^2+T_2^2\right) \quad (6)$$

where, qradiative is the radiative heat transfer, hequivalent is the combined convective and radiative heat transfer coefficient, T_1 and T_2 are the surface and the environment temperatures between which the radiative and convective heat transfer occurs and ε and σ are emissivity and the Stefan-Boltzmann constant, respectively.

In the second part of the analysis, heat dissipation inside the components was defined. Radiative heat transfer between the heater plate and the electronic board was ignored, since the temperature difference between them was low enough. Heat was transferred between the plate and the electronic board by conduction and convection. The temperature values were defined at the legs of the PCB as Dirichlet boundary condition for both stages of the analysis, since the heater plate was not included in the model.

Thermal contact resistance was defined for the component and the PCB interfaces. Nevertheless, thermal contact resistance was ignored at the interface between the PCB-legs and legs-heater plate, because those parts were mounted tightly.

Mesh Independency Study for FEM

A mesh independency study was performed to determine the optimal mesh size. The temperature distribution on a path shown in Fig. 4 was used for the mesh independency study. Analyses for a dummy boundary condition were performed for mesh sizes of 5, 2.5, 1.25, and 0.625 mm.

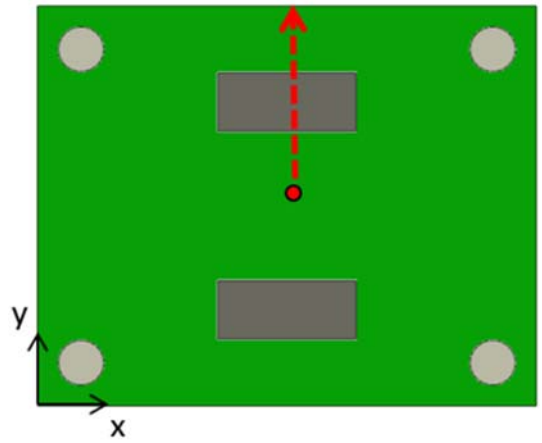

Figure 4. The path on which the temperature distribution was extracted at 600 s in conduction-based FEM analyses.

The results of the temperature distribution on the path for the predetermined mesh sizes are shown in Fig. 5. 1.25 mm and sizes lower than that are proper for accurate results, as it is seen in Fig. 5. Therefore, a 1.25 mm average mesh size was used for all analyses from this point on.

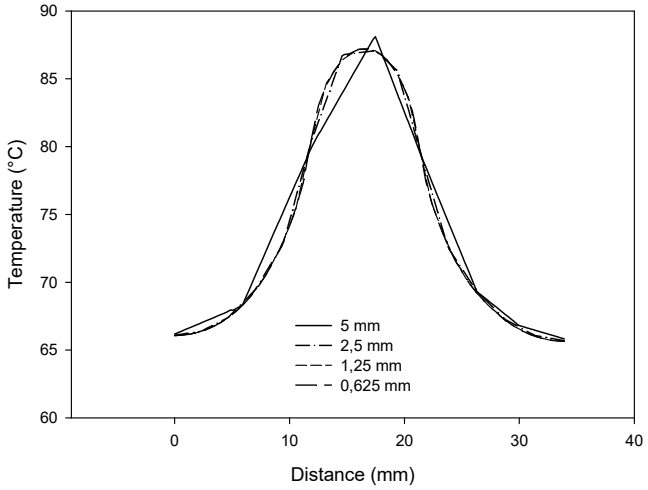

Figure 5. Temperature distribution on PCB at 600 s for different mesh sizes.

CORRECTION OF THE CONDUCTION-BASED FEM

The unknown input parameters in this study were the heat transfer coefficients on the surfaces, thermal contact resistance values between the components and the PCB, and the power generation rate of the components, occurring at high temperatures.

The determination procedure of the unknown input parameters should have been performed in an appropriate sequence, to minimize the number of unknowns at the same process. Thermal contact resistance values must be known in any case, since the heat will flow through the components and PCB interface if there is a temperature difference between the components and the PCB. The convective heat transfer coefficients were also necessary for all analyses. On the other hand, the power generation rate was necessary only when the components were powered on. Considering these phenomena, an analysis model correction had to be conducted, starting from the case where the components

were powered off. Hence, the number of unknown parameters was reduced in one of the correction steps. That is the reason why the experiments were conducted in two sessions, as mentioned before.

All of the unknown input parameters were determined by an iterative process. Initially, some values were chosen from a physically acceptable range of the unknown input parameters. Then, an initial analysis was run with the initially guessed values of the unknown input parameters. The results from the experiments and the initial analysis were compared, and the guessed values were updated according to the difference between them. This process continued until the results of the analysis and the experiment matched within an acceptable error band. The foregoing correction procedure was repeated for all unknown input parameters. This iterative procedure was performed using Isight, a commercial integrator software.

Determination of Thermal Contact Resistances

The thermal contact resistance values were determined using the first part of the experiment and the analysis, where the components were powered off. The only heat source in the system in that part was the heater plate. The outer part of the components was made of ceramic. The surface of the PCB was mid-level rough. No extra pressure was applied on the components. With these facts, a range of 1–100 m^2K/W was chosen, within which the thermal contact resistance values were changed iteratively (Gilmore and Donabedian, 2003).

Since the temperature of the system was not very high in the first part of the experiment, and there was only a small temperature gradient in the system, the heat transfer coefficient of all surfaces was taken to be 5 W/m^2K. By this assumption, the number of unknowns was reduced with a small loss in accuracy. Conduction-based thermal FEM analyses were performed for thermal contact resistance values, R, of 1, 10, and 100 m^2K/W. The results of those analyses have been presented in Fig. 6, together with experimental results for S-2 point. Only the results of the S-2 point were presented, since the deviation between the results is seen more clearly than at other points.

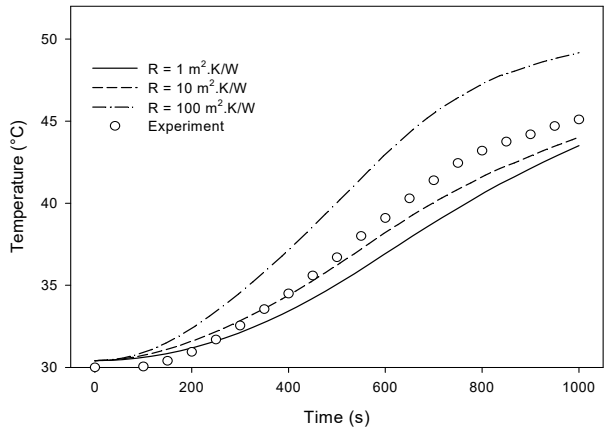

Figure 6. Comparison of FEM and experimental results of the variation of temperature of S-2 point with time for 1, 10, and 100 m^2K/W thermal contact resistance values with h = 5 W/m^2K for all surfaces.

The next step was to repeat the analysis by changing the thermal contact resistance values within the range of 1–100 m^2K/W, until the deviations of the results of the analysis from the experiment were minimized. A total of 500 analyses were run to get the optimum result. The results of the analysis with the final values of the thermal contact resistances and the experimental results are represented in Fig. 7.

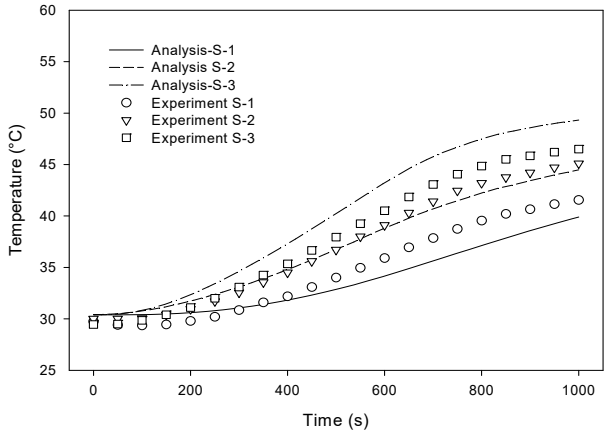

Figure 7. Comparison of FEM and experimental results of the variation of temperature with time for the final values of thermal contact resistances between components and PCB.

Small differences, not exceeding 5°C, have been obtained between the analysis and the experimental results. The main reason for these errors was choosing average constant values for the convective heat transfer coefficients for all surfaces. However, this level of error is acceptable, considering the problem structure.

Determination of Power Deration Rate and Heat Transfer Coefficients

In the second part of the analysis, the power deration rate and the heat transfer coefficients remained as unknown input parameters. The same procedure was followed as in the first part. A physically acceptable range of the power deration value was chosen to make the initial guess.

Power deration rate is generally 10–20%/10 °C for resistor-type components. In order to see the effect of power deration rate on the electronic board temperature, analyses were performed for 10, 15, and 20%/10 °C values of component power deration rate, by keeping the heat transfer coefficient value constant as 5 W/m^2K. The results are shown in Fig. 8, where it is seen that great differences may occur, by up to 10–15 °C, especially for the component temperature.

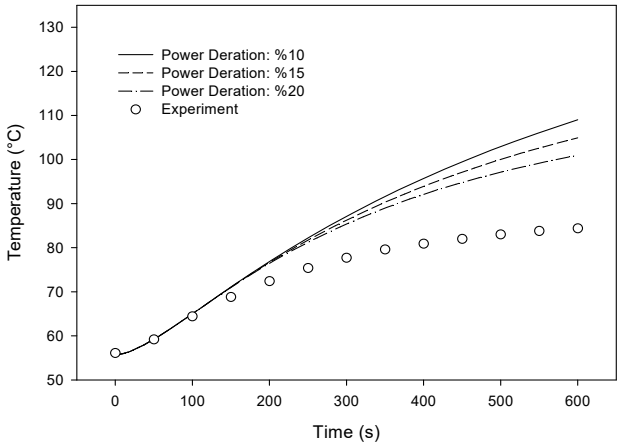

Figure 8. Comparison of FEM and experimental results of the variation of temperature of S-2 point with time for 10%/10 °C, 15%/10 °C and 20%/10 °C component power deration rate values with h = 5 W/m^2K for all surfaces.

The heat transfer between the electronic board and the surrounding air occurs by natural convection, since there was no active cooling element in the experimental setup. The natural convective heat transfer coefficient for air at approximately 1 atm pressure is between 2 and 25 W/m²K (Steinberg, 1991). A sensitivity analysis for the heat transfer coefficients was performed, keeping the component power deration rate at a constant value of 15%/10 °C. The analyses were performed for 5, 15, and 25 W/m²K values of heat transfer coefficients for all surfaces. The results of those analyses are shown in Fig. 9, where it is seen that, for different values of the heat transfer coefficients, differences of up to 20–25°C may be seen, especially for the temperature of the component.

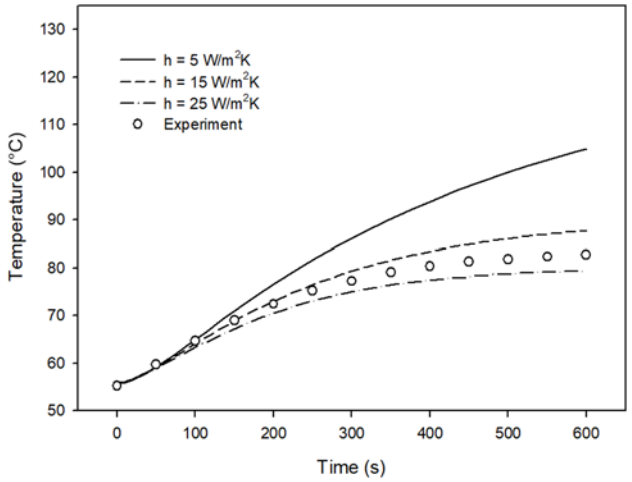

Figure 9. Comparison of FEM and experimental results of the variation of temperature of S-2 point with time for 5, 15, and 25 W/m²K heat transfer coefficient values on all surfaces with component power deration rate is 15%/10 °C.

Considering that the working temperature limits of electronic components are generally around 85 °C, the differences that may rise up to 20–25°C, which were deduced from the analyses, cannot be accepted for a reliable design. This indicates that the component power deration rate and the heat transfer coefficient values have to be determined close to their actual values, to achieve accurate results.

A similar procedure was followed to tune the unknown input parameters, power deration rate, and the heat transfer coefficient values as in the thermal contact resistance values. Shortly, a physically acceptable range of the unknown parameters, and subsequently, the initial values of these parameters were determined. After determining the range of the initial guess and the initial values of the parameters, initial analysis and the iterative analyses were performed. The iteration continued until the results of the analysis and the experiment matched. The component power deration rate and the heat transfer coefficient values were determined in the same tune-up procedure, changing the values concurrently.

The value range of the component power deration was chosen to be 10–20%/10 °C, which is a common range for the component power deration rate. The initial values were chosen to be the mid-value, 15%/10 °C. There are different empirical methods to calculate the heat transfer coefficient on the surfaces of the electronics inside an enclosure. One of them was employed in this study, and it is shown in Eq. (7) (Steinberg, 1991).

$$h = 0.52C\left(\frac{\Delta T}{L}\right)^{0.25} \quad (7)$$

In Eq. (7), h is the heat transfer coefficient (W/m²K), ΔT is the difference between the surface and ambient temperature (°C), and L is the characteristic length of the surface (m). 'C' is a coefficient which depends on the geometry, orientation, and surrounding environment's effects on the surface. This coefficient can only be determined experimentally.

The initial value of the heat transfer coefficient was taken to be 5 W/m²K for all surfaces. The range of the C value was determined as 1–10, considering literature values (Steinberg, 1991). An analysis was performed with the initial values of the component power deration rate and the heat transfer coefficients, where the thermal contact resistance values between the component and the PCB were known. The results of the initial analysis and the experiments are shown in Fig. 10.

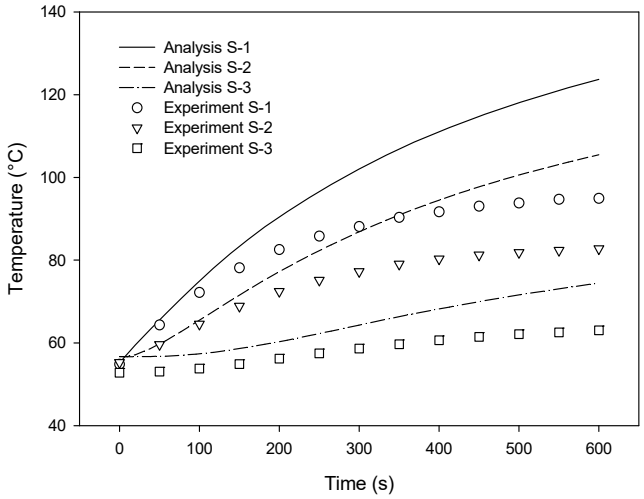

Figure 10. Comparison of FEM and experimental results of the variation of temperature with time for initial values of heat transfer coefficient and component power deration rate (5 W/m²K, %15/10 °C).

Table 2. Corrected 'C' coefficients for surfaces of PCB and components.

Surface	C
Upper Surface of Components	6.8
Long Side Surfaces of Components Facing Each Other	3.9
Long Side Surfaces of Components Facing Outside	3.4
Short Side Surfaces of Components	4.9
Upper Side of PCB Near Components	8.7
Upper Side of PCB Away from Components	2.4
Bottom Side of PCB Near Components	6.8
Bottom Side of PCB Away from Components	5.8

In Fig. 11, it is seen that the maximum difference between the results of the experiments and the analysis is less than 2–3°C. This level of error is quite low for a numerical analysis of this kind of problem. This indicates that a correct analysis model was set up. As long as critical modifications, such as geometry and material properties of the system are not made, the corrected analysis model can be employed to examine the system's thermal behavior under different configurations and boundary conditions. Hence, quick and accurate parametrical analyses can be performed.

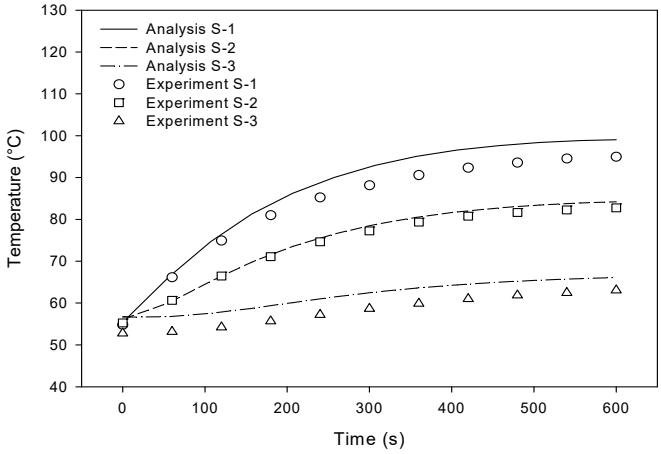

Figure 11. Comparison of FEM and experimental results of the variation of temperature with time for the corrected analysis model.

RESULTS AND DISCUSSION

Parametrical thermal analyses were performed using the corrected analysis model, and the results are presented in this part. The examined parameters were: component power (Q), initial temperature of the whole system ($T_{initial}$), and the heater plate temperature ($T_{heaterplate}$). Realistic values of the parameters were used. For example, 0.5, 1, 2, and 4 mW/mm^3 component power values were used for parametrical analyses, since heat dissipation values are in this order in practical application of electronic components. Initial temperature values were selected as 20, 30, 40, and 50 °C, whereas the effects of the heater plate temperature on the system behavior were examined for 20, 40, 60, and 80 °C, representing the external heat sources' effects.

The main objective of this study was to set up a correct conduction-based FEM analysis model and then to examine the electronic board's thermal behavior for different boundary conditions, using the corrected analysis model. The results of the analyses are presented as the change of the temperature values at some or all of the sensor positions (S-1, S-2, and S-3) during 600 s, and temperature distribution on the upper surfaces of the PCB and components as contour graphs at the final time of 600 s. The results were shown in a way that the effect of one parameter was examined, while the values of the other two parameters were kept constant. The constant values were selected to be the highest and the lowest among all values for which the analyses were performed.

Effect of Q for $T_{initial}$=20°C and $T_{heaterplate}$=20°C

For different values of Q, while $T_{initial}$ = 20 °C and $T_{heater\ plate}$ = 20 °C, the temperature variations of chosen locations on the board and the component are shown in Fig. 12, and the temperature distribution of the upper surface of the board and the components is presented in Fig. 13.

There were two heat sources in the system: the components and the heater plate. The temperature of the S-1 was greatly affected by the component power, while the heater plate temperature had a small effect. On the contrary, the temperature of the S-3 was mainly affected by the heater plate, while it was not much influenced by the component power. S-1 temperature shows a 25–30 °C increase for 4 mW/mm^3 component power, and only a 3–4 °C increase for 0.5 mW/mm^3 component power. S-3 point experienced temperature changes very close to each other for different values of the component power. Since the S-2 point was between S-1 and S-3 in terms of the thermal path, it shows a thermal behavior approximately between the results of S-1 and S-3.

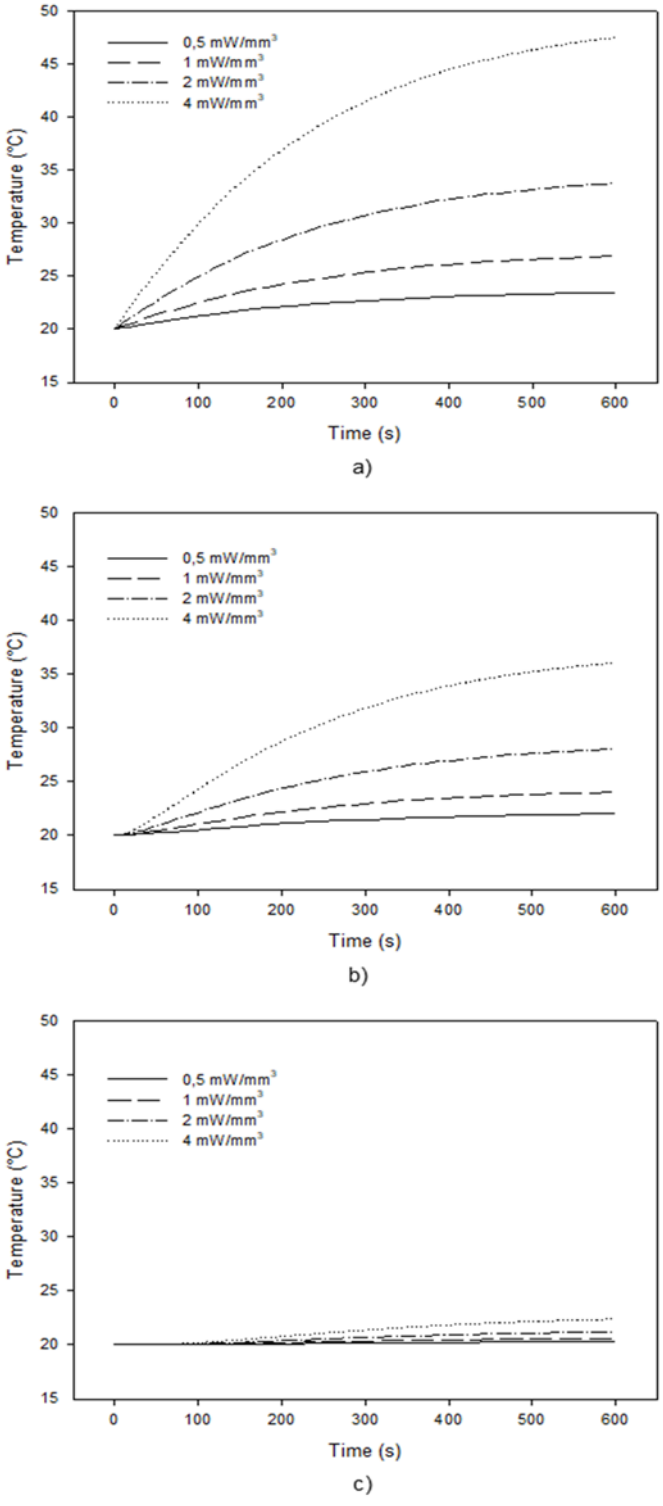

Figure 12. Temperature change with time for different values of component power while $T_{initial}$ = 20 °C and $T_{heater\ plate}$ = 20 °C, a) S-1, b) S-2, c) S-3.

Effect of Q for $T_{initial}$=20°C and $T_{heaterplate}$=80°C

Temperature values of the measurement points for 600 s duration and the temperature contour plot of the upper side of the electronic board and the components are shown in Fig. 14 and Fig. 15, respectively for this boundary condition. For this condition, the heater plate's effect on the sensor points

can be seen, compared with the previous results. According to Fig. 14, S-1 temperature shows a similar increase profile for $T_{initial}$ = 20 °C and $T_{heater\ plate}$ = 80 °C, as is the case for $T_{initial}$ = 20 °C and $T_{heater\ plate}$ = 20 °C, since the heater plate temperature has little effect on S-1 temperature. Temperature of the S-3 increased by about 10–15 °C, when Theater plate = 80 °C for all component power values.

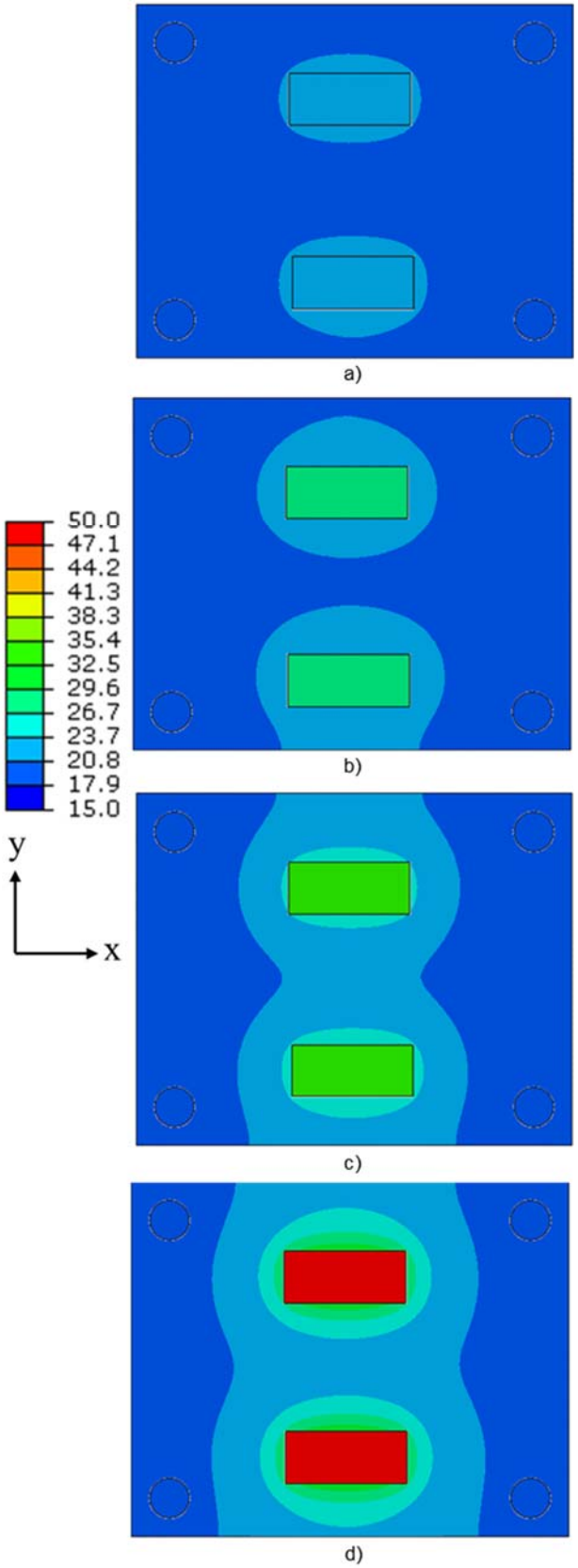

Figure 13. Surface contour plots of temperature at 600 s for $T_{initial}$ = 20 °C and $T_{heater\ plate}$ = 20 °C, a) Q = 0.5 mW/mm³, b) Q = 1 mW/mm³, c) Q = 2 mW/mm³, d) Q = 4 mW/mm³.

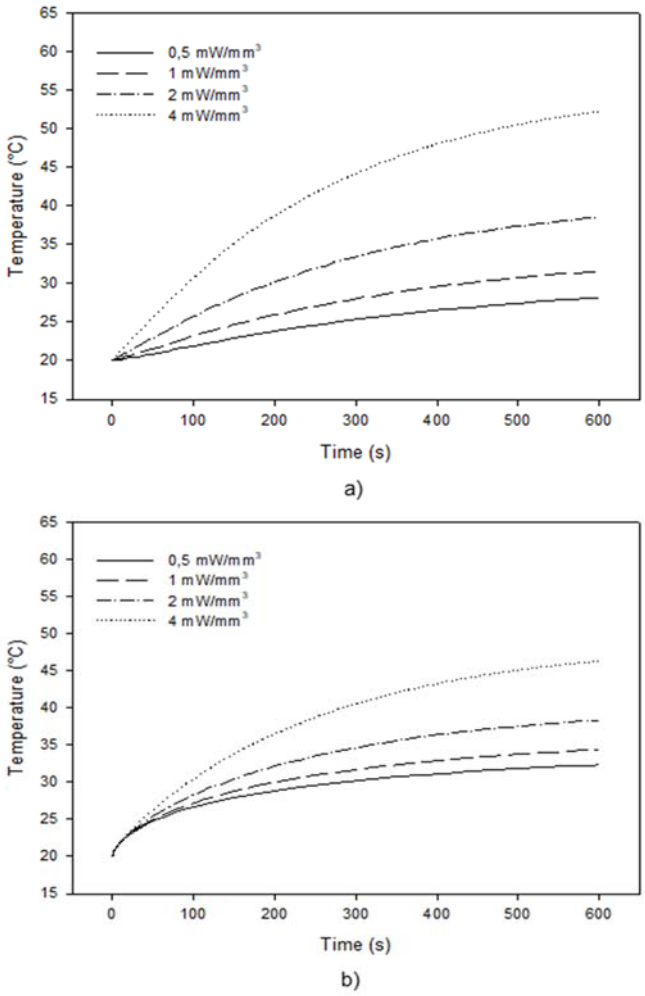

Figure 14. Temperature change with time for different values of component power while $T_{initial}$ = 20 °C and $T_{heaterplate}$ = 80 °C, a) S-1, b) S-2.

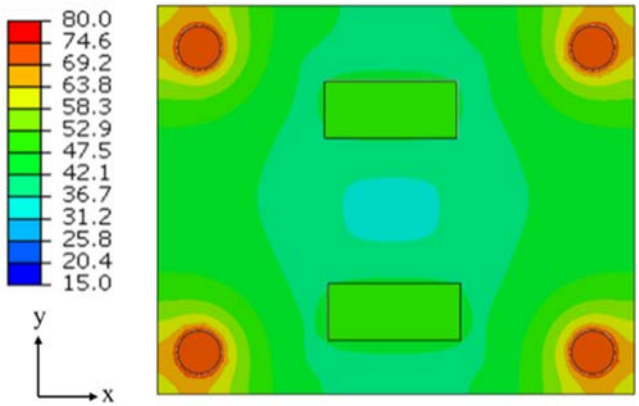

Figure 15. Surface contour plots of temperature at 600 s for $T_{initial}$ = 20 °C and $T_{heater\ plate}$ = 80 °C, Q = 4 mW/mm³.

Effect of $T_{heaterplate}$ for $T_{initial}$=20°C and Q=0.5 mW/mm³

The thermal behavior of the system for different values of the heater plate, while $T_{initial}$ = 20 °C and Q = 0.5 mW/mm³ was examined, and the results are shown in Fig. 16 and Fig. 17, respectively. For this boundary condition, S-1 was not expected to be affected much, since the component power was at its minimum value. On the other hand, S-3 point was expected to heat up quite a lot for $T_{heater\ plate}$ = 80 °C, and not to heat up more than a few degrees for $T_{heater\ plate}$ = 20 °C. In Fig. 16, these expected phenomena can be seen clearly. S-2 again shows a thermal behavior between S-1 and S-3. Moreover, the legs holding the PCB were heated up parallel with the heater plate, since they were in tight contact.

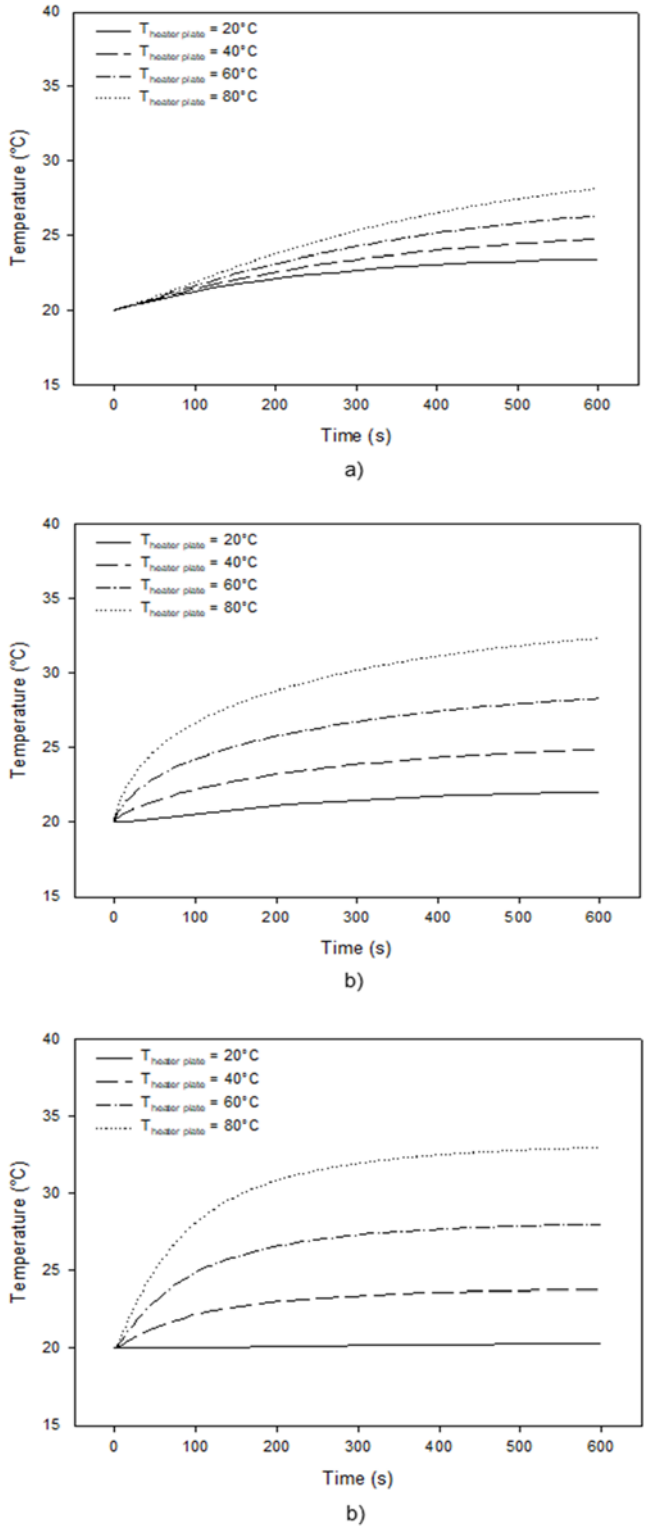

Figure 16. Temperature change with time for different values of $T_{heater\ plate}$ while $T_{initial}$ = 20 °C and Q = 0.5 mW/mm³, a) S-1, b) S-2, c) S-3.

Effect of $T_{heaterplate}$ for $T_{initial}$=20°C and Q=4.0 mW/mm³

For values of $T_{heater\ plate}$ while $T_{initial}$ = 20 °C and Q = 4 mW/mm³, the temperature changes of the measurement points on the board and the component are shown in Fig. 18, and the temperature distribution of the upper surface of the board and the components is presented in Fig. 19. S-3 point represented a temperature change similar to the boundary condition, for which the different values of $T_{heater\ plate}$ were examined, while $T_{initial}$ = 20 °C and Q = 0.5 mW/mm³. However, the temperature values of the S-1 point increased a lot for all values of the heater plate. Again, these results show the effect of the parameters on S-1, S-2, and S-3 points. The PCB legs were affected by the heater plate, similar to the previous results.

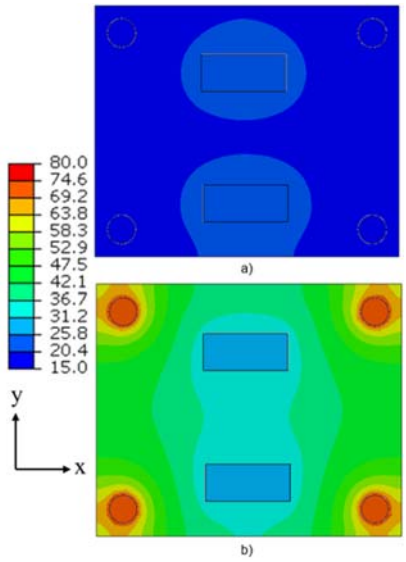

Figure 17. Temperature change with time for different values of $T_{heater\ plate}$ while $T_{initial}$ = 20 °C and Q = 0.5 mW/mm³, a) S-1, b) S-2, c) S-3.

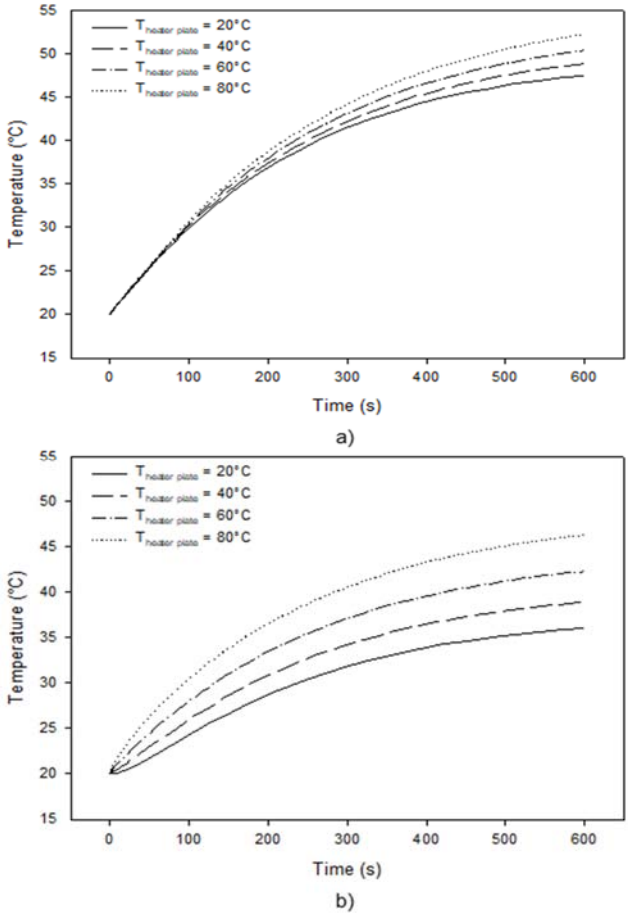

Figure 18. Temperature change with time for different values of $T_{heater\ plate}$ while $T_{initial}$ = 20 °C and Q = 4 mW/mm³, a) S-1, b) S-2.

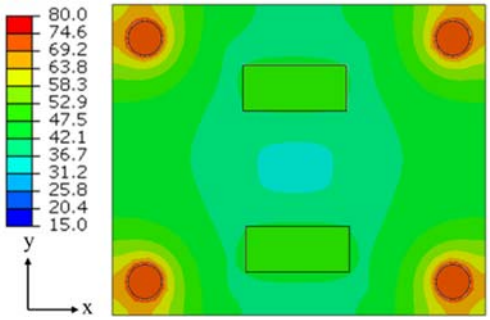

Figure 19. Surface contour plots of temperature at 600 s for $T_{initial}$ = 20 °C and Q = 4 mW/mm³, $T_{heater\ plate}$ = 80 °C.

Effect of $T_{heaterplate}$ for $T_{initial}$=50°C and Q=0.5 mW/mm³

Up to this point, the results of the analyses where $T_{initial}$ = 20 °C, while the other two parameters changed were presented. In Fig. 20 and Fig. 21, results for $T_{initial}$ = 50 °C are presented. 50°C was the maximum value in the interval among which Tinitial was selected. Thermal behaviors of the chosen locations differ for various values of the initial temperature. For the values of the heater plate temperature greater than the initial temperature of the system, temperatures of all three locations increase. However, when the heater plate temperature was lower than the system's initial temperature, the heater plate behaves as a cooler plate. In Fig. 20, especially for Theater plate = 20 °C, the cooling effect of the plate can be seen clearly for all three locations. In Fig. 21, the temperature of the legs also shows this behavior.

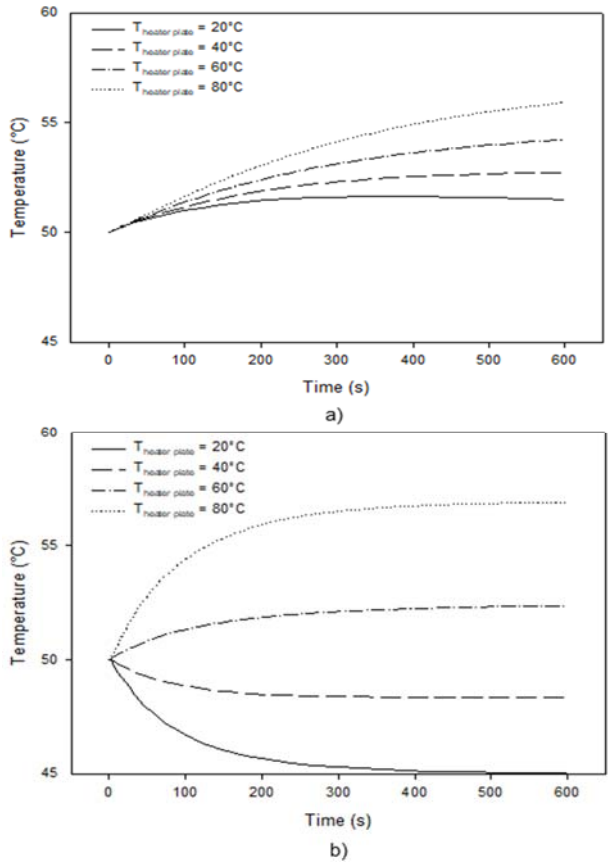

Figure 20. Temperature change with time for different values of $T_{heater\ plate}$ while $T_{initial}$ = 50 °C and Q = 0.5 mW/mm³, a) S-1, b) S-3.

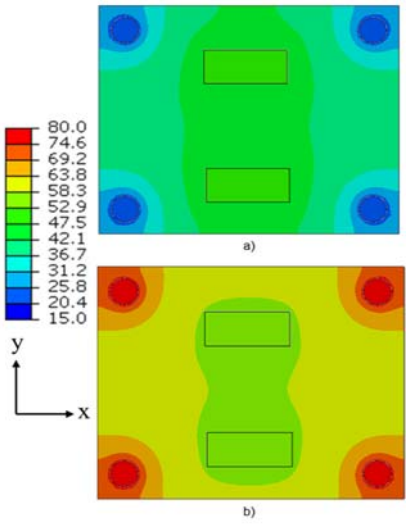

Figure 21. Surface contour plots of temperature at 600 s for $T_{initial}$ = 50 °C and Q = 0.5 mW/mm³, a) $T_{heater\ plate}$ = 20 °C, b) $T_{heater\ plate}$ = 80°C.

Effect of $T_{heaterplate}$ for $T_{initial}$=50°C and Q=4.0 mW/mm³

The results of the analyses performed to see the effect of the heater plate's temperature on the system for $T_{initial}$ = 50 °C and Q = 4 mW/mm³ are shown in Fig. 22 and Fig. 23, respectively. For the S-3 location, the heater plate behaves as a cooler plate for about 200 s. For S-2, this trend was seen for a shorter time, approximately 15–20 s, due to a high heating effect of the components. Temperature of the S-1 point was increasing during the whole time of the analyses for all variations of the heater plate temperature, due to the strong heating effect of the components. The contour plot shown in Fig. 23 is similar to the previous results, in terms of the temperature distribution of legs and region on PCB near legs.

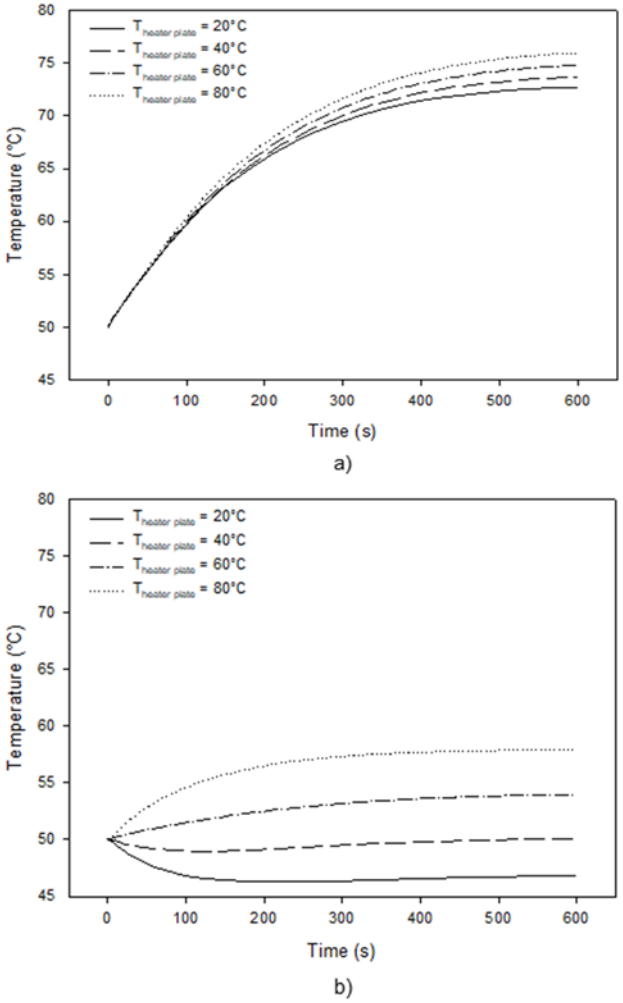

Figure 22. Temperature change with time for different values of $T_{heater\ plate}$ while $T_{initial}$ = 50 °C and Q = 4 mW/mm³, a) S-1, b) S-3.

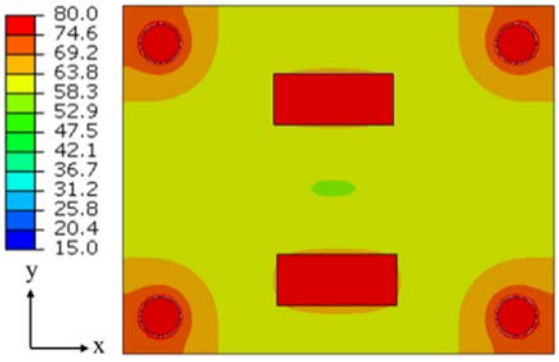

Figure 23. Surface contour plots of temperature at 600 s for $T_{initial}$ = 50 °C and Q = 4 mW/mm³, $T_{heater\ plate}$ = 80 °C.

Effect of $T_{initial}$ for $T_{heaterplate}$=20°C and Q=0.5 mW/mm³

This time, different values of $T_{initial}$ were examined for $T_{heater\ plate}$ = 20 °C and Q = 0.5 mW/mm³, and the results are shown in Fig. 24 and Fig. 25, respectively. Since the component power and the heater plate temperatures were at their minimum values, for all values of the initial temperature, S-1 temperature increased by just a few degrees. It should be noted that the temperature values of the legs were almost the same as in Fig. 25, due to the constant values of the heater plate temperature.

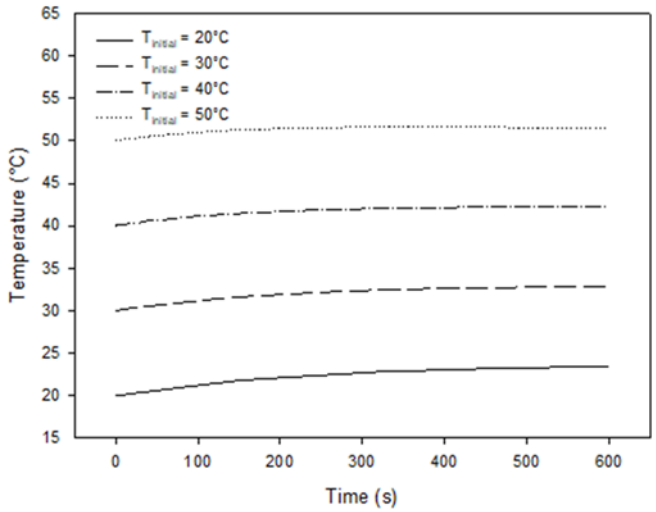

Figure 24. Temperature change with time for different values of $T_{initial}$ while $T_{heater\ plate}$ = 20 °C and Q = 0.5 mW/mm³, S-1.

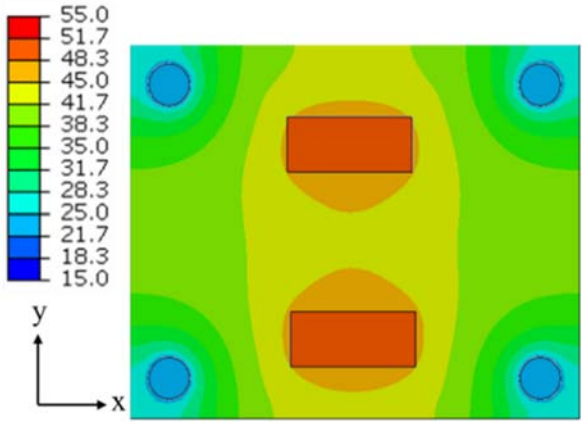

Figure 25. Surface contour plots of temperature at 600 s for $T_{heater\ plate}$ = 20 °C and Q = 0.5 mW/mm³, $T_{initial}$ = 50 °C.

Effect of $T_{initial}$ for $T_{heaterplate}$=20°C and Q=4.0 mW/mm³

Lastly, the results from analyses for different values of the initial temperature while $T_{heater\ plate}$ = 20 °C and Q = 4 mW/mm³ are shown in Fig. 26 and Fig. 27, respectively. As S-3 was not much affected from the component power, the results for location S-3 resemble the previous results of Q = 0.5 mW/mm³. On the other hand, the S-1 point, which was the most affected point from the component power, shows an increase through 600 s, just by temperature shift with various values of initial temperature, since the initial temperature value has no heating effect. Again, the leg temperatures were almost the same because of the heater plate temperature.

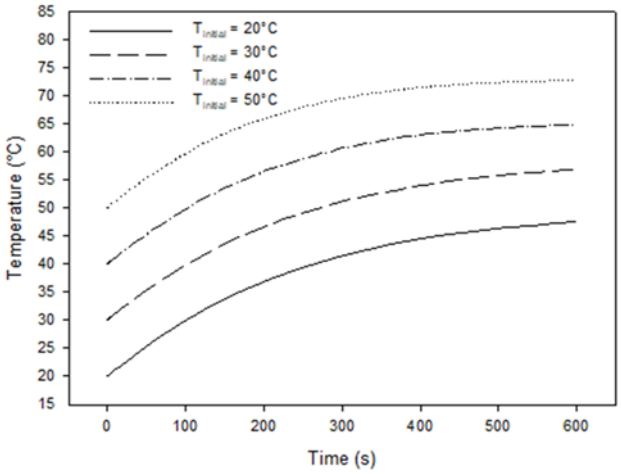

Figure 26. Temperature change with time for different values of $T_{initial}$ while $T_{heater\ plate}$ = 20 °C and Q = 4.0 mW/mm³, S-1.

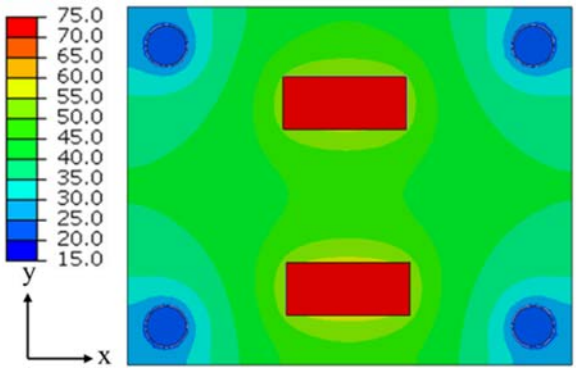

Figure 27. Surface contour plots of temperature at 600 s for $T_{heater\ plate}$ = 20 °C and Q = 4.0 mW/mm³, $T_{initial}$ = 50 °C.

CONCLUSIONS

In this study, a conduction-based FEM analysis model was set up for an electronic board inside an enclosure under transient natural convection conditions. It was aimed to determine the analysis model input parameters which were unknown or uncertain. These were the thermal contact resistance values between the components and the PCB, component power deration rate, and coefficients for calculating the natural convective HTCs at PCB and component surfaces. The unknown input parameters of the analysis were determined using the results of an experimental investigation, which was conducted for the purpose of the correction of the analysis model. The amount of deviations of the results, less than 2-3°C, obtained at the end of the correction process showed that the correct analysis model was set up to perform further analyses for different cases. The findings of the present study could be concluded as follows;

- Preliminary results showed that thermal contact resistance showed best agreement for R=10 m²K/W, where a temperature difference of less than 5°C occurred.
- By using a correlation for the heat transfer coefficient from the literature, it was observed that the deviation of the numerical results compared to experimental results is around 2-3°C.
- It was observed that with the increase in component power for a maximum temperature of around 45.5°C has been obtained under $T_{initial}$ = 20 °C and $T_{heaterplate}$ = 20 °C conditions.

• It was also seen that the heat increase in the heater plate increases the maximum temperature at S-1 to around 50°C with the increase of Q under $T_{initial}$ = 20 °C conditions.
• The effect of heater plate temperature at S-1 is less compared to locations S-2 and S-3 under constant Q and $T_{initial}$ conditions.
• For Q=0.5 mW/mm^3 it was observed that the temperature values become almost constant after around 50 s, whereas for Q=4.0 mW/mm^3 it was seen that the temperature values become constant after around 300 s.

The findings of the present study showed that unless a critical change is made in the system, such as the geometry or the type of the electronic board and the components, material properties, fluid environment, the system under natural convection, or forced convection, the analysis model can be employed for different boundary conditions, with small changes, in order to examine the system's thermal behavior. One of the most important developments which should be considered for future research is to include the ambient temperature as the unknown input parameter and to somehow calculate it in the iterative analyses.

ACKNOWLEDGMENT

The authors would like to thank Roketsan Inc., Ankara, Turkey for funding and technical support.

REFERENCES

Battula, N.K., Daravath, S., Gampa, G.K. (2024). Numerical studies on conjugate convection from discretely heated electronic board. *World Journal of Engineering*, 21(1), 107-114.

Byon, C., Choo, K., Kim, S.J. (2011). Experimental and analytical study on chip hot spot temperature. *International Journal of Heat and Mass Transfer*, 54(9-10), 2066–2072.

Chavan, S., Sathe, A. (2016). Natural convection cooling of electronic enclosure. *International Journal of Trend in Research and Development*, 3(4), 93–97.

Chen, W.H., Cheng, H.C., Shen, H.A. (2003). An effective methodology for thermal characterization of electronic packaging. *IEEE Transactions on Components and Packaging Technologies*, 26(1), 222–232.

Cheng, H.C., Chen, W.H., Cheng, H.F. (2008). Theoretical and experimental characterization of heat dissipation in a board-level microelectronic component. *Applied Thermal Engineering*, 28(5-6), 575-588.

Cheng, H.C., Ciou, W.R., Chen, W.H., Kuo, J.L., Lu, H.C., Wu, R.B. (2013). Heat dissipation analysis and design of a board-level phased-array transmitter module for 60-GHz communication. *Applied Thermal Engineering*, 53(1), 78–88.

Deng, Q.H. (2008). Fluid flow and heat transfer characteristics of natural convection in square cavities due to discrete source–sink pairs. *International Journal of Heat Mass Transfer*, 51(25–26), 5949–5957.

Devellioğlu Y. (2008). *Electronic packaging and environmental test and analysis of an emi shield electronic unit for naval platform*. M.Sc. thesis, Middle East Technical University, Ankara, Turkey.

Ellison, G.N. (2020). *Thermal Computations for Electronics: Conductive, Radiative, and Convective Air Cooling.* (2. Ed.), Boca Raton, FL : CRC Press/Taylor & Francis Group.

Eveloy, V., Rodgers, P., Lohan, J. (2002). *Comparison of numerical predictions and experimental measurements for the transient thermal behavior of a board-mounted electronic component*, ITherm 2002 Eighth Intersociety Conference on Thermal and Thermomechanical Phenomena in Electronic Systems, San Diego, California, USA, 36-45.

Eveloy, V., Rodgers, P. (2005). Prediction of electronic component-board transient conjugate heat transfer. *IEEE Transactions on Components and Packaging Technologies*, 28(4), 817–829.

Gilmore, D.G., Donabedian, M. (2003). *Spacecraft Thermal Control Handbook*. Reston, Virginia: American Institute of Aeronautics and Astronautics.

Han, C.K., Jung, H. (2017). *A study on thermal behavior prediction for automotive electronics unit based on CFD*. 23rd International Workshop on Thermal Investigations of ICs and Systems (THERMINIC), Amsterdam, Holland, 1-4.

Holman, J.P. (1994). *Experimental Methods for Engineers.* (Sixth Ed.), McGraw-Hill, New York.

Joshy, S., Jellesen, M., Ambat, R. (2017). *Effect of interior geometry on local climate inside an electronic device enclosure*. 16th IEEE Intersociety Conference on Thermal and Thermomechanical Phenomena in Electronic Systems (ITherm), Orlando, Florida, USA, 779-783.

Khatamifar, M., Lin, W., Armfield, S.W., Holmes, D., Kirkpatrick, M.P. (2017). Conjugate natural convection heat transfer in a partitioned differentially-heated square cavity. *International Communications in Heat and Mass Transfer*, 81, 92–103.

Lim, C.H., Abdullah, M.Z., Aziz, I.A., Khor, C.Y., Aziz, M.S.A. (2021). Optimization of flexible printed circuit board's cooling with air flow and thermal effects using response surface methodology. *Microelectronics International*, 38(4), 182-205.

Lira, E., Greenlee, C. (2007) *Thermal analysis and testing of missile avionics systems*, AIAA Thermophysics Conference, Miami, Florida, USA.

Nogueira, R.M., Martins, M.A., Ampessan F. (2011). Natural convection in rectangular cavities with different aspect ratios. *Revista De Engenharia Térmica*, 10(1-2), 44-49.

Ocak M. (2010). *Conduction-based compact thermal modeling for thermal analysis of electronic components.* M.Sc. thesis, Middle East Technical University, Ankara, Turkey.

Otaki, D., Nonaka, H., Yamada, N. (2022). Thermal design optimization of electronic circuit board layout with transient heating chips by using Bayesian optimization and

thermal network model. *International Journal of Heat and Mass Transfer*, 184, 122263.

Pang Y.F. (2005). *Assessment of thermal behavior and development of thermal design guidelines for integrated power electronics modules*. Ph.D. dissertation, Virginia Polytechnic Institute and State University, Blacksburg, Virginia, USA.

Rakshith, B.L., Asirvatham, L.G., Angeline, A.A., Manova, S., Bose, J.R., Raj, J.P.S., Mahian, O., Wongwises, S. (2022). Cooling of high heat flux miniaturized electronic devices using thermal ground plane: An overwiev. *Renewable and Sustainable Energy Reviews*, 170, 112956.

Rodgers, P., Eveloy, V., Lohan, J., Fager, C.M., Tiilikka, P., Rantala, J. (1999). *Experimental validation of numerical heat transfer predictions for single and multi-component printed circuit boards in natural convection environments*. Fifteenth Annual IEEE Semiconductor Thermal Measurement and Management Symposium, San Diego, California, USA, 54-64.

Rosten, H.I., Parry, J.D., Addison, J.S., Viswanath, R., Davies, M., Fitzgerald, E. (1995). *Development, validation and application of a thermal model of a plastic quad flat pack*, 45th Electronic Components and Technology Conference, Las Vegas, Nevada, USA, 1140-1151.

Stancato, F., dos Santos, L.C., Pustelnik, M. (2017). Electronic package cooling analysis in an aircraft using CFD. *SAE Technical Paper Series*, 1.

Steinberg, D.S. (1991). *Cooling Techniques for Electronic Equipment,* (2nd ed.), Nashville, TN: John Wiley & Sons.

Taliyan, S.S., Sarkar, S., Biswas, B.B., Kumar, M. (2010) *Finite element based thermal analysis of sealed electronic rack and validation*, 2nd International Conference on Reliability, Safety and Hazard - Risk-Based Technologies and Physics-of-Failure Methods (ICRESH), Mumbai, India, 443-447.

Wang, Z., Zheng, S., Xu, S., Dai, Y. (2024). Investigation on the thermal and hydrodynamic performances of a micro-pin fin array heat sink for cooling a multi-chip printed circuit boards. *Applied Thermal Engineering*, 239, 122178.

Xu, G. (2017). *Multi-core server processors thermal analysis.* 16th IEEE Intersociety Conference on Thermal and Thermomechanical Phenomena in Electronic Systems (ITherm), Orlando, Florida, USA, 416-421.

Zahn, B.A., Stout, R.P. (2002). *Evaluation of isothermal and isoflux natural convection coefficient correlations for utilization in electronic package level thermal analysis*. Thirteenth Annual IEEE Semiconductor Thermal Measurement and Management Symposium, Austin, Texas, USA.

Zaman, F.S., Turja, T.S., Molla, M.M. (2013). Buoyancy driven natural convection flow in an enclosure with two discrete heating from below. *Procedia Engineering*, 56, 104–111.

Journal Homepage: https://dergipark.org.tr/tr/pub/isibted

Isı Bilimi ve Tekniği Dergisi

Archive: https://tibtd.org.tr/dergi

Numerical Investigation of Water Addition into Intake Air in Modern Automobiles Diesel Engines

Mustafa TUTİ [1, *], Zehra ŞAHİN [2], Orhan DURGUN [3]

[1] *Karadeniz Teknik Üniversitesi, Deniz Bilimleri Fakültesi, Gemi İnşaatı ve Gemi Makineleri Mühendisliği Bölümü, Sürmene, 61530, Trabzon, Türkiye*
[2] *Karadeniz Teknik Üniversitesi, Mühendislik Fakültesi, Makine Mühendisliği Bölümü, Ortahisar, 61080, Trabzon, Türkiye*
[3] *Avrasya Üniversitesi, Mühendislik Mimarlık Fakültesi, Makine Mühendisliği Bölümü, Yomra, 61250, Trabzon, Türkiye*

A R T I C L E I N F O

2024, vol. 44, no.2, pp. 308-321

doi: 10.47480/isibted.1563972

Research Article
Received: 02 October 2023
Accepted: 21 July 2024

* *Corresponding Author*
e-mail: mtuti@ktu.edu.tr

Keywords:
Thermodynamic cycle model
Water using
Heat release rate
NO emission

ORCID Numbers in author order:
0000-0002-2309-3735
0000-0002-7140-2061
0000-0001-6381-0690

A B S T R A C T

In the present study, the effects of water addition into intake air (WAIA) on combustion, engine performance, and NO emission in diesel engines were investigated numerically. Here, Ferguson's thermodynamic-based zero-dimensional single-zone cycle model was used and improved with new approaches for neat diesel fuel (NDF) and WAIA. After controlling the model's accuracy for NDF and WAIA, the effects of WAIA were first investigated in the Renault K9K diesel engine. For (5 and 7.5)% water ratios (WRs), effective power decreased by 4.26% and 7.37%, brake specific fuel consumption (BSFC) increased by 6.95% and 10.56%, and NO emission reduced by 12.43% and 16.39%, respectively. In the second application, the effects of (3, 6, and 9)% WRs on combustion, engine performance, and NO emission in the Renault M9R diesel engine were investigated at 4000 rpm by using this developed model. For (3, 6, and 9)% WRs, BSFC increased by 0.97%, 3.39%, and 8.25%, and NO emission decreased by 10.31%, 17.66%, and 34.20%, respectively. For (3 and 6)% WRs effective power increased, and NO emission decreased significantly without considerable deterioration in the BSFC at 4000 rpm. Cylinder pressure values and heat release rate increased for (3 and 6)% WRs and decreased for 9% WR.

Modern Otomobil Dizel Motorlarında Emme Havasına Su Eklenmesinin Sayısal İncelenmesi

M A K A L E B İ L G İ S İ

Anahtar Kelimeler:
Termodinamik Çevrim Modeli
Su kullanımı
Açığa çıkan ısı oranı
NO emisyonu

Ö Z E T

Sunulan çalışmada, dizel motorlarda emme havasına su eklenmesinin (EHSE) yanma, motor performansı ve NO emisyonu üzerindeki etkileri sayısal olarak incelenmiştir. Burada Ferguson'un termodinamik esaslı sıfır-boyutlu tek-bölgeli çevrim modeli kullanılmıştır ve söz konusu model saf dizel yakıtı (SDY) için yeni yaklaşımlarla geliştirilmiştir ve daha sonra geliştirilen çevrim modeli EHSE durumu için uyarlanmıştır. Modelin SDY ve EHSE için doğruluğu kontrol edildikten sonra, EHSE'nin etkileri ilk olarak Renault K9K dizel motorunda incelenmiştir. Seçilen %(5 ve 7.5) su oranları için; efektif güç %4.26 ve %7.37 düzeylerinde azalmış, özgül yakıt tüketimi (ÖYT) %6.95 ve %10.56 oranlarında artmış ve NO emisyonu ise %12.43 ve %16.39 düzeylerinde azalmıştır. İkinci sayısal uygulamada ise; %(3, 6 ve 9) gibi üç farklı su oranının kullanımının yanma, motor performansı ve NO emisyonu üzerindeki etkileri Renault M9R dizel motorunda 4000 d/d devir sayısında incelenmiştir. %(3, 6 ve 9) su oranları için; ÖYT, sırasıyla %0.97, %3.39 ve %8.25 oranlarında artmış ve NO emisyonu ise sırasıyla % 10.31, %17.66 ve %34.20 oranlarında azalmıştır. %(3 ve 6) su oranlarında, efektif güç artmış ve NO emisyonu, ÖYT'de önemli bir kötüleşme olmadan önemli ölçüde azalmıştır. Silindir basınçları ve açığa çıkan ısı oranları %(3 ve 6) su oranlarında artmış, %9 su oranında ise azalmıştır.

NOMENCLATURE

b_e, BSFC	brake spesific fuel consumption (kg/kWh)
Ne	effective power (kW)
NDF	neat diesel fuel
Y_{NO}	mole fraction of nitrojen oxide
WAIA	water adding into the intake air
CA	crank angle
ZDSZ	zero dimensional single zone
ε	compression ratio
ID	ignition delay
HRR	heat release rate (J/deg.)

INTRODUCTION

It is well known that in modern industries possible maximum reduction of time and money spent on the development and preparation of various products and the rapid implementation of changes in product design parameters and operating modes are required. Costly and time-consuming experimental tests can be modeled under the same conditions, significantly increasing the efficiency of research and development with the improvement and implementation of various computer modeling studies (Zhang et al., 2023; Bondar et. Al, 2020). Modeling studies are also important and necessary for internal combustion engines, especially diesel engines which are one of the main sources of mechanical energy for propulsion of ships (seagoing ships) and land vehicles. Actually, the modeling of diesel engine cycles is an important research area from the past to the present, and various types of engine cycle models are developed and applied to calculate diesel engine cycles. In practice, by using these diesel engine cycle models and other simulation methods, the number of costly systematic experiment studies could be reduced and optimum engine design parameters can be calculated in a very short time. By this way, very useful results can be reached. Thus, these models reduce the cost and time required for engine development and help to reach the most suitable designs. Therefore, nowadays new simulation models are constantly being developed and improved (Bedford et al., 2000; Pasternak et al., 2009; Shristava et al., 2002; Heywood 1988; Jurić et al., 2023). In the following section, the main models applied in combustion and cycle calculations in diesel engines have been briefly introduced. Moreover; some of the results obtained from the application of these models for NDF and also for alternative fuels and for alternative solutions given in the main literature were been summarized.

Literatur Review

Various combustion types and complete cycle models have been developed for diesel engines, typically categorized as thermodynamic-based models and multi-dimensional models (MDMs) (Sahin and Durgun, 2008). Thermodynamic-based models rely on the application of the first law of thermodynamics to the engine cylinder or its manifolds, yielding a system of ordinary differential equations governing cylinder pressure, temperature, work, and heat transfer. These equations are solved to compute the diesel engine cycle accurately, facilitating the determination of engine performance parameters and exhaust emissions. Conversely, MDMs involve numerically solving fundamental differential equations governing fluid motion and combustion processes within finely meshed engine cylinders. While MDMs offer detailed spatial and temporal resolution, they demand extensive computational resources and time due to the complexity of meshing irregular combustion chamber geometries. Consequently, MDMs are primarily utilized for analyzing flow motion in non-combustible states and optimizing combustion chamber geometry, rather than modeling entire engine cycles or determining performance parameters. Therefore, for comprehensive engine cycle calculations and parametric studies related to engine performance and exhaust emissions, thermodynamic-based models are generally preferred (Sahin and Durgun, 2008; Kökkülünk et al., 2013).

Many thermodynamic-based models (Sahin and Durgun, 2008; Kökkülünk et al., 2013; Oiang, 1992) and MDMs (Savioli, 2015; Tutak and Jamrozik, 2016) can be found in the literature. Tutak et al. (2016) improved a CFD model for a turbocharged diesel engine, confirming its accuracy with test engine data, then used it to optimize the engine cycle, noting a significant increase in NOx and soot emissions for optimal efficiency. They emphasized its value in optimizing internal combustion engines for thermodynamic parameters and emissions.

Sahin and Durgun (2008) developed a multi-zone combustion model for NDF, ethanol, and gasoline fumigation in diesel engines, studying their effects on combustion dynamics, efficiency, and emissions. Their findings showed ethanol fumigation reduced BSFC and NO concentration, while gasoline fumigation decreased NO concentration with minimal impact on BSFC.

Many thermodynamic-based models (Sahin and Durgun, 2008; Kökkülünk et al., 2013; Oiang, 1992) and MDMs (Savioli, 2015; Tutak and Jamrozik, 2016) have been performed to calculate the diesel engine cycle for NDF, for using of alternative various fuel additives, water, etc. in the literature. These modeling studies have provided valuable information to scientists and the automotive sector. Today, numerical studies and also experimental studies for related to alternative fuel additives, improving of engine design, developing combustion process, etc. continue intensively. The main purposes of these studies are to reduce environmental pollution and to improve engine performance. Since the adding water in internal combustion engines, especially in diesel engines consists of an effective method to reduce NO_x emissions, research on this subject continues. In fact; since the 1950s, adding water in different ways in diesel engines has been attracted the interest of many scientists and a lot of numerical and experimental studies have been carried out on this subject. In recent years, the number of numerical studies on using of alternative fuels and water in diesel engines has increased, especially with the increase in the speed and capacity of computers (Sahin and Durgun, 2008; Kökkülünk, 2012; Lamas et al., 2013; Gonca et al., 2015; Sandeep et al., 2019; Tamma et al., 2003). Some examples of numerical studies on the adding of water or various water-alternative fuels in diesel engines can be summarized as follows:

Bedford et al. (2000) explored cylinder water injection's impact on diesel engine performance using Kiva-3v based CFD simulations, finding that it lowered NO_x emissions and soot formation due to water evaporation and increased gas specific

heat around the flame. Sandeep et al. (2019) investigated the impact of water addition into intake air (WAIA) on engine performance and emissions in a turbocharged diesel engine, employing both experimental and numerical methods. Simulations were carried out using a one-dimensional package computer program (DPCP) for different water injection amounts, revealing that increased injection reduced NO_x emissions but increased smoke levels. Optimal performance was observed with 2.8 mg of water injection, leading to a notable decrease in cylinder temperature and an 8-10% reduction in NO_x emissions, despite a 20% increase in smoke. Kannan and Udayakumar (2009) developed a thermodynamic-based ZDSZ model to investigate the effects of water emulsion on cylinder pressure, engine performance, and NO concentration. Their study reveals that water emulsion increases BSFC but decreases NO concentration. Kökkülünk et al. (2013) investigated the effects of water addition into the intake air as steam on engine performance and exhaust emissions through experimental and numerical methods. In their numerical analysis, Ferguson's (1986) thermodynamic-based ZDSZ cycle model was refined and adapted for a 20% water-steam ratio. Employing an electronically controlled injection system, water was introduced into the intake air as steam. Their findings revealed that steam injection improved engine performance and reduced NO emissions, with no significant impact on CO, CO_2, and HC emissions. As can be seen from the above literature survey, many studies have been carried out, including dimensional package computer programs and thermodynamic-based ZDSZ models to calculate diesel engine cycles for NDF, various alternative fuels, and different water adding applications. Although there are many studies on the modeling of NDF (Pasternak et al., 2009; Shristava et al., 2002; Sindhu et al., 2014) and different alternative fuels (Nemati et al., 2016; Rakopoulos et al., 2008) studies on the numerical examination of water adding in diesel engines are more limited. In fact, the experimental investigation of water adding in diesel engines has been carried out widely. In these studies; researchers generally have preferred three different methods for the application of water in diesel engines. These methods can be classified as adding of water into the intake air, mixing of the water with the diesel fuel, as known as the emulsion method, and injection of the water directly into the combustion chamber with a separate injector. Water adding in diesel engines by these three methods has been explained to be very effective in reducing NO_x emissions (Gowrishankar et al., 2020; Jhalani et al., 2023; Ece and Ayhan, 2019). Zhu et al. (2019) made the following statements about the water adding in internal combustion engines in their review research. Water adding is a promising technique to reduce the cylinder temperature and exhaust temperature, mitigate combustion knock, improve combustion phasing and decrease NO_x emissions. Also, they stated that since mechanisms of water injection with different aims are distinct, benefits on engine performances and emissions are also varied.

Out of these; considering the NO_x emission reduction potential of water adding, nowadays water has been preferred to use with the above-explained methods as a third additive along with the other alternative fuels in diesel engines (Wang et al., 2018; Vellaiyan et al., 2019; Maawa et al., 2020). For example, Maawa et al. (2020) experimentally investigated the effects of biodiesel-diesel fuel blends (B20) emulsified with varying proportions of water on engine performance, combustion characteristics, and exhaust emissions. They utilized conventional diesel fuel, blended palm oil methyl ester/diesel fuel (B20), and B20 emulsified with different water proportions (B20E5, B20E10, B20E20, and B20E30) in their study. Their findings suggest that water emulsification with biodiesel-diesel fuel blends effectively reduces exhaust emissions, particularly NO_x, without compromising engine performance.

Our literature review confirms that water adding is one of the best methods that can be applied to reduce NO_x emissions in diesel engines. Therefore, it is worthwhile important to numerically and experimentally examine the effects of water adding on combustion, engine performance parameters, and exhaust emissions in current automotive diesel engines. Besides, as can be stated from the above brief literature review modeling studies on water adding are more limited than experimental studies. For this reason, in the present study, the water adding into the intake air has been numerically investigated in two different diesel engines, used by current automobiles. Also, an experimental investigation of WAIA in an automotive diesel engine has been carried out and the experimental data have been compared with numerical results. Here, to calculate the diesel engine cycle, thermodynamic-based ZDSZ model, which is practical and easy to implement, was improved and applied for NDF and WAIA. In this model, modeling of the intake and exhaust processes, which are not usually calculated in the cycle calculations in the literature, were also performed. Then, the mentioned model was adapted for water adding to the intake air with new suppositions, and the accuracy control of this program was verified by comparing with the experimental data and by numerical results of the studies given in the literature. Also, systematic numerical applications were carried out to understand the effects of WAIA on the combustion process, engine performance, and NO concentration for two different automobile diesel engines, using in road vehicles today. Thus, the results obtained from this study can be transferred directly to the automotive industry. More importantly, the present study fills a critical research gap by developing and using a thermodynamic-based ZDSZ model to investigate the effects of WAIA on engine performance and NO emissions in automotive diesel engines.

BRIEF DESCRIPTION OF PRESENT MODEL FOR NDF

In the present study, a thermodynamic-based single-zone model for calculating the complete diesel engine cycle is adapted and improved. Here, intake and exhaust processes are modeled with a practical calculation method developed by Durgun (1991). Compression, combustion, and expansion processes were computed by adapting the model originally developed and given by Ferguson (1986). Firstly, the above- mentioned complete diesel engine cycle model was improved for NDF, and its accuracy was checked. Then, this model has been adapted for the WAIA.

a) Modeling of Intake and Exhaust Processes: Intake and exhaust processes are modeled with a practical calculation method developed by Durgun (1991). This model will be introduced very briefly here. Detailed information on this subject can be found in the reference (Durgun, 1991). The pressure at the intake process was calculated using the following relation by applying the well-known Bernoulli equation to the engine intake system.

$$P_a\,(\mathrm{MPa}) = P_c' - \left(\beta^2 + \xi\right)\left[\frac{V_m \cdot n}{n_N}\right]^2 \cdot \frac{\rho_a}{2} \cdot 10^{-6} \qquad (1)$$

where P_c' is turbocharger compressor outlet pressure, $(\beta^2 + \xi)$ is the coefficient showing the total losses in the intake system, n and n_N are the actual engine speed and nominal engine speed, respectively, V_m is the maximum flow speed in the intake system, ρ_a is the density of air. Here, since turbocharged diesel engines are used, the pressure and temperature at the outlet of the compressor of the turbocharger were determined by using the semi-empirical relation (2) and (3) given in Table 1. Also, residual gases have been taken into account by using γ_r the coefficient of the residual gases in the present model and γ_r was calculated by using relation (4) given in Table 1.

Table 1. Some relations used in the intake and exhaust process calculation

Equation and equation number	***Explanation of some parameters in the relations***
P_c' MPa) $=1.5P_0$ low-turbocharged (2a) P_c' (MPa) = (1.5-2.2)P_0 mid-turbocharged (2b) P_c' (MPa) = (2.2-2.5)P_0 high-turbocharged (2c)	*P_0 : Ambient pressure*
$T_c'(K) = T_0.\left(\frac{P_c'}{T_c'}\right)^{\frac{n_c-1}{n_c}}$ (3)	*T_0:Ambient temperature* *n_c: Polytropic compression exponent of the compressor*
$\gamma_r = \frac{T_c'+\Delta T}{T_r}\cdot\frac{\varphi_s.P_r}{\varepsilon.\varphi_{ed}.P_a-\varphi_s.P_r}$ (4) $P_C' = P_0$ $T_C' = T_0$ for naturally aspirated engines	*φ_{ed}: Additional charge coefficient* *φ_s: Scavenging coefficient of supercharged* *ε : Compression ratio of the engine* *ΔT: Amount of preheating of the intake charge* *T_r: Temperature of the exhaust gases*
$T_r' = \frac{T_b}{\sqrt[3]{P_b/P_r}}$, $\left\lvert\frac{T_r'-T_r}{T_r'}\right\rvert \le 3\ \%$ (5a, 5b) $T_r = (600-1000)K$ $P_r = (0.75-0.98)P_C'$	*T_r': The calculated exhaust temperature* *P_r , T_r :The selected exhaust gas pressure and temperature* *T_b , P_b: Temperature and pressure at the end of the expansion stroke*

The temperature at the end of the exhaust process was calculated by using relation (5a) given in Table 1, depending on the temperature at the end of the intake. The exhaust gas temperature calculated at the end of the cycle calculations is compared with the selected exhaust gas temperature at the beginning of the cycle. If the difference between the two values is less than 3%, the cycle calculations and empirical data selections can be considered compatible. This difference ratio can be called as the accuracy of the cycle. If the difference exceeds this value, the cycle might be repeated by taking the last calculated exhaust gas temperature as the residual gas temperature value. The cycle calculation continues iteratively until the difference becomes less than %3. Thus, complete cycle calculation control has been reached. Exhaust temperature comparison procedure is carried out by using relation (5b) given in Table 1.

b) ***Modeling of Compression, Combustion and Expansion Processes*****:** Applying the first law of thermodynamics to the gas mixture in the cylinder, the following set of differential equations can be obtained by applying the energy balance where work, heat losses, and mass losses are also considered. This set of differential equations in question is solved from the beginning of the compression process to the end of the expansion process step by step and the cylinder pressure, cylinder temperature, and cycle work values are determined. Here, the set of ordinary differential equations numbered (6-11) is solved simultaneously by Butcher's (1995) 5th Order Runge-Kutta method during the compression, combustion and expansion processes. Detailed information on the deriving of these equations can be found in the references (Tuti, 2022; Ferguson, 1986). Also, at the end of a step, cylinder temperature and pressure values were calculated the next crankshaft angle by using (12) and (14) equations, given in Table 2. These equations were solved by Newton-Raphson method in 0.5° CA steps.

$$\frac{dm_a}{d\theta} = -\frac{1}{\omega}\cdot\left(\frac{\dot{m}_l}{1+\phi.F_s}\right) \quad (6)$$

$$\frac{dm_f}{d\theta} = \frac{1}{\omega}\cdot\left(\dot{m}_{f,i} - \frac{\dot{m}_l.\phi.F_s}{1+\phi.F_s}\right) \quad (7)$$

$$\frac{dU}{d\theta} = -\frac{\dot{Q}_l}{\omega} - P\cdot\frac{dV}{d\theta} + \frac{\dot{m}_f.h_f}{\omega} - \frac{\dot{m}_l.h_l}{\omega} \quad (8)$$

$$\frac{dW}{d\theta} = P\cdot\frac{dV}{d\theta} \quad (9)$$

$$\frac{\dot{Q}_l}{\omega} = \frac{h\left(\frac{\pi B^2}{2}+\frac{4V}{B}\right)(T-T_w)}{\omega} \quad (10)$$

$$\frac{\dot{m}_l.h_l}{\omega} = \frac{C.m.h_l}{\omega} \quad (11)$$

Eq.6 and Eq.7 give the rates of change of the masses of air and fuel in the cylinder in respect of the crankshaft angle. In these equations, m_l is the loss of mass escaping from the valves and piston rings, $m_{f,i}$ is the total mass of fuel to be injected, ϕ is the equivalence ratio, and F_s is the stoichiometric fuel-air ratio. Eq.8 is the first law of thermodynamics or the energy equation for a closed system which is applied to the cylinder contents during compression, combustion, and expansion strokes. The terms on the right-hand side of this equation show heat transfer, work, energy provided by injected fuel, and blowby, respectively. The work, heat transfer, and blowby have been modeled by using relations (9-11), respectively.

In Eq.10, B is the cylinder bore, T_w is the wall temperature, V is the volume of cylinder and h is the convection heat transfer coefficient of the gas in the cylinder. Here, h has been determined from Woschni's (1967) correlation.

In Eq.11, m_l is the mass flow rate of gas escaping from the rings and valves, C is the blowby coefficient. Thus, as explained above V, m_a, m_f, U, W, Q_l and h_l values can be determined numerically by solving this ordinary differential equation system. Here U internal energy, V the cylinder volume, and h enthalpy values in the differential equations have been calculated in the following forms by using Olikara and Borman (1998) method.

Table 2. The used equations for calculation of cylinder temperature and pressure.

$T_{i+0.5} = T_i + \Delta T$	(12)
$\Delta T = \frac{-V.\left[\frac{10.\left(\frac{du}{d\theta}\right)}{\frac{\partial \ln v}{p\partial \ln p}} + \frac{du}{d\theta}\left(\frac{\partial \ln v}{\partial \ln T} + \frac{\partial \ln v}{\partial \ln P}\right)\right]}{\frac{V^2}{T}\left[\left(-\frac{10 c_p T}{pV} + \frac{\partial \ln v}{\partial \ln T}\right).\left(-\frac{\partial \ln v}{\partial \ln P}\right) + \frac{\partial \ln v}{\partial \ln T}.\left(\frac{\partial \ln v}{\partial \ln T} + \frac{\partial \ln v}{\partial \ln P}\right)\right]}$	(13)
$P_{i+0.5} = P_i + \Delta T$	(14)
$\Delta P = \frac{-\frac{pV}{T}.\left[\frac{10 c_p T}{pV} - \frac{\partial \ln v}{\partial \ln T}\right].\frac{du}{d\theta} - \frac{10\left(\frac{du\,\partial \ln v}{d\theta\,\partial \ln T}\right)}{p}}{\frac{V^2}{T}\left[\left(-\frac{10 c_p T}{pV} + \frac{\partial \ln v}{\partial \ln T}\right).\left(-\frac{\partial \ln v}{\partial \ln P}\right) + \frac{\partial \ln v}{\partial \ln T}.\left(\frac{\partial \ln v}{\partial \ln T} + \frac{\partial \ln v}{\partial \ln P}\right)\right]}$	(15)

After determining the complete diesel engine cycle, engine performance parameters such as effective power, effective efficiency, and BSFC are calculated from the relationships given by Heywood (1988) and Durgun (1991, 2022). For example; in the present study, effective engine characteristics have been computed by using the following semi-empirical mean effective pressure relationship given by Durgun (1991, 2022), while here and in the literature generally indicated engine characteristics have been obtained.

$$P_{m,m}(MPa) = 10.\left(a + b.V_{p,m}\right)\frac{P'_c}{P_{m,i}} \quad (16a)$$

$$P_{m,e}(MPa) = P_{m,i} - P_{m,m} \quad (16b)$$

In Eq. 16a and Eq.16b, $P_{m,i}$ is the mean indicated pressure, and $V_{p,m}$ is the mean piston velocity. a and b are coefficients depending on the engine type and for the Renault K9K 700 type test engine and Renault Talisman M9R type engine, these values of a and b were selected as 0.089 and 0.0118, $P_{m,i}$ value has been calculated as follows by using cycle data ($P_{m,i}$=W/V).

The Adaptations of the Present Model for WAIA

a) The temperature at the end of the intake process: In the present study, the developed cycle model for NDF is adapted to WAIA by applying some modifications. In the WAIA experiment, water can be introduced into the air charge by using a simple carburetor. Thus, the temperature at the end of the intake process decreases because of water vaporization in the intake manifold. The decrease in the temperature has been calculated by using of the following relation.

$$T_{a,WAIA}(K) = \frac{T'_c + \Delta T + \gamma_r.T_r}{T_r} - \frac{M_w \cdot Q_w}{M_1 \cdot c_p} \quad (17)$$

Here, Q_w is the heat of evaporation or latent heat of the water, M_w is the mole number of the water added into the inlet channel for 1 kg diesel fuel, and M_1 is the mole number of the fresh charge.

b) Calculation of the thermodynamic properties of the mixture at low temperature: For WAIA, water, air, and residual exhaust gases are compressed during the compression process. Therefore, the following combustion reaction was used to determine the thermodynamic properties of the mixture, such as enthalpy, and specific heat, in the cylinder at low temperatures. For this, first of all, the mole fractions of combustion products formed at low temperatures were determined. In Table 3, the number of moles and mole fraction of the combustion products formed at low temperatures are given (Ferguson 1986).

$$X_1\varepsilon_m\phi C_cH_hO_{oy}N_n + X_2\varepsilon_m\phi H_2 + (0.21O_2 + 0.79N_2) \rightarrow \nu_1CO_2 + \nu_2H_2O + \nu_3N_2 + \nu_4O_2 + \nu_5CO + \nu_6H_2 \quad (18)$$

where $X_1\varepsilon_m\phi$ and $X_2\varepsilon_m\phi$ are the amount of diesel fuel added per 1 mol air, and the amount of water added per 1 mol of air respectively. Also, here X_1 and X_2 are the volumetric percentages of diesel fuel and water in the mixture, respectively. The term of ε_m is the amount of oxygen required to burn 1 mol of fuel and it has been calculated by using the following simple relation $\varepsilon_m = (c+h/4-o_y/2)$. Here c, h, and o_y are the atomic numbers of carbon, hydrogen, and oxygen in the chemical formula of the fuel.

After determining the mol fractions of each substance in the mixture by this way, the thermodynamic properties of the mixture were calculated using Ferguson (1986) ve Heywood (1988) references.

Table 3. υ_i mol numbers and y_i mol fraction ratios for WAIA at low temperature (Tuti, 2022).

Products	υ_i (mol/mol air)	ϕ<1	mole fractions, $y_i=\upsilon_i/n_t$*
CO_2	υ_1	$X_1.\varepsilon_m.\phi.c$	$y_{CO_2} = (X_1.\varepsilon_m.\phi.c)/n_t$
H_2O	υ_2	$X_1.\varepsilon_m.\phi.h/2 + X_2.\varepsilon_m.\phi$	$y_{H_2O} = (\varepsilon_m.\phi.(X_1.h/2 + X_2))/n_t$
N_2	υ_3	$X_1.\varepsilon_m.\phi.n/2 + 0.79$	$y_{N_2} = (X_1.\varepsilon_m.\phi.n/2 + 0.79)/n_t$
O_2	υ_4	$0.21(1-\phi X_1)$	$y_{O_2} = 0.21(1-\phi X_1)/n_t$
CO	υ_5	0	
H_2	υ_6	0	

*n_t is the total mol number of combustion products formed at low temperatures.

c) Calculation of the thermodynamic properties of the mixture at high temperature: For the WAIA, the combustion equation is arranged as follows to calculate the mol numbers of the combustion products during the combustion process (Ferguson, 1986).

$$X_1\varepsilon_m\phi C_cH_hO_{oy}N_n + X_2\varepsilon_m\phi H_2 + (0.21O_2 + 0.79N_2) \rightarrow \nu_1CO_2 + \nu_2H_2O + \nu_3N_2 + \nu_4O_2 + \nu_5C + \nu_6H_2 + \nu_7H + \nu_8O + \nu_9OH + \nu_{10}N \quad (19)$$

where ν_1, ν_2, ν_3, ν_4, ν_5, ν_6, ν_7, ν_8, ν_9, and ν_{10} are the mole number of the combustion products and they have been determined by using Olikara's (1998) method. Once the combustion products are determined, the thermodynamic properties and their derivatives with respect to temperature, pressure, and equivalence ratio can be calculated. Detailed information on this subject can be found in the references such as Tuti (2022) and Ferguson (1986).

RESULTS AND DISCUSSION

The Accuracy Control of the Developed Model for NDF and WAIA

Here, firstly, the numerical results obtained from the present model for NDF are compared with the experimental and thermodynamic model results of Rajak et al. (2018). Rajak et al. (2018) used in their numerical studies, a professional ready-made package computer program prepared as a thermodynamic-based multi-zone combustion model. In Fig. 3(a) and (b), cylinder pressure and HRR values obtained from the present model are compared with the experimental and thermodynamic model results of Rajak et al. (2018) for 18.5 compression ratio under full load at 1500 rpm. It can be seen from Fig. 3(a) that, the tendencies of Rajak et al.'s (2018) numerical and experimental pressure curves are similar to that of the present model. The maximum cylinder pressure values of the experiments and model of Rajak et al. (2018) are given 87.15 bar at 11.37 °CA, and 90.13 bar at 2.42 °CA, respectively. However, the maximum cylinder pressure value has been calculated as 86.80 bar at 8 °CA by using the present model. Thus, the difference of the present model in respect to Rajak's (2018) model and experimental results for maximum cylinder pressure was 3.42%. On the other hand, the difference between the maximum pressure value obtained from the present model and Rajak's (2018) experiment has been determined as 0.402%. Hence, it can be said that the maximum pressure value obtained from the developed model is closer to Rajak's (2018) experimental result than that of Rajak's (2018) model.

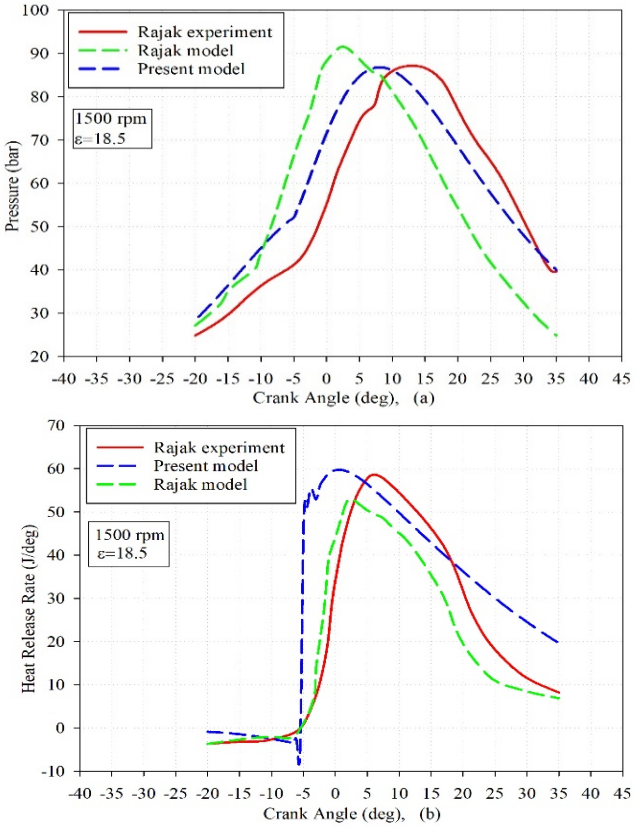

Fig. 3. Comparison **a)** cylinder pressure and **b)** HRR values obtained from the present model with the experimental and model results of Rajak et al. (2018).

HRR curves with respect to various crank angles for the present model and Rajak's (2018) experimental and theoretical results are shown in Fig. 3(b). As can be seen in this figure, the tendency of the HRR curve obtained in this model and the tendency of Rajak's (2018) experimental and numerical HRR curves are most similar. The maximum value of HRR calculated from the present model and the experimental and model results from Rajak et al. (2018) are 59.77 J/deg at 0.5 °CA, 58.34 J/deg at 5.43 °CA and 53.06 J /deg at 2.29°CA, respectively. The difference between Rajak's (2018) model and experimental maximum HRR values was found as 8.12%. However, the maximum HRR value obtained from our model is closer to Rajak's (2018) experimental HRR and the difference was found to be 2.44%. Thus, it is clear from Fig. 3(a) and (b) that our model results are in good agreement with Rajak's (2018) experimental results than that of their own results. The values and comparison results of effective efficiency obtained from the developed model and Rajak et al.'s (2018) model and experimental results are shown in Table 4. As can be seen from this table, effective efficiency in the present model was determined as 31.63%. Rajak et al.'s (2018) experimental and numerical effective efficiency values were given as 32.5%, and 32.59%, respectively. Here, there is a 0.277% difference between Rajak et al.'s (2018) model and their experimental effective efficiency values. However, there is a 2.667% difference between our model result and the experimental value of Rajak et al. (2018). Possible reasons for this difference can be explained as follows. In the present model, it is assumed that all of the fuel is injected into the cylinder as the main injection. That is to say, pilot and main fuel injections are not taken into account separately in the present model.

In addition, it is also assumed that the injected fuel burns immediately and detailed calculations of the penetration, evaporation, and disintegration of the sprayed fuel have not been taken into account. In fact, the 2.667% difference can be considered an acceptable error level, and it can be said that the predicted results by our model agree reasonably with the Rajak et al. (2018) data.

In another numerical application, the results of the present model were compared with experimental results performed by authors for NDF, 6%, and 10% water adding ratios (WRs) at 2000 rpm and 4000 rpm under full throttle. The experimental and numerical variations of cylinder pressure, cylinder temperature, and HRR are comparatively presented in Fig. (4-7). Also, experimental and numerical values of engine torque, effective power, BSFC, and effective efficiency are given in Tables (5-6). It can be seen from these figures, the tendencies of the pressure, temperature, and HRR curves obtained from this model for NDF, 6%, and 10% WRs at 2000 and 4000 rpms are quite similar to that of experimental. The maximum pressure determined by applying the developed model for the test engine is 155.288 bar and it occurred at 8 °CA and the maximum pressure measured is 155.288 bar at 8 °CA for 6 % WR at 2000 rpm. Thus, it can be seen that the difference between maximum pressure is 1.11%. Similarly, the maximum numerical and experimental temperature values for the same conditions are 2053 K at 22.18 °CA and 2015 K at 19.5 °CA, respectively, and thus the difference ratio between maximum temperatures has been 1.85%. HRR values are also reasonably close to each other and the difference between experimental and model data for maximum HRR values has been calculated as 4.25%. However, as can be seen in Fig. 4(c), combustion started earlier in the model and the HRR curve is slightly shifted to the left than that of the test results. Possible reasons of this situation can be explained as follows.

Table 4. Comparison of the HRR, effective efficiency, and peak cylinder pressure obtained from the present model with the experimental and numerical results of Rajak et al. (2018).

ε=18.5	*Rajak's exp.*	*Rajak's model*	*Present model*	*Diff. Rajak' exp. and model (%)*	*Diff. Rajak' exp. and present model (%)*
HRR, J/deg	58.34	53.06	59.77	9.050	-2.451
η_e, %	32.5	32.59	31.63	-0.277	2.677
P_{max}, bar	87.15	90.13	86.8	-3.419	0.402
$dP/d\theta_{max}$	5.45	5.3	4.63	2.752	15.045

As explained above, in the developed model, it is assumed that all of the fuel is injected in the main combustion phase and the injected fuel burns immediately. In addition, phenomena such as the penetration of the injected fuel in the combustion chamber, the evaporation of the droplets, etc. could not be taken into account. As a result, the variations of the experiment and numerical HRR curves have been somewhat different. Similarly, acceptable proximity for cylinder pressure, temperature, HRR, and engine performance parameters values occurred for 10% WR at 2000 rpm as can be seen in Table 5. As can be shown in this table, the results of engine performance parameters calculated from the developed numerical model for 6% and 10% WRs at 2000 rpm are also very close to the experimental data. The results of cylinder pressure, temperature, and HRR at 4000 rpm for NDF, 6%, and 10% WRs under full load conditions are shown in Fig. (6) and Fig. (7) and engine performance parameters results for the same conditions are also given in Table 6.

As can be seen from these figures and table, the model results are found to be in good agreement with the experimental results. Therefore, it can be concluded that the present model can reasonably predict the complete cycles of diesel engines for NDF and WAIA. Also, as can be seen in the Fig. (4-7)(b), WAIA decreases the cylinder temperatures for 6% and 10 % WRs at 2000 and 4000 rpms

Table 5. Comparison of engine performance parameters, cylinder, temperature, and HRR calculated from the developed model for 6% and 10% WRs at 2000 rpm with the experimental results of Sahin, Durgun, and Tuti (2018, 2012).

2000 rpm	NDF			*6% WR*			*10% WR*		
	Exp.	*Model*	*Diff. %*	*Exp.*	*Model*	*Diff. %*	*Exp.*	*Model*	*Diff. %*
M_d (Nm)	144.068	152.635	-5.94	149.935	151.00	-0.71	150.413	148	1.60
N_e (kW)	30.173	31.968	-5.95	31.823	31.502	1.01	31.486	31.067	1.33
b_e (kg/kWh)	0.215	0.223	-3.72	0.221	0.210	4.99	0.226	0.216	4.31
η_e (%)	39.9	38.5	3.51	38.4	40.2	-4.71	37.51	39.05	-4.11
P_{max} (bar)	155.832	156.011	0.11	157.025	155.288	1.11	156.516	154.634	1.20
HRR_{max} (J/deg.)	55.272	52.077	5.78	54.389	51.177	4.25	54.195	50.395	7.01
T_{max} (K)	2168	2062	4.93	2053	2015	1.85	2028	1998	1.48

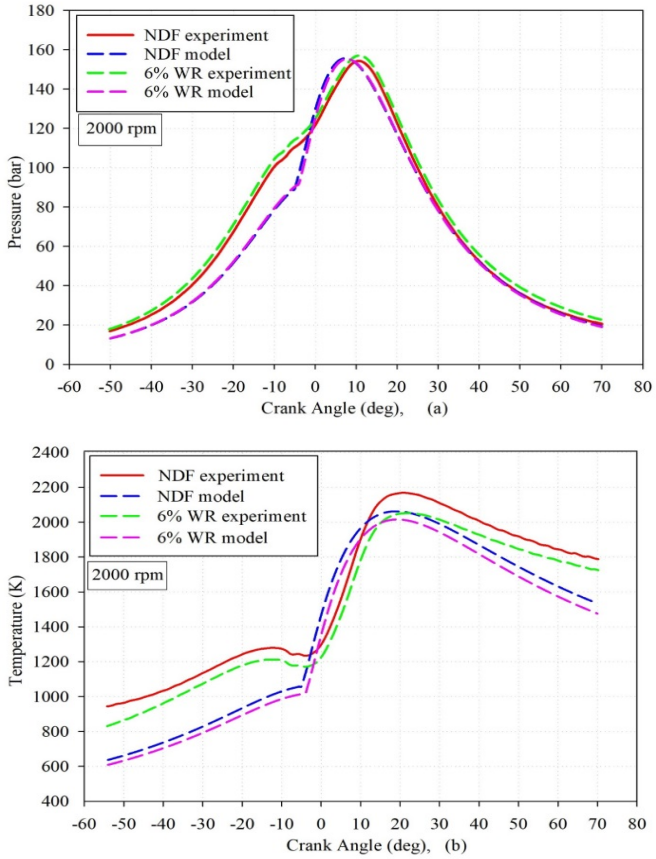

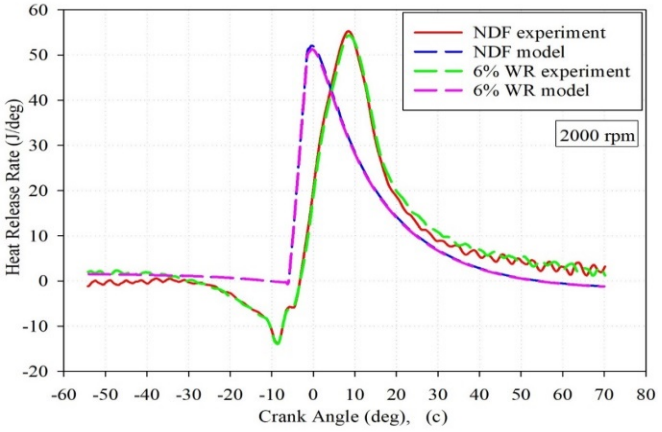

Fig. 4. Comparison **a)** cylinder pressure, **b)** cylinder temperature, and **c)** HRR variations of the present model for 6% WR at 2000 rpm with the experimental results of Sahin, Durgun, and Tuti (2018) and Tuti (2012).

Similar results were found in the relevant studies in the literature (Sindhu et al., 2014; Tauzia et al., 2010; Ma et al., 2014). Tauzia et al. (2010) stated that the evaporation of water in the combustion chamber and dilution of the existing mixture with the additional water causes a decrease in the temperatures of the cylinder gas content. As a result of this, it can be guessed that lower cylinder temperatures may reduce NO_x emissions (Heywood, 1988; Khatri and Goyal, 2020; Subramanian, 2011). Thus, from the following numerical applications, it can be said that WAIA reduces NO_x.

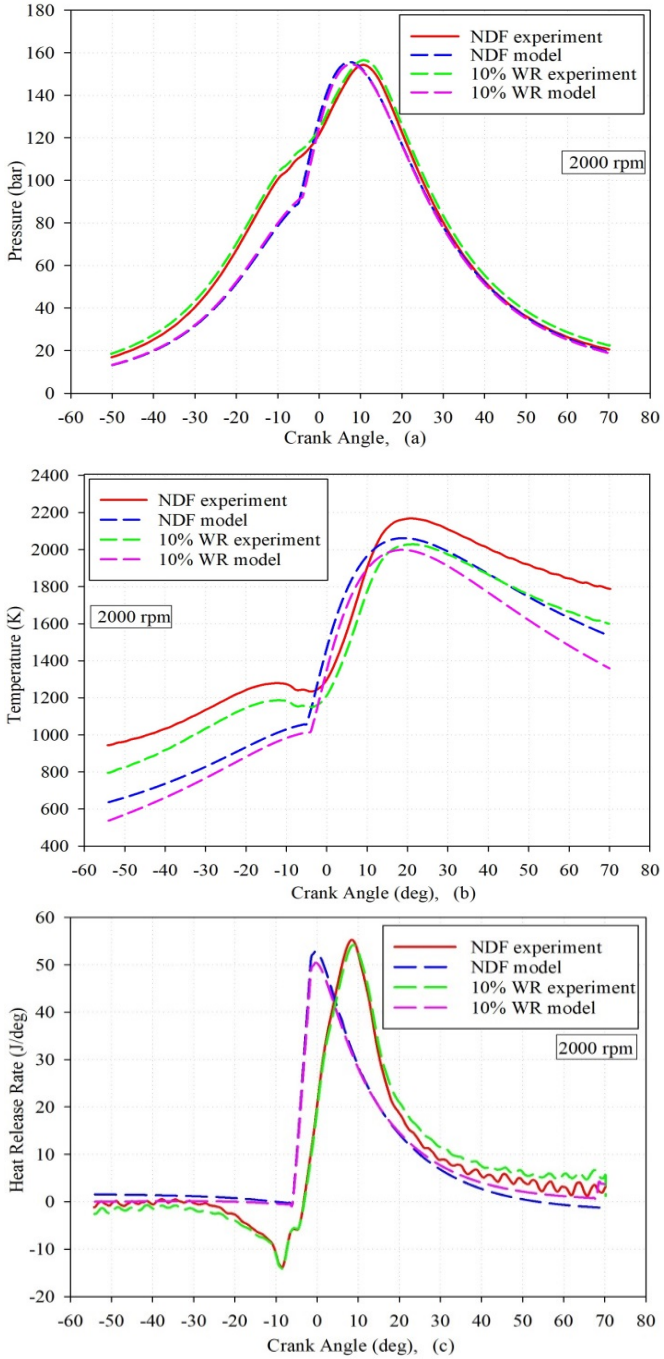

Fig. 5. Comparison **a)** cylinder pressure, **b)** cylinder temperature and **c)** HRR variations of the present model for 10% WR at 2000 rpm with the experimental results of Sahin, Durgun, and Tuti (2018) and Tuti (2012).

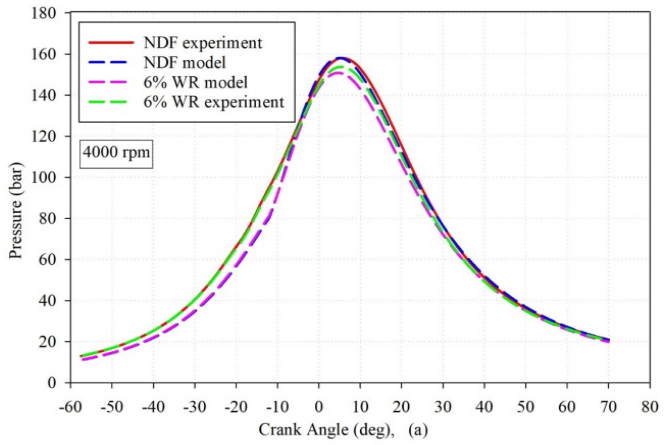

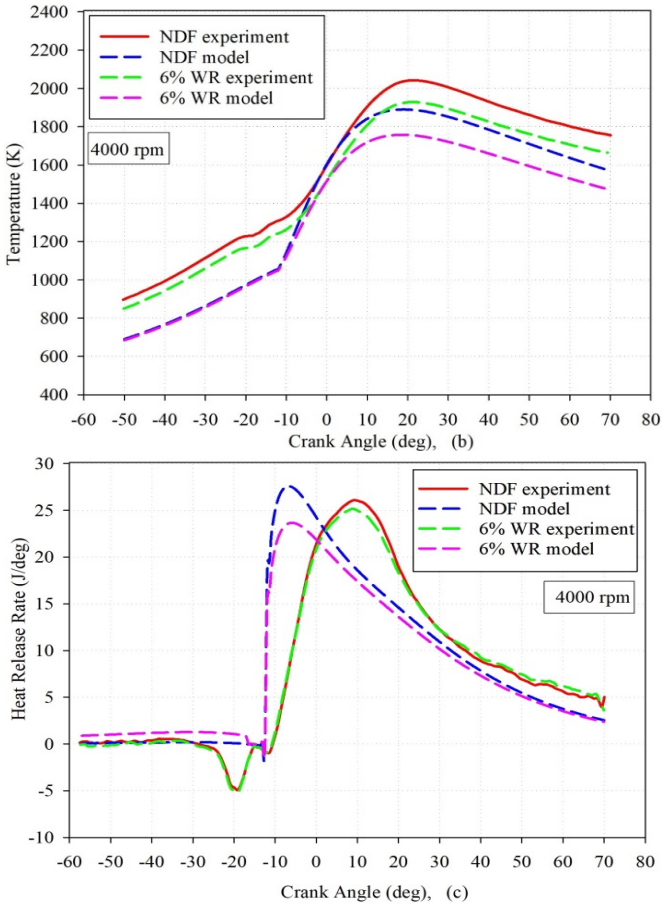

Fig. 6. Comparison **a)** cylinder pressure, **b)** cylinder temperature and **c)** HRR variations of the present model for 6% WR at 4000 rpm with the experimental results of Sahin, Durgun, and Tuti (2018) and Tuti (2012).

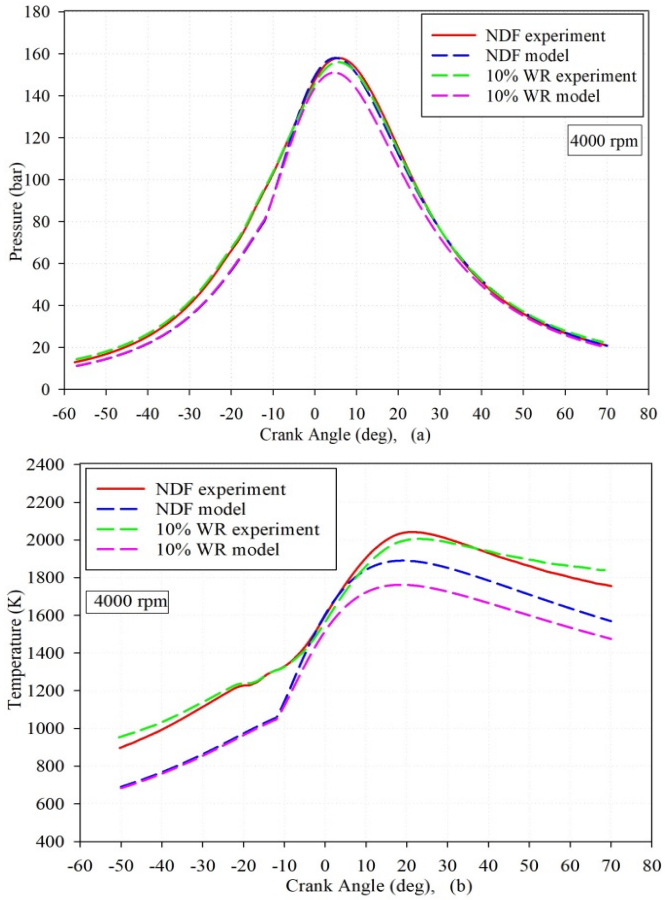

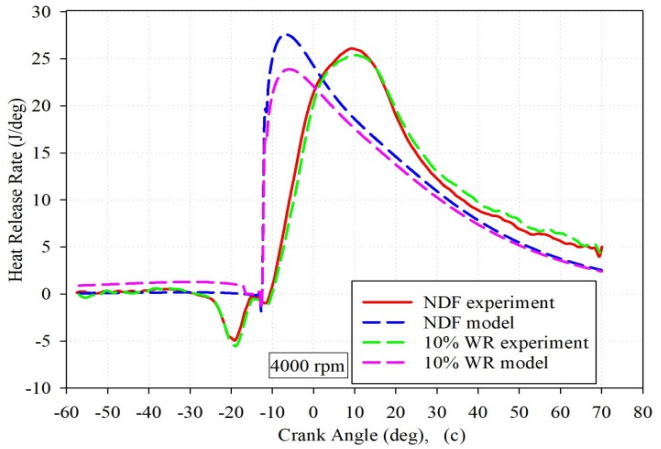

Fig. 7. Comparison **a)** cylinder pressure, **b)** cylinder temperature and **c)** HRR variations of the present model for 10% WR at 4000 rpm with the experimental results of Sahin, Durgun, and Tuti (2018) and Tuti (2012).

Numerical Evaluation of the Use of WAIA in Current Automotive Diesel Engines

In this paragraph, firstly, the developed computer code has been run for NDF, 5%, and 7.5% WRs at 2250 rpm, which could not be tested for the Renault K9K-700 type diesel engine, and the obtained experimental results are presented below in tables and graphics. By this way, the effects of WAIA on the Renault M9R type diesel engine, used in the Talisman model automobile were investigated numerically, and reached results have been presented and evaluated.

Table 6. Comparison of engine performance parameters, cylinder pressure, temperature, and HRR calculated from the developed model for 6% and 10% WRs at 4000 rpm with the experimental results of Sahin, Durgun, and Tuti (2018) and Tuti (2012).

4000 rpm	*NDF*			*6% WR*			*10% WR*		
	Exp.	*Model*	*Diff. %*	*Exp.*	*Model*	*Diff. %*	*Exp.*	*Model*	*Diff. %*
M_d (Nm)	117.980	119.280	-1.10	116.016	114.542	1.27	114.108	112.789	1.15
N_e (kW)	49.394	49.964	-1.15	48.596	47.979	1.25	47.732	47.245	1.02
be (kg/kWh)	0.264	0.269	-1.17	0.274	0.265	3.28	0.260	0.273	-5.04
η_e (%)	32.0	31.4	1.87	31.2	32.2	-3.21	32.7	30.9	5.31
P_{max} (bar)	157.994	158.032	0.02	154.741	151.808	1.89	156.053	151.018	3.23
HRR_{max} (J/deg.)	26.079	27.572	-5.72	25.160	23.667	5.78	25.407	23.884	5.99
T_{max}(K)	2041	1898	7	1928	1758	8.82	2005.64	1762.10	12.14

Renault K9K-700 Type Diesel Engine

As can be seen from Fig. 8(a), the maximum pressure values for NDF, 5%, and 7.5% WRs were determined as 156.243, 154.267, and 153.145 bar, respectively. By inspection of this figure, it can be said that WAIA decreases cylinder pressure. For 5% and 7.5% WRs, the reduction ratios in maximum pressure values compared to NDF have been obtained as 1.26% and 1.98%, respectively. Similar results are also reported in the relevant literature. For example, Ma et al. (2014) determined that WAIA reduces cylinder pressure and temperature Also, WAIA decreases cylinder temperature values, as can be seen in Fig. 8(b). For example, the maximum temperature values for NDF, 5% and 7.5% WR were determined as 1973.98 K, 1917.25 K, and 1896.74 K, respectively. Thus, reduction ratios of the maximum temperatures for 5% and 7.5% WRs compared to NDF were computed as 2.87% and 3.91%, respectively. The variations of HRR for NDF, 5%, and 7.5% WRs have also been shown in Fig. 8(c) the maximum values of HRR for NDF, 5%, and 7.5% WR have been determined as 42.11 J/deg, 40.23 J/deg, and 39.49 J/deg, respectively. From this figure, it can be said that WAIA reduces HRRs. For 5% and 7.5% WRs, the maximum HRR values are reduced by 4.46% and 6.22%, respectively, compared to NDF. The probable reason of this result might be arisen from heat losses, which occurred by evaporation of latent heat of the water.

Table 7 shows the effects of WAIA on the effective power, BSFC, ignition delay (ID), and volumetric ratio of NO emission. Here, NO emission has been calculated by applying the chemical equilibrium mechanism, given by Olika and Borman (1998) using maximum combustion temperature. In Table 7, the improvements and worsening effects of WAIA on the engine performance and NO are shown in green and yellow colors respectively. For NDF, 5%, and 7.5% WRs, the effective power values were determined as 36.793 kW, 35.227 kW, and 34.081 kW, respectively. Thus, effective power values for 5% and 7.5% WRs have decreased by 4.26% and 7.37%, respectively, compared to NDF.

Table 7. Effective power, BSFC, NO and ID values for NDF, 5% and 7.5% WRs at 2250 rpm

2250 rpm,WRs	*N_e (kW)*	*b_e (g/kWh)*	*$Y_{NO}*1000$*	*T_{max} (K)*	*ID (°CA)*
NDF	36.793	216.33	5.191	1973.98	2.096115
5% WR	35.227	231.38	4.546	1917.25	2.098760
7.5% WR	34.081	239.17	4.340	1896.74	2.098664

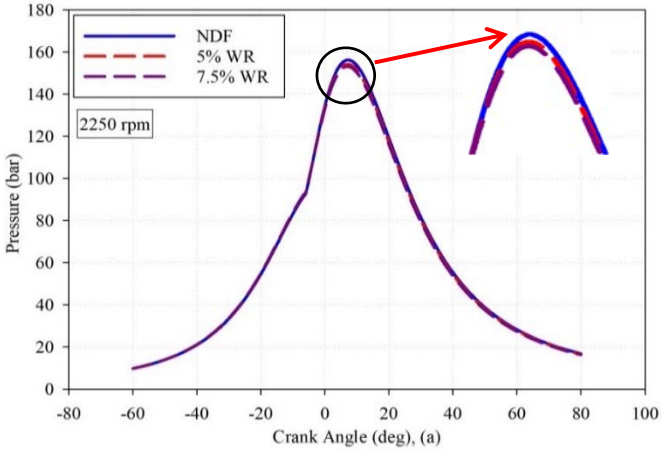

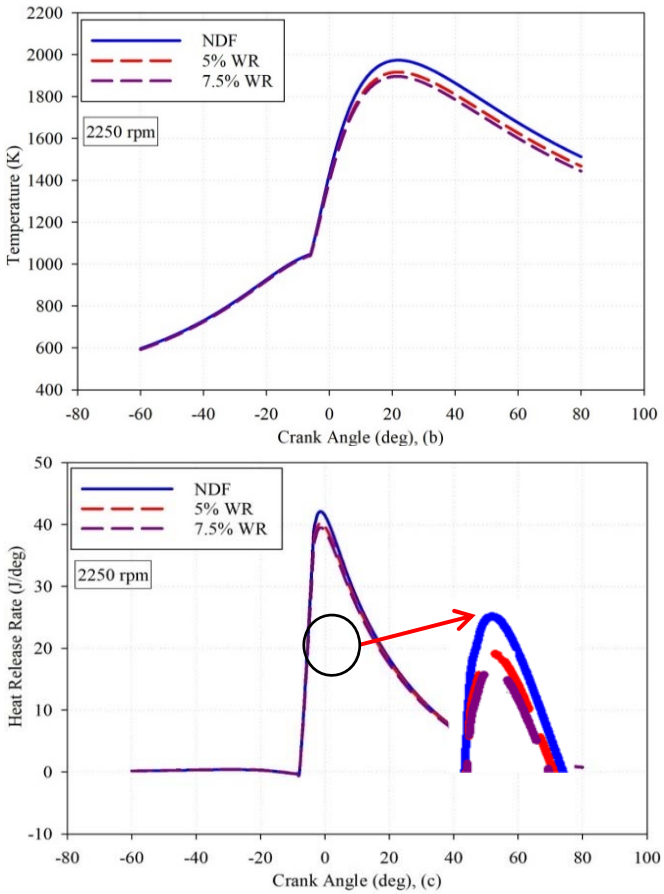

Fig. 8. Variations of **a)** cylinder pressure, **b**) cylinder temperature and **c)** HRR values obtained from the present model for NDF, 5% and 7.5% WRs at 2250 rpm

This is due to the reduction in the pressure and temperature by the effect of the vaporization of water as explained above. However, evaporation of water reduces combustion temperature and thus NO emissions. For example, as can be seen in Table 7, mole fraction values of NO for NDF, 5%, and 7.5% WRs were determined as 5.191, 4.546, and 4.340. Thus, mole fraction values of NO for 5% and 7.5% WRs were decreased by 12.43% and 16.39%, respectively, compared to NDF. As can be seen in Table 7, WAIA increases ID. WAIA application decreases the intake and the compression processes temperature values, which results in increased ID.

Renault M9R Type Diesel Engine

In another numerical application, the turbocharged Renault M9R type diesel engine with common-rail injection system, which is also used in the current 2021 model Renault Talisman automobile, has been used and the effects of WAIA in this engine have been investigated theoretically (Automobile Catalog, 2021). The main technical specifications of this engine are given in Table 8. Before investigating the effects of WAIA on this engine, the catalog values of the effective power and the fuel consumption values of this engine, and the effective power and fuel consumption values calculated from the present model were compared. The catalog value of effective power (nominal effective power) of the Renault Talisman is given as 118 kW. The calculated effective power of this engine by using the present model is 127.27 kW. Thus, it can be seen that there is a 7.86% difference between the effective power values. The fuel consumption value of the vehicle (q_{90}) at 100 km for a constant 90 km/h velocity, is given as 4.81 L/100 km in the catalog. The calculated fuel consumption by using the present model for NDF is 4.5 L/100 km. Thus, a difference at the level of 6.88 occurred between these fuel consumption values. It can be understood from these results that the present model calculates engine performance parameters reasonably close to the catalog values of the engine for NDF. After this step, the developed model was applied to 3%, 6%, and 9% WRs under full load at 4000 rpm, which is the nominal speed. The variations of cylinder pressure, cylinder temperature, and HRR have been shown in Fig. 9 (a), (b) and (c). Also, some engine performance parameters and the mole fraction values of NO are presented in Table 9.

As can be seen in Fig. 9(a) that the tendencies of pressure curves for NDF, 3%, 6%, and 9% WRs are similar to each other and the determined maximum pressure values were 153.562, 157.721, 158.368, and 149.969 bar for NDF, 3%, 6%, and 9% WRs, respectively. For low WRs such as 3% and 6%, the cylinder pressure values increase slightly, but for 9% WR the cylinder pressure value reduces. It can be said that the use of low WAIA such as 3% and 6% improves combustion.Similar results have been reported in the relevant literature. For example, Kannan and Udayakumar (2009) stated in their numerical study that WAIA improved combustion to some extent by increasing the cylinder pressure values. The use of additives such as alternative fuels and water at low ratios is suggested by some researchers in the literature (Sahin et al., 2014; Kumar and Sharma, 2013; Vigneswaran et al., 2018). Durgun (1988); Sahin et al., (2014); and Sahin et al., (2015) have determined and suggested the most suitable ratio for ethanol and gasoline fumigation and for water was approximately 6 %, which is called the magic ratio.

As can be seen from Fig. 9(b), the temperature values for 3%, 6%, and 9% WRs are lower than that of NDF. For 3%, 6%, and 9% WRs, the maximum temperature values were reduced by 2.02%, 3.88%, and 8.14%, respectively. Numerical and experimental analysis performed in the relevant literature showed also that the presence of water vapor within the fuel-rich regions decreases the flame temperature. Thus, the chemical reaction rate in the flame zone decreases, leading to reduced temperature and pressure values. As mentioned above, any effort to decrease the cylinder temperature would contribute to a significant reduction in NO_x emissions (Sandeep et al., 2019; Gowrishankar et al., 2020; Ma et al., 2014). HRR variations as functions of CAs for 3%, 6%, and 9% WRs are shown in Fig. 9(c). As can be seen in these figures, any significant differences in the HRR profiles at the selected WRs have not been observed. However, for 3%, and 6% WRs, HRR increases, but for 9% it decreases. The maximum HRR values have increased by 5.71% and 6.15%, for 3%, and 6% WRs, respectively, and it has decreased by 6.2% at 9% WR, compared to NDF.

Table 8. Technical specifications of Renault Talisman M9R engine.

Injection system and injection Pressure	Common-rail and max: 2500 bar
Compression ratio	15.1
Cylinder bore and stroke length	85 mm and 88 mm
Number of cylinder and displacement	4 and 1997 cm^3
Maximum power and nominal engine speed	118 kW, 4000 rpm
Maximum torque and speed	360 Nm, (1500-2750) rpm

As explained before, it is thought that WAIA at low ratios such as 3% and 6% would improve the combustion process. Some substantial engine performance parameters and the mole fraction values of NO are presented in Table 9. As can be seen in this table, similar to the variation in HRR and pressure values, the effective power increases for 3% and 6% WRs, and it decreases for 9% WR. Effective power increases by 6.19% and 5.01% for 3% and 6% WRs, respectively, and decreases by 1.39% for 9% WR. For 3% and 6 % WRs, as dictated in the relevant literature, the entrainment of the air-water mixture into the fuel spray, the evaporation, and the separation of these water molecules in the fuel spray (micro-explosion phenomena) enhance the formation of the air-fuel mixture and would enhance atomization and could promote complete combustion, which would result in an increase of in the effective power (Subramanian, 2011). According to Gowrishankar et al. (2020), there were no significant decreases in the cylinder temperature values to cause deteriorated combustion efficiency at low water ratios. However, it is thought that at a high water ratio such as 9% combustion process started to worsen.

Table 9. Effective power, BSFC, q90 fuel consumption as liter at 100 km, the mole fraction values of NO, ID values for NDF and at (3-6-9)% WRs in the Renault Talisman vehicle. In addition, the ratios of increase and decrease of these values according to NDF.

4000 rpm	*NDF*	*3% WR*	*Diff.(%)*	*6% WR*	*Diff.(%)*	*9% WR*	*Diff.(%)*
N_e (kW)	127.27	135.15	6.19	133.65	5.01	125.50	-1.39
b_e (g/kWh)	206	208	0.97	213	3.39	223	8.25
*Y_{NO}×1000	4.558	4.088	-10.31	3.753	-17.66	2.981	-34.20
q_{90} (L/100 km)	4.80	4.846	0.96	4.96	3.33	5.19	8.13
ID (°CA)	4.5237	4.7070	4.05	4.7346	4.66	4.7342	4.65

*Y_{NO} is the mole fraction of NO calculated from the chemical equilibrium. ($y_{NO} = \frac{n_{NO}}{n_T} = \frac{mol}{mol}$, n_T is the total mol number of combustion products)

Table 9 shows BSFC values and q_{90} fuel consumption values at 100 km of Renault Talisman for NDF and selected 3%, 6%, and 9% WRs. Additionally, the variation of q_{90} fuel consumption values at 100 km are presented in Fig. 10(a). As can be seen in this table, WAIA increases BSFC. For 3%, 6%, and 9% WRs BSFC values have increased by 0.97%, 3.39%, and 8.25%, respectively, compared to NDF. The increase ratios in BSFC for 3% and 5% WRs are lower than that of a high WR of 9%. Similarly, q90 fuel consumption values at 100 km also have increased with selected WRs. q90 fuel consumption as a liter at 100 km has increased from 4.8 liters to 5.13 liters for 9% WR. These results are in agreement with the results given in the relevant literature Bedford et al. (2000). As can be seen in Table 9 and Fig.10(b), WAIA decreases considerably the mole fraction of NO. The mole fraction of values NO for 3%, 6%, and 9% WRs have reduced by 10.31%, 17.66%, and 34.20%, respectively, compared to NDF.

Primarily the cylinder temperature values primarily influence the rate of formation of nitric oxide according to the well-known Zeldovich mechanism (Heywood, 1988). Thus, any effort to decrease cylinder temperature would result in beneficial effects to reduce the mole fraction of NO. As it is known from the relevant literature, the use of water in diesel engines is one of the most effective methods to reduce NO emission without worsening BSFC (Kökkülünk, 2012; Ma et al., 2014). For example, Kannan and Udayakumar (2009) stated that they achieved approximately 20% reductions in NO emission by adding water as diesel-water emulsion in their numerical study.

The ID values for NDF and selected WRs are given in Table 8. ID values for 3%, 6%, and 9% WRs increase by 4.05%, 4.66%, and 4.65%, respectively, compared to NDF. With the WAIA application, the temperature values during fuel injection would be lower because injected water during the intake stroke will vaporize and cool the air, which leads to a rise in ID. Also, increasing ID may cause more fuel to be burned around TDC. It is well-known in the literature that without knocking the burning of fuel around TDC increases the effective power and efficiency of diesel engines (Heywood, 1988; Durgun, 2022).

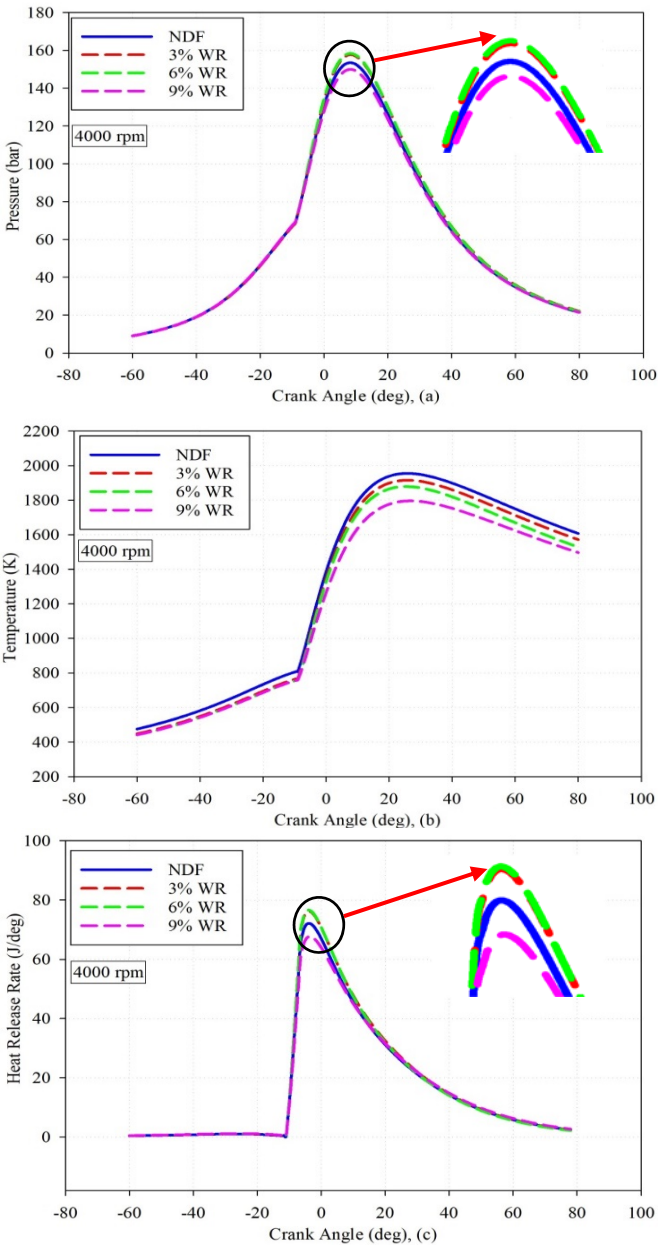

Fig. 9. Variations of **a)** cylinder pressure, **b)** cylinder temperature and **c)** HRR obtained from the presented model for NDF, 3%, 6% and 9% WRs at 4000 rpm in the M9R type diesel engine used in Renault Talisman automobile

CONCLUSIONS

In this study, a computer code based on the thermodynamic-based ZDSZ model originally proposed and given by Ferguson (1986) for diesel engine cycles has been improved with some additional modifications for NDF and WAIA. This developed model can calculate diesel engine cycles with sufficient accuracy for NDF and WAIA. The accuracy control results of this model and the results of the applications for water adding into intake air at different ratios, on engine performance and NO emission in two different automotive diesel engines are briefly given below.

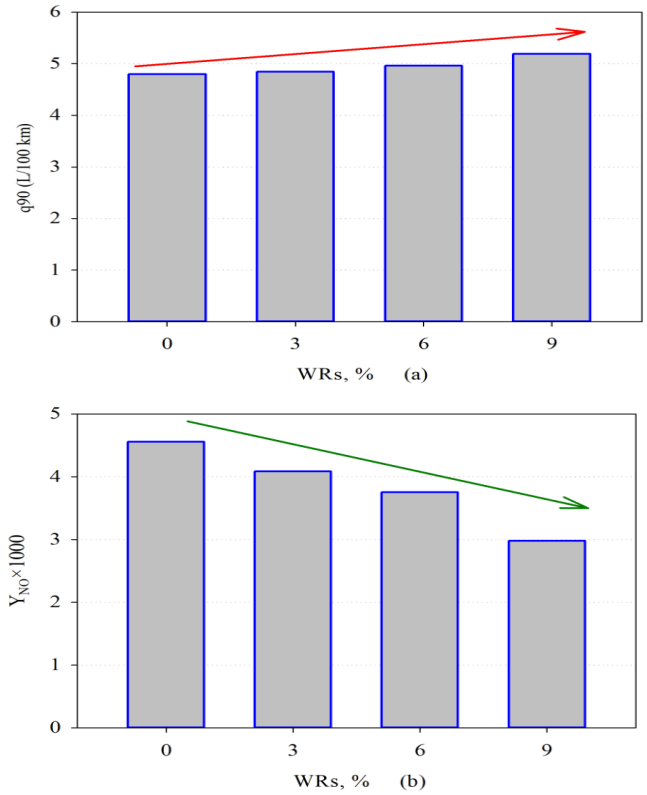

Fig. 10. Variations of **(a)** q90 fuel consumption as liter at 100 km and **(b)** the mole fraction values of NO versus different WRs at 4000 rpm in the M9R type diesel engine used in Renault Talisman automobile

1. The accuracy of our model was validated using experimental data from tests conducted at 2000 rpm and 4000 rpm, with 6% and 10% WAIA levels. For instance, at 2000 rpm, the maximum pressure difference between our model and experimental results was 1.1% for 6% WAIA, and 1.2% for 10% WAIA. Similar differences were observed at 4000 rpm. Overall, differences in cylinder pressure, temperature, and heat release rate ranged from 0.02% to 12.14% across all conditions.

2. The present model could calculate motor performance parameters with sufficient accuracy for NDF and WAIA. The q_{90} fuel consumption value of the Renault Talisman at 100 km for 90 km/h constant velocity is given as 4.81 L in the vehicle catalog. The calculated fuel consumption by using the present model for NDF is obtained as 4.5 L. Thus, a 6.88 % difference was calculated between the q_{90} fuel consumption values.

3. The results obtained at the end of the numerical study for two different automotive diesel engines can be summarized separately as follows. In the first application, the developed model has been applied for NDF, 5%, and 7.5% WRs at 2250 rpm in Renault K9K-700 type diesel engine.

3.a) WAIA decreases cylinder pressure, temperature, and HRR values for selected operating conditions for this engine. For 5% and 7.5% WRs, cylinder temperature values, and the maximum HRR ratios have decreased by (2.87%, and 3.91%) (4.46% and 6.22%), respectively, compared to that of NDF.

3.b) WAIA reduces effective power and NO emissions but increases BSFC for this engine. Compared to NDF, effective power and NO emissions decreased by (4.26%, 7.37%) and (12.43%, 16.39%) for 5% and 7.5% WRs, respectively. Meanwhile, BSFC increased by 6.95% and 10.56% for 5% and 7.5% WRs, respectively. Additionally, ID values slightly increased with WAIA at 2250 rpm.

4. The second numerical application was made for the Talisman automobile engine and the numerical comparison results obtained from the present model at 3%, 6%, and 9% at 4000 rpms in this engine are given below.

4.a) 3% and 6% WRs increase slightly the cylinder pressure values, but 9% WR reduces the cylinder pressure values. For 3% and 6% WRs, the increase ratio of maximum pressure values compared to NDF was determined as 2.71% and 3.13%, respectively. At 9% WR, the decrease ratio of maximum pressure value was calculated as 2.34%.

4.b) 3%, 6%, and 9% WRs reduce the cylinder temperature values. For 3%, 6%, and 9% WRs, the maximum temperature values decreased by 2.02%, 3.88%, and 8.14%, respectively.

4.c) For 3 % and 9 % WRs, HRR increase, but for 9 % it decreases. The maximum HRR values have increased by 5.71% and 6.15%, for 3 % and 6% WRs, respectively, but it has decreased by 6.2% at 9% WR, compared to NDF.

4.d) BSFC values and the q_{90} fuel consumption values at 100 km of Renault Talisman increase with application of 3%, 6%, and 9% WAIA. For 3%, 6%, and 9% WRs BSFC values have increased by 0.97%, 3.39%, and 8.25%, respectively, compared to NDF.

4.e) WAIA decreases considerably NO emissions of this engine. NO emission values for 3%, 6%, and 9% WRs have reduced by 10.31%, 17.66%, and 34.20%, respectively, compared to NDF.

4.f) WAIA increases ID values in this engine. ID values for 3%, 6%, and 9% WRs increase by 4.05%, 4.66%, and 4.65%, respectively, compared to NDF.

REFERENCES

Automobile Catalog, 2021. (Accessed 8. November. 2021). https://www.automobilecatalog.com/car/2022/2986985/renault_talisman_blue_dci_160_edc.html#gsc.tab=0.

Bedford, F.W.F., C. Rutland, P. Dittrich, A. Raab. 2000. Effects of direct water injection on DI diesel engine combustion. *SAE Tech. Pap. 01:12*. https://doi.org/https://doi.org/10.4271/2000-01-2938.

Bondar, V., S. Aliukov, A. Malozemov, A. Das. 2020. Mathematical model of thermodynamic processes in the intake manifold of a diesel engine with fuel and water injection. *Energies* 13(17):4315. https://doi.org/10.3390/en13174315.

Borman, G.L., and K.W. Ragland. 1998. Combustion Engineering, *McGraw-Hill*. https://books.google.com.tr/books?id=ZxdFPgAACAAJ.

Butcher, J.C., 1995. On fifth order Runge-Kutta methods, *BIT Numerical Mathematics* 35:202–209. https://doi.org/10.1007/BF01737162.

Durgun, O. 1988. Using Ethanol in Spark Ignition Engine, *UCTEA Chamb. Mech. Eng. J.* 29: 24–26.

Durgun, O. 1990. Experimental Methods in the Internal Combustion Engines.

Durgun, O. 1991. A practical method for calculation engine cycles, *Union Chambers Turkish Eng. Arc., Chamb. Mech. Eng.* 383:18–29.

Durgun, O. 2022. Internal Combustion Engines Basic Principles, Turkish Chamber of Naval Architect and Marine Engineers.

Ece, Y.M., and V. Ayhan. 2019. Investigation of the Effect of Direct Water Injection on Performance and Emissions of a Single Cylinder Diesel Engine. *J. Adv. Technol. Sci.* 8: 11–21. (In Turkish). https://dergipark.org.tr/tr/download/article-file/719644

Ferguson, C. R., 1986. Internal Combustion Engines Applied Thermodynamics.

Gowrishankar, A.K.S., P. Bhasker J, and P. Rastogi. 2020. Investigations on NO_x and smoke emissions reduction potential through water-in-diesel emulsion and water fumigation in a small-bore diesel engine, *SAE Tech. Pap.* 32:12. https://doi.org/https://doi.org/10.4271/2020-32-2312.

Heywood, J. B., 1988. Internal Combustion Engine Fundamentals.

Jhalani, A., D. Sharma, S.L. Soni, P.K. Sharmai. 2023. Effects of process parameters on performance and emissions of a water-emulsified diesel-fueled compression ignition engine. *Energy Sources, Part A Recover. Util. Environ. Eff.* 45:4242–4254. https://doi.org/10.1080/15567036.2019.1669739.

Jurić, F., M. Krajcar, N. Duić, M. Vujanović. 2023. Investigating the pollutant formation and combustion characteristics of biofuels in compression ignition engines: A numerical study. *Therm. Sci. Eng. Prog*. 43:101939. https://doi.org/10.1016/J.TSEP.2023.101939.

Kannan, K., M. Udayakumar. 2009. Modeling of nitric oxide formation in single cylinder direct injection diesel engine using diesel-water emulsion. *Am. J. Appl. Sci*. 6:1313–1320. https://doi.org/10.3844/ajassp.2009.1313.1320.

Khatri, D., and R. Goyal. 2020. Performance, emission and combustion characteristics of water diesel emulsified fuel for diesel engine: A review. *Mater. Today Proc*. 28: 2275–2278. https://doi.org/10.1016/J.MATPR.2020.04.560.

Kökkülünk, G. 2012. Analysis of the Effects of Exhaust Gas Recirculation (EGR) on Diesel Engine with Steam Injection System to Performance and Emission Parameters, YTU, (In Turkish Thesis).

Kökkülünk, G., G. Gonca, V. Ayhan, I. Cesur, A. Parlak. 2013. Theoretical and experimental investigation of diesel engine with steam injection system on performance and emission parameters. *Appl. Therm. Eng*. 54:161–170. https://doi.org/10.1016/J.APPLTHERMALENG.2013.01.034

Kumar, V.V.N, and A. Sharma. 2013. Performance analyses of diesel engine at different injection angles using water diesel emulsion, *SAE Tech. Pap.* 01:10. https://doi.org/https://doi.org/10.4271/2013-01-2170

Lamas, M.I., C.G. Rodríguez, J.D. Rodríguez, J. Telmo. 2013. Internal modifications to reduce pollutant emissions from marine engines. A numerical approach, *Int. J. Nav. Archit. Ocean Eng.* 5:493–501. https://doi.org/10.2478/IJNAOE-2013-0148.

Ma, X., F. Zhang, K. Han, Z. Zhu, Y. Liu. 2014. Effects of intake manifold water injection on combustion and emissions of diesel engine. *Energy Procedia* 61:777–781. https://doi.org/10.1016/J.EGYPRO.2014.11.963.

Maawa, W.N., R. Mamat, G. Najafi, L.P.H. De Goey. 2020. Performance, combustion, and emission characteristics of a CI engine fueled with emulsified diesel-biodiesel blends at different water contents. *Fuel* 267:117265. https://doi.org/10.1016/J.FUEL.2020.117265.

Nemati, P., S. Jafarmadar, and H. Taghavifar. 2016. Exergy analysis of biodiesel combustion in a direct injection compression ignition (CI) engine using quasi-dimensional multi-zone model, *Energy* 115:528–538. https://doi.org/10.1016/J.ENERGY.2016.09.042.

Parlak, A., G. Gonca, Y. Üst, B. Sahin, A. Safa. 2019. A comprehensive comparison of steam injected diesel engine and miller cycled diesel engine by using two zone combustion model. *Journal of the Energy Institute* 88(1):43-52. https://doi.org/10.1016/j.joei.2014.04.007.

Pasternak, M., F. Mauss, and H. Bensler. 2009. Diesel engine cycle simulation with a reduced set of modeling parameters based on detailed kinetics. *SAE Tech. Pap. 01:13.* https://doi.org/https://doi.org/10.4271/2009-01-0676.

Qiong, Li. 1992. Development of a quası-dimensional diesel engine simulation for energy and availability analysis. University of Illinois at Urbana-Champaign. Doktoral thesis.

Rajak, U., P. Nashine, T.S. Singh, T.N. Verma. 2018. Numerical investigation of performance, combustion and emission characteristics of various biofuels. *Energy Convers. Manag.* 156: 235–252. https://doi.org/10.1016/J.enconman.2017.11.017.

Rakopoulos, C.D., K.A. Antonopoulos, D.C. Rakopoulos, D.T. Hountalas. 2008. Multi-zone modeling of combustion and emissions formation in DI diesel engine operating on ethanol–diesel fuel blends. *Energy Conversion and Management.* 49:625–643. https://doi.org/10.1016/J.enconman.2007.07.035.

Sahin, Z., M. Tuti, and O. Durgun. 2014. Experimental investigation of the effects of water adding to the intake air on the engine performance and exhaust emissions in a DI automotive diesel engine. *Fuel* 115:884–895. https://doi.org/10.1016/J.FUEL.2012.10.080.

Sahin, Z., and O. Durgun. 2008. Multi-zone combustion modeling for the prediction of diesel engine cycles and engine performance parameters. *Appl. Therm. Eng.* 28:2245-2256. https://doi.org/10.1016/J.APPLTHERMALENG.2008.01.002

Sahin, Z., O. Durgun, and M. Tuti. 2018. An experimental study on the effects of inlet water injection of diesel engine heat release rate, fuel consumption, opacity, and NO_x emissions, *Exergetic, Energ. Environ. Dimens.* 981–996. https://doi.org/10.1016/B978-0-12-813734-5.00055-X.

Sahin, Z., O. Durgun, and O.N. Aksu. 2015. Experimental investigation of n-butanol/diesel fuel blends and n-butanol fumigation-evaluation of engine performance, exhaust emissions, heat release and flammability analysis. *Energy Convers. Manag.* 103 778–789. https://doi.org/10.1016/J.enconman.2015.06.089.

Sandeep, S., D.S. Kumar, S. Krishnan, S.K. Pandey. 2019. Assessment of atomized water injection in the intake manifold of a heavy duty diesel engine for NOx reduction potential. *IOP Conf. Ser. Mater. Sci. Eng.*577:12186. https://doi.org/10.1088/1757-899X/577/1/012186.

Savioli, T. 2015. CFD analysis of 2-stroke engines. *Energy Procedia.*81:723–731. https://doi.org/10.1016/J.EGYPRO.2015.12.078.

Senčić, T., V. Mrzljak, P. Blecich, I. Bonefačić. 2019. 2D CFD simulation of water injection strategies in a large marine engine. *J. Mar. Sci. Eng.* 7:296. https://doi.org/10.3390/jmse7090296.

Shrivastava, R., R. Hessel, and R.D. Reitz. 2002. CFD optimization of DI diesel engine performance and emissions using variable intake valve actuation with boost pressure, EGR and multiple injections. *SAE Tech. Pap.* 111:1612-1629. https://doi.org/10.4271/2002-01-0959.

Sindhu, R., G.A.P. Rao, and K.M. Murthy. 2014. Thermodynamic modelling of diesel engine processes for predicting engine performance. *Int. J. Appl. Eng. Technology.*4:101-114. https://api.semanticscholar.org/CorpusID:56402776.

Subramanian, K.A. 2011. A comparison of water–diesel emulsion and timed injection of water into the intake manifold of a diesel engine for simultaneous control of NO and smoke emissions. *Energy Conversion Management.* 52:849–857. https://doi.org/10.1016/J.enconman.2010.08.010.

Tamma, B., J.C. Alvarez, and A.J. Simon. 2003. Water Addition in Diesel Engine Intake for NO_x Reduction: Comparison of Modeling and Experiments. *Internal Combustion Engine Division Fall Technical Conference (ICEF),* 0749:245–249. https://doi.org/10.1115/ICEF2003-0749.

Tauzia, X., A. Maiboom, and S.R. Shah. 2010. Experimental study of inlet manifold water injection on combustion and emissions of an automotive direct injection Diesel engine. *Energy* 35:3628–3639. https://doi.org/10.1016/J.energy.2010.05.007.

Tutak, W., and A. Jamrozik. 2016. Validation and optimization of the thermal cycle for a diesel engine by computational fluid dynamics modeling. *Appl. Math. Model* 40:6293–6309. https://doi.org/10.1016/J.APM.2016.02.021.

Tuti, M. 2012. Experimental Investigation of the Effects of Water Adding to the Intake Air on the Engine Performance and Exhaust Emissions in a Diesel Engine, Karadeniz Technical University, Master thesis. (In Turkish).

Tuti, M. 2022. Experimental and Numerical Investigation of the Effects of Adding Water to the Intake Air on Engine Performance, Combustion and Exhaust Emissions in Diesel Engines. Karadeniz Technical University. Doktoral thesis (In Turkish).

Vellaiyan, S., A. Subbiah, and P. Chockalingam. 2019. Multi-response optimization to obtain better performance and emission level in a diesel engine fueled with water-biodiesel emulsion fuel and nanoadditive. *Environment Science Pollution Reserch* 26:4833–4841. https://doi.org/10.1007/s11356-018-3979-6.

Vigneswaran, R., K. Annamalai, B. Dhinesh, R. Krishnamoorthy. 2018. Experimental investigation of unmodified diesel engine performance, combustion and emission with multipurpose additive along with water-in-diesel emulsion fuel. *Energy Convers. Manag.* 172: 370–380. https://doi.org/10.1016/J.enconman.2018.07.039.

Wang, Z., S. Wu, Y. Huang, S. Huang, S. Shi, X. Cheng, R. Huang. 2018. Experimental investigation on spray, evaporation and combustion characteristics of ethanol-diesel, water-emulsified diesel and neat diesel fuels, *Fuel* 231:438–448. https://doi.org/10.1016/J.FUEL.2018.05.129.

Woschni, G. 1967. A Universally applicable equation for the instantaneous heat transfer coefficient in the internal combustion engine. *SAE Tech. Pap.* 670931:19. https://doi.org/https://doi.org/10.4271/670931.

Zhang, J., Y.Meng, D.Liu, L.Liu, X.Ma, C. Jiang, X. Li, L. Huang. 2023. Modelling and multi-objective combustion optimization of marine engine with speed maintaining control target. *Therm. Sci. Eng. Prog.* 41:101852. https://doi.org/10.1016/J.TSEP.2023.101852.

Zhu, S., B. Hu, S. Akehurst, C. Copeland, A. Lewis, H. Yuan, I. Kennedy, J. Bernards, C. Branney. 2019. A review of water injection applied on the internal combustion engine, *Energy Convers. Manag.* 184:139–158. https://doi.org/10.1016/J.enconman.2019.01.042.

Journal Homepage: https://dergipark.org.tr/tr/pub/isibted

Journal of Thermal Science and Technology

Archive: https://tibtd.org.tr/dergi

Assessment of Multigrid Schemes with Fixed Patterns for a Two-Dimensional Heat Transfer Problem

Dr. Mustafa Serdar TEKÇE [1, *], Prof. Dr. Kürşad Melih GÜLEREN [2]

[1] *Turkish AeroSpace, Aircraft Vice Presidency, Air Vehicle Engineering, Aerodynamics – Jet Aircrafts, Kahramankazan, 06980, Ankara, Türkiye*
[2] *Eskişehir Osmangazi University, Faculty of Engineering and Architecture, Department of Aeronautical Engineering, Odunpazarı, 26040, Eskişehir, Türkiye*

A R T I C L E I N F O

2024, vol. 44, no.2, pp. 322-338

doi: 10.47480/isibted.1403905

Research Article
Received: 12 December 2023
Accepted: 31 July 2024

* *Corresponding Author*
e-mail:
mustafaserdar.tekce@tai.com.tr

Keywords:
Thermal Diffusion
Multigrid Scheme
Computational Cost

ORCID Numbers in author order:
0009-0002-2070-9036
0000-0003-3464-7956

A B S T R A C T

Heat transfer problems and their solutions are of critical importance in almost all areas of engineering and technology While many real-world problems are inherently three-dimensional, simplifying them to 2D models offer practical advantages with reasonable models. With being fundamental class of problem of heat transfer, 2D thermal diffusion problem was selected for the study. Multigrid methods were referred as standing out in terms of cost reduction while keeping solution accuracy. Effectivity of multigrid methods employing fixed pattern schemes were subject to investigation. In order to fairly setup a numerical experimentation, authentic code generation effort was given that implements basic finite volume method, intergrid operations and iterative solvers. A reference case with an analytical Laplace solution was selected and properly validated by results. Variety of multigrid schemes with fixed patterns were explored around parameters; iterations per sweep and maximum coarsening level. Results were compiled on the focal points of cost and performance. Comparison of the direct iterative methods with multigrid schemes proved the effectivity of multigrid schemes. Multigrid schemes generated convergent solutions with only 1.2% cost of direct iterative method for the reference case. With the assessment of the cost and performance outcomes of parameter explorations, it is concluded that any multigrid scheme should visit maximum coarsest level possible while keeping a minimum number of iterations on each grid resolution.

Sabit Şemalı Çoklu Ağ Döngülerinin İki Boyutlu Bir Isı Transfer Problemi Kapsamında İncelenmesi

M A K A L E B İ L G İ S İ

Anahtar Kelimeler:
Isıl Yayınım
Çoklu Ağ Şeması
Hesaplama Maliyeti

Ö Z E T

Isı transferi problemleri ve çözümleri, mühendislik ve teknolojinin neredeyse tüm alanlarında kritik öneme sahiptir. Birçok gerçek problem doğası gereği üç boyutludur, ancak bunları makul biçimlerde iki boyutlu modellere basitleştirmek, pratik avantajlar sunmaktadır. Dolayısıyla, iki boyutlu ısıl yayınım problemi, ısı transferinin temel bir problem sınıfından olması nedeniyle çalışma alanı olarak seçildi. Çoklu ağ yöntemleri, çözüm doğruluğunu koruduğu halde maliyeti ciddi oranda azaltmasıyla anılmaktaydı. Böylelikle, sabit şemaya sahip çoklu ağ yöntemlerinin etkinliği araştırma konusu olarak seçildi. Düzgün bir sayısal deney düzeneği kurulabilmesi için, temel seviyede sonlu hacimler yöntemi, çözünürlükler arası işlemler ve iteratif çözüm yöntemleri uygulayan özgün bir kod yazıldı. Analitik Laplace çözümü bulunan referans bir vaka seçildi ve sonuçlarla doğrulandı. Sabit şemalı çoklu ağ yöntemlerinin başarımı, bir çözünürlük seviyesindeki iterasyon sayısı ve azami seyreklik seviyesi parametreleri etrafında araştırıldı. Sonuçlar maliyet ve başarım odak noktalarına göre derlendi. Doğrudan iteratif yöntemlerin çoklu ağ şemaları ile karşılaştırılması, çoklu ağ şemalarının etkinliğini kanıtladı. Referans vaka için çoklu ağ şemaları, doğrudan iteratif yöntemin sadece %1.2 maliyeti ile yakınsayan çözümler üretti. Parametre keşiflerinden gelen maliyet ve başarım sonuçlarının değerlendirilmesiyle, herhangi bir çoklu ağ şemasının, her çözünürlükte asgari bir iterasyon yapması gerekirken mümkün olan en seyrek çözünürlük seviyesini ziyaret etmesi gerektiği sonucuna varıldı.

NOMENCLATURE

A	Coefficient Matrice of Systems of Equations
A	Denotation for Area
a	Discretized Coefficient
aij	An Element of Coefficient Matrice
b	Constants Vector of Systems of Equations
B	Denotation for Boundary
C, c	Generic Denotation for Cell
E, e	Denotation for East
F	Finalization
FVM	Finite Volume Method
h	Denotation for Grid Resolution Level
I	Initialization
i	Cell Indice in the first direction of domain
i	Denotation for Cell Number
ID	Identification number of the cell
j	Cell Indice in the second direction of domain
k	Heat Transfer Coefficient
L	Lower Part of Decomposed Coefficient Matrice
N, n	Denotation for North
P	Prolongation
P	Denotation for the Cell being processed
q, Q	Heat Flux
r	Residual Vector
R	Mean Residual
R	Restriction
RWU	Reference Work Unit
S	Source Term
S	Standard Deviation
S	Sweep of Iterations
S, s	Denotation for South
T	Temperature
U	Upper Part of Decomposed Coefficient Matrice
V	Volume
W, w	Denotation for West
x	Solution Vector
x	Location in the first direction of domain
y	Intermediate Solution Vector
y	Location in the second direction of domain
Γ	Coefficient of Diffusive Property
ζ	Spatial Location
φ	Physical Property

INTRODUCTION

Heat transfer, a fundamental aspect of engineering physics and numerous engineering problems, influencing the design and performance of a vast array of systems (Annaratone, 2010). The challenge lies not only in understanding the principles of heat transfer but also in devising effective methods to predict, control, and optimize thermal behaviour within complex structures. The diversity of engineering heat transfer problems spans from the microscopic scales of electronic devices, where efficient heat dissipation is paramount, to the macroscopic scales of power plants, where thermal efficiency and material durability are critical.

The complexities of heat transfer problems necessitate various methodologies for engineers to choose from. Analytical methods, rooted in mathematical elegance, provide solutions under simplified conditions and crude assumptions. However, applicability of analytical methods often hinders realizability of real-world complexities, such as irregular geometries or nonlinearities. Numerical methods, on the other hand, offer a versatile approach, capable of handling solution by discretizing the problem into manageable components (Axelsson, 1996). The choice between analytical elegance and numerical versatility emphasizes that the way towards solutions should balance accuracy, computational efficiency, and applicability to diverse engineering contexts. Cost efficiency is the key aspect towards establishing a high performing solution method.

Dimension of the heat transfer problem is another aspect to consider. While many real-world problems are inherently three-dimensional (Onur et al., 2011; Kürekçi and Özcan, 2012; Aydar and Ekmekçi, 2012; Uğurlubilek, 2012; Karaaslan et al., 2013; Sert et al., 2019; Yıldızeli and Çadırcı, 2023), simplified 2D models (Bali, 2006; Aykan and Dursunkaya, 2008; Mançuhan et al., 2011; Alpman, 2012; Doğan et al., 2012; Şimşek et al., 2020; Yetik and Mahir, 2020; Uzuner et al., 2023) can offer practical advantages without significant loss of accuracy, provided certain assumptions are reasonable. The transition from three-dimensional (3D) heat transfer problems to their two-dimensional (2D) counterparts is a common strategy in engineering and science (Annaratone, 2010).

There are several rationales beneath the assumptions for dimensional reduction in heat transfer problems. Systems/geometries/problems exhibiting some form of symmetry along an axis can be solved in two-dimensional domain with proper modelling. Likewise, there may be a dominant dimension with overwhelming difference in either size or gradients that can be solved via dimensional reduction. Many real-world applications, such as heat exchangers, electronic devices, and building materials, exhibit a primary heat transfer direction anyway. Modelling these systems in 2D often provides accurate results for the specific heat transfer aspects of interest. Simplified 2D model can also be used a stepping stone towards higher fidelity models. 2D models are often used as a benchmark for validating more complex 3D simulations. If the 2D model adequately represents the behaviour observed in experiments, it lends confidence to the accuracy of the simplification. Additionally, starting with 2D models helps researchers grasp fundamental heat transfer principles before tackling the increased complexity of 3D problems. Furthermore, solving 3D heat transfer problems computationally can be resource-intensive. By simplifying to 2D, simulations and analyses become more computationally efficient, enabling quicker and more practical solutions. However, it is imperative to acknowledge the limitations of 2D simplifications. The validity of assumptions must be carefully considered, and the impact of neglecting certain dimensions should be assessed to ensure the model's accuracy in a given context.

Various heat transfer problems can be modelled in two-dimensional domain. In electronic devices, heat generated by

components on a circuit board needs to be efficiently dissipated to prevent overheating. The thin layers of a circuit board often allow for the simplification of heat transfer analysis to a 2D plane, considering heat flow along the surface. Heat exchangers in various industries, such as automotive and HVAC systems, involve the transfer of thermal energy between fluids. Many heat exchanger configurations exhibit a primary flow direction, allowing for 2D modelling to capture the essential heat transfer mechanisms. Analysing the thermal behaviour of building materials, like walls or windows, is crucial for energy efficiency and climate control in structures. Heat transfer through building materials often occurs primarily in two dimensions, such as through the thickness of a wall. 2D models are suitable for these analyses. Heat transfer through the thickness of the plate can also be modelled in 2D, especially if the plate is thin compared to its length and width. The 2D model would involve analysing temperature gradients along the surface and through the thickness. These examples illustrate how 2D heat transfer models are applicable to analyse heat conduction in plates, where the heat transfer primarily occurs in two dimensions. Temperature variations across the plate's surface or through its thickness can be modelled and solved for practical engineering applications.

Numerical Methods

Numerical methods stand as a compromise between theoretical formulations and the practical demands of engineering. Finite Difference Methods, efficient in their simplicity, discretize the spatial domain into a grid and employ iterative schemes to approximate the temporal evolution of temperature. Finite Element Methods, renowned for their versatility, decompose structures into finite elements with distinct mathematical representations, accommodating complex geometries and material heterogeneities. Within various of numerical techniques, Finite Volume Methods (FVM) occupy a distinctive value (Versteeg and Malalasekera, 2007).

FVM approaches the 2D heat transfer problem by dividing the domain into finite control volumes, ensuring the conservation of energy within each volume. This conservation-centric philosophy makes FVM particularly well-suited for scenarios where the preservation of global quantities is crucial. By discretizing the problem in this manner, FVM facilitates a detailed understanding of spatial variations in temperature within the 2D plate. Its application extends beyond mere computation; it provides a comprehensive picture of how heat distributes across the plate, capturing thermal gradients and material properties.

In the context of the 2D heat transfer problem on a homogeneous plate, FVM offers distinct advantages. By dividing the plate into finite control volumes, FVM acknowledges the localized nature of thermal interactions. This granularity allows for the preservation of global quantities, ensuring that the simulation accurately reflects the overall energy balance within the system. The application of FVM to the 2D plate not only provides numerical results but also affords a deeper understanding of the thermal dynamics, shedding light on how temperature gradients evolve across the plate.

The computational framework of FVM involves discretizing the governing heat conduction equation over these control volumes and iteratively solving for temperature distribution. The method excels in scenarios where conservation laws play a pivotal role, making it particularly applicable to heat transfer problems characterized by intricate geometries and varying boundary conditions. FVM's ability to handle non-uniform material properties and adapt to irregular geometries positions it as a versatile and powerful tool in the numerical simulation of 2D heat transfer.

Main problem with any numerical solution endeavour is that available computational resource is almost always limited in any situation compared to desired amount, regardless of context and case. Thus, any effort is highly valuable that achieves solution at a desired accuracy while keeping resource (memory, processor, time, power) costs minimal (Versteeg and Malalasekera, 2007). Compromization between accuracy and cost is crucial for efficiency while using iterative methods to solve the given problem. Multigrid methods were found promising for cost efficiency towards accurate solutions.

Multigrid

Although there are several approaches to reduce computational cost, multigrid methods stand out in terms of cost reduction while keeping solution accuracy (Trottenberg et al., 2001). Multigrid methods and algorithms reduce computational cost dramatically (Brandt and Livne, 2011). Additionally, multigrid methods do not conflict with most of the other cost reduction approaches, making it a much more versatile and reliable tool while amplifying effectivity.

The multigrid approach arises from the recognition that not all features of a solution need the same level of detail. In the context of 2D heat transfer on a homogeneous plate, multigrid methods offer a hierarchical solution strategy. Coarser grids capture the overarching trends of temperature distribution, while finer grids address localized variations. This multiscale approach allows the solver to efficiently navigate the solution space, accelerating convergence and significantly reducing computational costs.

The multigrid approach complements the strengths of Finite Volume Methods, providing an additional layer of efficiency in solving 2D heat transfer problems. By operating on multiple resolutions, the multigrid method stands as a testament to the continual evolution of numerical techniques, offering a powerful solution for engineers and researchers grappling with the computational demands of intricate heat transfer simulations.

In a multigrid cycle, the grid is successively coarsened and refined in a consequential manner. This process involves moving between different levels of grid resolution. At each level, a relaxation method, often a simple iterative technique like Gauss-Seidel, is applied to smooth out errors in the solution. The process of moving between grid levels allows for the transfer of information, helping to correct errors more effectively. The W-cycle and F-cycle are variations of the V-cycle, introducing more coarsening and refinement steps in the multigrid scheme. These fixed-pattern multigrid schemes aim to address issues with convergence by taking

advantage of grid hierarchy and the interactions between different resolutions.

Multigrid schemes are a category of methods to accelerate convergence in iterative solvers. Fixed-pattern multigrid schemes, such as the V-cycle, W-cycle, and F-cycle, are widely used and have demonstrated their effectiveness in improving convergence speed (Trottenberg et al., 2001).

Multigrid cycles are procedural integration of various grid operations, solution iterations and decision checks composed in a specific algorithm. Various multigrid cycle definitions are present in literature and are used in software. Selecting, defining or setting an appropriate multigrid cycle depends on the case and requires exercise before execution. Multigrid cycles improve convergence rates of iterative solutions anyway, but reckless execution of multigrid cycles may hinder effectivity. Fixed-pattern multigrid schemes are robust and well-established, making them prior choice for many numerical simulations (Versteeg and Malalasekera, 2007).

Most of the multigrid cycle definitions have predetermined sequential order of operations and iterations. Figure 1 and Figure 2 illustrates V cycle and W cycle that are mentioned (without further elaboration) to be members of the μ cycles where μ parameter is 1 and 2 respectively (Wesseling, 1992). Figure 3 illustrates F cycle that is defined with a specified pattern that progressively increases the top level of fine grid resolutions (Briggs et al., 2000).

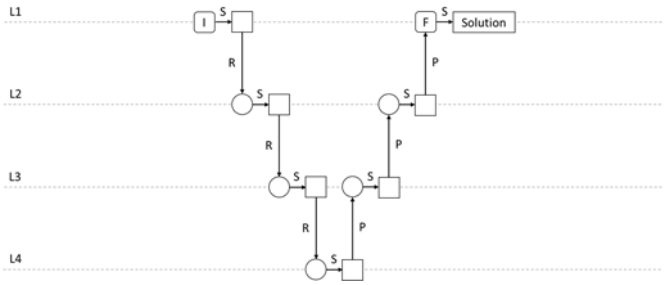

Figure 1. Pattern of a V multigrid cycle with four grid levels.

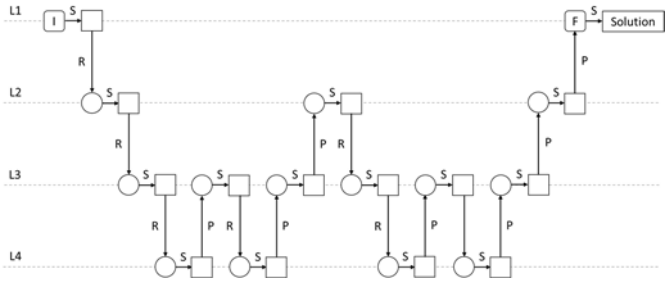

Figure 2. Pattern of a W multigrid cycle with four grid levels.

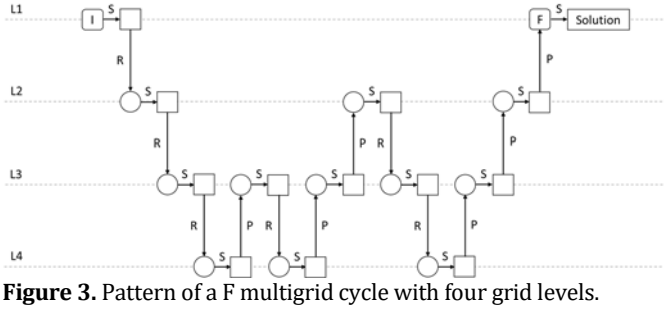

Figure 3. Pattern of a F multigrid cycle with four grid levels.

To transfer information between grids with different resolutions, multigrid employs restriction and prolongation operations (Briggs et al., 2000). Restriction operators aggregate data from finer grids to coarser grids, while prolongation operators interpolate data from coarser grids to finer grids. The entire process of transferring between grids, smoothing, and correction is repeated iteratively until a desired level of accuracy is achieved. Multigrid can significantly accelerate the convergence of iterative solvers, reducing the number of iterations required to reach a solution (Brandt and Livne, 2011).

The power of multigrid lies in its ability to address error components at different scales efficiently (Briggs et al., 2000). High-frequency error components are more effectively treated on finer grids, while low-frequency error components are addressed on coarser grids. This hierarchical approach can dramatically improve the convergence rate, making it a popular choice for solving complex problems with fine grids, where other solvers may struggle to converge in a reasonable amount of time (Brandt and Livne, 2011).

Multigrid on Heat Transfer

Multigrid methods have been used to solve heat transfer problems on numerous cases accompanied with varying numerical methods. Relevant studies were compiled below while emphasizing conclusions about multigrid methods.

In an early study, full-approximation-storage multigrid strategy had been applied to the heat conduction equation by using several iterative schemes to drive the multilevel process (Arnone and Sestini, 1991). Comparisons between single and multiple grid calculations for both explicit and implicit time-dependent schemes, in addition to stationary ones were given (Arnone and Sestini, 1991). The study concluded that multilevel technique had proven to be a very powerful and flexible strategy for speeding up convergence of both steady and unsteady formulations (Arnone and Sestini, 1991).

In another study, steady three-dimensional natural convection in a rectangular parallelepiped with a saturated porous medium was analysed numerically (Dawood and Burns, 1992). Convergence of the current three-dimensional model was enhanced using a multigrid method (Dawood and Burns, 1992). The multigrid method had been shown to work extremely well for problems of conduction and heating yielding speedup factors up to 22 (Dawood and Burns, 1992).

A multigrid algorithm was developed along with an implicit multiblock pressure-based solver for calculating flow and heat transfer problems on nonorthogonal grids (Przekwas and Lai, 1996). The full approximation scheme (FAS) was used due to nonlinearity of the Navier-Stokes equations (Przekwas and Lai, 1996). Optimum performance has been achieved for the multigrid multiblock calculations (Przekwas and Lai, 1996).

To assess the performance of a new full multigrid algorithm in which there is no restriction procedure for variables except for residuals; an algorithm was used in combination with the SIMPLE algorithm to solve fluid flows with heat transfer, using collocated grids and higher-order schemes for convective fluxes (Yan and Thiele, 1998). The modified full multigrid version of the SIMPLE algorithm using collocated grids was shown to be efficient for the calculation of fluid flow and heat transfer, with a speed-up factor of up to 25 (Yan and Thiele, 1998).

The performance of the symmetrically coupled Gauss-Seidel (SCGS) based multigrid method was investigated by applying it to three-dimensional conjugate heat transfer in two different configurations with discrete heat sources (Tang and Joshi, 1999). With multigrid SCGS (MG-SCGS), performance enhancement was even more impressive, and speed up factor can be as high as 19 (Tang and Joshi, 1999). SIMPLER failed to generate a converged solution for strong convection in a high aspect ratio channel while MG-SCGS were able to generate converged results in a timely fashion for all test cases (Tang and Joshi, 1999).

Steady-state two-dimensional solutions to the full compressible Navier–Stokes equations were computed for laminar convective motion of a gas in a square cavity with large horizontal temperature differences (Vierendeels et al., 2004). This line solver was used in a multistage stepping scheme and accelerated with the multigrid method (Vierendeels et al., 2004). The convergence of the solution method was stated as "very fast" and was shown to be independent of the Rayleigh number, the number of grid cells and the grid aspect ratio (Vierendeels et al., 2004).

A numerical tool, "Thermoflow" was developed for simulating the three-dimensional incompressible viscous flow and heat transfer on unstructured meshes (Wang and Joshi, 2006). Four iterative linear solvers have been implemented. The hybrid solver called AgMG/CG, employing agglomerated multigrid method and conjugate gradient, was found to be the best, for the symmetric equations arising from the pressure correction and heat conduction (Wang and Joshi, 2006).

A parallel multigrid-Schwarz method was used for the solution of hydrodynamics and heat transfer problems (Galante and Rizzi, 2007). The solution was obtained by a multigrid method parallelized by domain decomposition techniques, more specifically by the additive Schwarz method (Galante and Rizzi, 2007). A module called MGTool was implemented for the generation of the hierarchy of meshes and for the assemblage of the systems of equations (Galante and Rizzi, 2007). For the problem of heat transference, the methods using multigrid had converged, on average, 2 times faster (Galante and Rizzi, 2007). The study concluded that the combination of methods multigrid and domain decomposition was beneficial option in the solution of equation systems generated with partially differential equation (PDE) discretization (Galante and Rizzi, 2007).

In a fairly recent study, a parallel spatial/angular agglomeration multigrid scheme was developed to accelerate the finite-volume method (FVM) for the computation of radiative heat transfer in absorbing, emitting, and scattering gray media (Lygidakis and Nikolos, 2014). The multigrid scheme was based on the solution of the radiative transfer equation (RTE) with the full approximation scheme (FAS) on successively coarser spatial and angular resolutions (Lygidakis and Nikolos, 2014). The multigrid schemes were based on solution of the RTE on successively coarser spatial and angular resolutions, employing the FAS via a V-cycle strategy (Lygidakis and Nikolos, 2014). Despite the wide establishment of the multigrid technique in computational fluid dynamics (CFD), the angular and the combined spatial/angular methodology were stated as a new approach for the prediction of radiative heat transfer using FVM (Lygidakis and Nikolos, 2014). The acceleration obtained by the proposed multigrid scheme increased with the corresponding increase in grid size; the greater the number of DoFs, the greater the acceleration gained (Lygidakis and Nikolos, 2014).

Common key points were found in the studies including multigrid methods on heat transfer problems. First of all, even though the numerical methods and complexity of the cases were different, speed up factors were reported to be consistently around approximately 20 and 2 at worst. To put it reverse in terms of computational cost; multigrid methods were reported to decrease computational cost to 50% at worst and to 5% on average for the respective reference cases. Thus, it is safe to say that multigrid methods indeed substantially decrease computational cost. Secondly, and perhaps more importantly, multigrid methods were observed to increase robustness of the solution process towards a convergent solution, regardless of the numerical approach in all studies. Additionally, multigrid methods displayed flexibility on various cases with varying algebraic and spatial implementations, even with newly suggested ones.

Even though consistent inferences were found throughout the literature, most of the studies were conducted on specific and/or advanced cases. Cost and performance of the multigrid schemes were not particularly studied with basic numerical methods. Effectivity of multigrid methods employing fundamental schemes still needs to be investigated with a fair numerical experimentation.

METHOD

Sensible approach to explore fundamental multigrid methods was seen as the generation of a simple finite volume method solver and building multigrid algorithms over the definite infrastructure. Generation/development of a code/algorithm from scratch enabled full authority over the controlled experiments of parameters and clarity over validation. Infrastructural certainty improved the merits of the study.

Main concern of the study was to discover the fundamentals of multigrid cycles while establishing a viable and valid execution base. Thus, efforts were focused on generation/development of multigrid algorithms rather than generation/development of a solver.

Boundary condition problem was assumed as a two-dimensional diffusion. Thermal diffusion problem on a homogenous plate was selected for the reference case which may have constant temperature and constant heat flux at boundaries. Thermal coefficients were assumed to be constant within the homogenous plate.

Domain was assumed to be represented with a structured grid of uniform elements. Structured grid enabled to use geometric multigrid methods while easing the implementation of finite volume method operations.

Geometric multigrid methods were assumed in order to ease the implementation of restriction and prolongation and to focus on multigrid cycle algorithms.

Central differencing was assumed for discretization which is adequate for the reference case and is convenient to implement on structured grids and to work with geometric multigrid methods.

Gauss Seidel method without any modification was assumed for iterating the solution which is adequate for the reference case. Convergence of the solution was measured with residual which is a fundamental concept for iterative numerical methods. Residual was assumed as the absolute value of differences of a property for grid cells on successive iterations. Mean residual was defined and was calculated with Equation 2 using residual vector as Equation 1 (Versteeg and Malalasekera, 2007). Both elements of residual vector and consequently mean residual converges to zero towards exact solution. "r" denotes residual, "y" denotes intermediate solution of a property, "c" is the subscript for "cell", "i" is the subscript for "iteration", "n" denotes the number of cells within given domain.

$$r_c = |(y_c)_i - (y_c)_{i-1}| \quad (1)$$

$$\bar{r} = \frac{1}{n}\sum_{c=1}^{n}(r_c) \quad (2)$$

Study was built upon a code from scratch which is consisted of functions with scalable infrastructure. Functions were generated to work with varying inputs and to return output in a definitive format. Output of a function is input of another function and vice versa.

Environment

Selection of the medium for the tool generation is the initial step to consider. Environment should fit to the scope and purpose of the code. Capable of meeting the infrastructure requirements; an object-oriented, functional, fast, high-level, open-source language is considered for tool development. "The Julia programming language" has been preferred with the claim of being both high-level and fast. According to shared benchmark data, Julia has proven to be as fast as Fortran, even though it is as high-level as Python (Internet, 2023). Figure 4 summarizes the results of various languages for various benchmark types. The vertical axis of Figure 4 shows each benchmark time normalized against C implementation.

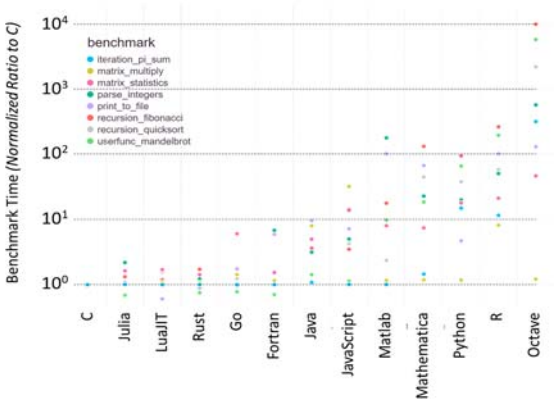

Figure 4. Benchmark results of various programming languages compared to C language (Internet, 2023).

Selection of the language led to specify which libraries to use while keeping tool development authentic as possible. Scope of the study focuses on the effectivity of multigrid methods and schemes. Thus, finite volume methods, iterative solvers and multigrid operations should be performed with authentic functions. Complimentary or basic infrastructure such as; mathematical functions, data base environment, graph plotting, file input output protocols, benchmark tools, are implemented by standard or imported libraries as seen in Table 1.

Table 1. Selected libraries for code infrastructure.

Library	***Origin***	***Explanation***
Dates	Standard	Provides functions that generates date and information in various/custom formats.
Printf	Standard	Enables macros that returns formatted output as string.
SparseArrays	Standard	Provides sparse vector/matrice infrastructure and functions.
Statistics	Standard	Offers basic and advanced statistical functions.
CSV	External	Input output interface/infrastructure for comma separated value files. Compatible with DataFrame library.
DataFrames	External	Offers database features with various filters and operations. Data can be processed in the desired format. Supports object-oriented data types.
Plots	External	Offers various plotting functions and features with various back-ends.
StatsPlots	External	Extension of Plots library. Contains many statistical recipes.

Finite Volume Method Functions

Basic operations regarding finite volume method were coded as functions. Definition of a boundary condition problem is sequential. Problem definition starts with domain description and grid generation. Once computational grid is present at desired resolution, a method for boundary condition inclusion follows. Discretization of the governing equations based on the grid and boundary conditions lead to coefficient matrices of systems of equations. Delivering the coefficient matrices of the problem completes finite volume method sequence of the solution procedure.

Generation of the domain is the very first step towards solution. Domain was assumed to be in rectangular shape on two dimensions. Size in each dimension may vary. Grid was assumed to be uniform in x and y directions. Number of divisions may vary in each direction. "initialize_domain" function works with two-dimensional size input and two number of division input. "initialize_domain" function returns the DataFrame object populated with all individual cell information regarding ID, i, j, x, y, T values. Figure 5 is an example output of the "initialize_domain" function.

6400×6 DataFrame

Row	ID	i	j	x	y	T
	Int64	Int64	Int64	Float64	Float64	Float64
1	1	1	1	0.01875	0.01875	0.0
2	2	2	1	0.05625	0.01875	0.0
3	3	3	1	0.09375	0.01875	0.0
4	4	4	1	0.13125	0.01875	0.0
5	5	5	1	0.16875	0.01875	0.0
⋮	⋮	⋮	⋮	⋮	⋮	⋮
6397	6397	77	80	2.86875	2.98125	0.0
6398	6398	78	80	2.90625	2.98125	0.0
6399	6399	79	80	2.94375	2.98125	0.0
6400	6400	80	80	2.98125	2.98125	0.0

6391 rows omitted

Figure 5. Output example of "initialize_domain" function.

Defining boundary conditions is essential for any boundary condition problem. Conventional denotations of boundaries are assumed as west, east, south and north (Versteeg and Malalasekera, 2007). Fix ("Dirichlet") and flux ("Neumann")

thermal boundary conditions are assumed. Temperature and heat flux values may vary at each boundary but does not vary within a boundary. Thus, "boundary_conditions" function works with four Dirichlet boundary condition input and four Neumann boundary condition input. Function then returns the DataFrame object contains boundary condition information to be later called as input to other functions. Figure 6 is an example output of the "boundary_conditions" function.

4×3 DataFrame

Row	boundary String	fix Float64	flux Float64
1	W	273.15	0.0
2	E	273.15	0.0
3	S	273.15	0.0
4	N	373.15	0.0

Figure 6. Output example of "boundary_conditions" function.

Validity of solutions based on finite volume method requires proper application of boundary conditions. Additionally, different grid resolutions of multigrid cycles require a compatible method for inclusion of boundary conditions. A method called link cutting using source terms of finite volume method (Versteeg and Malalasekera, 2007) while preserving discretization equations is generated in order to maintain a viable multigrid cycle execution. Boundary condition inputs are assumed as physically feasible. Since reference case was selected, constants and relations of thermal diffusion problem were assumed to be predetermined. "apply_boundary_conditions" function works with domain and boundary condition input which were assumed to be compatible.

Equation 3 and Equation 4 are used to calculate source coefficients (Versteeg and Malalasekera, 2007). Figure 7 illustrates the transformation of boundary conditions to source terms. Derivation of the source term contributions are given under the "discretised_form" function below. Source coefficient calculations assume cells to be equal in size at each direction.

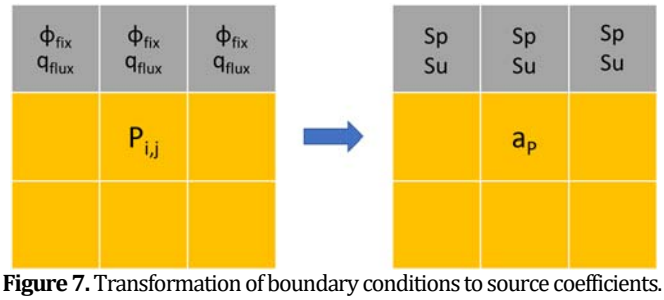

Figure 7. Transformation of boundary conditions to source coefficients.

$$S_p = -\frac{2k_B A_B}{\Delta\zeta} \tag{3}$$

$$S_u = q_B - S_p\,\phi_B \tag{4}$$

Figure 8 is an example output of the "apply_boundary_conditions" function.

6724×9 DataFrame

Row	ID Int64	i Int64	j Int64	x Float64	y Float64	T Float64	q Float64	Sp Float64	Su Float64
1	1	1	1	-0.01875	-0.01875	273.15	0.0	-20.0	5463.0
2	2	2	1	0.01875	-0.01875	273.15	0.0	-20.0	5463.0
3	3	3	1	0.05625	-0.01875	273.15	0.0	-20.0	5463.0
4	4	4	1	0.09375	-0.01875	273.15	0.0	-20.0	5463.0
5	5	5	1	0.13125	-0.01875	273.15	0.0	-20.0	5463.0
⋮	⋮	⋮	⋮	⋮	⋮	⋮	⋮	⋮	⋮
6721	6721	79	82	2.90625	3.01875	373.15	0.0	-20.0	7463.0
6722	6722	80	82	2.94375	3.01875	373.15	0.0	-20.0	7463.0
6723	6723	81	82	2.98125	3.01875	373.15	0.0	-20.0	7463.0
6724	6724	82	82	3.01875	3.01875	373.15	0.0	-20.0	7463.0

6715 rows omitted

Figure 8. Output example of "apply_boundary_conditions" function.

Prerequisite to generate coefficient matrices of an iterative solution is to write down system of equations in a discretized form. Discretization method directly effects iterative solution progress alongside grid resolution. Gradients of physical properties are captured either inherently by grid resolution or numerically by discretization method.

Discretization method assumed as central differencing with linear interpolation. Figure 9 illustrates cell denotations used in discretization (Versteeg and Malalasekera, 2007) for a two-dimensional finite volume method. Equation 5 and Equation 6 are used for two-dimensional diffusion problem (Versteeg and Malalasekera, 2007). Equation 7 and Equation 8 are the gradually discretized form of the diffusion problem (Versteeg and Malalasekera, 2007). By distributing Equation 6 while using source terms given in Equation 9, discretized form is written as seen in Equation 10 for two-dimensional diffusion problem (Versteeg and Malalasekera, 2007). Table 2 summarizes the expressions of coefficients of discretized form.

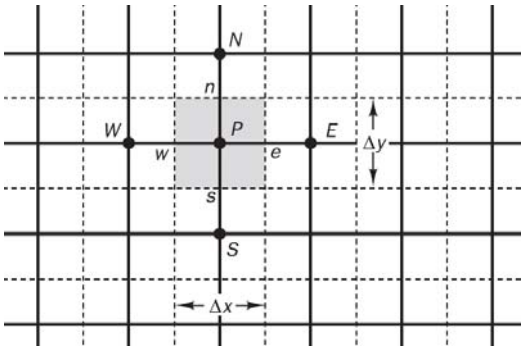

Figure 9. Denotations for discretization function (Versteeg and Malalasekera, 2007).

$$\frac{\partial}{\partial x}\left(\Gamma\frac{\partial\phi}{\partial x}\right) + \frac{\partial}{\partial y}\left(\Gamma\frac{\partial\phi}{\partial y}\right) + S_\phi = 0 \tag{5}$$

$$\int_{\Delta V}\frac{\partial}{\partial x}\left(\Gamma\frac{\partial\phi}{\partial x}\right)dx\,dy + \int_{\Delta V}\frac{\partial}{\partial y}\left(\Gamma\frac{\partial\phi}{\partial y}\right)dx\,dy + \int_{\Delta V} S_\phi\,dV = 0 \tag{6}$$

$$\left[\Gamma_e A_e\left(\frac{\partial\phi}{\partial x}\right)_e - \Gamma_w A_w\left(\frac{\partial\phi}{\partial x}\right)_w\right] + \left[\Gamma_s A_s\left(\frac{\partial\phi}{\partial x}\right)_s - \Gamma_n A_n\left(\frac{\partial\phi}{\partial x}\right)_n\right] + \bar{S}\Delta V = 0 \tag{7}$$

$$\Gamma_e A_e\frac{(\phi_E-\phi_P)}{\delta x_{PE}} - \Gamma_w A_w\frac{(\phi_P-\phi_W)}{\delta x_{WP}} + \Gamma_n A_n\frac{(\phi_N-\phi_P)}{\delta x_{PN}} - \Gamma_s A_s\frac{(\phi_P-\phi_S)}{\delta x_{SP}} + \bar{S}\Delta V = 0 \tag{8}$$

$$\bar{S}\Delta V = S_u + S_p\phi_P \tag{9}$$

Table 2. Coefficients of discretized form.

a_W	a_E	a_S	a_N	a_P
$\frac{\Gamma_w A_w}{\delta x_{WP}}$	$\frac{\Gamma_e A_e}{\delta x_{PE}}$	$\frac{\Gamma_s A_s}{\delta y_{SP}}$	$\frac{\Gamma_n A_n}{\delta y_{PN}}$	$a_W + a_E + a_S + a_N - S_p$

$$a_P\phi_P = a_W\phi_W + a_E\phi_E + a_S\phi_S + a_N\phi_N + S_u \tag{10}$$

"discretised_form" function works with DataFrame input which contains domain and boundary condition information. Equation 11 is used to calculate Sp values, Equation 12 is used to calculate aP values and Equation 13 is used to calculate Su values. Eventually, a DataFrame object is returned as output containing grid information and respective coefficients of discretization. Figure 10 is an example output of the "discretised_form" function.

$$S_{p_P} = S_{p_W} + S_{p_E} + S_{p_S} + S_{p_N} \quad (11)$$

$$a_P = a_W + a_E + a_S + a_N - S_p \quad (12)$$

$$S_{u_P} = S_{u_W} + S_{u_E} + S_{u_S} + S_{u_N} \quad (13)$$

6400×12 DataFrame

Row	ID	i	j	x	y	aW	aE	aS	aN	Sp	aP	Su
	Int64	Int64	Int64	Float64	Float64	Float64	Float64	Float64	Float64	Float64	Float64	Float64
1	1	1	1	0.01875	0.01875	0.0	10.0	0.0	10.0	-40.0	60.0	10926.0
2	2	2	1	0.05625	0.01875	10.0	10.0	0.0	10.0	-20.0	50.0	5463.0
3	3	3	1	0.09375	0.01875	10.0	10.0	0.0	10.0	-20.0	50.0	5463.0
4	4	4	1	0.13125	0.01875	10.0	10.0	0.0	10.0	-20.0	50.0	5463.0
5	5	5	1	0.16875	0.01875	10.0	10.0	0.0	10.0	-20.0	50.0	5463.0
⋮	⋮	⋮	⋮	⋮	⋮	⋮	⋮	⋮	⋮	⋮	⋮	⋮
6397	6397	77	80	2.86875	2.98125	10.0	10.0	10.0	0.0	-20.0	50.0	7463.0
6398	6398	78	80	2.90625	2.98125	10.0	10.0	10.0	0.0	-20.0	50.0	7463.0
6399	6399	79	80	2.94375	2.98125	10.0	10.0	10.0	0.0	-20.0	50.0	7463.0
6400	6400	80	80	2.98125	2.98125	10.0	0.0	10.0	0.0	-40.0	60.0	12926.0

6391 rows omitted

Figure 10. Output example of "discretised_form" function.

Last step before venturing towards iterative solution is to generate coefficients of matrices using discretised form of domain. Generating coefficients of matrices is basically writing down system of equations by cell number instead of neighbouring denotations. "coefficient_matrices" function merely transforms/rearranges discretised form of the domain.

"coefficient_matrices" function works with DataFrame input which contains grid information and respective coefficients of discretization. Equation 14 and Equation 15 show the output format of the matrices. Figure 11 is an example output of the "coefficient_matrices" function.

$$\begin{bmatrix} a_{11} & a_{12} & \dots & a_{1n} \\ a_{21} & a_{22} & \dots & a_{2n} \\ \vdots & \vdots & \ddots & \vdots \\ a_{n1} & a_{n2} & \dots & a_{nn} \end{bmatrix} \begin{bmatrix} \phi_1 \\ \phi_2 \\ \vdots \\ \phi_n \end{bmatrix} = \begin{bmatrix} b_1 \\ b_2 \\ \vdots \\ b_n \end{bmatrix} \quad (14)$$

$$A\,x = b \quad (15)$$

A

6400×6400 Matrix{Float64}:

60.0	-10.0	0.0	0.0	0.0	0.0	…	0.0	0.0	0.0	0.0	0.0
-10.0	50.0	-10.0	0.0	0.0	0.0		0.0	0.0	0.0	0.0	0.0
0.0	-10.0	50.0	-10.0	0.0	0.0		0.0	0.0	0.0	0.0	0.0
0.0	0.0	-10.0	50.0	-10.0	0.0		0.0	0.0	0.0	0.0	0.0
0.0	0.0	0.0	-10.0	50.0	-10.0		0.0	0.0	0.0	0.0	0.0
0.0	0.0	0.0	0.0	-10.0	50.0	…	0.0	0.0	0.0	0.0	0.0
0.0	0.0	0.0	0.0	0.0	-10.0		0.0	0.0	0.0	0.0	0.0
⋮					⋮	⋱	⋮				
0.0	0.0	0.0	0.0	0.0	0.0		-10.0	0.0	0.0	0.0	0.0
0.0	0.0	0.0	0.0	0.0	0.0	…	50.0	-10.0	0.0	0.0	0.0
0.0	0.0	0.0	0.0	0.0	0.0		-10.0	50.0	-10.0	0.0	0.0
0.0	0.0	0.0	0.0	0.0	0.0		0.0	-10.0	50.0	-10.0	0.0
0.0	0.0	0.0	0.0	0.0	0.0		0.0	0.0	-10.0	50.0	-10.0
0.0	0.0	0.0	0.0	0.0	0.0		0.0	0.0	0.0	-10.0	60.0

b

6400-element Vector{Float64}:

10926.0
5463.0
5463.0
5463.0
5463.0
5463.0
5463.0
⋮
7463.0
7463.0
7463.0
7463.0
7463.0
12926.0

Figure 11. Output example of "coefficient_matrices" function.

Iterative Solution Functions

Iterative solution functions based on iteration per sweep count were generated in order to properly engage in multigrid scheme exploration. Iterator function itself was assumed as Gauss-Seidel iterative method without modifications or relaxations. Equation 16 to Equation 20 summarizes Gauss-Seidel method used in iterative solutions (Axelsson, 1996).

$$A = L_* + U \quad (16)$$

$$L_* = \begin{bmatrix} a_{11} & 0 & \dots & 0 \\ a_{21} & a_{22} & \dots & 0 \\ \vdots & \vdots & \ddots & \vdots \\ a_{n1} & a_{n2} & \dots & a_{nn} \end{bmatrix} \quad (17a)$$

$$U = \begin{bmatrix} 0 & a_{12} & \dots & a_{1n} \\ 0 & 0 & \dots & a_{2n} \\ \vdots & \vdots & \ddots & \vdots \\ 0 & 0 & \dots & 0 \end{bmatrix} \quad (17b)$$

$$L_* x = b - Ux \quad (18)$$

$$x^{(k+1)} = L_*^{-1}(b - Ux^{(k)}) \quad (19)$$

$$x_i^{(k+1)} = \frac{1}{a_{ii}}\left(b_i - \sum_{j=1}^{i-1} a_{ij} x_j^{(k+1)} - \sum_{j=i+1}^{n} a_{ij} x_j^{(k)}\right)$$

$$i = 1,2,\dots,n \quad (20)$$

Iterator function works with matrices (A) and vectors (b, x) input and performs one iteration with Gauss-Seidel method. Intermediate solution vector (x) is returned as output of "gauss_seidel_iterate" function.

Iterative solution function for cycles works with matrices (A), vectors (b, x, r) and iteration count (ic) input and performs consecutive iterations. Example output of "iterate_solution_count_for_cycles" are given in Figure 12, Figure 13 and Figure 14. DataFrame object as seen in Figure 12 contains mean residual (R), standard deviation of residual (S) and time stamp (t) values of each iteration as columns. DataFrame object as seen in Figure 13 contains solution vectors of each iteration as columns. DataFrame object as seen in Figure 14 contains residual vectors of each iteration as columns.

8×3 DataFrame

Row	R	S	t
	Float64	Float64	Int64
1	274.729	12.0958	79943600
2	0.154425	0.563102	156054400
3	0.146266	0.517291	232470400
4	0.139211	0.478872	308532200
5	0.133032	0.446151	384623900
6	0.127562	0.41792	460654500
7	0.122675	0.393291	542912800
8	0.118274	0.371599	620959000

Figure 12. "iteration_history" output example of "iterate_solution_count_for_cycles" function.

6400×8 DataFrame

Row	x1	x2	x3	x4	x5	x6	x7	x8
	Float64	Float64	Float64	Float64	Float64	Float64	Float64	Float64
1	273.15	273.15	273.15	273.15	273.15	273.15	273.15	273.15
2	273.15	273.15	273.15	273.15	273.15	273.15	273.15	273.15
3	273.15	273.15	273.15	273.15	273.15	273.15	273.15	273.15
4	273.15	273.15	273.15	273.15	273.15	273.15	273.15	273.15
5	273.15	273.15	273.15	273.15	273.15	273.15	273.15	273.15
⋮	⋮	⋮	⋮	⋮	⋮	⋮	⋮	⋮
6397	358.2	358.755	359.208	359.586	359.906	360.18	360.418	360.626
6398	355.701	356.112	356.446	356.723	356.957	357.157	357.33	357.482
6399	348.046	348.291	348.49	348.655	348.794	348.913	349.017	349.107
6400	322.352	322.431	322.496	322.55	322.596	322.635	322.668	322.698

6391 rows omitted

Figure 13. "field_history" output example of "iterate_solution_count_for_cycles" function.

6400×8 DataFrame

Row	x1	x2	x3	x4	x5	x6	x7	x8
	Float64	Float64	Float64	Float64	Float64	Float64	Float64	Float64
1	272.15	0.0	0.0	0.0	0.0	0.0	0.0	0.0
2	272.15	0.0	0.0	0.0	0.0	0.0	0.0	0.0
3	272.15	0.0	0.0	0.0	0.0	0.0	0.0	0.0
4	272.15	0.0	0.0	0.0	0.0	0.0	0.0	0.0
5	272.15	0.0	0.0	0.0	0.0	0.0	0.0	0.0
⋮	⋮	⋮	⋮	⋮	⋮	⋮	⋮	⋮
6397	357.2	0.554634	0.453622	0.37796	0.319825	0.27419	0.237708	0.208083
6398	354.701	0.410606	0.334163	0.277349	0.233961	0.200071	0.173088	0.151249
6399	347.046	0.244645	0.199065	0.165214	0.139376	0.119198	0.103136	0.0901361
6400	321.352	0.0794711	0.0648093	0.0538891	0.0455332	0.0389943	0.0337793	0.0295523

6391 rows omitted

Figure 14. "residual_history" output example of "iterate_solution_count_for_cycles" function.

Intergrid Operations Functions

Initialization, restriction, prolongation and finalization are basic operations for any multigrid cycle. Initialization and finalization operations are covered with iterative solution functions. Restriction and prolongation operations require individual and complimentary functions. Thus, functions that changes the resolution of the solution were generated for multigrid cycles to use.

Restriction is basically downgrading the resolution. Geometric multigrid operations were assumed. Domain was assumed as rectangular in two dimensions. Grid was assumed cell centred, uniform and structured. Weighting method with linear interpolation was assumed. Equation 21 was used to calculate property values of cells at downgraded resolution. Figure 15 illustrates restriction operation in two dimensions.

$$C_{i,j}^{h+1} = \frac{1}{4}\left(C_{2i-1,2j-1}^{h} + C_{2i,2j-1}^{h} + C_{2i-1,2j}^{h} + C_{2i,2j}^{h}\right) \quad (21)$$

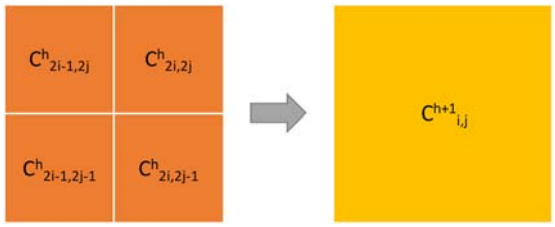

Figure 15. Restriction operation on two dimensions.

Coarsening function works with DataFrame object input that contains grid information (ID, i, j, x, y) and cell properties (T, r). Input is assumed to be compatible for a feasible restriction operation. When all cells are processed, function returns the DataFrame object populated with all individual cell information of the coarse grid. Figure 16 is an example output of the "restrict" function.

1600×7 DataFrame

Row	ID	i	j	x	y	T	r
	Int64	Int64	Int64	Float64	Float64	Float64	Float64
1	1	1	1	0.0375	0.0375	273.15	0.0
2	2	2	1	0.1125	0.0375	273.15	0.0
3	3	3	1	0.1875	0.0375	273.15	0.0
4	4	4	1	0.2625	0.0375	273.15	0.0
5	5	5	1	0.3375	0.0375	273.15	0.0
⋮	⋮	⋮	⋮	⋮	⋮	⋮	⋮
1597	1597	37	40	2.7375	2.9625	331.586	0.0208765
1598	1598	38	40	2.8125	2.9625	331.586	0.0208765
1599	1599	39	40	2.8875	2.9625	331.191	0.0199269
1600	1600	40	40	2.9625	2.9625	315.864	0.00838497

1591 rows omitted

Figure 16. Output example of "restriction" function.

Prolongation is basically upgrading the resolution. Geometric multigrid operations were assumed. Domain was assumed as rectangular in two dimensions. Grid was assumed cell centred, uniform and structured. Linear interpolation was assumed. Equation 23 was derived by distributing Equation 22 and by arranging the expression. Equations 23 to 26 are used to calculate property values of cells at upgraded resolution. Figure 17 illustrates prolongation operation in two dimensions. Uppercase letters denote coarse grid cells while lowercase letters denote fine grid cells.

$$a = \frac{1}{4}\left(A + \frac{A+B}{2} + \frac{A+C}{2} + \frac{A+B+C+D}{4}\right) \quad (22)$$

$$a = \frac{1}{16}(9A + 3B + 3C + D) \quad (23)$$

$$b = \frac{1}{16}(3A + 9B + C + 3D) \quad (24)$$

$$c = \frac{1}{16}(3A + B + 9C + 3D) \quad (25)$$

$$d = \frac{1}{16}(A + 3B + 3C + 9D) \quad (26)$$

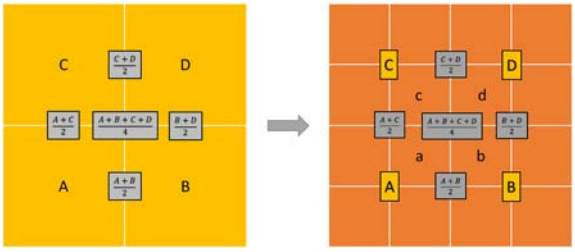

Figure 17. Prolongation operation on two dimensions.

Prolongation function works with boundary condition input in addition to DataFrame object input that contains grid information (ID, i, j, x, y) and cell properties (T, r) while calling "face_and_node_values" function to generate necessary additional information. "face_and_node_values" function calculates neighbouring cell, face and node information while respecting boundary conditions. Input is assumed to be compatible for a feasible prolongation operation. When all cells are processed, function returns the DataFrame object populated with all individual cell information of the fine grid. Figure 18 is an example output of the "prolong" function.

25600×7 DataFrame

Row	ID	i	j	x	y	T	r
	Int64	Int64	Int64	Float64	Float64	Float64	Float64
1	1	1	1	0.009375	0.009375	273.15	0.0
2	2	2	1	0.028125	0.009375	273.15	0.0
3	3	3	1	0.046875	0.009375	273.15	0.0
4	4	4	1	0.065625	0.009375	273.15	0.0
5	5	5	1	0.084375	0.009375	273.15	0.0
⋮	⋮	⋮	⋮	⋮	⋮	⋮	⋮
25597	25597	157	160	2.93437	2.99062	360.068	0.00352723
25598	25598	158	160	2.95312	2.99062	357.477	0.00257343
25599	25599	159	160	2.97187	2.99062	351.602	0.00155082
25600	25600	160	160	2.99062	2.99062	322.693	0.000514068

25591 rows omitted

Figure 18. Output example of "prolongation" function.

Multigrid Scheme Functions

Running an iterative solution with any multigrid cycle requires working algorithms on convenient data structure. Although algorithms may vary, consistent data structure enables fair comparison between cycles/algorithms. Accessibility to recordings of solution progress is another rationale to have a practical data structure. Table 3 summarizes the columns of the DataFrame object that records run of a multigrid cycle/algorithm with brief explanations. Some of the columns may be seen as excessive in terms of computational cost, however accessibility and practicality of available information reduced the efforts towards tool development and result generation.

Excluding columns of DataFrame objects containing field and history information enables summarizing run history in a compact fashion. Figure 19 is an example to a run history that summarizes what transpires during a multigrid cycle.

Execution of any multigrid cycle is consisted of calling finite volume method and iterative solution functions while steering through resolution levels. Any multigrid cycle goes through initialization, resolution change (restriction and prolongation), iterative solution sweeps at multigrid levels and finalization activities. Figure 20 illustrates conceptual flowchart of any multigrid cycle run. Initialization and finalization activities are at initial resolution level and does not require additional functions rather than iterative solution functions. Pre-process and initial generation of data structure activities were merged under a function. Resolution changes, iteration sweeps, monitoring, conditioning, steering and other complimentary activities of multigrid cycles were merged including initialization and finalization under a function. Post-process of the run was not included within the multigrid algorithms.

10×11 DataFrame

Row	step	level	n_cell	nx	ny	initial_residual	final_residual	iteration_count	iteration_duration	operation_duration	FVM_duration
	Int64	Int64	Int64	Int64	Int64	Float64	Float64	Int64	Int64	Int64	Int64
1	1	0	6400	80	80	1.0	1.0	1	0	116400	23529600
2	2	0	6400	80	80	1.59544	0.316303	3	257544000	4800	34509400
3	3	1	1600	40	40	0.464135	0.503073	3	17744200	128600	3211300
4	4	2	400	20	20	0.845009	0.88932	3	1526200	90100	867800
5	5	3	100	10	10	1.48021	1.48271	3	269500	36100	369900
6	6	4	25	5	5	2.21309	1.88699	3	103200	37300	184100
7	7	3	100	10	10	1.39117	0.312344	3	328200	419400	281400
8	8	2	400	20	20	0.272293	0.0745363	3	1946500	771700	712800
9	9	1	1600	40	40	0.0675594	0.0198555	3	19569800	2443200	3514000
10	10	0	6400	80	80	0.0182567	0.0054156	3	258939500	11056700	32870300

Figure 19. Example to a run history of a multigrid cycle.

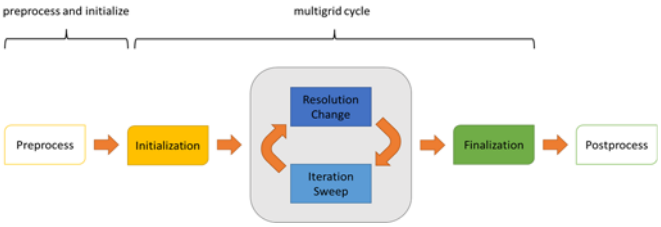

Figure 20. Conceptual flowchart of a multigrid run.

Table 3. Columns of DataFrame object that records the run.

Column	Data Type	Explanation
step	Integer	Steps of the run.
level	Integer	Resolution level of each step.
n_cell	Integer	Number of cells for the resolution on each step.
nx	Integer	Number of divisions in first direction for each step.
ny	Integer	Number of divisions in second direction for each step.
initial_residual	Float	Initial mean residual value at the beginning of each step.
final_residual	Float	Final mean residual value at the end of each step.
iteration_count	Integer	Iteration count for each step.
iteration_duration	Integer	Elapsed time while iterating the solution for each step.
operation_duration	Integer	Elapsed time while executing intergrid (restriction or prolongation) operations preceding finite volume method functions for each step.
FVM_duration	Integer	Elapsed time while executing finite volume method functions preceding iterations for each step.
initial_field	DataFrame	Initial field information (ID, i, j, x, y, T, r) at the beginning of each step.
final_field	DataFrame	Final field information (ID, i, j, x, y, T, r) at the end of each step.
iteration_history	DataFrame	Iterative solution history of mean residual (R), standard deviation of residual (S) and time stamps of each step.
field_history	DataFrame	Solution vector history of iterative solution of each step.
residual_history	DataFrame	Residual vector history of iterative solution of each step.

Every run starts with pre-process activities that generates grid upon domain input while specifying boundary conditions and solver model. Since solver model is predefined with study scope, generating grid and executing initial finite volume method operations are assumed to be the pre-process of multigrid cycles.

Creating container of run data as described in Table 3 and storing initialization phase completes preparation towards execution of multigrid cycles.

Creating algorithms to execute multigrid cycles with predefined patterns are straightforward in terms of complexity. Multigrid cycles with fixed conceptual patterns vary with the iteration count of sweeps on resolution levels in addition to desired or maximum coarsening level.

Multigrid cycle that follows fixed V pattern as illustrated in Figure 1 belongs to the μ cycle family (Briggs et al., 2000). Constant number of iterations per sweep was assumed for resolution levels. Maximum coarsening level was assumed as the maximum feasible level for multigrid methods works. Initialization phase and finalization phase was assumed to be included in the iterations on initial resolution level.

"run_fixed_V_cycle" function works with initialized data structure, boundary conditions, desired coarsening level and number of iteration per sweep input. Initialized data is copied to be later populated with run data. Maximum coarsening level is determined using a complimentary function that checks if desired coarsening level is feasible and assigns maximum possible level instead if it is not. Once maximum coarsening level is set, an array is generated that holds the sequential resolution levels of the cycle. For loop is executed for the level values in the array. Within the for loop; resolution change operations are carried out according to level direction; values of step, number of cells, number of divisions are assigned; finite volume method functions are called for the field on process; iterative solution function for cycles is called according to input; data structure is populated with the information of each step. Finalization phase of multigrid cycle inherently included with the iterative solution of the field on initial resolution at the end of the cycle. Eventually, "run_fixed_V_cycle" function returns DataFrame that contains run data as output. Figure 21 is an example output of the "run_fixed_V_cycle" function.

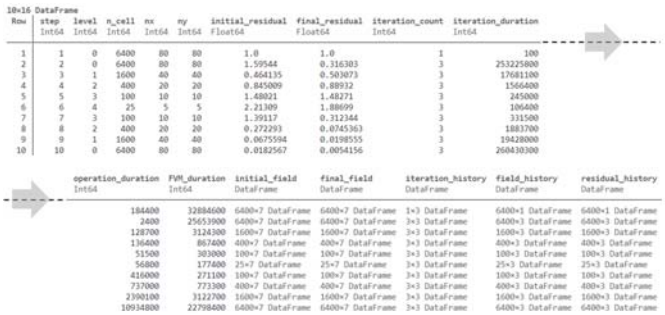

Figure 21. Output example of "run_fixed_V_cycle" function.

"run_fixed_W_cycle" and "run_fixed_F_cycle" functions are exactly same as "run_fixed_V_cycle" besides the sequence of grid resolutions which is also called pattern or scheme. They work with same type of inputs while generating same type of output.

RESULTS

Results were presented with increasing complexity starting with validation of the tools (procedures) at disposal. Validation pack serves the answer to the question "do procedures get to correct solution?". Parameter explorations were conducted to answer to questions "which parameters effect the way and/or the cost to solution?".

In order to fairly compare performances of different multigrid cycles as well as same one with differing input parameters an objective indicator should be defined. Even though there was a cost definition (Briggs et al., 2000) called "work unit" based on memory allocation for iterative methods applicable to multigrid cycles, a new and more comprehensive concept was suggested. This new concept, was also inspired by "work unit" definition was called "reference work unit" which is defined as the elapsed time of performing one iteration on the finest grid. Time cost inherently includes any varying parameter of

the environment, algorithm and system that multigrid cycle works on. Time cost also includes the energy cost to power the computer system during the process. Thus, measuring computational cost in terms of elapsed time was seen as much more convenient and comprehensive for comparing performance of multigrid cycles.

Validation

Two-dimensional thermal diffusion problem on a homogenous plate was selected for the reference case which may have constant temperature and constant heat flux at boundaries. Selecting thermal diffusion case which has analytical Laplace solution as reference inherently enabled proper validation of methods.

Thermal diffusion case has constant temperature and constant heat flux at boundaries (Patil and Prasad, 2014). Thermal coefficients and thickness are constant within the homogenous plate (Patil and Prasad, 2014). Reference case has certain dimensions on both directions (Patil and Prasad, 2014). Number of divisions of the domain were specifically selected to clearly present results before exploring higher grid resolutions.

Figure 22 was given to illustrate the reference case. Thermal conductivity was assumed constant as 1000 W/mK within the homogenous plate (Patil and Prasad, 2014). Thickness of the plate was assumed constant as 1cm (Patil and Prasad, 2014). Thermal diffusion case has constant temperature values at boundaries West, East, South and North as 0 °C, 0 °C, 0 °C and 100 °C respectively. Reference case has dimensions of 3m in both directions. Reference domain was generated with 80 division of cells in both directions.

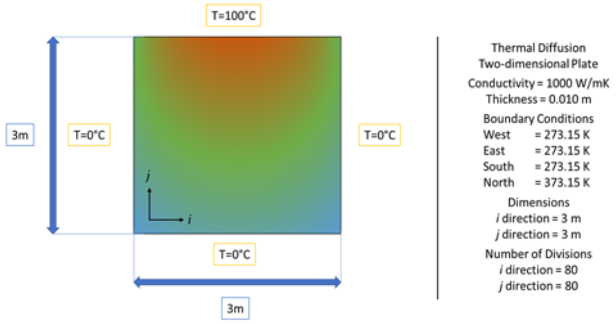

Figure 22. Illustration of the reference case definition.

Thermal diffusion case can be solved by Laplace transform using boundary conditions (Patil and Prasad, 2014). Equation 29 was used to generate temperature solutions within the domain at any location (Patil and Prasad, 2014).

$$\nabla^2 u = \frac{\partial^2 u}{\partial x^2} + \frac{\partial^2 u}{\partial y^2} = 0 \quad x = [0, a]\ ;\ y = [0, b] \tag{27}$$

$$u(0, y) = 0°C\ ; u(a, y) = 0°C \tag{28a}$$

$$u(x, 0) = 0°C\ ; u(x, b) = 100°C \tag{28b}$$

$$u(x, y) = \frac{400\ °C}{\pi} \sum_{k=1}^{\infty} \frac{sin\left(\frac{n\pi x}{a}\right) sinh\left(\frac{n\pi y}{b}\right)}{n sinh(n\pi)} \qquad n = 2k - 1 \tag{29}$$

Field contour plot was given in Figure 23 to illustrate exact solution of the case. Since solution is exact and residual is practically zero; analytical solution of the case can be used to measure any error within the domain which are generated by other numerical methods.

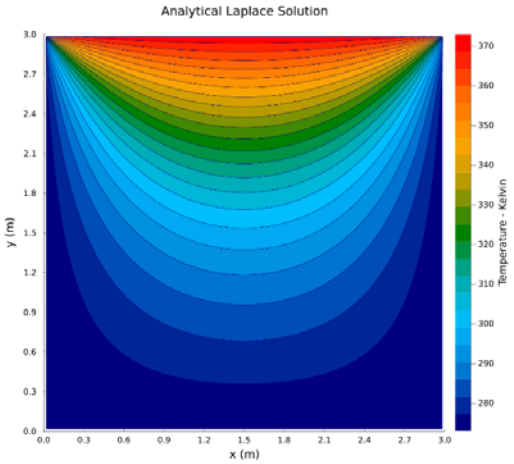

Figure 23. Analytical Laplace solution field contour plot of the reference case.

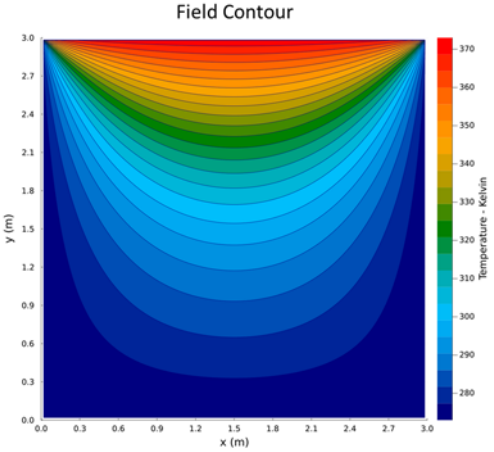

Figure 24. Direct iterative solution field contour plot (left) and residual scatter (right) plot of the reference case.

Reference case was solved via Gauss-Seidel iterative method as described after preprocessing the input by finite volume method functions. Constant initial guess value was given to the domain. Constant initial guess value was calculated as 298.15 °K by averaging temperature values of boundary conditions. Acceptable results were obtained when mean residual value was at 0.001 (°K) mean residual and was reached after 1028 iterations.

Field contour plot and residual scatter plot were given in Figure 24 to illustrate direct iterative solution and residual distribution of the reference case for a qualitative validation. Even though convergence criterion was fairly precise, uneven distribution of residual values was apparent as seen in Figure 24 for direct iterative solution. Figure 26 was given to illustrate temperature and error values over a diagonal line, a horizontal line and a vertical line as described in Figure 25 for quantitative validation of solution.

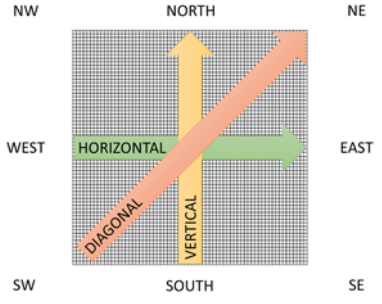

Figure 25. Data extraction lines for validation figures.

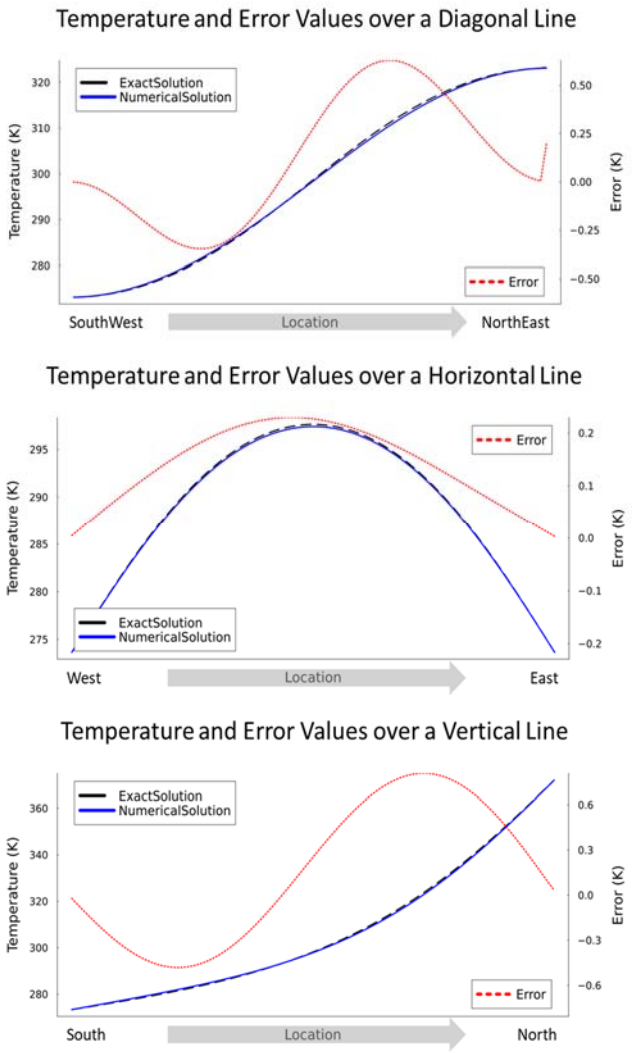

Figure 26. Validation figures of solutions regarding temperature and error values.

Verification

It is imperative to show that methods and procedures generate output changing with varying input. In order to verify that methods and code works with varying input, different sets of boundary conditions were applied to reference case.

Code accepts Dirichlet and Neumann boundary conditions for the thermal diffusion case. Dirichlet boundary conditions were given as temperature values in the unit of Kelvin. Neumann boundary conditions were given as heat flux values in the unit of Watts.

Randomized boundary condition values were selected from arrays of; 200, 300, 400, 500 °K for Dirichlet and -2000, -1500, -1000, 500, 0, 500, 1000, 1500, 2000 W for Neumann; to each West, East, South and North boundaries. Numerous solutions were generated with the runs using randomized boundary conditions in order to check if methods and/or procedures fail at some. No failures were returned for over hundred cases which verified that methods and procedures work with various boundary conditions. Examples of field contours to such solutions were given in Figure 27 and Figure 28 to emphasize that methods and procedures were capable of generating varying solutions with varying input.

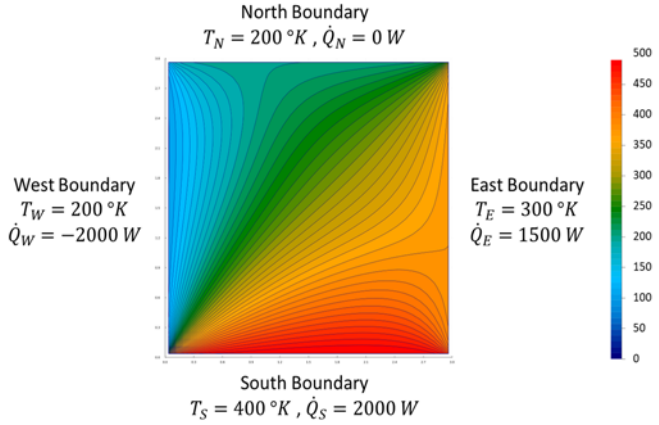

Figure 27. Example #1 of field contour plot to randomized boundary condition cases.

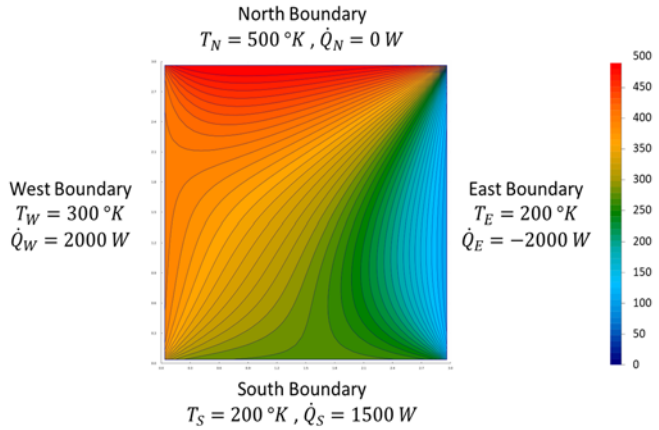

Figure 28. Example #2 of field contour plot to randomized boundary condition cases.

Parameters of Cycles

Verification of finite volume methods and iterative solution proceeded with multigrid cycle runs for varying input parameters. Multigrid cycles with fixed schemes (V, W, F) were explored around maximum coarse grid level and iterations per sweep. Restriction beyond maximum coarse grid level was infeasible and/or was limited. Iterations per sweep value was the iteration count of solution on each step of multigrid cycle. Exploration was designed to generate cost and convergence values with varying maximum coarse grid level and iteration per sweep. Each multigrid cycle was explored separately.

Maximum coarse grid levels were selected as 2, 3, 4, 5 to capture the effect on cost and convergence. Initial grid resolution was selected as 160x160, so minimum grid resolutions are 40x40, 20x20, 10x10, 5x5 respectively. Iterations per sweep values were selected as 1, 2, 3, 4, 5 to capture parameters for minimal cost at acceptable convergence.

Metrics of the exploration of V, W and F cycle that varied maximum coarse grid level and iterations per sweep were given in Table 4 to Table 9 for cost and convergence respectively. Response surface and contour plot of the exploration of V cycle were given in Figure 29 to Figure 34 to visualise exploration metrics for cost and convergence respectively.

Table 4. Exploration metrics of V cycle with varying maximum coarse level and iterations per sweep regarding cost in reference work unit.

Cost in RWU				Iterations per Sweep				
				1	2	3	4	5
Max. Coarse Level	2	Min. Grid Res.	40x40	2.996	5.119	7.241	9.512	11.530
	3		20x20	2.974	5.110	7.246	9.405	11.510
	4		10x10	2.959	5.137	7.231	9.397	11.541
	5		5x5	2.979	5.116	7.253	9.410	11.540

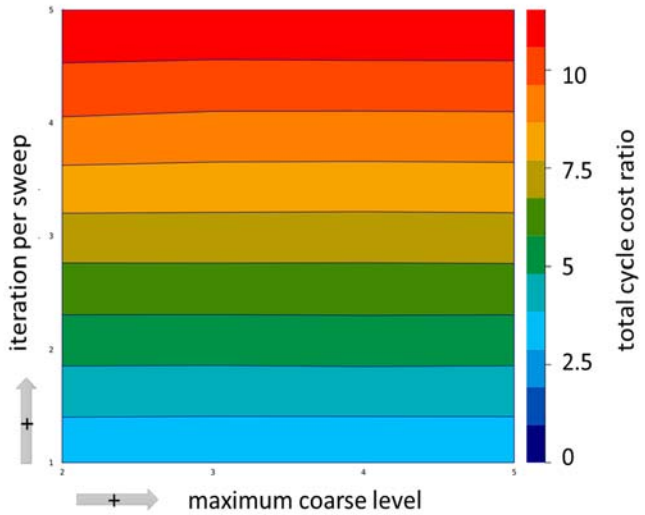

Figure 29. Contour plot of cost in reference work unit for exploration of V cycle.

Table 5. Exploration metrics of V cycle with varying maximum coarse level and iterations per sweep regarding convergence level of mean residual.

Convergence Level (Mean Residual)				Iterations per Sweep				
				1	2	3	4	5
Max. Coarse Level	2	Min. Grid Res.	40x40	~~2.45719~~	0.04608	0.03634	0.03056	0.02663
	3		20x20	~~3.55250~~	0.01975	0.01492	0.01204	0.01007
	4		10x10	~~5.52550~~	0.00703	0.00448	0.00300	0.00205
	5		5x5	~~6.83194~~	0.00137	0.00070	0.00048	0.00038

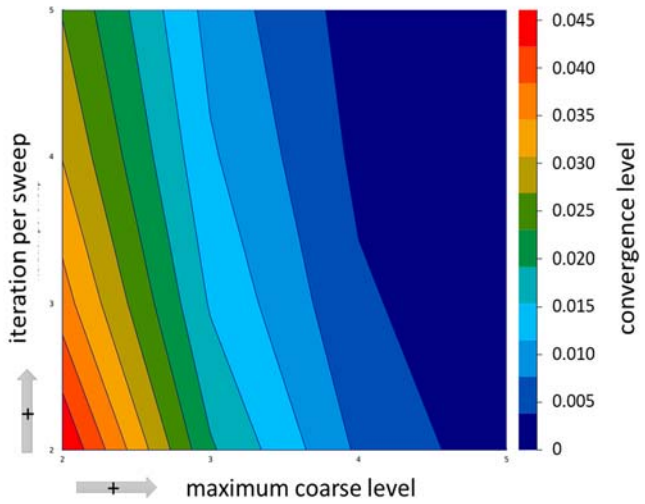

Figure 30. Contour plot of convergence of mean residual for exploration of V cycle.

Table 6. Exploration metrics of W cycle with varying maximum coarse level and iterations per sweep regarding cost in reference work unit.

Cost in RWU				Iterations per Sweep				
				1	2	3	4	5
Max. Coarse Level	2	Min. Grid Res.	40x40	3.523	5.593	7.953	10.334	12.671
	3		20x20	3.083	5.320	7.582	9.776	12.050
	4		10x10	3.083	5.300	7.523	9.770	11.972
	5		5x5	3.091	5.275	7.544	9.742	11.990

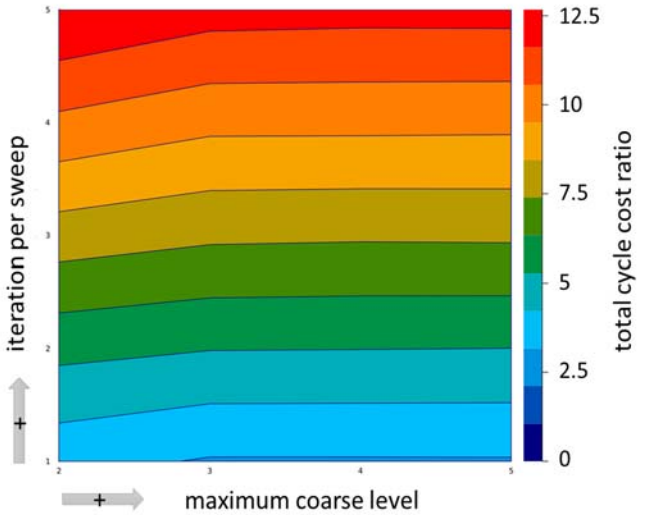

Figure 31. Contour plot of cost in reference work unit for exploration of W cycle.

Table 7. Exploration metrics of W cycle with varying maximum coarse level and iterations per sweep regarding cost in reference work unit.

Convergence Level (Mean Residual)				Iterations per Sweep				
				1	2	3	4	5
Max. Coarse Level	2	Min. Grid Res.	40x40	~~2.88776~~	0.02155	0.01660	0.01359	0.01152
	3		20x20	~~4.24468~~	0.00748	0.00494	0.00342	0.00242
	4		10x10	~~5.27066~~	0.00138	0.00068	0.00046	0.00036
	5		5x5	~~3.41220~~	0.00091	0.00064	0.00048	0.00039

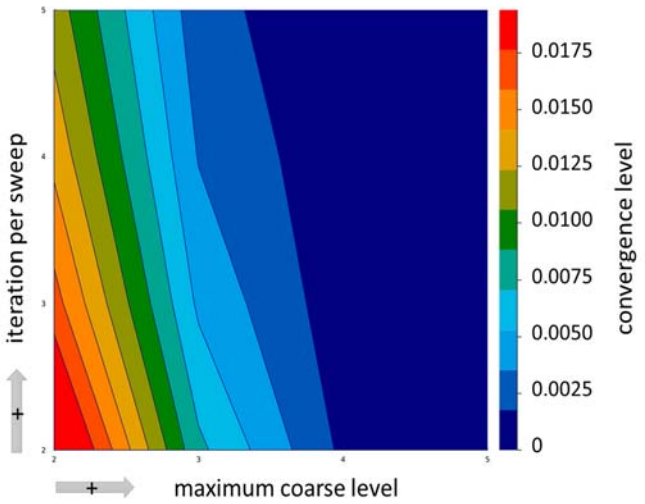

Figure 32. Contour plot of convergence of mean residual for exploration of W cycle.

Table 8. Exploration metrics of F cycle with varying maximum coarse level and iterations per sweep regarding cost in reference work unit.

Cost in RWU				Iterations per Sweep				
				1	2	3	4	5
Max. Coarse Level	2	Min. Grid Res.	40x40	3.062	5.260	7.485	9.668	11.885
	3		20x20	3.082	5.339	7.541	9.773	12.012
	4		10x10	3.075	5.325	7.562	9.789	11.999
	5		5x5	3.106	5.337	7.563	9.781	12.028

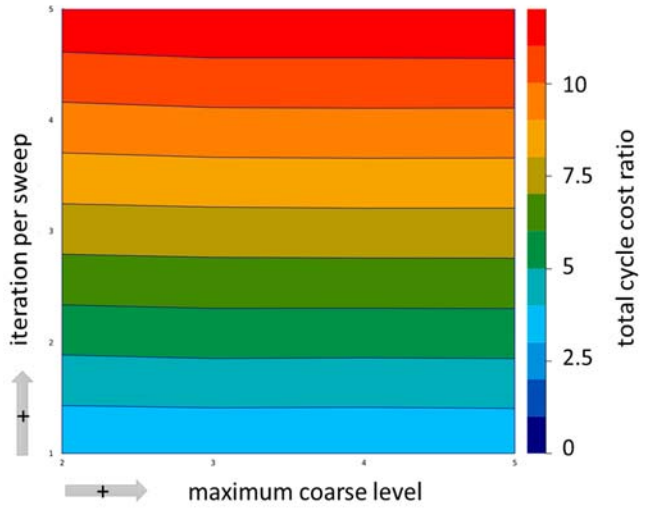

Figure 33. Contour plot of cost in reference work unit for exploration of F cycle.

Table 9. Exploration metrics of F cycle with varying maximum coarse level and iterations per sweep regarding cost in reference work unit.

Convergence Level (Mean Residual)				Iterations per Sweep				
				1	2	3	4	5
Max. Coarse Level	2	Min. Grid Res.	40x40	~~2.55164~~	0.03227	0.02530	0.02110	0.01823
	3		20x20	~~4.27735~~	0.00930	0.00644	0.00470	0.00352
	4		10x10	~~5.28459~~	0.00128	0.00065	0.00045	0.00036
	5		5x5	~~2.68124~~	0.00092	0.00064	0.00048	0.00039

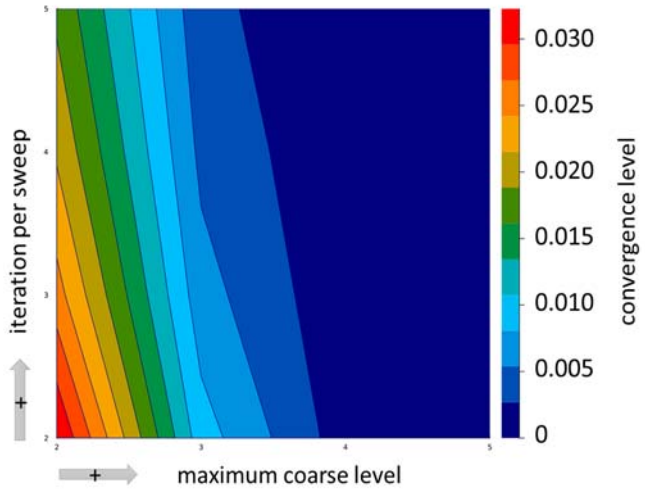

Figure 34. Contour plot of convergence of mean residual for exploration of F cycle.

Even though numbers do slightly change, explorations of V, W and F multigrid cycles resulted with same inferences. Single iterations per sweep generated unacceptable solutions as seen in Table 5, Table 7 and Table 9 regarding convergence levels of mean residual. Results of single iterations per sweep was also not comparable with other results of iterations per sweep and were excluded from illustrations.

Cost in reference work unit was directly proportional to iterations per sweep while maximum coarse level had little or no effect on cost. Convergence level of mean residual improved with increasing maximum coarse grid level. Although iterations per sweep had an effect on convergence, maximum coarse level was dominant factor relatively on convergence.

Comparison

Following the exploration of parameters (iteration per sweep and maximum coarse level) of multigrid cycles of fixed schemes; reference values for input parameters were set in order to present comparison results. Considering the exploration results of domain with 160x160 cells, it is observed that; for the grid resolution with 160x160 cells, 2 iteration per sweep and 5 coarsening was indeed satisfactory, regarding the convergence level. Since 2 was also the minimum number of iterations per sweep, differing values of input parameters were selected for comparison in order to include iteration per sweep contribution.

Comparison metrics are given in Table 10 with number of iterations per sweep as 5 and maximum coarse level as 5, while Figure 35 illustrates comparison of the residual distribution across the domain with 80x80 number of cells. Residual scatter plot given in Figure 35 was generated by marking all cells with higher than convergence target with red colour, thus enabling to filter how many cells actually converged rather than settling with monitoring mean residual.

First of all, multigrid cycles cost incredibly low compared to direct iterative solution. Multigrid cycles also performed significantly better compared to direct iterative method in terms of residual distribution while having approximately similar mean residual levels. Multigrid V, W and F cycle solutions appeared comparably same regarding residual distributions as well as mean residual levels.

Table 10. Comparison metric of Direct Iterative and Multigrid Cycle solutions.

	Direct Iterative	V Cycle	W Cycle	F Cycle
(Operation, Iteration) Count	(1, 1028)	(10, 45)	(20, 95)	(22, 105)
Mean Residual Convergence Level	0.001	0.00117	0.00122	0.00122
Converged Cell Number Percentage	54.6%	71.1%	72.4%	72.4%
Cost in Reference Work Units	1028.29	12.56	12.96	13.12
Cost with respect to Direct Iterative	100%	1.22%	1.26%	1.28%

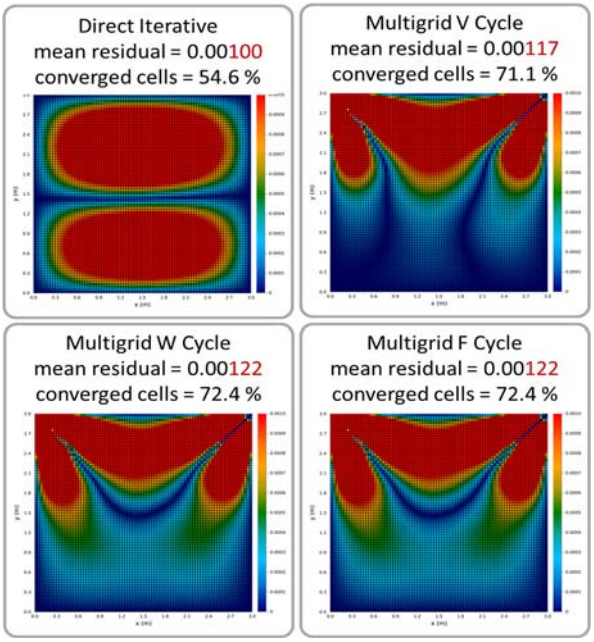

Figure 35. Comparison of converged cells of direct iterative and multigrid cycle solutions.

Figure 36 was given to illustrate residual progress with respect to computational cost while comparing direct iterative solution with multigrid cycle solutions. Figure 36 was designed with three frames with different zoom levels. At the first frame with logarithmic x axis, it is apparent that all multigrid cycles cost much less compared to direct iterative solutions regardless of the scheme. At the second frame, differences in effectivity between finest and coarser grid levels are emphasized while still comparing with the direct iterative solution progress. At the third frame, differences in solution progress between varying multigrid cycles are made visible.

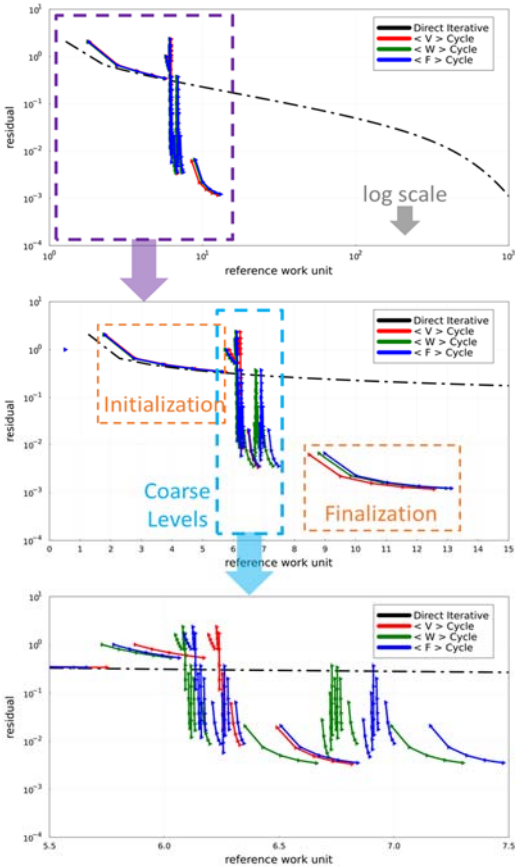

Figure 36. Effectivity of multigrid cycles compared to direct iterative method.

When compared, it was confirmed that residual progress with respect to computational cost curves found with study is indeed similar to literature (Brandt, 1973) as given in Figure 37 below.

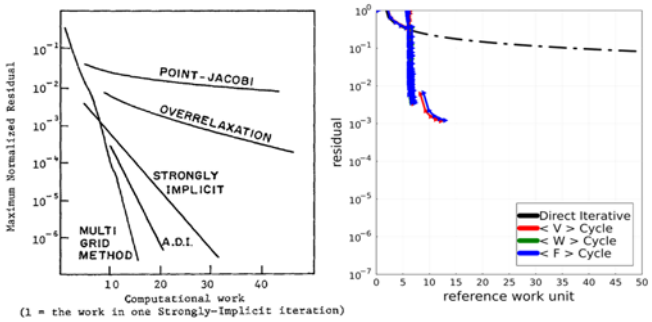

Figure 37. Effectivity of various methods (Brandt, 1973) (left) compared to study results (right).

Considering limitation of number of iterations per sweep, a unit cycle can be defined to generate reference values for minimum cost at fallout performance (convergence). Unit cycle was defined with V cycle scheme having minimum number of (2) iterations per sweep and maximum coarsest grid resolution level possible. Defining such reference enabled fair comparison of different multigrid cycles. Figure 38 was given to illustrate the metrics of the unit cycle for the reference case.

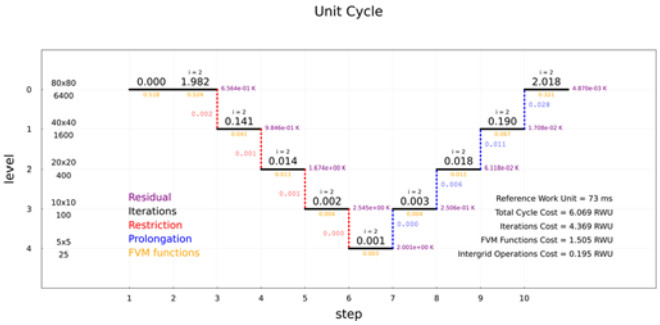

Figure 38. Detailed illustration of metrics of the unit cycle of the reference case.

Essential metrics of the results were given in Table 11 which presents clear inferences. All multigrid cycles at given input parameters performed comparably same while costing comparably same too. W and F cycle solutions may be slightly favorable considering residual distribution as seen in Figure 35. Intergrid operations and Finite Volume Methods costs consisted of approximately 12.5% of the total cost for all cycles. Iteration cost consisted almost 87.5% of the total cost for all cycles. Iterations on initialization and finalization phases cost the most of all as seen in Figure 36. Most of the effective work towards convergence was carried out on coarse grid resolutions. Iterations on initial grid resolution was also found to be the least effective in terms of convergence per computational cost. Figure 39 was given to illustrate residual progress with respect to computational cost while comparing unit cycle with multigrid cycles. Figure 40 was given to illustrate residual progress with respect to operation/iteration count in order to clearly present the scheme comparison of multigrid cycles.

Table 11. Multigrid cycle performance data compared to unit cycle.

COST	Unit Cycle	V Cycle	W Cycle	F Cycle
Intergrid Operations (RWU)	0.195	0.216	0.267	0.289
Finite Volume Method (RWU)	1.505	1.465	1.338	1.399
Iterative Solution (RWU)	4.369	10.881	11.359	11.435
Total (RWU)	6.069	12.561	12.964	13.123
Total (% of Unit Cycle)	100%	207%	214%	216%
Convergence (mean residual)	0.00487	0.00117	0.00122	0.00122

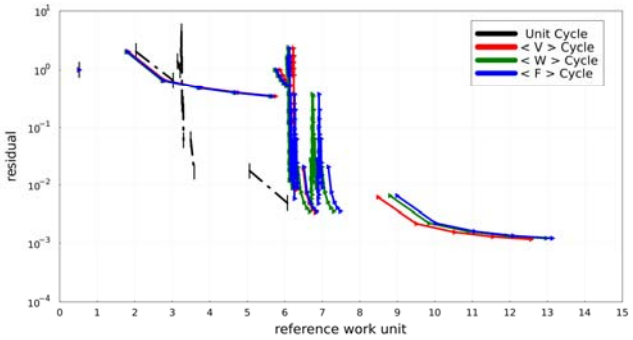

Figure 39. Multigrid cycle performance comparison plot with respect to reference work unit.

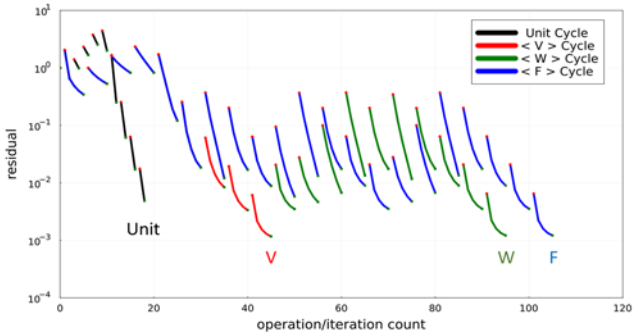

Figure 40. Multigrid cycle performance comparison plot with respect to operation/iteration count.

CONCLUSION

Simplifying a heat transfer problem with appropriate assumptions and modelling the problem over a two-dimensional domain and solving the problem with numerical methods would certainly provide advantages while also providing acceptable solution accuracy. One of the main drivers to simplify a case would be motivated by an optimization or exploration of parameters regarding a design or a process. Since the rationale of simplification is to get solutions from many runs as possible, any further convergence acceleration technique over numerical methods would be invaluable. Multigrid methods offer exceptional contribution to convergence acceleration of numerical methods while keeping solution accuracy intact if not better.

Multigrid cycles with fixed schemes proved to have incredibly reduced cost while having comparably same convergence level compared to direct iterative counterparts. Although the iterations on finest grid level seemed to have similar convergence rate compared to direct iterative counterpart; iterations on coarser grid levels had extremely high rate of convergence rate. It is imperative to state that most of the useful work towards convergence are carried out at coarse grid levels for multigrid cycle solutions. Cost reduction down to 1% of direct iterative solution infers that up to 100 more cases or parameter sets can be solved at the same time and/or computational cost.

Cost and convergence levels of multigrid cycles with fixed schemes were explored with varying iterations per sweep and maximum coarse grid level. Exploration of multigrid cycles with fixed schemes revealed that there is a minimum number of iterations per sweep for an acceptable solution accuracy. Iteration per sweep values lower than the minimum limit ended up with unacceptable solutions. Multigrid cycle cost increased with iterations per sweep while maximum coarse level did not affect cost. Little or no cost increase observed with increasing maximum coarse level parameter; because of the very nature of iterative solution which is in fact that solution cost increases with number of elements to be solved within the domain. Since coarser grid levels inherently have much smaller number of elements than finest grid level, it had almost no impact at cost. On the other hand, maximum coarse level was founded much more effective than iterations per sweep to obtain better convergence levels. It is because of the simple fact that convergence rate of solution at coarser grid levels are higher than finer grid levels. Furthermore, this effect is amplified exponentially with each consequent coarser grid level. Shortly, most of the computational work is done at minimal cost at coarse grid levels, while prolonging to finest grid level provides accurate solution.

Unit multigrid cycle was defined as a reference according to the results of the exploration of cycles with fixed schemes. Unit multigrid cycle was used to compare multigrid cycles within each other. Comparison results showed that establishing a reference baseline for cycles was indeed useful. Rationale beneath the utility of the unit cycle definition was the reference work unit definition. Reference work unit definition served as a non-dimensional cost indicator for any multigrid cycle. Reference work unit is now confidently suggested as an indicator to computational cost and proved to be simple yet comprehensive.

Effectivity of the multigrid cycles may be defined as convergence per cost at conceptual level. Uncontrollable and/or nuisance factors such as operating system, library performance, data structure, computational power; was blocked by the reference work unit definition. Thus, using the non-dimensional cost indicator enabled fair comparison of effectivity of multigrid cycles with fixed schemes. Although all of the (V, W, F) cycles performed similarly, slight nuances were observed. W and F cycles that traverse more through coarser grid levels ended up with slightly more evenly distributed residual across the domain; at a negligible computational cost compared to V cycle. In any situation, employing multigrid cycles with any scheme was proved extremely beneficial for iterative solution of heat transfer problems at two-dimensional domain, compared direct iterative methods.

Convection with a pressure-velocity coupling algorithm may be the first improvement to the code suite. Domains with varying dimensions (1D, 2D, 3D) would be a great addition to the tool. FVM methods that could operate on non-uniform grids will enhance applicability to complex geometries. Irregular or innovative multigrid schemes may be an interesting subject to study.

REFERENCES

Alpman, E. (2012). Blast Wave Simulations Using Euler Equations and Adaptive Grids, *Journal of Thermal Sciences and Technology*, 32 (2), 1-9.

Annaratone, D. (2010). *Engineering Heat Transfer*, Springer.

Arnone, A., Sestini, A. (1991). Multigrid Heat Transfer Calculations Using Different Iterative Schemes, *Numerical Heat Transfer, Part B: Fundamentals: An International Journal of Computation and Methodology*, 19 (1), 1-11.

Axelsson, O. (1996) *Iterative Solution Methods*, Cambridge University Press.

Aydar, E., Ekmekçi, İ. (2012). Thermal Efficiency Estimation of the Panel Type Radiators with CFD Analysis, *Journal of Thermal Sciences and Technology*, 32 (2), 63-71.

Aykan, F.S., Dursunkaya, Z. (2008). İki Boyutlu Yüzeylerde Isıl Aşınma Sayısal Analizi, *Isı Bilimi ve Tekniği Dergisi*, 28 (1), 43-49.

Bali, T. (2006). Numerical Analysis of Laminar and Turbulent Swirl Flows, *Journal of Thermal Sciences and Technology*, 26 (1), 1-8.

Brandt, A. (1973). Multi-level Adaptive Technique (MLAT) for Fast Numerical Solution to Boundary Value Problems, *Lecture Notes on Physics*, 18, Springer.

Brandt, A., Livne, O.E. (2011). *Multigrid Techniques: 1984 guide with applications to fluid dynamics*, Society for Industrial and Applied Mathematics.

Briggs, W.L., Henson, V.E., McCormick, S.F. (2000). *A Multigrid Tutorial*, Society for Industrial and Applied Mathematics.

Dawood, A.S., Burns, P.J (1992). Steady Three-Dimensional Convectivie Heat Transfer in A Porous Box Via Multigrid, *Numerical Heat Transfer, Part A: Applications: An International Journal of Computation and Methodology*, 22 (2), 167-198.

Doğan, A., Akkuş, S., Başkaya, Ş. (2012). Numerical Analysis of Natural Convection Heat Transfer from Annular Fins on a Horizontal Cylinder, *Journal of Thermal Sciences and Technology*, 32 (2), 31-41.

Galante, G., Rizzi, R.L. (2007). A Multigrid-Schwarz Method for the Solution of Hydrodynamics and Heat Transfer Problems in Unstructured Meshes, *19th International Symposium on Computer Architecture and High Performance Computing*, 87-94.

Internet, (2023). The Julia Programming Language, *Julia Micro-Benchmarks*, https://julialang.org/benchmarks/

Karaaslan, S., Hepkaya, E., Yücel, N. (2013). CFD Simulation of Longitudinal Ventilation Systems in a Scaled Short Tunnel, *Journal of Thermal Sciences and Technology*, 33 (1), 63-77.

Kürekçi, N.A., Özcan, O. (2012). An Experimental and Numerical Study of Laminar Natural Convection in a Differentially-Heated Cubical Enclosure, *Journal of Thermal Sciences and Technology*, 32 (1), 1-8.

Lai, Y.G., Przekwas, A.J. (1996). A Multigrid Algorithm for A Multiblock Pressure-Based Flow and Heat Transfer Solver, *Numerical Heat Transfer, Part B: Fundamentals: An International Journal of Computation and Methodology*, 30 (2), 239-254.

Lygidakis, G.N., Nikolos, I.K. (2014). Using a Parallel Spatial/Angular Agglomeration Multigrid Scheme to Accelerate the FVM Radiative Heat Transfer Computation—Part I: Methodology, *Numerical Heat Transfer, Part B: Fundamentals: An International Journal of Computation and Methodology*, 66 (6), 471-497.

Lygidakis, G.N., Nikolos, I.K. (2014). Using a Parallel Spatial/Angular Agglomeration Multigrid Scheme to Accelerate the FVM Radiative Heat Transfer Computation—Part II: Numerical Results, *Numerical Heat Transfer, Part B: Fundamentals: An International Journal of Computation and Methodology*, 66(6), 498-525.

Mançuhan, E., Küçükada, K., Alpman, E. (2011). Mathematical Modeling and Simulation of the Preheating Zone of a Tunnel Kiln, *Journal of Thermal Sciences and Technology*, 31 (2), 79-86.

Onur, N., Turgut, O., Arslan, K. (2011). Three-Dimensional Numerical Analysis of Forced Convection Flow and Heat Transfer in a Curved Square Duct, *Journal of Thermal Sciences and Technology*, 31 (2), 13-24.

Patil, P.V., Prasad, K. (2014). Numerical Solution for Two Dimensional Laplace Equation with Dirichlet Boundary Conditions, *IOSR Journal of Mathematics*, 6, 66-75.

Sert, Z., Timuralp, Ç., Tekkalmaz, M. (2019). Heat Transfer in Three-Dimensional Rectangular Cavities with Pins, *Journal of Thermal Sciences and Technology*, 39 (1), 39-49.

Şimşek, B., Uslu, S., Ak, M.A. (2020). Validation of Aerodynamic Heating Prediction Tool, *Journal of Thermal Sciences and Technology*, 40 (1), 53-63.

Tang, L., Joshi, Y.K. (1999). Application of Block-Implicit Multigrid Approach to Three-Dimensional Heat Transfer Problems Involving Discrete Heating, *Numerical Heat Transfer, Part A: Applications: An International Journal of Computation and Methodology*, 35 (7), 717-734.

Trottenberg, U., Oosterlee, C.W., Schüller, A. (2001). *Multigrid*, Academic Press.

Uğurlubilek, N. (2012). Numerical Investigation of Heat Transfer and Flow in a Twisted-Shaped Square Duct, *Journal of Thermal Sciences and Technology*, 32 (2), 121-131.

Uzuner, M.K., Başol, A.M., Mischo, B., Jenny, P. (2023). Numerical Analysis and Diffuser Vane Shape Optimization of a Radial Compressor with the Open-Source Software SU2, *Journal of Thermal Sciences and Technology*, 43 (2), 233-242.

Versteeg, H., Malalasekera, W. (2007). *An Introduction to Computational Fluid Dynamics: The Finite Volume Method*, Pearson.

Vierendeels, J., Merci, B., Dick, E. (2004). A multigrid method for natural convective heat transfer with large temperature differences, Journal of Computational and Applied Mathematics, 168, 509-517.

Wang, Q., Joshi, Y. (2006). Algebraic Multigrid Preconditioned Krylov Subspace Methods for Fluid Flow and Heat Transfer on Unstructured Meshes, *Numerical Heat Transfer, Part B: Fundamentals: An International Journal of Computation and Methodology*, 49 (3), 197-221.

Wesseling, P. (1992). *An Introduction to Multigrid Methods*, John Wiley & Sons.

Yan, J., Thiele, F. (1998). Performance and Accuracy of a Modified Full Multigrid Algorithm for Fluid Flow and Heat Transfer, *Numerical Heat Transfer, Part B: Fundamentals: An International Journal of Computation and Methodology*, 34 (3), 323-338.

Yetik, Ö., Mahir, N. (2020). Flow and Forced Heat Transfer from Tandem Square Cylinders Near a Wall, *Journal of Thermal Sciences and Technology*, 40 (1), 99-112.

Yıldızeli, A., Çadırcı, S. (2023). Numerical Investigation of Plate Cooling Using Multiple Impinging Jets in Different Alignments, *Journal of Thermal Sciences and Technology*, 43 (1), 1-10.

Journal Homepage: https://dergipark.org.tr/tr/pub/isibted

Isı Bilimi ve Tekniği Dergisi

Archive: https://tibtd.org.tr/dergi

Unit-Based Optimization Approaches for the Thermal Design of Residential Buildings

Sadik YIGIT [1, *], Semih CAGLAYAN [2]

[1] *Zurich University of Applied Sciences, Centre for Building Technologies and Processes, 8401 Winterthur, Switzerland*
[2] *Sakarya University of Applied Sciences, Department of Civil Engineering, 54050 Sakarya, Türkiye*

A R T I C L E I N F O

2024, vol. 44, no.2, pp. 339-350

doi: 10.47480/isibted.1416709

Research Article
Received: 21 January 2024
Accepted: 19 July 2024

* *Corresponding Author*
e-mail: sadik.yigit@zhaw.ch

Keywords:
Unit-based optimization
Thermal performance
Genetic algorithm
Energy efficiency
Climate change

ORCID Numbers in author order:
0000-0002-6257-1306
0000-0003-2052-0954

A B S T R A C T

Building regulations, energy scarcity, and climate change have compelled designers to seek energy-efficient design alternatives for buildings. Current regulations only focus on the total energy requirements of buildings, disregarding the significant variations in energy performance across different units within a building, leading to discomfort among occupants. Conventional optimization approaches based on these regulations thus lack the capacity to address this issue. Addressing the variability in thermal performance within units necessitates the adoption of unit-based optimization approaches. This study elucidates the inadequacy of conventional optimization approaches and proposes two alternative methods that account for this issue. Within this framework, the thermal design of a typical five-story residential building with six apartment units on each floor was optimized using the conventional optimization approach. A simulation-based optimization system employing Distributed Evolutionary Algorithms in Python (DEAP) and Energy Plus was utilized. Differences in energy performance among different units were observed under three distinct climate conditions. Subsequently, two approaches were proposed: (i) single-phase multi-objective optimization and (ii) multi-phase single-objective optimization, with the objectives of optimizing overall building performance and balancing variance within units. The study's findings demonstrated that multi-phase single-objective optimization returned better results.

Konut Binalarının Termal Tasarımı için Birim Tabanlı Optimizasyon Yaklaşımları

M A K A L E B İ L G İ S İ

Anahtar Kelimeler:
Birim bazlı optimizasyon
Termal performans
Genetik algoritma
Enerji verimliliği
İklim değişikliği

Ö Z E T

Bina yönetmelikleri, enerji kıtlığı ve iklim değişikliği, tasarımcıları binalar için enerji verimli tasarım alternatifleri aramaya zorlamıştır. Mevcut yönetmelikler yalnızca binaların toplam enerji gereksinimlerine odaklanmakta, bir bina içindeki farklı birimler arasındaki enerji performansındaki önemli farklılıkları göz ardı etmekte ve bu da bina sakinleri arasında rahatsızlıklara yol açmaktadır. Bu yönetmelikleri baz alan geleneksel optimizasyon yaklaşımları bu nedenle bu sorunu çözme kapasitesinden yoksundur. Birimler içindeki termal performanstaki değişkenliğin ele alınması, birim bazlı optimizasyon yaklaşımlarının benimsenmesini gerektirir. Bu çalışma, geleneksel optimizasyon yaklaşımlarının yetersizliğini ortaya koymakta ve bu konuyu açıklayan iki alternatif yöntem önermektedir. Bu çerçevede, her katında altı daire bulunan beş katlı tipik bir konut binasının termal tasarımı, geleneksel optimizasyon yaklaşımı kullanılarak optimize edilmiştir. Distributed Evolutionary Algorithms in Python (DEAP) ve Energy Plus kullanan simülasyon tabanlı bir optimizasyon sisteminden faydalanılmıştır. Üç farklı iklim koşulunda farklı üniteler arasındaki enerji performansı farklılıkları gözlemlenmiştir. Sonrasında, genel bina performansını optimize etme ve birimler içindeki varyansı dengeleme amacına yönelik iki yaklaşım önerilmiştir: (i) tek aşamalı çok amaçlı optimizasyon ve (ii) çok aşamalı tek amaçlı optimizasyon. Çalışmanın bulguları, çok aşamalı tek amaçlı optimizasyonun daha iyi sonuçlar verdiğini göstermiştir.

INTRODUCTION

The use of fossil fuels in energy generation has increased significantly due to rapid industrialization in recent decades. Environmental damage necessitates the need to decrease nonrenewable energy consumption on a global scale (Zune et al., 2020). Achieving carbon neutrality by 2050 requires promoting energy efficiency and selecting decarbonization options with no environmental side effects (Buonomano et al., 2022). In addition to mitigating climate change and local pollution, energy conservation can enhance the health of occupants and national energy supply security (Bertoldi, 2022).

The rapidly increasing energy demand on the global scale has raised a worldwide concern. Energy-efficient technologies and eco-friendly policies have been insufficient to counterbalance the demand (Kaya and Caglayan, 2023). In this direction, the European Union has aimed at achieving an energy efficiency of 32.5% by 2030. Member States need to take radical energy efficiency measures to accomplish the national energy efficiency objectives (Malinauskaite et al., 2019). The objective of Türkiye has been stated as reducing the energy intensity by 35.3% in the 2020-2035 period, which requires a major transformation in all industries (MENR, 2022).

The building industry is significantly energy-dependent and consumes approximately 40% of the total energy consumed worldwide (Somu and Ramamritham, 2020). The industry is responsible for about one-third of carbon emissions (Gao et al., 2023) and has great potential to mitigate environmental damage (Caglayan et al., 2020a). Consequently, identifying energy-efficient designs and systems for buildings has become a popular field for both researchers and designers (Yigit, 2021). In particular, determining the most efficient thermal design has been the main subject of numerous international studies (Caglayan et al., 2022).

Recently published review studies have presented new methodologies for designing energy-efficient buildings (Pooyanfar and Topal, 2018; Longo et al., 2019; He et al., 2022). A relatively new technique known as simulation-based optimization has been recognized as a promising way to analyze energy-efficient building design alternatives. The results of certain benchmarking studies show that such optimization methods can reduce building energy consumption by up to 30% (Yu et al., 2021). The general strategy for building energy optimization is presented in Figure 1. The design alternatives are provided by the optimization algorithms, and the building configuration is modified based on feedback from the energy simulation tool (Si et al., 2016).

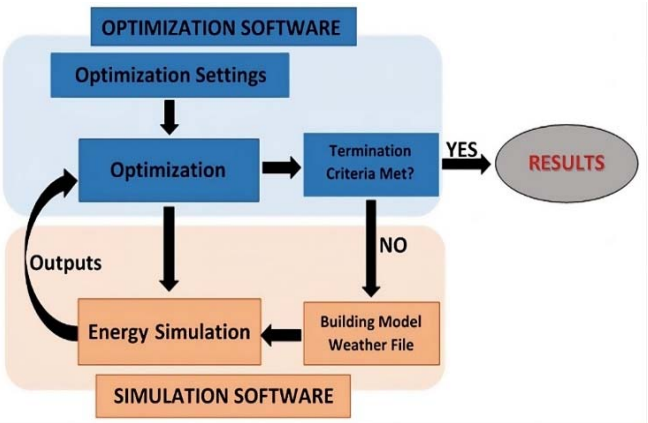

Figure 1. General strategy for building energy optimization.

RESEARCH BACKGROUND

In the architecture, engineering, and construction industry, designers are critical members who make decisions associated with building energy performance. They mostly benefit from parametric trial and error methods to identify the most energy-efficient design alternatives. Nonetheless, passive trial and error methods have been proved ineffective and more time-consuming than simulation-based optimization methods (Wang et al., 2023). Therefore, researchers have recently proposed the use of simulation-based building optimization tools consisting of building simulation and search tools (Sharif and Hammad, 2019).

The most common technique used to develop a building energy optimization system is to integrate numerical simulations and search algorithms (Huang and Niu, 2016; Barber and Krarti, 2022). Researchers have focused on single- and multi-objective design problems with multiple constraints, considering all design parameters that influence building energy performance. They have developed simulation-based optimization systems integrated with search algorithms such as ant colony optimization (Bamdad et al., 2017; Anupong et al., 2023; Khan et al., 2023), grey wolf optimizer (Ghalambaz et al., 2021; Li et al., 2021), particle swarm optimization (Delgarm et al., 2016; Zhou et al., 2020), simulated annealing (Junghans and Darde, 2015; Kheiri, 2021), and genetic algorithm (Ascione et al., 2015; Niemelä et al., 2016; Ascione et al., 2017; Gilles et al., 2017; Al-Saadi and Al-Jabri, 2020).

The integrated systems have been developed using generic platforms and optimization software such as MATLAB, GenOpt, and CAMOS (Bigot et al., 2013; Perera et al., 2016; Li et al., 2020; Ucar, 2024). The search algorithm tools have been coupled with energy simulation software like EnergyPlus, TRNSYS, and DOE-2 to conduct the simulation process (Asadi et al., 2012; Ferrara et al., 2014; Ascione et al., 2016). The developed simulation-based optimization system has been used to optimize thermal comfort (Yu et al., 2016; Naderi et al., 2020; Yue et al., 2021), building envelope and geometry (Song et al., 2017; Yigit and Ozorhon, 2018; Zhou et al., 2018; Caglayan et al., 2020b; Ozel, 2022), insulation thickness (Jin et al., 2017; Ghafoori and Abdallah, 2022), and energy consumption (Griego et al., 2015; Eskander et al., 2017; Ge et al., 2018; Lin and Yang, 2018; Ren et al., 2018; Yigit and Ozorhon, 2018; Lee et al., 2019).

The majority of the studies have targeted optimizing the whole building energy performance, while a limited number of studies have observed the situation for certain building units and rooms (Yu et al., 2008; Kontoleon and Eumorfopoulou, 2010). The apartment units on different floors and orientations may show notably different energy performances. Even though whole building energy optimization is effective in reducing total energy consumption, it ignores the fact that varying energy performance across different units can lead to discomfort among occupants. The problem might be addressed by using a detailed optimization process with a large number of variables. However, energy optimization processes already take quite some time, and the increasing number of variables would make the processes unmanageable.

This study proposes simple optimization approaches that balance the performance variance within units and thus tip

the scales in favor of the underperforming apartment units. In this regard, the thermal design of a typical five-story residential building was determined using three different unit-based optimization approaches. The first approach was the conventional optimization approach with the sole objective of minimizing total energy consumption. The variance in the energy performances of different units was observed. Two additional approaches, aiming to minimize both total energy consumption and variance across the units, were introduced. The results of the three approaches were compared to identify the most appropriate approach.

RESEARCH METHODOLOGY

The flowchart of methodology is presented in Figure 2. The methodology is composed of three main stages. The conventional single-phase single-objective optimization was conducted in the first stage to observe the variance in the annual energy requirements of different units. The optimization process focused solely on the minimization of the total building energy consumption with a budget constraint of 50,000 USD. The thermal performance of each unit was investigated and the variance across the units was observed.

In the second stage, in an attempt to balance the variance in the thermal performances of different units, two optimization approaches were proposed: (i) single-phase multi-objective optimization and (ii) multi-phase single-objective optimization. The former utilized the NSGA-II (Non-Dominated Sorting Genetic Algorithm II) technique to minimize both total energy consumption and variance across the units within a budget of 50,000 USD. The latter was a two-phase optimization process, where total energy consumption was minimized by using 90% of the budget (45,000 USD) in the first phase, and the remaining 10% budget (5,000 USD) was used to manually enhance the thermal properties of certain parts in the second phase.

The results of the proposed approaches were compared in the last stage of the methodology. The decision variables resulting in the optimum value were revealed, the annual heating/cooling energy requirements were calculated, and the variances across the units were evaluated. The simulation tool (Energy Plus) was coupled with the optimization tool (DEAP) for the execution of the process in all three approaches (Fortin et al., 2012). Energy Plus was used to calculate the annual energy requirement of the building while DEAP was utilized for the optimization purposes. Python programming language was used to provide the integration between them.

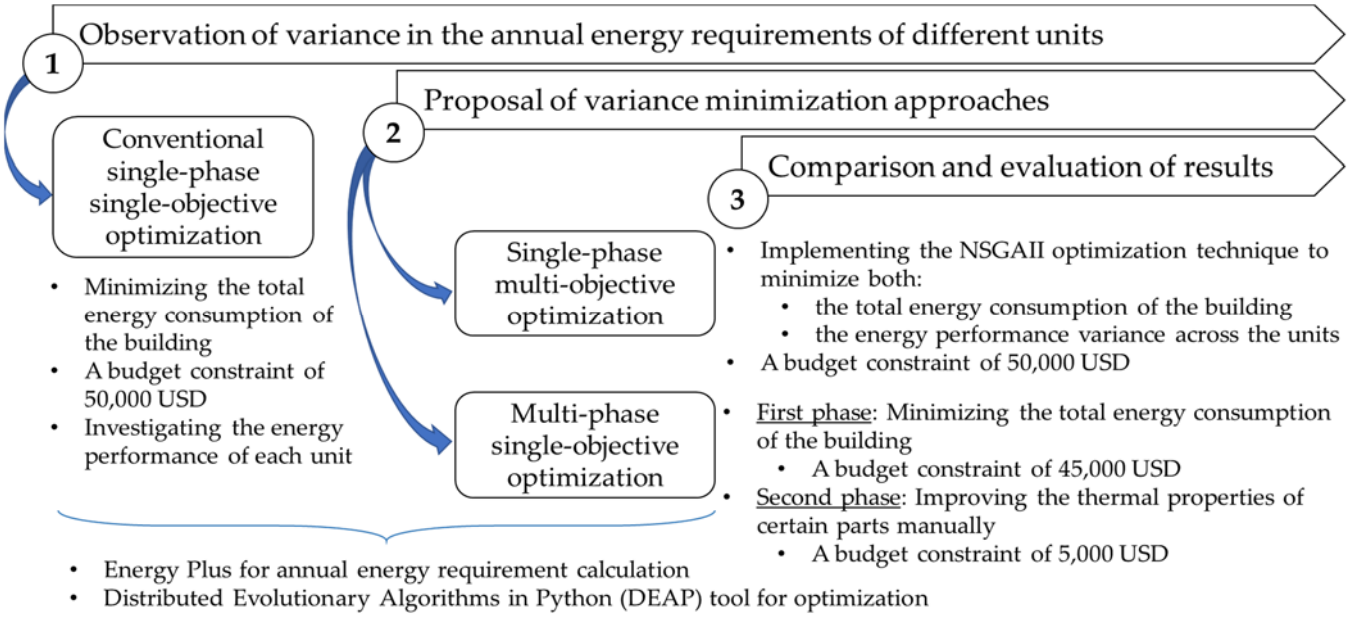

Figure 2. The flowchart of methodology.

Execution of the Optimization Process

The NSGA-II optimization process is presented in Figure 3. The process commences by generating a random population of building designs, with each design represented by a unique combination of parameters related to the building envelope. These parameters include insulation thickness and window-to-wall ratio, among others. Each building configuration in this population undergoes evaluation through simulation using EnergyPlus, automated by a Python script developed by the authors. Following simulation, the energy performance of each building design is assessed based on energy consumption.

The optimization process iterates until termination criteria are satisfied, signaling either the achievement of desired energy performance or reaching a predefined limit on the number of iterations. To evolve the population towards improved solutions, genetic operations including selection, mutation, and crossover are applied. Selection favors individuals with higher fitness (i.e., better energy performance), while mutation introduces random changes to foster exploration of new design spaces. Crossover facilitates the exchange of genetic material between selected individuals, generating offspring with combined features from parent designs. Through this repetitive process of simulation, evaluation and refinement, the optimization algorithm progressively improves the population, eventually converging towards building designs that exhibit higher energy performance. This methodology offers a systematic approach to addressing the complex design space of building envelopes and outputs near-optimal/Pareto-optimal results in the end.

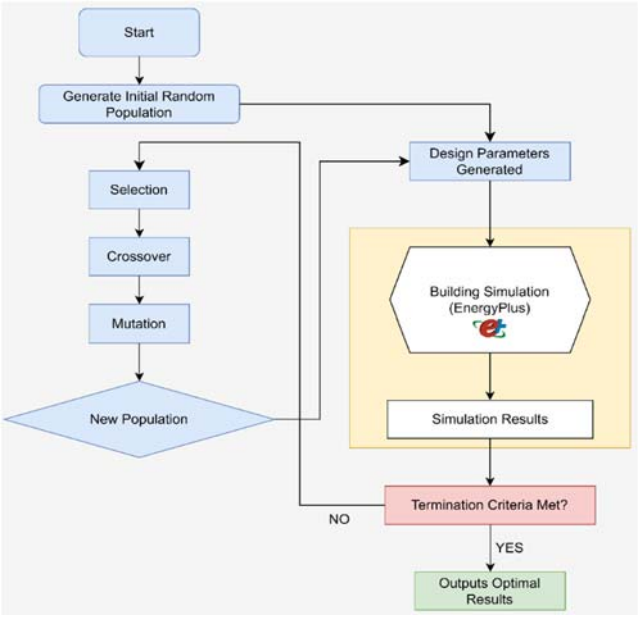

Figure 3. NSGA-II optimization process.

Characteristics of the Reference Building

A typical five-story residential building was selected as the reference building. The architectural plan and side view of the building are shown in Figure 4. The building had a footprint area of 600 m^2. Each floor had six units of equal sizes, and the height was 3 m. The window-to-wall ratios of the east, west, north, and south facades were set as variables to be optimized. The ranges of these variables are expressed in the section called settings and design parameters.

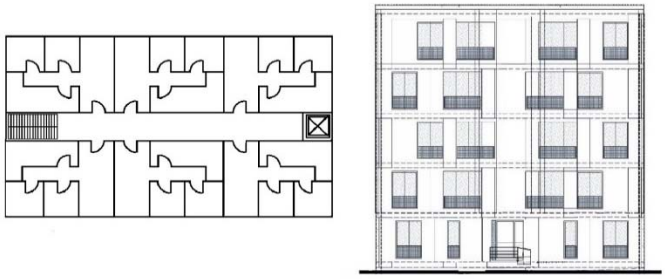

Figure 4. Architectural plan and side view of the residential building.

The simplified model of the building is presented in Figure 5. The building had a total of 30 apartment units. To observe the variance in the energy performance of different units, the model created in EnergyPlus was composed of 30 different zones. The building was cooled above 24°C and heated below 20°C. The orientation of the building was fixed due to land constraints in urbanized areas, and the building was oriented to the North.

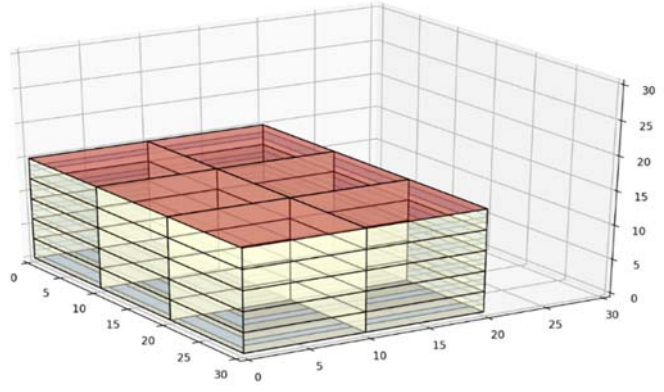

Figure 5. Simplified 3D model of the building.

Energy Efficiency Measures

An extended market investigation was conducted to determine the energy efficiency measures for the reference building. A variety of construction materials is available in the market, but contractors mainly prefer certain types of materials due to their functionality and cost-effectiveness. Expanded polystyrene (EPS) is the most popular insulation material applied to the exterior walls. Extruded polystyrene (XPS), on the other hand, is mostly preferred for the basement and roof due to its greater compressive strength. The thicknesses of the insulation materials are the variables to be optimized. Double-glazed PVC frames are widely used for windows in the market. Therefore, the building envelope was designed with the most commonly used construction materials. The cross-sectional details of the building envelope components are presented in Table 1.

Table 1. Cross-sectional details of the building envelope.

Component	*Cross-sectional elements*	*Thickness*
Basement	Acoustic tile	2 cm
	XPS (to be optimized)	2 – 15 cm
	Heavy weight concrete	12 cm
Roof	Slag or stone	2 cm
	Felt and membrane	1 mm
	XPS (to be optimized)	2 – 15 cm
	Heavy weight concrete	12 cm
Interior slabs	Acoustic tile	2 cm
	Heavy weight concrete	12 cm
Exterior walls	Dense face brick	10 cm
	EPS (to be optimized)	2 – 15 cm
	Light weight concrete	5 cm
	Plaster or gyp board	2 cm
Interior walls	Plaster or gyp board	2 cm
	Dense face brick	10 cm
	Plaster or gyp board	2 cm
Windows	PVC frame double glazed	16 mm

Locations and Meteorological Data

The optimization process was repeated for three cities representing different climate conditions of Türkiye. These three regions were selected based upon their climate conditions and urbanization levels. Ankara, Istanbul, and Izmir are the most urbanized cities of Türkiye and the majority of the population in Türkiye is concentrated in these cities.

The geographic properties and climate conditions of these cities are presented in Table 2. The cities are located at latitudes between 30° and 40° and longitudes between 27° and 33°. The time zone in all three cities is +2. Ankara is situated at a considerably higher elevation. The climate of Ankara is characterized as continental Mediterranean, featuring hot-dry summers and cold winters. The climate in Istanbul is transitional Mediterranean, which implies hot-humid summers and cold winters. The climate of Izmir is classified as Mediterranean, with hot-dry summers and mild winters.

Table 2. Geographic properties and climate conditions of Ankara, Istanbul, and Izmir.

	Ankara	*Istanbul*	*Izmir*
Latitude	40.12	30.97	38.50
Longitude	32.98	28.82	27.02
Time zone	+2	+2	+2
Elevation	949.00 m	37.00 m	5.00 m
Climate	Continental Mediterranean	Transitional Mediterranean	Mediterranean

The weather data for Ankara, Istanbul, and Izmir were obtained from the official website of EnergyPlus (EnergyPlus, 2020). The average and standard deviation of temperature and relative humidity ratio for each city are presented in Table 3. The average temperature ranges between -1.32°C and 20.68°C, 5.38°C and 23.10°C, and 8.60°C and 24.64°C in Ankara, Istanbul, and Izmir, respectively. Similarly, the relative humidity ratio ranges between 46.79% and 80.79%, 64.54% and 82.75%, and 49.50% and 80.79% in Ankara, Istanbul, and Izmir, respectively. The optimization process also considered the standard deviations in the analyses.

Settings and Design Parameters

The settings of the genetic algorithm radically influence the probability of obtaining the optimal solution, as the number of iterations and population diversity are defined by these parameters. However, no mathematical formula has been suggested for the accurate calculation of these parameters. Instead, the parameters are mostly determined based on a rule of thumb depending on the complexity of the problem or through trial-and-error methods for each optimization problem. The settings determined after iterative runs are presented in Table 4.

In configuring the genetic algorithm for optimization, a group of 30 potential solutions was preferred, referred to as the population. The algorithm was allowed to iterate 50 times, expecting its ability to locate the most favorable solution(s). To add variety to the solutions, the solutions were permitted to exchange certain characteristics (crossover) 80% of the time. Additionally, each solution had a 5% chance of independently undergoing slight changes (mutation) to maintain diversity. The selected crossover and mutation methods are particularly suitable for problems involving continuous variables. Utilizing the non-domination sorting method enabled the identification of top solutions and ensured the exploration of diverse possibilities. The algorithm was concluded after 50 repetitions to conserve computational resources.

The number and ranges of the decision variables should be carefully determined to identify the energy-optimal building design. They should allow for the consideration of all possible options in the optimization process. On the other hand, they should be determined so that the optimization problem becomes manageable, and the calculations are completed within a reasonable time period. It has already been mentioned that the orientation and gross floor area were kept fixed due to land constraints and dense urbanization. The window-to-wall ratios of the façades, solar absorption values of the roof and exterior walls, and insulation thicknesses of the basement, exterior walls, and roof were selected as the decision variables to be optimized. The design parameters and their ranges are presented in Table 5.

Table 3. Weather data used in the optimization process.

Months	***Ankara***				***Istanbul***				***Izmir***			
	Temp (°C)		*Relative Humidity (%)*		*Temp. (°C)*		*Relative Humidity (%)*		*Temp. (°C)*		*Relative Humidity (%)*	
	Avg.	*Std.*	*Avg.*	*Std.*	*Avg.*	*Std.*	*Avg.*	*Std.*	*Avg.*	*Std.*	*Avg.*	*Std.*
January	-1.32	4.59	78.67	8.02	6.20	1.99	78.71	3.84	9.10	2.05	80.79	5.99
February	1.39	3.99	67.46	9.20	5.38	2.28	68.58	4.91	8.60	2.36	71.17	6.78
March	3.20	4.09	65.29	11.74	7.50	2.07	75.50	5.98	10.65	3.15	73.08	9.01
April	9.04	3.74	65.79	12.69	12.08	2.53	66.67	7.42	14.07	3.21	71.04	8.86
May	13.39	4.66	64.13	15.85	16.25	3.03	72.46	6.86	20.13	5.04	58.58	12.66
June	16.46	5.45	56.63	16.57	20.72	4.08	64.54	8.86	23.33	6.11	55.00	13.98
July	20.68	5.47	48.42	13.29	23.04	4.63	70.58	13.05	24.64	6.03	49.50	11.48
August	20.22	5.77	46.79	13.28	23.10	4.70	74.63	9.44	24.16	6.07	57.79	12.56
September	16.52	5.53	56.04	19.03	19.99	3.91	66.00	12.46	22.02	5.62	58.79	13.26
October	10.28	3.87	62.96	12.66	15.97	2.87	70.08	11.19	16.42	3.94	65.04	11.02
November	4.24	3.16	71.83	8.36	11.24	1.71	74.92	5.34	11.30	3.19	66.50	9.27
December	1.60	3.46	80.79	6.81	8.11	1.40	82.75	3.22	9.89	1.92	73.38	6.00

Table 4. Settings of the genetic algorithm optimization.

Parameter	***Value***
Population size	30
Number of generations	50
Crossover rate	0.8
Mutation rate	0.05
Crossover	Simulated binary bounded
Selection	Non-domination rank
Mutation	Polynomial bounded
Termination	Maximum generation

Table 5. Optimization design parameters.

Parameter	***Component***	***Lower Bound***	***Upper Bound***
Window-to-wall ratio	North façade	0.3	0.9
	South façade	0.3	0.9
	East façade	0.3	0.9
	West façade	0.3	0.9
Solar absorption	Roof	0.3	0.8
	Exterior walls	0.3	0.8
Insulation thickness	Roof	2 cm	15 cm
	Exterior walls	2 cm	15 cm
	Basement	2 cm	15 cm

Characteristics of the Optimization Approaches

This study has introduced three different approaches to investigate the energy performance of the apartment units for three different climate conditions. The characteristics of these approaches are summarized in Table 6. The first approach is the conventional single-phase single-objective optimization, which focuses only on the total energy consumption of the building. It attempts to find the optimal design within a budget constraint of 50,000 USD and does not consider the variation of the performance across the units. The second approach is a single-phase multi-objective optimization, which utilizes the NSGA-II optimization technique to minimize both the total energy consumption and variance within the units. The approach uses the same amount of budget. The third approach is a multi-phase single-objective optimization, which attempts to minimize the total energy consumption in the first phase and varying performance of different units in the second phase. The approach uses 90% of the budget (45,000 USD) in the first phase to minimize the whole building energy consumption, and the remaining 10%

of the budget (5,000 USD) is used in the second phase to manually improve the thermal properties of certain parts.

Table 6. The characteristics of the introduced approaches.

Approach	*Budget Constraint*	*Characteristics*
Single-phase single-objective optimization	50,000 USD	The conventional approach attempting to minimize solely the total energy consumption of the building
Single-phase multi-objective optimization	50,000 USD	The approach attempting to minimize both (i) the total energy consumption and (ii) variance within the apartment units
Multi-phase single-objective optimization	Phase I: 45,000 USD Phase II: 5,000 USD	The approach attempting the minimize the total energy consumption in the first phase and variance within the units in the second phase

RESEARCH RESULTS AND DISCUSSION

Single-Phase Single-Objective Optimization

The reference building design was optimized in three different climate conditions with the aim of minimizing the energy demand of the building. The purpose of these runs is to investigate the performance variance between the housing units of an energy-optimized residential building. Additionally, these runs demonstrate the effectiveness of conventional optimization methods in balancing the energy performance of each apartment unit. The upper and lower boundaries of the parameters are presented in Table 5. The convergence of the optimization process is shown in Figure 6.

The building design parameters obtained from the optimization process are presented in Table 7. Despite the varying climate conditions of Ankara, Istanbul, and Izmir, the energy-optimal design parameters selected by the genetic algorithm optimization tool were quite similar. The window-to-wall ratios were higher on the north façade. The solar absorption values of the exterior walls were greater than those of the roofs (except for Izmir). The insulation thicknesses were greatest in the exterior walls, followed by the roof and basement.

The optimal design configurations were simulated in the EnergyPlus energy simulation software. The heating and cooling loads of the building located in Ankara were obtained as 118,345 kWh and 64,308 kWh, respectively. The total energy consumption of the units ranged between 2,800 kWh and 10,978 kWh, with a standard deviation of 2,299 kWh. The heating load of the building located in Istanbul was 66,700 kWh, and the cooling load was 103,807 kWh. The total energy consumption of the units varied between 2,502 kWh and 9,285 kWh, with a standard deviation of 1,938 kWh. The building located in Izmir had heating and cooling loads of 27,260 kWh and 138,048 kWh, respectively. The total energy consumption of the units ranged between 2,342 kWh and 8,582 kWh, with a standard deviation of 1,834 kWh. As expected, the building located in Izmir had the highest cooling loads, while the building located in Ankara had the highest heating loads. The energy consumptions of each unit are demonstrated in Figure 7. Sections A, B, C, D, E, and F represent the northwest, north, northeast, southwest, south, and southeast corner units, respectively. In the next sections, the proposed variance minimization approaches are implemented to reduce the performance differences across the units.

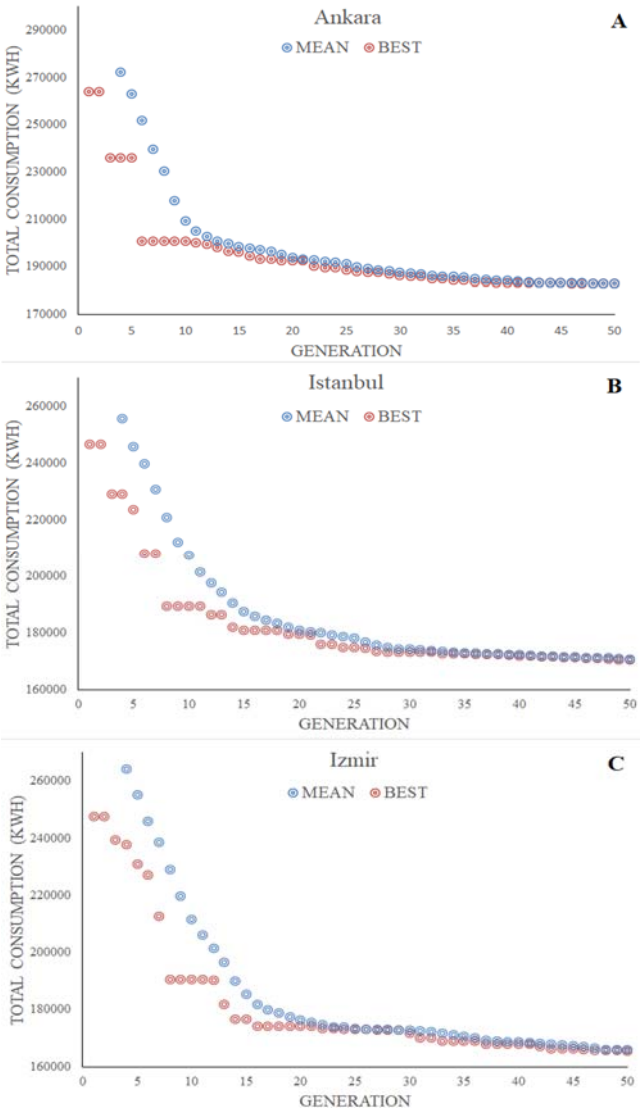

Figure 6. The convergence of the single-phase single-objective optimization process.

Table 7. Optimal design parameters for the single-phase single-objective optimization approach.

Parameter	*Component*	*Ankara*	*Istanbul*	*Izmir*
Window-to-wall ratio	North façade	0.381	0.328	0.315
	South façade	0.311	0.303	0.305
	East façade	0.301	0.301	0.300
	West façade	0.300	0.317	0.304
Solar absorption	Roof	0.313	0.312	0.662
	Ext. walls	0.537	0.589	0.324
Insulation thickness	Ext. walls	14.9 cm	13.6 cm	14.6 cm
	Roof	9.2 cm	8.7 cm	9.6 cm
	Basement	2 cm	4.4 cm	2.3 cm

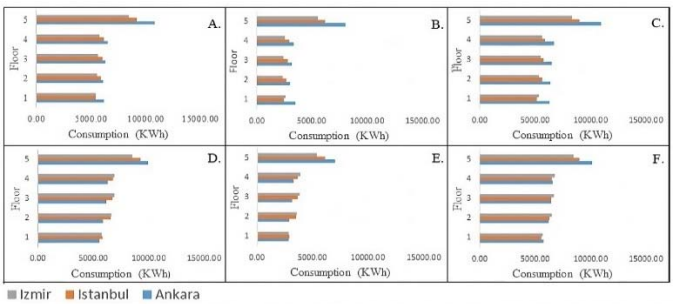

Figure 7. Simulation results of the single-phase single-objective optimization approach.

Single-Phase Multi-Objective Optimization

The single-phase multi-objective optimization approach was conducted to minimize both the total energy consumption and variance within the units. An NSGA-II optimization methodology was implemented to carry out the optimization process in three different climate conditions. The aim of these runs was to investigate the effectiveness of the proposed approach in reducing the energy performance variance within the units and providing a more balanced energy demand profile. A large number of test runs were conducted to find optimal generation numbers and population size. The test runs demonstrated that although increasing these parameters could provide slightly better results, the optimization time periods were greatly increased. Therefore, the parameters such as the number of generations, population size, and offspring size were kept constant to obtain results in a reasonable time period. The upper and lower boundaries of the parameters are presented in Table 5. The results of the optimization process are presented in Figure 8.

The building design parameters obtained from the single-phase multi-objective optimization process are presented in Table 8. The window-to-wall ratios were almost similar except for the south façade of the building in Ankara. The solar absorption values of the exterior walls were greater than those of the roofs. The solar absorption values were slightly greater in Ankara than in Istanbul and Izmir. The insulation thicknesses of the basement were considerably less than those of the roof and exterior walls.

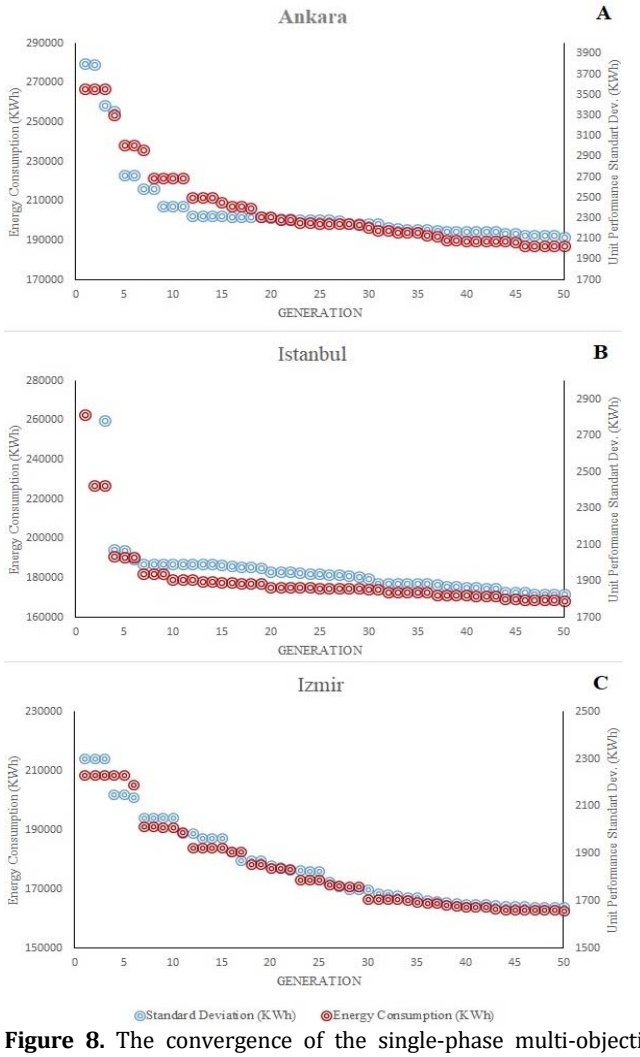

Figure 8. The convergence of the single-phase multi-objective optimization process.

The optimal design configurations obtained from the single-phase multi-objective optimization approach were simulated in EnergyPlus software. The heating and cooling loads of the building located in Ankara were 120,485 kWh and 66,346 kWh, respectively. The total energy consumption of units ranged between 2,928 kWh and 10,432 kWh, with a standard deviation of 2,126 kWh. The heating load for the building located in Istanbul was 68,293 kWh, and the cooling load was 96,900 kWh. The total energy consumption of the units varied between 2,485 kWh and 9,042 kWh, with a standard deviation of 1,879 kWh. The building located in Izmir had heating and cooling loads of 29,134 kWh and 133,306 kWh, respectively. The total energy consumption of the units ranged between 2,335 kWh and 8,118 kWh, with a standard deviation of 1,724 kWh. The energy consumptions of each unit are demonstrated in Figure 9. The figure shows that the unit performance of the optimized building located in Ankara was slightly more balanced. The performance variance between the units of the building located in Izmir was significantly reduced, and the total energy performance of the building was increased. The unit performance of the building located in Istanbul was also moderately balanced.

Table 8. Optimal design parameters for the single-phase multi-objective optimization approach.

Parameter	*Component*	*Ankara*	*Istanbul*	*Izmir*
Window-to-wall ratio	North façade	0.312	0.302	0.302
	South façade	0.356	0.301	0.303
	East façade	0.307	0.304	0.300
	West façade	0.301	0.301	0.302
Solar absorption	Roof	0.421	0.301	0.315
	Ext. walls	0.457	0.399	0.375
Insulation thickness	Ext. walls	8.1 cm	12.5 cm	10.7 cm
	Roof	13.8 cm	9.4 cm	10.8 cm
	Basement	4.4 cm	4.7 cm	3.6 cm

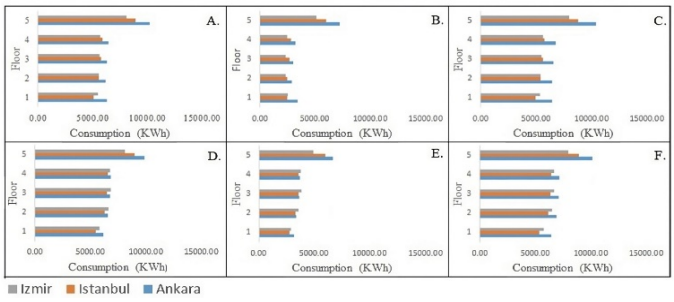

Figure 9. Simulation results of the single-phase multi-objective optimization approach.

Multi-Phase Single-Objective Optimization

The approach is conducted in two phases. In the first phase, a single-objective genetic algorithm optimization was conducted to minimize the total energy demand of the building. The only constraint defined in the optimization process was the budget corresponding to 90% of the total amount (45,000 USD). A small portion of the budget was withheld to be used in the second phase. The aim of the first phase was to obtain an energy-optimized building design, which would be manually adjusted in the next phase. In this way, the designers had the chance to balance the varying energy performance of different units in the second phase by conducting a trial-and-error design process. The parameters of the genetic algorithm were kept constant to obtain results in a reasonable time period. The upper and lower boundaries of the parameters are presented in Table 5. The results of the optimization process are presented in Figure 10.

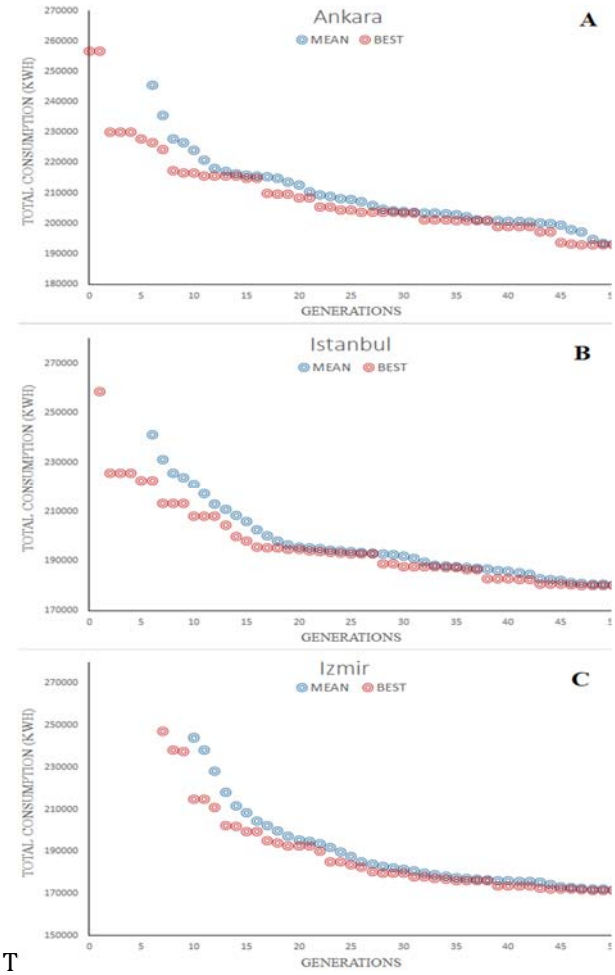

Figure 10. The convergence of the multi-phase single-objective optimization process.

T

he building design parameters obtained from the first phase of the multi-phase single-objective optimization process are presented in Table 9. The cost of the obtained design configurations was 45,000 USD. In the second phase, the designer could reduce energy demand and balance the energy performance of each unit with manual adjustments. In the second phase of the approach, a trial-and-error method was implemented to balance the energy performance of the housing units. The results of the previous analyses showed that the top-floor units had the lowest energy performance. Additionally, it was observed that the insulation material used in the basement was not cost-effective. Therefore, in the second phase, the design configuration obtained from the first phase of the optimization process was modified to increase the thermal performance of the top-floor units.

Considering the budget constraints and using the information gained from the previous simulations, the following measures were taken to minimize energy consumption and balance the energy performance of the units:

- Increasing the insulation thickness of the roof,
- Increasing insulation thickness of the top floor exterior walls,
- Adding Low-E glazing to the top floor windows (it is not possible to use Low-E glazing for the whole building due to the high costs),
- Reducing the insulation thickness of the basement to provide additional budget,
- Increasing the insulation thickness of the exterior wall for the whole building if required,
- Reducing the window area of the building to create an extra budget.

The modified building design parameters and the additional design changes obtained from the second phase of the optimization process are presented in Table 10. Low-E glazing was used on the top floor for all three cities. The insulation thickness of the exterior walls was increased to 15 cm on the top floor, but only for the case of Istanbul.

Table 9. Optimal design parameters for the first phase of the multi-phase single-objective optimization approach.

Parameter	*Component*	*Ankara*	*Istanbul*	*Izmir*
Window-to-wall ratio	North façade	0.312	0.300	0.303
	South façade	0.303	0.300	0.301
	East façade	0.303	0.378	0.320
	West façade	0.301	0.302	0.304
Solar absorption	Roof	0.472	0.404	0.304
	Ext. walls	0.397	0.400	0.382
Insulation thickness	Ext. walls	6.2 cm	6.7 cm	7.6 cm
	Roof	9.6 cm	8.7 cm	6.7 cm
	Basement	3.0 cm	4.0 cm	4.7 cm

Table 10. Optimal design parameters for the second phase of the multi-phase single-objective optimization approach.

Parameter	*Component*	*Ankara*	*Istanbul*	*Izmir*
Window-to-wall ratio	North façade	0.300	0.300	0.303
	South façade	0.300	0.300	0.301
	East façade	0.300	0.300	0.300
	West façade	0.300	0.300	0.304
Solar absorption	Roof	0.472	0.404	0.300
	Ext. walls	0.397	0.400	0.300
Insulation thickness	Ext. walls	8.0 cm	11.0 cm	7.6 cm
	Roof	15.0 cm	10.0 cm	15.0 cm
	Basement	2.0 cm	2.0 cm	2.0 cm
Additional modifications on the top floor	Low-E glazing (all three cities) Exterior wall insulation thickness: 15cm (Istanbul)			

The optimal design configurations obtained from the second phase of the multi-phase single-objective optimization process were simulated in the EnergyPlus software. The heating and cooling loads of the building located in Ankara were 116,706 kWh and 58,379 kWh, respectively. The total energy consumption of each unit ranged between 2,883 kWh and 9,295 kWh, with a standard deviation of 1,869 kWh. The heating load for the building located in Istanbul was 65,501 kWh, and the cooling load was 96,661 kWh. The total energy consumption of each unit varied between 2,503 kWh and 8,496 kWh, with a standard deviation of 1,717 kWh. The building located in Izmir had heating and cooling loads of 28,997 kWh and 131,927 kWh, respectively. The total energy consumption of each unit ranged between 2,419 kWh and 7,757 kWh, with a standard deviation of 1,627 kWh. The energy consumptions of each unit are demonstrated in Figure 11. The figure shows that the unit performances of the optimized design were more balanced compared to the unit performances in the other approaches. Additionally, in some cases, the total energy demands of the buildings were also lower compared to the other design solutions.

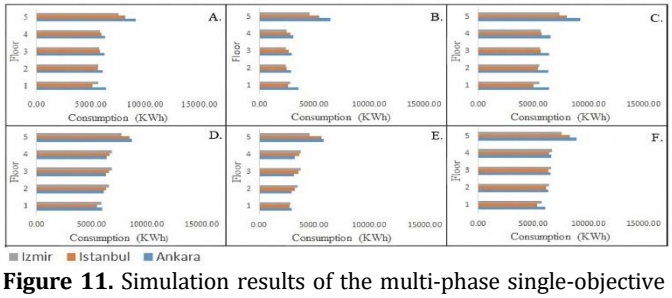

Figure 11. Simulation results of the multi-phase single-objective optimization approach.

Evaluation of the Results

Table 11 summarizes the results obtained from the three optimization approaches. The results of the first approach demonstrated that designing the building envelope based on the conventional single-phase single-objective optimization produced a design with imbalanced thermal performance. The top floor units and corner units performed poorly, while comparatively better performances were observed in the other units. Although the total energy was reduced, a remarkable performance difference was observed among the units.

Table 11. The summary of the results.

Approach	*Location*	*Heating (kWh)*	*Cooling (kWh)*	*Min-Max Range (kWh)*	*Std. Dev. (kWh)*
Single-phase	Ankara	118,345	64,308	2,800-10,978	2,299
single-objective	Istanbul	66,700	103,807	2,502-9,285	1,938
optimization	Izmir	27,260	138,048	2342-8,582	1,834
Single-phase	Ankara	120,485	66,346	2,928-10,432	2,126
multi-objective	Istanbul	68,293	96,900	2485-9,042	1,879
optimization	Izmir	29,134	133,306	2,335-8,118	1724
Multi-phase	Ankara	116,706	58,379	2,883-9,295	1,869
single-objective	Istanbul	65,501	96,661	2,503-8,496	1,717
optimization	Izmir	28,997	131,927	2,419-7,757	1,627

The imbalanced thermal performance obtained from the conventional optimization approach necessitated the introduction of optimization approaches focusing on balancing the energy performance of the apartment units and minimizing the total energy demand of the building. The introduced methodologies were tested, and the results indicated that both methods could be useful in providing designs with balanced thermal performance. The multi-phase single-objective optimization approach resulted in slightly better outputs compared to other approaches. It provided more balanced unit performances and also reduced the total energy consumption of the building by 3–5%.

The performance difference between the top floor and other floors was significantly diminished with the implementation of the introduced unit-based optimization approaches. The difference between the middle and corner units could not be reduced due to the building geometry. The corner units, by their nature, have two external surfaces and a larger area of window surface compared to middle units. Thus, they require more energy to maintain acceptable thermal comfort. The trial-and-error analyses in the multi-phase single-objective optimization also confirmed that balancing the energy performance of the middle and corner units was not cost-effective and reduced the total energy performance of the building.

The study aimed to optimize the envelope design of a typical five-story residential building and examined the performances of three different optimization approaches with single/multi-phase and single/multi-objective objectives. Even though multi-phase and multi-objective optimization approaches have been employed in a number of studies for thermal design improvement (Kim and Clayton, 2020; Wang et al., 2020; Ciardiello et al., 2020), none of the studies have considered the varying energy performance across different units and compared the capabilities of different approaches to obtain the desired outcome. The proposed approaches enabled the execution of unit-based optimization techniques that can overcome the imbalanced thermal performance phenomenon. In that sense, the study presents pioneering research in the field of thermal design optimization.

CONCLUSIONS

Governmental regulations and climate changes have compelled designers to construct energy-efficient buildings. Simulation-based optimization approaches have proven effective methods in finding energy-efficient building designs. Designers commonly use energy optimization approaches to minimize the total building energy demand. They should also consider the performance variance within the apartment units. For this purpose, three different optimization approaches were analyzed in three different climate conditions to observe the performance difference and evaluate the results of the introduced optimization approaches.

The results of the conventional optimization approach pointed out a significant thermal performance imbalance among the units. The approach was implemented solely to minimize the energy consumption of the building. It was also observed that the performance difference between the housing units couldn't be reduced to a considerable level without increasing the number of design parameters. The increasing number of design parameters eventually reduced the manageability of the problem and greatly increased the optimization periods. The optimization periods of the conventional optimization approach were already beyond the acceptable level. Thus, increasing optimization periods would significantly impact the practicality and usability of the approach.

The proposed approaches were tested in the second and third case runs. The results indicated that both approaches could diminish the varying energy performance within the units. The single-phase multi-objective optimization approach was easy to implement and required no extra pre-process and post-process work. Therefore, it can easily be integrated into the daily work of a designer. On the other hand, even though the multi-phase single-objective optimization approach required post-process work, it resulted in better outputs. In the second phase, the designers were able to evaluate and modify the thermal performance of the building without any parameter limit. The proposed approaches increased the performance of the underperforming units and decreased the total energy demand. The results showed that the proposed methodologies were easy to implement, effective, and could be used to optimize the building thermal design.

The study contributes to the literature by addressing a common but largely neglected problem for the thermal design of residential buildings and proposing a couple of unit-based optimization approaches that take the issue into account. The study is expected to raise awareness among design professionals and companies about the varying thermal performance within the units. The study has also

demonstrated that conventional optimization approaches could have difficulty overcoming the problem, and thus, design professionals and companies should become familiar with the proposed unit-based optimization approaches to design convenient buildings.

The proposed optimization approaches were performed for a frequently used five-story residential building design. The findings might be subjected to changes for buildings with different geometries, which can be regarded as a limitation. Further studies may focus on repeating the methodology for other building types and revealing the differences in the findings. Moreover, the analyses included the climate properties of the most popular and crowded three cities in Turkey, namely Ankara (continental Mediterranean), Istanbul (transitional Mediterranean), and Izmir (Mediterranean). Prospective studies should involve other climate types to obtain universal results.

REFERENCES

Al-Saadi, S. N. & Al-Jabri, K. S. (2020). Optimization of envelope design for housing in hot climates using a genetic algorithm (GA) computational approach. *Journal of Building Engineering*, 32, 101712.

Anupong, W., Muda, I., AbdulAmeer, S. A., Al-Kharsan, I. H., Alviz-Meza, A., & Cárdenas-Escrocia, Y. (2023). Energy consumption and carbon dioxide production optimization in an educational building using the supported vector machine and ant colony system. *Sustainability*, 15(4), 3118.

Asadi, E., da Silva, M. G., Antunes, C. H., & Dias, L. (2012). A multi-objective optimization model for building retrofit strategies using TRNSYS simulations, GenOpt and MATLAB. *Building and Environment*, 56, 370-378.

Ascione, F., Bianco, N., De Masi, R. F., Mauro, G. M., & Vanoli, G. P. (2015). Design of the building envelope: A novel multi-objective approach for the optimization of energy performance and thermal comfort. *Sustainability*, 7(8), 10809-10836.

Ascione, F., Bianco, N., De Masi, R. F., Mauro, G. M., & Vanoli, G. P. (2017). Energy retrofit of educational buildings: Transient energy simulations, model calibration and multi-objective optimization towards nearly zero-energy performance. *Energy and Buildings*, 144, 303-319.

Ascione, F., De Masi, R. F., de Rossi, F., Ruggiero, S., & Vanoli, G. P. (2016). Optimization of building envelope design for nZEBs in Mediterranean climate: Performance analysis of residential case study. *Applied Energy*, 183, 938-957.

Bamdad, K., Cholette, M. E., Guan, L., & Bell, J. (2017). Ant colony algorithm for building energy optimisation problems and comparison with benchmark algorithms. *Energy and Buildings*, 154, 404-414.

Barber, K. A. & Krarti, M. (2022). A review of optimization based tools for design and control of building energy systems. *Renewable and Sustainable Energy Reviews*, 160, 112359.

Bertoldi, P. (2022). Policies for energy conservation and sufficiency: Review of existing policies and recommendations for new and effective policies in OECD countries. *Energy and Buildings*, 264, 112075.

Bigot, D., Miranville, F., Boyer, H., Bojic, M., Guichard, S., & Jean, A. (2013). Model optimization and validation with experimental data using the case study of a building equipped with photovoltaic panel on roof: Coupling of the building thermal simulation code ISOLAB with the generic optimization program GenOpt. *Energy and Buildings*, 58, 333-347.

Buonomano, A., Barone, G., & Forzano, C. (2022). Advanced energy technologies, methods, and policies to support the sustainable development of energy, water and environment systems. *Energy Reports*, 8, 4844-4853.

Caglayan, S., Ozorhon, B., Ozcan-Deniz, G., & Yigit, S. (2020a). A life cycle costing approach to determine the optimum insulation thickness of existing buildings. *Journal of Thermal Science and Technology*, 40(1), 1-14.

Caglayan, S., Yigit, S., Ozorhon, B., & Ozcan-Deniz, G. (2020b). A genetic algorithm-based envelope design optimisation for residential buildings. *Proceedings of the Institution of Civil Engineers - Engineering Sustainability*, 173(6), 280-290.

Caglayan, S., Ozorhon, B., & Kurnaz, L. (2022). Nationwide mapping of optimum wall insulation thicknesses: A stochastic approach. *Journal of Thermal Science and Technology*, 42(2), 169-202.

Ciardiello, A., Rosso, F., Dell'Olmo, J., Ciancio, V., Ferrero, M., & Salata, F. (2020). Multi-objective approach to the optimization of shape and envelope in building energy design. *Applied Energy*, 280, 115984.

Delgarm, N., Sajadi, B., Kowsary, F., & Delgarm, S. (2016). Multi-objective optimization of the building energy performance: A simulation-based approach by means of particle swarm optimization (PSO). *Applied Energy*, 170, 293-303.

EnergyPlus (2020, October 30). Turkish Weather for Energy Calculations (TWEC) for Energy Plus. https://energyplus.net/weather-region/europe_wmo_region_6/TUR

Eskander, M. M., Sandoval-Reyes, M., Silva, C. A., Vieira, S. M., & Sousa, J. M. (2017). Assessment of energy efficiency measures using multi-objective optimization in Portuguese households. *Sustainable Cities and Society*, 35, 764-773.

Ferrara, M., Fabrizio, E., Virgone, J., & Filippi, M. (2014). A simulation-based optimization method for cost-optimal analysis of nearly Zero Energy Buildings. *Energy and Buildings*, 84, 442-457.

Fortin, F. A., Rainville, F. M. D., Gardner, M. A., Parizeau, M., & Gagné, C. (2012). DEAP: Evolutionary algorithms made easy. *Journal of Machine Learning Research*, 13, 2171-2175.

Gao, H., Wang, X., Wu, K., Zheng, Y., Wang, Q., Shi, W., & He, M. (2023). A review of building carbon emission accounting and prediction models. *Buildings*, 13(7), 1617.

Ge, J., Wu, J., Chen, S., & Wu, J. (2018). Energy efficiency optimization strategies for university research buildings with hot summer and cold winter climate of China based on the adaptive thermal comfort. *Journal of Building Engineering*, 18, 321-330.

Ghalambaz, M., Yengejeh, R. J., & Davami, A. H. (2021). Building energy optimization using grey wolf optimizer (GWO). *Case Studies in Thermal Engineering*, 27, 101250.

Ghafoori, M. & Abdallah, M. (2022). Simulation-based optimization model to minimize equivalent annual cost of existing buildings. *Journal of Construction Engineering and Management*, 148(2), 04021202.

Gilles, F., Bernard, S., Ioannis, A., & Simon, R. (2017). Decision-making based on network visualization applied to building life cycle optimization. *Sustainable Cities and Society*, 35, 565-573.

Griego, D., Krarti, M., & Hernandez-Guerrero, A. (2015). Energy efficiency optimization of new and existing office buildings in Guanajuato, Mexico. *Sustainable Cities and Society*, 17, 132-140.

He, Y., Chu, Y., Song, Y., Liu, M., Shi, S., & Chen, X. (2022). Analysis of design strategy of energy efficient buildings based on databases by using data mining and statistical metrics approach. *Energy and Buildings*, 258, 111811.

Huang, Y. & Niu, J. L. (2016). Optimal building envelope design based on simulated performance: History, current status and new potentials. *Energy and Buildings*, 117, 387-398.

Jin, Q., Favoino, F., & Overend, M. (2017). Design and control optimisation of adaptive insulation systems for office buildings. Part 2: A parametric study for a temperate climate. *Energy*, 127, 634-649.

Junghans, L. & Darde, N. (2015). Hybrid single objective genetic algorithm coupled with the simulated annealing optimization method for building optimization. *Energy and Buildings*, 86, 651-662.

Kaya, R. & Caglayan, S. (2023). Potential benefits of thermal insulation in public buildings: Case of a university building. *Buildings*, 13(10), 2586.

Khan, F. A., Ullah, K., ur Rahman, A., & Anwar, S. (2023). Energy optimization in smart urban buildings using bio-inspired ant colony optimization. *Soft Computing*, 27(2), 973-989.

Kheiri, F. (2021). Optimization of building fenestration and shading for climate-based daylight performance using the coupled genetic algorithm and simulated annealing optimization methods. *Indoor and Built Environment*, 30(2), 195-214.

Kim, H. & Clayton, M. J. (2020). A multi-objective optimization approach for climate-adaptive building envelope design using parametric behavior maps. *Building and Environment*, 185, 107292.

Kontoleon, K. J. & Eumorfopoulou, E. A. (2010). The effect of the orientation and proportion of a plant-covered wall layer on the thermal performance of a building zone. *Building and Environment*, 45(5), 1287-1303.

Lee, D. Y., Seo, B. M., Yoon, Y. B., Hong, S. H., Choi, J. M., & Lee, K. H. (2019). Heating energy performance and part load ratio characteristics of boiler staging in an office building. *Frontiers in Energy*, 13(2), 339-353.

Li, L., Fu, Y., Fung, J. C., Qu, H., & Lau, A. K. (2021). Development of a back-propagation neural network and adaptive grey wolf optimizer algorithm for thermal comfort and energy consumption prediction and optimization. *Energy and Buildings*, 253, 111439.

Li, S., Liu, L., & Peng, C. (2020). A review of performance-oriented architectural design and optimization in the context of sustainability: Dividends and challenges. *Sustainability*, 12(4), 1427.

Lin, Y. & Yang, W. (2018). Application of multi-objective genetic algorithm based simulation for cost-effective building energy efficiency design and thermal comfort improvement. *Frontiers in Energy Research*, 6, 25.

Longo, S., Montana, F., & Sanseverino, E. R. (2019). A review on optimization and cost-optimal methodologies in low-energy buildings design and environmental considerations. *Sustainable Cities and Society*, 45, 87-104.

Malinauskaite, J., Jouhara, H., Ahmad, L., Milani, M., Montorsi, L., & Venturelli, M. (2019). Energy efficiency in industry: EU and national policies in Italy and the UK. *Energy*, 172, 255-269.

MENR (2022). *Republic of Türkiye Ministry of Energy and Natural Resources*. Türkiye National Energy Plan.

Naderi, E., Sajadi, B., Behabadi, M. A., & Naderi, E. (2020). Multi-objective simulation-based optimization of controlled blind specifications to reduce energy consumption, and thermal and visual discomfort: Case studies in Iran. *Building and Environment*, 169, 106570.

Niemelä, T., Kosonen, R., & Jokisalo, J. (2016). Cost-optimal energy performance renovation measures of educational buildings in cold climate. *Applied Energy*, 183, 1005-1020.

Ozel, M. (2022). Determination of indoor design temperature, thermal characteristics and insulation thickness under hot climate conditions. *Journal of Thermal Science and Technology*, 42(1), 49-64.

Perera, D. W. U., Winkler, D., & Skeie, N. O. (2016). Multi-floor building heating models in MATLAB and Modelica environments. *Applied Energy*, 171, 46-57.

Pooyanfar, M. & Topal, H. (2018). Assessing effectiveness of integrated building design parameters on energy performance and emissions in health care facilities by means of building energy modelling. *Journal of Thermal Science and Technology*, 38(2), 151-165.

Ren, H., Lu, Y., Wu, Q., Yang, X., & Zhou, A. (2018). Multi-objective optimization of a hybrid distributed energy system using NSGA-II algorithm. *Frontiers in Energy*, 12(4), 518-528.

Sharif, S. A. & Hammad, A. (2019). Simulation-based multi-objective optimization of institutional building renovation considering energy consumption, life-cycle cost and life-cycle assessment. *Journal of Building Engineering*, 21, 429-445.

Si, B., Tian, Z., Jin, X., Zhou, X., Tang, P., & Shi, X. (2016). Performance indices and evaluation of algorithms in building energy efficient design optimization. *Energy*, 114, 100-112.

Somu, N., MR, G. R., & Ramamritham, K. (2020). A hybrid model for building energy consumption forecasting using long short term memory networks. *Applied Energy*, 261, 114131.

Song, X., Ye, C., Li, H., Wang, X., & Ma, W. (2017). Field study on energy economic assessment of office buildings envelope retrofitting in southern China. *Sustainable Cities and Society*, 28, 154-161.

Ucar, A. (2024). The annual CO2 emissions and energy costs of different exterior wall structures in residential buildings in Türkiye. *Journal of Thermal Science and Technology*, 44(1), 1-17.

Wang, R., Lu, S., & Feng, W. (2020). A three-stage optimization methodology for envelope design of passive house considering energy demand, thermal comfort and cost. *Energy*, 192, 116723.

Wang, Z. L., Funada, T., Onda, T., & Chen, Z. C. (2023). Knowledge extraction and performance improvement of Bi2Te3-based thermoelectric materials by machine learning. *Materials Today Physics*, 31, 100971.

Yigit, S. (2021). A machine-learning-based method for thermal design optimization of residential buildings in highly urbanized areas of Turkey. *Journal of Building Engineering*, 38, 102225.

Yigit, S. & Ozorhon, B. (2018). A simulation-based optimization method for designing energy efficient buildings. *Energy and Buildings*, 178, 216-227.

Yu, J., Yang, C., & Tian, L. (2008). Low-energy envelope design of residential building in hot summer and cold winter zone in China. *Energy and Buildings*, 40(8), 1536-1546.

Yu, L., Qin, S., Zhang, M., Shen, C., Jiang, T., & Guan, X. (2021). A review of deep reinforcement learning for smart building energy management. *IEEE Internet of Things Journal*, 8(15), 12046-12063.

Yu, Z. J., Chen, J., Sun, Y., & Zhang, G. (2016). A GA-based system sizing method for net-zero energy buildings considering multi-criteria performance requirements under parameter uncertainties. *Energy and Buildings*, 129, 524-534.

Yue, N., Li, L., Morandi, A., & Zhao, Y. (2021). A metamodel-based multi-objective optimization method to balance thermal comfort and energy efficiency in a campus gymnasium. *Energy and Buildings*, 253, 111513.

Zhou, G., Moayedi, H., Bahiraei, M., & Lyu, Z. (2020). Employing artificial bee colony and particle swarm techniques for optimizing a neural network in prediction of heating and cooling loads of residential buildings. *Journal of Cleaner Production*, 254, 120082.

Zhou, Z., Wang, C., Sun, X., Gao, F., Feng, W., & Zillante, G. (2018). Heating energy saving potential from building envelope design and operation optimization in residential buildings: A case study in northern China. *Journal of Cleaner Production*, 174, 413-423.

Zune, M., Pantua, C. A. J., Rodrigues, L., & Gillott, M. (2020). A review of traditional multistage roofs design and performance in vernacular buildings in Myanmar. *Sustainable Cities and Society*, 60, 102240.

Journal Homepage: https://dergipark.org.tr/tr/pub/isibted

Isı Bilimi ve Tekniği Dergisi

Archive: https://tibtd.org.tr/dergi

Investigation of Flow and Heat Transfer Performance of Gyroid Structure as Porous Media

Alper Mete GENÇ [1,2] *, Ziya Haktan KARADENİZ [3]

[1] *Graduate School of Natural and Applied Sciences, Izmir Kâtip Celebi University, Izmir, Türkiye*
[2] *Bosch Thermotechnology, Manisa, Türkiye*
[3] *Energy Systems Engineering, Izmir Institute of Technology, Izmir, Türkiye*

A R T I C L E I N F O

2024, vol. 44, no.2, pp. 351-358

doi: 10.47480/isibted.1471713

Research Article
Received: 22 April 2024
Accepted: 20 August 2024

* *Corresponding Author*
e-mail: alper.m.genc@gmail.com

Keywords:
Heat exchanger
Heat transfer
TPMS
Gyroid
Porous media

ORCID Numbers in author order:
0000-0002-1290-9962
0000-0001-7850-7942

A B S T R A C T

There are active and passive methods used to improve heat transfer. One of the passive methods is utilising porous media with high heat transfer surface area. Porous media are divided into two groups: regular and irregular structures. One of the regular structures is triply periodic minimal surfaces (TPMS), which have been studied quite frequently recently. In this study, heat transfer and flow analysis of a Gyroid geometry, one of the most used TPMS in the literature, is investigated numerically considering the conjugate heat transfer conditions. A single porosity is considered (ε = 0.6), and aluminium, ceramic and PLA are selected for the heat exchanger material to examine the temperature change in the heat exchanger. To understand the different flow characteristics, Reynolds numbers are assumed to be 19.12, 95.61 and 172.09. The fluid inlet temperature is assumed to be constant at 298.15 K, and the initial temperature of the heat exchanger is assumed to be constant at 278.15 K to be consistent with the regenerative heat recovery temperature difference in ventilation standards. Nusselt numbers under different operating conditions are compared, and it is the ceramic material with low thermal diffusivity is at the highest level despite its low thermal conductivity. At the highest Reynolds number, it provided approximately 6% better heat transfer than the aluminium heat exchanger.

Gözenekli Ortam Olarak Gyroid Yapısının Akış ve Isı Transferi Performansının İncelenmesi

M A K A L E B İ L G İ S İ

Anahtar Kelimeler:
Isı değiştirici
Isı transfer
ÜYPMY
Gyroid
Gözenekli yapı

Ö Z E T

Isı transferini iyileştirmek için aktif ve pasif yöntemler kullanılmaktadır. Pasif yöntemlerden biri yüksek ısı transfer yüzey alanına sahip gözenekli ortamlardan faydalanmaktır. Gözenekli ortamlar düzenli ve düzensiz yapılar olmak üzere iki gruba ayrılır. Düzenli yapılardan biri de son zamanlarda sıkça çalışılan üçlü periyodik minimal yüzeylerdir (TPMS). Bu çalışmada, literatürde en çok kullanılan TPMS'lerden biri olan Gyroid geometrisinin ısı transferi ve akış analizi, eşlenik ısı transferi koşulları dikkate alınarak sayısal olarak incelenmiştir. Tek bir gözeneklilik (ε = 0.6) dikkate alınmış ve ısı değiştiricideki sıcaklık değişimini incelemek için ısı değiştirici malzemesi olarak alüminyum, seramik ve PLA seçilmiştir. Farklı akış karakteristiklerini anlamak için Reynolds sayılarının 19.12, 95.61 ve 172.09 olduğu varsayılmıştır. Akışkan giriş sıcaklığının 298,15 K'de sabit olduğu ve ısı değiştiricinin başlangıç sıcaklığının havalandırma standartlarındaki rejeneratif ısı geri kazanım sıcaklık farkıyla tutarlı olması için 278,15 K'de sabit olduğu varsayılmıştır. Farklı çalışma koşulları altındaki Nusselt sayıları karşılaştırılır ve düşük termal iletkenliğine rağmen düşük termal difüziviteye sahip seramik malzeme en yüksek seviyededir. En yüksek Reynolds sayısında, alüminyum ısı değiştiriciden yaklaşık %6 daha iyi ısı transferi sağlamıştır.

NOMENCLATURE

α	Thermal Diffusivity [m^2/s]	h	Heat Transfer Coefficient [W/m^2K]
a_p	Specific Area [m^2/m^3]	k	Thermal Conductivity [W/mK]
c_p	Specific Heat Capacity [J/kgK]	L	Length [m]
d_h	Hydraulic Diameter [m]	t	Time [s]
d_{hf}	Hydraulic Diameter [m]	μ	Dynamic Viscosity [Ns/m^2]
d_p	Pore Diameter [m]	D	Diameter [m]
ε	Porosity [-]	ΔP	Pressure Drop [Pa]
f	Friction factor [-]	Nu	Nusselt Number [-]
F_v^2	Pressure Exerted by the Fluid [Pa]	Re	Reynolds Number [-]
ρ	Density [kg/m^3]	V	Velocity [V]

INTRODUCTION

The advancement of technology has prompted researchers to explore various methods to enhance heat transfer effectively. Two primary approaches in this regard are active and passive methods. Active methods involve imparting additional energy to the heat-transferring fluid using external means, such as mechanical auxiliaries, rotating surfaces, mechanical mixing of flows, high or low-frequency surface vibration, flow vibration, and electrostatic fields. On the other hand, passive methods aim to improve heat transfer without additional energy input. This can be achieved through strategies such as coating heat transfer surfaces with materials of higher thermal conductivity, altering the heat transfer surface geometry, or creating intricate surface designs to increase surface area.

Increased heat transfer surface areas are commonly utilized in heat exchangers to enhance thermal efficiency. Among passive methods, the use of porous media has gained popularity due to its ability to increase heat transfer through a combination of high surface area and the formation of vortices within its complex structure. Porous media are light, compact, and can also be load-bearing materials. They find applications in diverse fields, such as aerospace engineering for evaporative cooling, electronic cooling, solar collectors, methane converters, catalytic converters, medical implantology, and heat exchangers.

Porous media can be categorized into two main types: periodic (regular) and stochastic (irregular) structures, distinguished primarily by the arrangement of pores which are shown in Figure 1 (Xu et al. 2015). Triply Periodic Minimal Surfaces (TPMS) are widely used structures among periodic porous media. TPMS consists of a combination of infinite, non-intersecting regions that repeat periodically in three main directions. These regions are qualified by having zero mean curvature (H = 0) at each point, which means that the curvature along the main curvature planes is equal. Neovius created his own structure in 1833 (Neovius, 1883), and Schwarz built up one of the most using structure, Diamond in 1865 (Schwarz, 1890). Subsequently, several other minimal surfaces, such as the Primitive and Hexagonal, were also discovered. In 1970, Schoen introduced many types of minimal surfaces, among which the Gyroid surface became particularly well-known (Schoen, 1970).

Femmer et al. (2015) found that the sheet-Diamond structure heat exchanger showed a better heat transfer performance according to the sheet-Gyroid, IWP, and Primitive geometries for a constant wall thickness (t=0.4 mm), under the laminar flow conditions (Re<15).

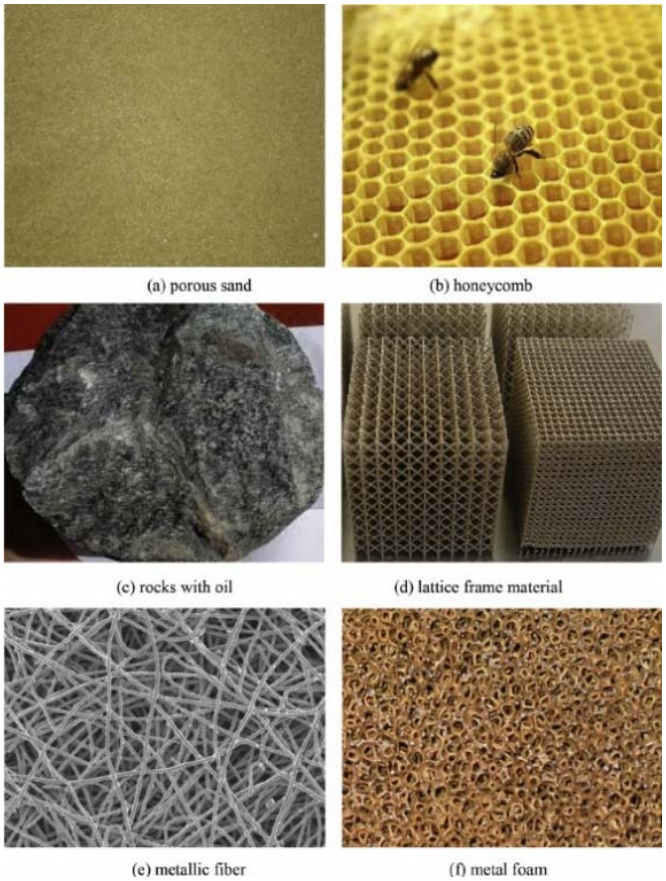

Figure 1. Different kinds of regular and irregular porous media (Xu et al. 2015)

Passos (2019) also indicated that sheet-diamond structure exhibited the best thermal performance. Iyer et al. (2022) emphasized that the sheet-Primitive geometry performed lowest heat performance, whereas the sheet-Diamond geometry had the best heat transfer performance. Reynolds (2020) found that Gyroid showed the best heat transfer performance compared to Diamond, flat plate heat exchanger and primitive for Re<2. Dharmalingam et al. (2022) presented that the TPMS heat exchangers improved heat transfer as 15–120% than a printed circuit heat exchanger for a constant pumping power. The Fischer Koch S heat exchanger increased the heat transfer performance as 23–356% at a constant pressure drop compared with the Diamond structure. Kaur and Singh (2021) numerically studied the comparison of the averaged heat transfer coefficient of the sheet-Gyroid and Primitive structures for a constant porosity and heat flux. According to the results, the sheet-Gyroid structure improved heat transfer coefficient more than the sheet-Primitive structure. Peng et al. (2019) observed that the Gyroid heat exchanger improved heat transfer rates by 7.5 times

compared to a traditional plate heat exchanger. Tang et al. (2023), focused on that heat transfer properties of TPMS geometries, distinctive TPMS structures of convective heat transfer mechanism and yield of heat distribution. Gyroid, Diamond, IWP and fins structures are evaluated. Based on this research, they conclude that the convective heat transfer coefficient of diamond 85% -207% higher, Gyroid 55%-137% higher, IWP 16%-55% higher than traditional heat transfer mechanism fins. In addition, diamond average convective heat transfer coefficient is 19.5%-37.2. % bigger than Gyroid. Reynolds et al. (2023) researched concentrates on the experimental characterization of pressure drop and heat transfer entire TPMS heat exchanger that produced via additive manufacturing. In order to observe temperature distribution in the heat exchanger, polymer has been chosen as heat exchanger material. This study focused on comparison of heat transfer and pressure drop of TPMS geometries and straight tube heat exchangers. In addition, this research Gyroid, Primitive, Diamond, F-K-S, F-K-C, IWP, Split P, F-RD, G Prime geometries are evaluated. In experimental test system, just straight tube heat exchanger and Gyroid heat exchanger are examined. After simulations and physical test results, when the pumping power is equal, Gyroid is 13% better Nusselt number than straight tube heat exchanger. Barakat and Bei Bei (2024) investigated heat transfer performance of sheet Gyroid, Diamond, SplitP and Lidinoid and five different sheet TPMS geometries which are proposed by them. According to their numerical results, TPMS2 which is proposed by authors showed better performance than sheet-Gyroid and sheet-Diamond geometries as 27.2% and 18%, respectively. Qian et al. (2024) experimentally investigated heat transfer characteristics of copper sheet- Gyroid, Primitive and Fischer- Koch S TPMS heat exchangers. Sheet Fischer-Koch S structure exhibited better heat transfer performance than sheet-Gyroid and sheet-Primitive structures. When comparing the three TPMS structures, the Fischer-Koch S structure performed 245.1% and 64.8% higher heat transfer performance than the Primitive and Gyroid structures, respectively. Alteneiji et al. (2022) numerically investigated the performance of sheet Primitive and Gyroid TPMS geometries. They found that the maximum convection heat transfer coefficient reached 1.400 W/m^{2}K for the Gyroid and 1.413 W/m^{2}K for the Primitive structures.

The aforementioned numerical studies consider work on the unit cell, which is composed of surfaces. There are very few studies that examine the specified geometries as periodic solid geometry instead of sheet unit cells. Also, there is no transient study to examine the real performance of TPMS heat exchangers. This study aims to investigate the flow and heat transfer performance of the Gyroid TPMS structure as a heat exchanger under transient conditions, which is one of the most used TPMS geometries, numerically. Creating the geometry as a solid model with a standard CAD program is very difficult. Therefore, a heat exchanger with a constant porosity value is used to understand the flow and thermal performance. For the stated reasons, this presented study is performed for a single porosity value of 0.6 for a periodic solid geometry. Aluminium, ceramic, and PLA are selected as heat exchanger materials to examine temperature changes in the heat exchanger. Reynolds numbers are chosen at 19.12, 95.61 and 172.09 to investigate the flow regime. Initial air inlet and solid temperatures are assumed to be 298.15 and 278.15 K, respectively, to be consistent with the regenerative heat recovery temperature difference in ventilation standards.

MATERIAL AND METHOD

Mathematical algorithms provide an exact method for Triply Periodic Minimal Surfaces (TPMS), leveraging the definition of minimal surfaces. Various approaches can be employed to design TPMS-based structures, including nodal approximation of the Weierstrass formula, numerical generation methods, and others. However, the simplest and most widely used approach is the level-set equation, which is derived from a sum defined in terms of the Fourier series.

In this study, a cylindrical Gyroid TPMS heat exchanger with 0.6 porosity is built according to Equation 1 by using Mathematica software and exported as .STL file extension. The built geometry is shown in Figure 2. Then, the geometry is imported with ANSYS Space Claim for cleaning, repairing, and fining the surface mesh to obtain the appropriate face size. It ensures that the surfaces generated on the solid model are not too small to produce a poor-quality volume mesh, which can cause convergence problems. The height and diameter of the heat exchanger and the inlet and outlet lengths of the system are chosen as 0.02 m due to reducing computational costs. To ensure that the surface area calculations and resulting heat transfer are not affected by the final surface resolution, the following procedure has been adopted.

$$\cos(x)\sin(y) + \cos(y)\sin(z) + \cos(z)\sin(x) = 0 \qquad (1)$$

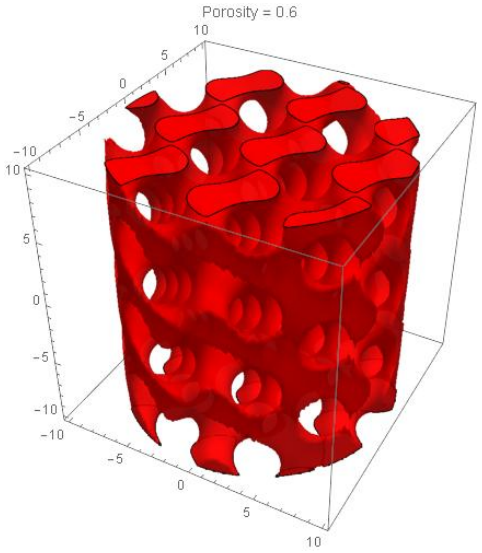

Figure 2. Created geometry by using Mathematica (https://github.com/metudust/RegionTPMS)

The transient 3D numerical model is developed by ANSYS CFX for heat transfer and fluid flow. The geometrical configuration of the computational domain and boundary conditions are shown in Figure 3. Analyses are carried out for Gyroid geometry for varied velocities of 0.1, 0.5 and 0.9 m/s, which correspond to 19.12, 95.61 and 172.09 Reynolds numbers, respectively, at laminar flow. As the boundary condition in the analysis, the outer surfaces of the fluid domain and the solid domain are defined as the walls. The inlet temperature of the fluid to the system is assumed to be 298.15 K, and the initial temperature of the heat exchanger is assumed to be 278.15 K. When choosing these temperatures, the change in the heat capacity of a certain mass over time is considered. Here, indoor, and outdoor temperatures used in ventilation systems are taken as the basis. It is envisaged to be used effectively in heat processes such as heat recovery. Aluminium, ceramic, and PLA are

chosen as heat exchanger materials to compare the differences in thermal properties. The thermophysical properties of the materials are given in Table 1. The thermophysical properties of air at 25 °C are used for the fluid. Natural convection effects have been neglected.

Table 1. Thermophysical properties of heat exchanger materials

Material	k (W/mK)	c_p (J/kgK)	ρ (kg/m³)	α (m²/s)	ρ^*c_p (J/m³K)
Aluminum	237.0	903.0	2700.0	9.71E-05	2.44E+06
Ceramic	1.50	1050.0	2400.0	5.95E-07	2.52E+06
PLA	0.13	1800.0	1300.0	5.58E-08	2.34E+06

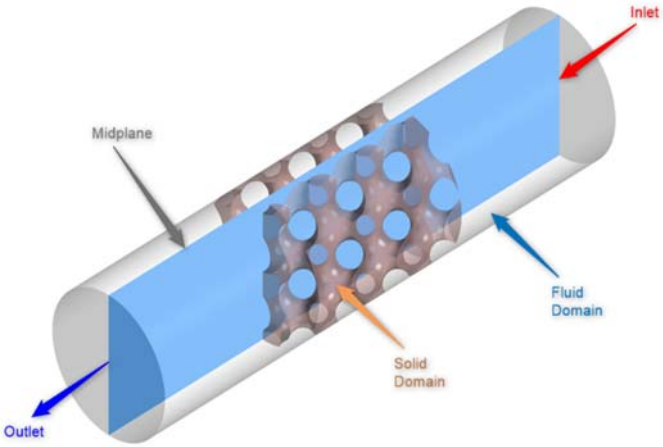

Figure 3. Geometrical configuration of the computational domain and boundary conditions

The Navier-Stokes equations are shown in Equations 2 and 3, respectively. The Shear Stress Transport (SST) turbulence model is used to understand the developed vortexes along the heat exchanger. SST model is prepared by Menter for some missing points of k- ω model. Menter improved the spurious free-stream sensitivity of k- ω model. Two region formularization which utilize k- ω model close wall, k- ε is used for the other part of flow are also improved (Sundén and Faghri, 2005). A high-resolution scheme is used to solve advection terms. For the transient scheme Second Order Backward Euler is used. Convergence criteria are set to 10−6 for all the governing equations.

$$\frac{\partial \rho}{\partial t} + \vec{\nabla}.\left(\rho \vec{V}\right) = 0 \tag{2}$$

$$\rho \frac{\partial V}{\partial t} = -\vec{\nabla}P + \rho \vec{g} + \mu \nabla^2 \vec{V} \tag{3}$$

Mesh independency analysis is conducted for four different mesh element numbers (M1 = 2371748, M2 = 3557621, M3 = 5352423 and M4 = 8884799). Heat rate values, which are critical parameters for the comparison of numerical data, are calculated using M1, M2, M3, and M4 to evaluate mesh independence. According to Figure 4, all meshes are matched up with each other. To evaluate temperature and velocity distributions at higher resolution with reduced computational costs, M2 is chosen. In here, fluid -solid interface element size 0.15 mm, fluid body element size 0.3 mm, solid-fluid interface 0.4 mm, solid body element size. It is determined as 0.8 mm. In places where the element size is small, more frequent mesh is generated. This allows the areas with frequent mesh to be analysed better. The grid quality is ensured with Skewness to be less than 0.8 for all meshes.

Time-step independency is also carried out for 0.05, 0.1, 0.2, 0.4 and 0.5 s. Figure 5 shows that 0.2 s is suitable for obtaining an accurate solution due to the occurring deviation for the first 5 s at 0.4 and 0.5 s time steps. The variation of the total number mesh and/or time step size do not cause any remarkable changes in the time-dependent variation of the heat rate. The maximum deviation between the M1 and the M4 mesh is found to be less than 0.1%. Besides, regarding the time-step size, the maximum difference is obtained as 0.1%. Consequently, the preliminary survey ensures that the results are independent of the mesh number and the time-step size.

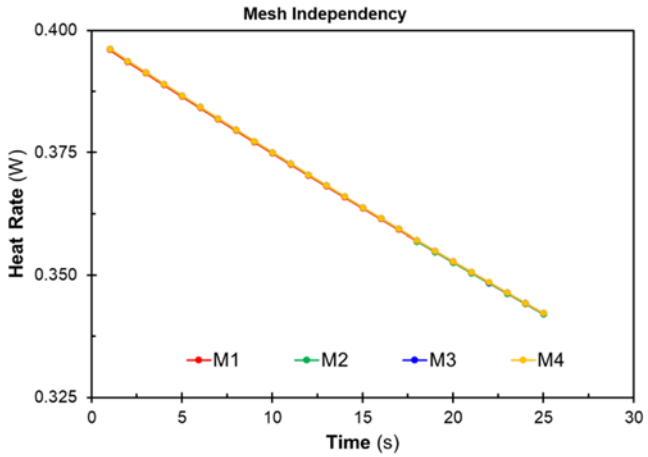

Figure 4. Mesh independency analysis.

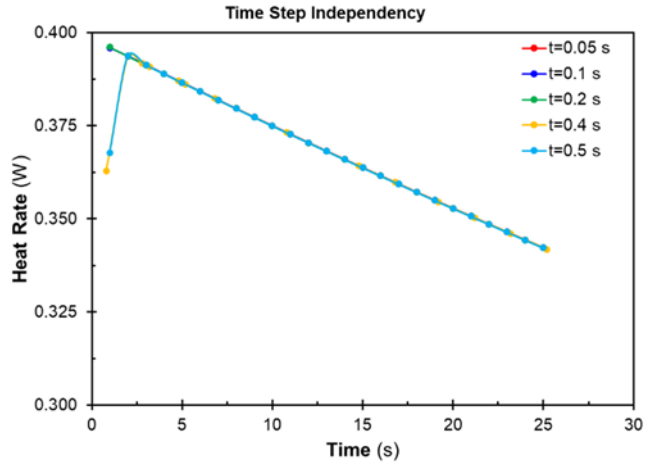

Figure 5. Time step independency

The Reynolds number, *Re,* of the gyroid structure is reported as a hydraulic property which is defined as:

$$Re = \frac{\rho V d_h}{\mu} \tag{4}$$

ρ is the density of the fluid, V is the velocity, d_h is the hydraulic diameter, and μ is the fluid's viscosity. d_h is defined as $4V/A_s$ where V is the domain volume, and A_s is the wetted surface area of the TPMS [6].

The average Nusselt number is defined below:

$$Nu = \frac{\bar{h} d_h}{k} \tag{5}$$

In here, $\bar{h}$ is the average heat transfer coefficient and k is thermal conductivity of the fluid. The averaged heat transfer coefficient, $\bar{h}$ is obtained from analysis results.

Bulk temperature has been calculated with the following equation:

$$T_{bulk} = T_s - (^{T_{inlet} + T_{outlet}}/_{2}) \quad (6)$$

Here, Ts is the surface temperature of the heat exchanger interface, which is conducted with fluid. T_{inlet} and T_{outlet} are the fluid inlet and outlet temperatures, respectively.

The fanning friction coefficient f is expressed as follows:

$$f = \frac{\Delta P d_h}{2\rho V^2 L} \quad (7)$$

where ΔP is the pressure drop; L is the length of the heat exchanger. ΔP was also obtained from analysis results for all velocities.

VALIDATION

Validation of the system was done by Rathore et al. (2023) is carried out according to the pressure drop values per unit length. There are several methods to obtain the pressure drop of porous media and TPMS geometries. One of these methods is presented by Fu et al. (2019), who investigated hydrodynamic and mass transfer performances for Diamond, Gyroid and Primitive TPMS geometries. The following equation is used to calculate the particle or pore diameter (d_p):

$$d_p = \frac{6(1-\varepsilon)}{a_p} \quad (8)$$

Here, ε represents the porosity or void ratio value. a_p is the specific area (m^2/m^3). The rearranged Re number is as follows:

$$Re = \frac{\rho_G V_G d_p}{(1-\varepsilon)\mu_G} = \frac{3}{2}\frac{\rho_G V_G d_{hf}}{\varepsilon \mu_G} \quad (9)$$

Also, d_{hf} means the hydraulic diameter.

$$d_{hf} = \frac{4\varepsilon}{a_p} \quad (10)$$

It is stated that the Re number would be in the range of 0-2500, and the fluid velocity would be in the range of 0-3.5 m/s (Fu et al., 2019). The pressure drop for unit length is calculated by Equation 11:

$$\frac{\Delta p}{\Delta L} = \psi \frac{1-\varepsilon}{\varepsilon}\frac{F_V{}^2}{d_p} \quad (11)$$

$$\psi = \frac{150}{Re} + 1.75 \quad (12)$$

$$F_V = \mu_G \sqrt{\rho_G} \quad (13)$$

The expression ψ is a resistance coefficient that comes from the Ergun equation (Equation 12). $F_V{}^2$ represents the amount of pressure exerted by the fluid (Equation 13).

The present results as shown in Figure 6 match perfectly and therefore indicate the accuracy of the present numerical model.

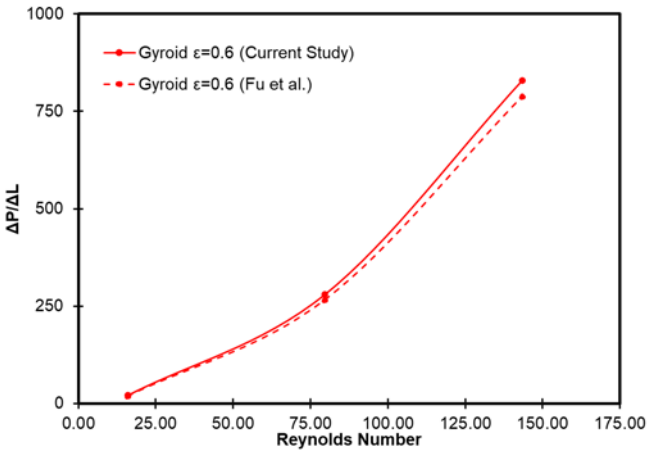

Figure 6. Variation in pressure drop per unit length for the validation study

RESULTS AND DISCUSSIONS

The transient 3D numerical model is developed by ANSYS CFX for heat transfer and fluid flow. Analyses are carried out for gyroid geometry for varied velocities of 0.1, 0.5 and 0.9 m/s and these values correspond to 19.12, 95.61 and 172.09 Reynolds numbers, respectively. All velocities are corresponded to laminar flow. As the boundary conditions, the outer surfaces of both domains are defined as adiabatic. The inlet temperature of the fluid to the system is assumed to be 298.15 K, and the initial temperature of the heat exchanger is assumed to be 278.15 K. Boundary conditions are shown in Figure 3. Also, the midplane is shown to provide a better understanding of the results. Transient analyses are carried out in 0.2 s time steps for a total of 25 s. Aluminium, ceramic and PLA are chosen as heat exchanger materials to compare the difference of thermal properties.

Figure 7. shows the comparison of the friction factor varying Reynolds numbers. The friction factor decreases with increasing Reynolds numbers. These results are similar to an experimental study by Genc et al. (2022).

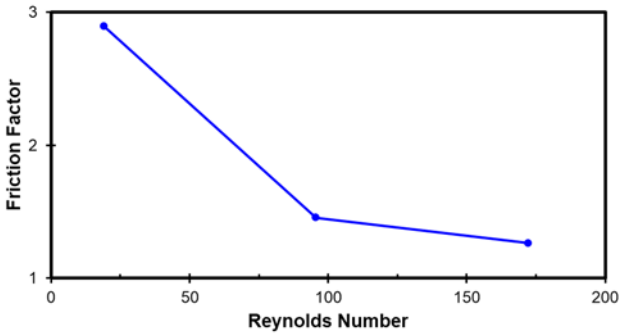

Figure 7. Friction factor against Reynolds number

Figure 8 shows velocity streamlines of 19.12, 95.61 and 172.09 Reynolds numbers for ceramic heat exchanger. While no obvious vortex formation is seen in Figure 7 (a), it begins to form in (b) and becomes most obvious in (c). This shows that as the velocity increases, the vortex formation in the exchanger increases. For a Reynolds number of 19.12, the flow passes through the exchanger at the same velocity, and for a Reynolds number of 95.61, it reaches 2.5 m/s in the exchanger. For the Reynolds number of 172.09, it reaches its highest value as 5 m/s. Similar results can be seen in Figure 8.

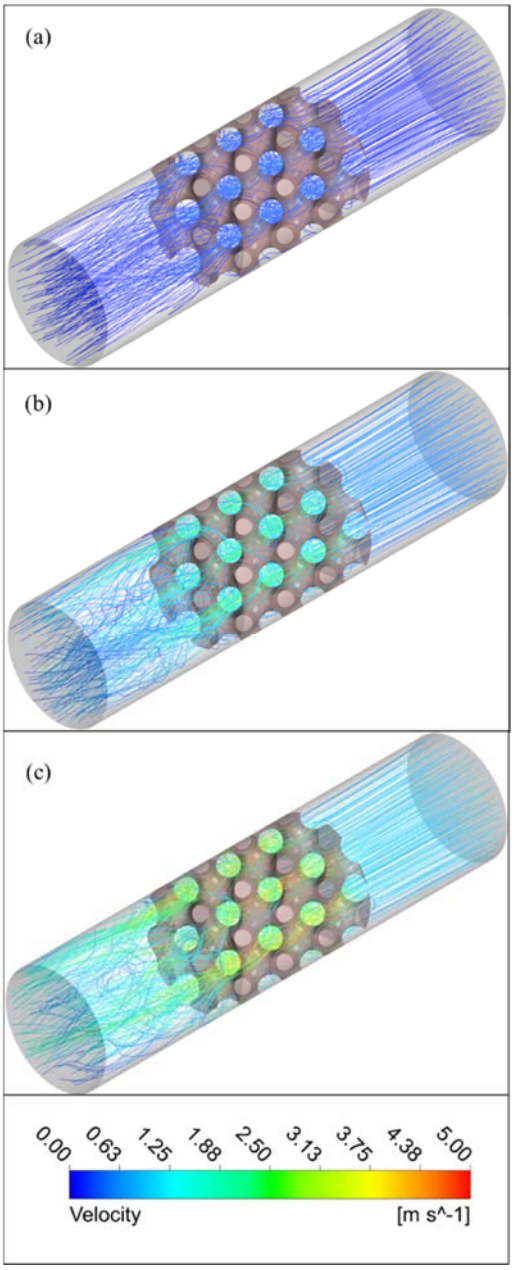

Figure 8. Velocity streamlines for (a) Re=19.12, (b) Re=95.61 and (c) Re=172.09 at 25 s.

Velocity streamlines are also shown in Figure 9 using the system's midplane. It is clear that vortices increase with increasing fluid inlet velocity. Vortices become more evident, especially after the fluid leaves the heat exchanger. This shows that after the fluid accelerates in the exchanger, a vortex forms right at the exchanger's outlet.

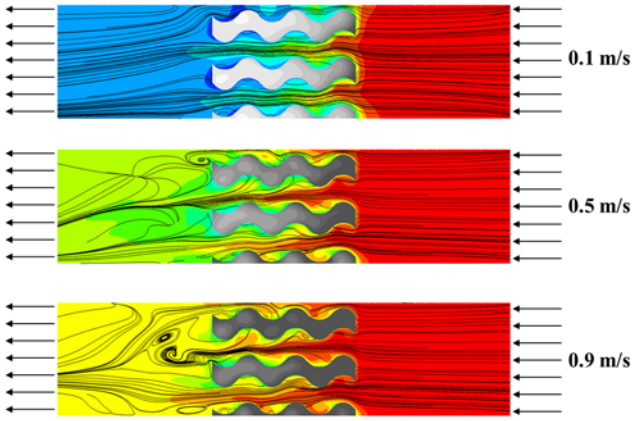

Figure 9. Velocity streamlines for all Reynolds numbers at 25 s.

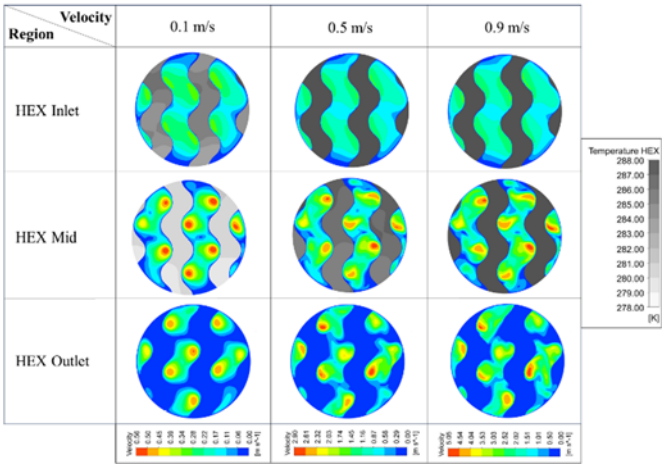

Figure 10. Velocity contours for HEX inlet, mid and outlet planes of ceramic heat exchanger at 25 s.

Figure 10 shows the velocity and temperature contours at the ceramic heat exchanger's HEX inlet, middle and outlet planes. The reason for choosing a ceramic heat exchanger is to achieve higher efficiency in terms of heat transfer. Here, while no significant change is observed for all velocities in the inlet section of the heat exchanger, the velocity increases significantly in the mid-plane and outlet plane, reaching approximately 3 m/s for Re = 95.61 and 5 m/s for Re = 172.09. It is seen that vortex formation begins at the outlet plane for Re = 95.61, and it becomes quite evident for Re = 172.09.

The Nu number against the Re number is shown in Figure 11 for all heat exchanger materials. The Nu number increases with increasing Re number for all. Here, it can be seen that the ceramic has the highest Nu number. As a result of the analysis, the material with the highest average convection coefficient was ceramic. Despite the thermal conductivity of the ceramic material, which is quite lower than the aluminium material, it provides a higher heat transfer rate with its high specific heat capacity and density multiplication (Table 1), that is, volume-specific heat capacity. According to the results, at the highest Re number, it provided approximately 6% better heat transfer than the aluminium heat exchanger.

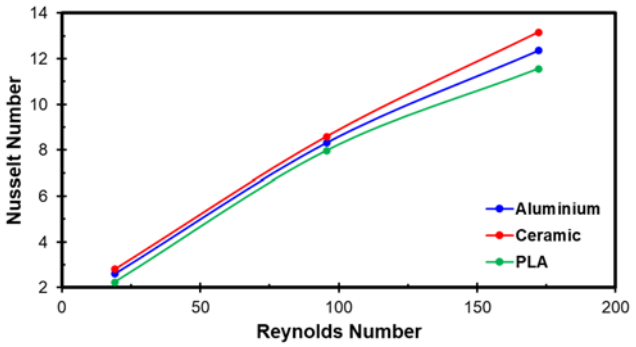

Figure 11. Nu number against Re number

Temperature contours for both solid and fluid domains are shown in Figure 12. There is no significant change in temperature distribution for the aluminium heat exchanger, while the temperature gradients in the ceramic and PLA heat exchanger are more pronounced. The reason for this was the thermal diffusivity. The fact that the ceramic material had a lower thermal diffusivity value ensures that it did not quickly remove the heat from its body (Table 1). At high velocities, the heat capacity of the ceramic heat exchanger decreases. This prevents temperature

distribution within the heat exchanger. However, for PLA heat exchangers, temperature distribution can also be seen at higher velocities. This can be explained by the higher specific heat capacity of PLA material (Table 1). At the highest Reynolds number (172.09), temperatures of 285 K can be observed in the ceramic heat exchanger, while the aluminium heat exchanger reaches 288 K. This value drops to 283 K in the PLA heat exchanger. This is due to its low thermal conductivity and high heat capacity of PLA.

Considering the fluid temperatures, at Re = 19.12, the temperature around the heat exchanger drops to 278 K for ceramic and PLA materials, while it is in the range of 280 - 282 K for the aluminium heat exchanger. While the fluid temperature drops to 286 K for PLA and ceramic materials, it is around 290 K for aluminium materials. In addition to that, at Re = 172.09, as the fluid passes quickly around the exchanger, the temperature generally drops to 292 K.

CONCLUSION

This study aims to numerically investigate the flow and heat transfer performance of the Gyroid structure as a heat exchanger under transient conditions, which is one of the most used TPMS geometries. Creating the geometry as a solid model with a standard CAD program is very difficult. Therefore, a heat exchanger with a porosity value of 0.6 was built to understand flow and thermal performance. For the stated reasons, this presented study was performed for a single porosity value (0.6) for a periodic solid geometry. Aluminium, ceramic, and PLA were selected as the heat exchanger material to examine the temperature change in the heat exchanger. Reynolds numbers are chosen at 19.12, 95.61 and 172.09 to investigate the flow regime. Initial air inlet and solid temperatures were assumed to be 298.15 and 278.15 K, respectively, to be consistent with the regenerative heat recovery temperature difference in ventilation standards.

According to the results:

The velocity increases, the vortex formation in the exchanger increases. For a Reynolds number of 19.12, the flow passes through the exchanger at the same velocity, and for a Reynolds number of 95.61, it reaches 2.5 m/s in the exchanger. For the Reynolds number of 172.09, it reaches its highest value as 5 m/s.

Ceramic material has the highest Nu number. As a result of the analysis, the material with the highest average convection coefficient was ceramic. Despite the thermal conductivity of the ceramic material, which is quite lower than the aluminium material, it provides a higher heat transfer rate with its high specific heat capacity and density multiplication, that is, volume-specific heat capacity and also low thermal diffusivity. According to the results, at the highest Re number, it provided approximately 6% better heat transfer than the aluminium heat exchanger.

While no specific change is observed in the temperature distribution in the aluminium heat exchanger, the temperature gradients are more pronounced in the ceramic and PLA heat exchangers. This is due to thermal diffusivity. The lower thermal diffusivity value of the ceramic and PLA materials ensure that the heat does not quickly dissipate from its body.

Even at low Re numbers, Gyroid geometry creates vortex which causes turbulence in the flow, thus providing high heat transfer. This shows that Gyroid TPMS structures can be used in heat transfer applications.

As future works:

Heat exchangers which have different porosities (0.5, 0.7, 0.8 etc.) and geometries (diamond, primitive) will be built to understand the effect of geometry and porosity.

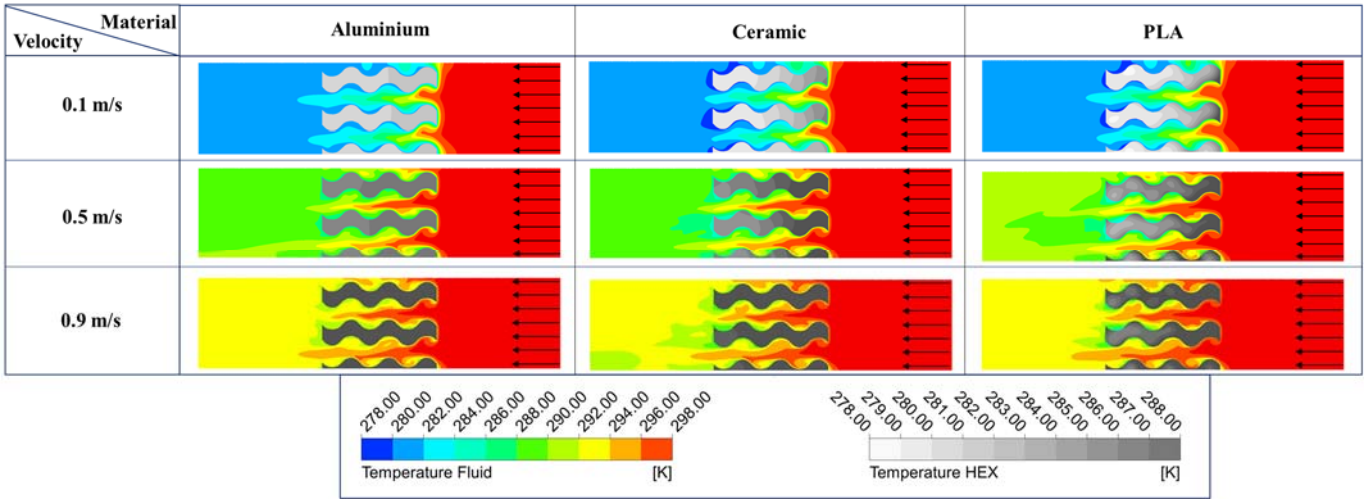

Figure 12. Temperature contours for all heat exchanger materials at 0.1, 0.5 and 0.9 m/s at 25s

REFERENCES

Alteneiji, M., Ali, M. I. H., Khan, K. A., & Al-Rub, R. K. A. Heat transfer effectiveness characteristics maps for additively manufactured TPMS compact heat exchangers, Energy Storage and Saving, Volume 1, Issue 3, 2022.

Barakat, A., & Sun, B. (2024). Enhanced convective heat transfer in new triply periodic minimal surface structures: Numerical and experimental investigation. International Journal of Heat and Mass Transfer, 227, 125538.

Dharmalingam, L.K.; Aute, V.; Ling, J. Review of Triply Periodic Minimal Surface (TPMS) based Heat Exchanger

Designs. In Proceedings of the International Refrigeration and Air Conditioning Conference at Purdue, West Lafayette, IN, USA, 10–14 July 2022.

Femmer, T., Kuehne, A. J., & Wessling, M. (2015). Estimation of the structure dependent performance of 3-D rapid prototyped membranes. Chemical Engineering Journal, 273, 438-445.

Fu, Y., Bao, J., Wang, C., Singh, R. K., Xu, Z., &Panagakos, G. (2019). CFD Study of Countercurrent Flow in Triply Periodic Minimal Surfaces withCO2BOL Solvent (No. PNNL-29590). Pacific Northwest National Lab. (PNNL), Richland, WA (United States).

Genç, A.M.; Vatansever, C.; Koçak, M.; Karadeniz, Z.H. Investigation of Additively Manufactured Triply Periodic Minimal Surfaces as an Air-to-Air Heat Exchanger. In Proceedings of the REHVA 14th HVACWord Congress, Rotterdam, The Netherlands, 22–25 May 2022.

https://github.com/metudust/RegionTPMS

Iyer, J., Moore, T., Nguyen, D., Roy, P., & Stolaroff, J. (2022). Heat transfer and pressure drop characteristics of heat exchangers based on triply periodic minimal and periodic nodal surfaces. Applied Thermal Engineering, 209, 118192.

Kaur, I., & Singh, P. (2021). Flow and thermal transport characteristics of Triply-Periodic Minimal Surface (TPMS)-based gyroid and Schwarz-P cellular materials. Numerical Heat Transfer, Part A: Applications, 79(8), 553-569.

Neovius E.R., Bestimmung Zweier Spezieller Periodischer Minimalflachen, Akad. Abhandlungen, Helsinki, Finland, 1883.

Peng, H., Gao, F., & Hu, W. (2019). Design, modeling and characterization on triply periodic minimal surface heat exchangers with additive manufacturing.

Qian, C., Wang, J., Zhong, H., Qiu, X., Yu, B., Shi, J., & Chen, J. (2024). Experimental investigation on heat transfer characteristics of copper heat exchangers based on triply periodic minimal surfaces (TPMS). International Communications in Heat and Mass Transfer, 152, 107292.

Rathore, S. S., Mehta, B., Kumar, P., & Asfer, M. (2023). Flow characterization in triply periodic minimal surface (TPMS)-based porous geometries: Part 1—Hydrodynamics. Transport in Porous Media, 146(3), 669-701.

Reynolds, B. W., Fee, C. J., Morison, K. R., & Holland, D. J. (2023). Characterisation of heat transfer within 3D printed TPMS heat exchangers. International Journal of Heat and Mass Transfer, 212, 124264.

Reynolds, B.W. Simulation of Flow and Heat Transfer in 3D Printable Triply Periodic Minimal Surface Heat Exchangers; University of Canterbury: Christchurch, New Zealand, 2020.

Schoen A. H., Infinite periyodik minimal surfaces without selfintersections, NASA Technical Note No. D-5541, NASA, 1970.

Schwarz H.A., Ueber ein Modell eines Minimalflachenst€uckes, welches langs seiner Begrenzung vier gegebene Ebenen rechtwinklig trifft. In: Gesammelte Mathematische Abhandlungen, Springer, Berlin, Heidelberg, pp. 149–150, 1890.

Sundén, B., & Faghri, M. (Eds.). (2005). Modelling and Simulation of Turbulent Heat Transfer (Vol. 15). WIT press.

Tang, W., Zhou, H., Zeng, Y., Yan, M., Jiang, C., Yang, P., ... & Zhao, Y. (2023). Analysis on the convective heat transfer process and performance evaluation of Triply Periodic Minimal Surface (TPMS) based on Diamond, Gyroid and Iwp. International Journal of Heat and Mass Transfer, 201, 123642.

Xu, H. J., Gong, L., Zhao, C. Y., Yang, Y. H., & Xu, Z. G. (2015). Analytical considerations of local thermal non-equilibrium conditions for thermal transport in metal foams. International Journal of Thermal Sciences, 95, 73-87.

Journal Homepage: https://dergipark.org.tr/tr/pub/isibted

Isı Bilimi ve Tekniği Dergisi

Archive: https://tibtd.org.tr/dergi

PV/T System Application for Renewable Heat and Electric Energy in Buildings: Performance and Techno-Economic Analysis

Kıvanç BAŞARAN [1, *], İlayda KOÇ [2]

[1] *Manisa Celal Bayar Üniversity, Faculty of Technology, Department of Electrical Engineering, Turgutlu, 45400, Manisa, Türkiye*
[2] *Eldor Electronics and Plastic Materials Manufacturing and Trading Co. Ltd., Department of Automation Planning, Gaziemir, 35410, Izmir, Turkey*

A R T I C L E I N F O

2024, vol. 44, no.2, pp. 359-373

doi: 10.47480/isibted.1477069

Research Article
Received: 02 May 2024
Accepted: 12 September 2024

* *Corresponding Author*
e-mail: kivanc.basaran@cbu..edu.tr

Keywords:
Photovoltaic/thermal systems
Techno-economic analysis
Renewable heating and electricity
Performance analaysis
Degradation rate

ORCID Numbers in author order:
0000-0001-9613-6620
0000-0002-9575-4088

A B S T R A C T

Electricity and thermal energy are used extensively in residential buildings. Meeting these needs with different systems cause loss of efficiency, and an increase initial investment cost which are critical when making investment decisions. Therefore, photovoltaic thermal (PV/T) systems are used to reduce the economic burden of home users. In this article, it is aimed to determine the performance of the PV/T system and to make an economic analysis by considering the instantaneous electrical and thermal efficiency. Net present value (NPV), payback period (PBP) and levelized cost of energy (LCOE) values were used to evaluate the system economically. The novelty of this study is the efficiency of the PV/T collectors, the ambient temperature as well as the main water temperature was taken into consideration and the heat and electrical energy to be produced were calculated by taking the efficiency values calculated on an hourly basis. Also, the losses and the annual degradation of the entire system are included in the calculation. As a result of the analyses, the LCOE, NPV, PBP, average electrical and thermal efficiencies were found as 0.091 €/kWh, 2718.5 €, 6 years, 14.7% and 62.3%, respectively, for a project size of 8.96 m² in a 25-year life cycle.

Binalarda Yenilenebilir Isı ve Elektrik Enerjisi için PV/T Sistem Uygulaması: Performans ve Tekno-Ekonomik Analiz

M A K A L E B İ L G İ S İ

Anahtar Kelimeler:
Fotovoltaik/termal sistemler
Tekno-ekonomik analiz
Yenilenebilir ısıtma ve elektrik
Performans analizi
Bozulma oranı

Ö Z E T

Konutlarda elektrik ve termal enerji yoğun olarak kullanılmaktadır. Bu ihtiyaçların farklı sistemlerle karşılanması verim kaybına ve yatırım kararları alırken kritik öneme sahip olan ilk yatırım maliyetinin artmasına neden olmaktadır. Bu nedenle, ev kullanıcılarının ekonomik yükünü azaltmak için fotovoltaik termal (PV/T) sistemler kullanılmaktadır. Bu makalede, PV/T sisteminin performansını belirlemek ve anlık elektriksel ve termal verimliliği dikkate alarak ekonomik bir analiz yapmak amaçlanmıştır. Sistemin ekonomik olarak değerlendirilmesinde net bugünkü değer (NPV), geri ödeme süresi (PBP) ve seviyelendirilmiş enerji maliyeti (LCOE) değerleri kullanılmıştır. Bu çalışmanın özgünlüğü, PV/T kollektörlerinin veriminin, ortam sıcaklığının yanı sıra şebeke suyu sıcaklığı da dikkate alınarak belirlenmiş olması ve saatlik bazda hesaplanan verim değerleri esas alınarak üretilecek ısı ve elektrik enerjisinin hesaplanmış olmasıdır. Ayrıca, tüm sistemin kayıpları ve yıllık bozulma oranı da hesaplamaya dahil edilmiştir. Yapılan analizler sonucunda, 25 yıllık yaşam döngüsünde 8,96 m² proje büyüklüğü için LCOE, NPV, PBP, ortalama elektriksel ve termal verimlilikler sırasıyla 0,091 €/kWh, 2718.5 €, 6 yıl, %14,7 ve %62,3 olarak bulunmuştur.

NOMENCLATURE

PV/T	photovoltaic/thermal
PV	photovoltaic
TMY	typical meteorological year
NPV	net present volue
PBP	pay back pariod
LCOE	levelized cost of energy
NOCT	nominal operating cell temperature
Q	suful heat gain
Tpm	Mean collector plate temperature
O&M	operating and maintanance
A	collector area
η	efficiency
Ta	ambient temperature
$G_{I,h}$	hourly total in-plane irradiance

INTRODUCTION

The sun is the largest energy source for the world. There are basically two ways to make available the energy provided by the sun. The first is to convert the solar energy into thermal energy and the other is to convert it into electrical energy. Because of their unique advantages, both technologies are increasingly used in residential and industrial applications. Because of the heat and electrical energy obtained from the sun often complement each other and to eliminate the disadvantages arising from the use of these two technologies separately, it is thought that it is more convenient to produce heat and electrical energy from the same panels. A PV/T collector is a module which combines the photovoltaic and thermal technologies into the same panel.

The technical and economic suitability of a water-based PV/T collector was first stated by Martin Wolf (Wolf, 1976) in 1976. Then in 1978 the first liquid-based PV/T was tested in a house by Böer and Tamm (Boer and Tamm, 2003) in 2003. After these two experimental studies, many researchers started to work in this field. In 1978, TRNSYST model was developed by using mathematical equations of active cooled PV/T collectors at Arizona State University (Florschuetz, 1979). In a study conducted at MIT's laboratories in 1978, the electrical and thermal efficiency of the PV/T collector were measured as 6.5% and 40%, respectively (Hendrie, 1982). After that, many studies have been done to increase the efficiency of the PV/T collectors in USA, Japan, Netherlands, Denmark, and Germany (Cox, 1985; Suzuki and Kitamura, 1979, Karl, 1979, Komp, 1985). Although studies on the PV/T collectors have been reduced due to low oil prices between 1980 and 1990, some studies done in Switzerland and Yugoslavia (Schwartz et al., 1983; Lalovic et al., 1986; Lalovic et al., 1988). In 1992, with the political recognition of global warming and climate change, efforts in the PV/T collectors have accelerated again. Especially in Germany, Denmark and the Netherlands, many projects were realized between 1990-2000 (Zondag et. al, 2003; Leenders et al., 2000; Bakker et al., 2002; Bakker et al., 2004; Rockendorf et al. 1999; Hausler and Rogass, 2000; Soerensen, 2001). In the following years, many countries such as Japan, India, Israel, Brazil, Taiwan, Cyprus, and the USA worked about the PV/T (Tripanagnostopoulos et al., 2002; Tselepis and Tripanagnostopoulos, 2002; Kalogirou, 2001; Bergene and Løvvik, 1995; Meir et al., 2002; Sandnes and Rekstad, 2002; Hayakashi, 1989; Fujisawa and Tani, 1997; Ito et al., 1999; Huang et al., 1999; Huang et al., 2001; Garg and Agarwal, 1995; Thomas et al., 2000; Krauter et al., 1999; Krauter et al., 2001)

The use of renewable distributed power plants is important to prevent environmental pollution caused by energy supply, to eliminate geopolitical risks and to prevent losses in the transmission of energy. In particular, the issue of producing energy where it is consumed has been frequently studied recently. It will be advantageous in many ways to produce the energy needed with a single system instead of installing separate systems for the supply of electrical energy and thermal energy in houses. The importance of this study is that it has been shown that electricity and thermal energy supply in residences can be met economically with PV/T collectors. The performance rate and efficiency of PV/T panels vary depending on the current meteorological and system conditions. Therefore, using a single value in calculating the amount of energy does not give accurate results. In addition, the amount of electricity produced in PV panels is lower every year than the previous year, even if all conditions are the same. The originality of this study is to calculate the performance and efficiency values under current conditions and to know the amount of energy to be produced according to these values. In addition, the amount of thermal and electrical energy to be produced by the system during its 25-year operating life is calculated by considering the annual degradation rate.

The structure of article as follows: Firstly, a detailed literature review was conducted, and related papers were presented in the introduction in accordance with the subject compliance and the date of presentation. We have organised the rest of this paper in the following way. The location, data set, PV/T collector, measurement sensors and reference house are described in the Section 2. In section 3, the market price of the system equipment's, electricity and thermal energy prices, financial parameters and assumptions were explained. The electrical and thermal model, the economic analysis model and the developed MATLAB/Simulink model of the PV/T collector were explained in section 4. The rest of the manuscript includes the results and conclusion sections.

Literature Review

The water-based PV/T collectors, which are the subject of this study, are widely used since they have higher efficiency than air-based collectors. Moreover, water-based collectors provide more uniform cooling of the PV cell than air-based collectors (Jai, 1994). Water based PV/T collectors can be manufactured in two ways such as glazed and unglazed. Due to the increase in heat, the electrical efficiency of the glazed PV/T collector is low while the thermal efficiency of the unglazed PV/T collector is low (Kim, 2012). The electrical and thermal efficiency of the PV/T collectors depend on the flow distribution of the water in the collector. Therefore, the design of water-carrying channels is of great importance. The water-carrying channels are optimized in such a way that they can effectively transfer heat from the collector to the fluid in the channel. Aste et al. (Aste et al., 2015) covered the upper surface of the PV/T collector with amorphous silicon and microcrystalline silicon solar cells. While the upper surface of the collector converts solar radiation to electrical energy, the lower surface of the collector converts solar radiation into thermal energy as it is sensitive to the infrared region. JieJia et al. (JieJia et al., 2006) investigated

the effects of packing factor and flow rate on PV / T efficiency and determined that the increase in packing factor decreased the thermal efficiency of the system.

The ambient and the collector temperature affect both the electrical and thermal efficiency of the PV/T. Temperature increase in PV/T collectors adversely affects the electrical efficiency. Since the panel temperature absorbed by the liquid fluid in PV/T collector, higher efficiency is obtained than similar PV panels. Saitoh et al. (Saitoh et al., 2003) analysed the electrical and thermal efficiency of water-based PV/T system experimentally. The results showed that the electrical efficiency varied from 10% to 13%, and the thermal efficiency ranged from 40% to 50%. Minglu et al. (Minglu, 2016) examined a PV/T system for Shanghai climate condition which has heat pump. They found that when the top temperature was 69.2 °C, the electrical conversion efficiency was 12.18% and when the operating temperature decrease to 45 °C the electrical efficiency increases to 13.4%. Another experimental study was carried out at Politecnico di Milano University. The experimental study was performed in outdoor conditions on a commercial PV/T at the three different locations. In that study, the electrical efficiency of water-based PV/T was found as 13%, 13.6%, 13.4% and the overall efficiency was found as 32.7%, 36.1 and 40.6 for Paris, Milan, Athens respectively (Niccolò, 2016). Fudholi et al (Fudholi, 2014) used the spiral flow absorber to increase the efficiency. Their results showed that the total a PV/T efficiency, PV efficiency and thermal efficiency as 68.4%, 13.8%, and 54.6%, respectively. The other study has indicated that the building integrated PV/T collector's thermal energy efficiency of about 55–62% and the maximum achieved electrical efficiency was 11.4% (Ibrahim, 2014). Kiran and Devadiga (Kiran and Devadiga,2014) reported that the electrical efficiency of PV/T was 7.58% without cooling and 8.16% with cooling and the overall efficiency was 58.97%. The other experimental study was conducted during the spring season in United Arab Emirates. The results showed that electrical efficiency increased from 15% to 20% and the thermal efficiency was found as %60 (Alzaabi, 2014). Rosa-Clot et al. (Rosa-Clot, 2016) performed the efficiency analysis of PV and PV/T in Italy. They found the electrical efficiency of PV and PV/T as 8.77% and 13.19%, respectively. Also, they found thermal efficiency of PV/T as 62%. In addition to experimental studies, simulation studies were conducted in the literature for PV/T. The results obtained in these studies differ according to the results of experimental studies. Because many factors which affect the efficiency can be easily changed as desired. For example, in the simulation study by Yazdanifard et al. (Yazdanifard, 2016), several parameters changed such as solar irradiation, the number of pipes, Reynolds number, packing factor, pipes diameter, and collector length to investigate the glass covered flat plate PV/T system's electrical and thermal efficiency. They found maximum electrical and thermal efficiency as 17% and 70% respectively. Daghigh et al. (Daghigh et al., 2011) conducted the simulation study for amorphous silicon and crystalline silicon water-based PV/T systems in Malaysia. The results showed that the electrical and thermal efficiency of amorphous silicon and crystalline silicon PV/T were 4.9% and 72% and 11.6% and 51%, respectively. As summarized above, the results obtained in the studies in the literature are different from each other. Conducting the studies in different regions, different ambient temperatures and different cooling water flows and overestimating the input parameters in some simulation studies caused the results to differ from each other. Madalina Barbu et al. (Madalina et al., 2023) analyzed their PV/T system in four different weather conditions. The analysis results have shown that the performance of PV/T panels is closely linked to the distribution of thermal energy stored in the thermal storage tank. Additionally, when PV/T collectors are used in appropriately sized facilities, they exhibit superior performance compared to PV panels based on the end-user's thermal energy requirements. Different studies are being carried out to increase the efficiency of PV/T systems. In another of these studies, efficient PV/T design was demonstrated by decoupling the operating temperature of photovoltaic and thermal processes. The results showed that the temperature of the solar cells was 7.7 °C lower than the leaving water temperature in the new PV/T system, revealing the temperature-decomposition effect. Compared with the traditional PV/T system, the leaving water temperature is 3.9 °C higher and the solar cell temperature is 9.4 °C lower in the proposed system, resulting in a comprehensive efficiency increase of 17.9% (Kegui et al., 2023). In order to increase the performance of PV/T collectors, the use of different fluids other than water and air is being investigated. Dongxing Song et al. proposed a two-fold spectrum split configuration with both Therminol VP-1/Ag nanofluid and pure water. The results showed that the nanofluid absorbs shorter inappropriate radiation and water captures it longer, the total exergy efficiency increases with solar concentration, and the total energy efficiency is 0.829 in this system (Dongxing et al., 2024). Siyan Chan et al developed a new concept by replacing the backplate with the traditional PV/T collector, which can adapt to different heat demands in different seasons by opening or closing the backplate and achieve better electrical performance in summer without affecting heating in winter. They conducted comparative experiments between switchable and conventional PV/T collectors to observe the performance advantage. The results showed that the maximum stagnation temperature of the switchable PV/T collector was 18.1 °C lower than the conventional one, which relatively increased the electrical efficiency by 8.6% (Siyan et al., 2024).

It has been seen in the detailed literature review that although there are many studies about PV/T collector performance analysis which are evaluated electrical and thermal efficiency using different design parameters, there are also some economic analysis studies. Different metrics can be used for the economic analysis such as payback period (PBP) (Herrando et al., 2014), net present value (NPV) (Buker et al., 2014), levelized cost of energy (LCOE) (Riggs et al., 2017), energy payback time (EPBT) (Wilson and Young, 1996), Return on investment (ROI) (Zhang et al., 2015), internal rate of return (IRR) (Zhang et al., 2015), benefit to cost ratio (BCR) and unit cost of energy (UCE) (Michael and Selvarasan, 2017). TRNSYS model created for analysis LCOE of domestic PV/T system which is based on amorphous silicon cells and crystalline silicon cells. In the study, monthly meteorological data which are in TRNSYS program is used and annual performance degradation of PV panels was not taken into consideration. The LCOE was found as 0.42 USD/kWh in ref (Coventry and Lovegrove, 2003). The performance and economic analysis of water-cooled PV/T system and standard PV system were studied by Tripanagnostopoulos et al. (Tripanagnostopoulos et al., 2005). However, they did not consider tax rebate or other cost reductions in the economic analysis. They found estimated cost payback period for electricity saving and electricity and

gas saving between 10.3-28.2 year and 17.2-30.8 year according to the different temperature and tilt angel. 300 m^2 of hybrid PV/T collectors with polycrystalline and amorphous types of PV cell and a 10 m3 water storage tank was evaluated for Cyprus, Greece, and Wisconsin (Kalogirou and Tripanagnostopoulos, 2007). In this study, Typical Meteorological Year (TMY) data is used in TRNSYS program. TMY was defined as a year, which was including all the meteorological data a period the mean life of the system. The authors found the electrical production of polycrystalline PV/T is more than the amorphous PV/T but the solar thermal fraction is slightly lower. Also, payback period was calculated for Cyprus, Greece, and Wisconsin as 26, 26, 28 years respectively. The water-cooled PV/T collector which has different PV cell such as c-Si, p-Si, a-Si (thin film), CdTe and CIGS evaluated and compared under New Delhi, India conditions. It was observer that the c-Si PV cell produced maximum electrical energy, maximum annual overall thermal energy, and exergy. Also, the results showed that the minimum and maximum values of EPBT for energy and exergy for c-Si and CIGS were 1.01-0.66 and 3.44-5.72 years, respectively (Mishra and Tiwari, 2013). Another economic analysis of water-cooled PV/T was carried out in UK. The authors introduced that the annual energy savings were 10.3 MW and the NPV was calculated as 19456.14 Dollar for the 25-year life span of and the cost of power generation was 0.0778 per kWh (Mahmut et al., 2014). Another water-cooled PV/T economic analysis study conducted in a real office to support its electricity and hot water demand via computer program simulations in Hong Kong. The discounted payback period was estimated to be 14.7 years in that study (Ka-Kui et al., 2016). Herrando and Markides (Herrando et al., 2014) studied on water cooled PV/T systems for distributed electricity and hot-water provision in a typical house in London, UK. The authors stated that higher coverage of total household energy demands, and higher CO_2 emission savings can be achieved if the system is installed under low irradiance and low ambient temperatures. In addition, they stated that they have 2.3 MWh of electricity production, which corresponds to approximately 51% of the electricity need of the household, and 1 MWh of water heating potential, which corresponds to approximately 36% of the hot water need. The techno-economic challenges of PV/T systems in the housing sector for different Europe locations, with local weather profiles and energy demand data relating to homes were studied by Alba et al. (Alba et al., 2017). In the study, TRNSYS simulation models were prepared for 4 different systems based on meeting electricity and thermal energy demand and the economic viability of the solutions is then assessed based on their LCOE. The results showed that the overall levelized cost of energy as the range of 0.06–0.12 €/kWh. Augusto et al. (Augusto et al., 2017) studied yearly heat and electricity production of the PV/T, separate PV and solar thermal collector plants based on one-year measured data set in Italy. They reported that PV/T is economical solution compared to the PV and solar thermal collectors to produce electricity and thermal energy. This experimental study has shown that the PV/T solar energy system can produce approximately 1362 kWh/year of electrical energy per kWp, and the annual heat production can vary between 443 and 267 kWh/m^2 depending on the average inlet temperature of the water. The LCOE value of the PV and thermal collector were determined as 0.082 Euro/kWh and 0.087 Euro/kWh and 0.092 Euro/kWh at different inlet water temperatures (35 °C, 40 °C and 45 °C), respectively. In this study, measured meteorological data were used. But no information was provided for annual produced the thermal and electrical energy degradation of PV/T collectors. Gaurav Patel and Dr. Lalit Kumar Khurana established a 20.5 kWp PV-T system and made an economic analysis of the system. The results show that, considering the thermal energy and electricity exchange obtained, the internal rate of return (IRR) of the investment project is 21% and the modified internal rate of return is 12%. The discounted payback period of the investment is calculated as 5 years and 3 months (Gaurav and Lalit, 2024). To evaluate the production potential, economic profitability and ecological balance of the photovoltaic/thermal (PV/T) system in Cameroon, different HTF configurations based on water, vegetable and synthetic oils combined with different forms of titanium dioxide (TiO_2) were used. The results show that the net present value, emission rate, annual cost, payback period and energy cost of the PV/T-Palm/TiO2 system are 568.45 $, 7.78 kg, 7.07 $, 5.97, 0.03 $, respectively (Armel et al., 2024). Another study examined the techno-economic performance of a hybrid photovoltaic-thermal (PV/T) solar-assisted heat pump system to meet the electricity, and hot water demands of a three-bedroom terraced house occupied by four people in Belfast, United Kingdom. In the study, analyses were made for PV/T collectors of different sizes, including 12-panel, 20-panel and 24-panel systems. The results show that, thanks to the lower initial investment cost, the most economically viable system configuration for the household considered in this study is based on a 12-panel PVT array covering a total area of 16.3 m^2. This system has the potential to produce 2.4 MWh of electricity and 2.0 MWh of hot water per year; this is equivalent to just over 30% of that household's electricity needs and 80% of its hot water demand. The discounted repayment period of the system in question is determined as 14 years (Mustapha et al., 2024).

Santhan Reddy Penaka et al present a techno-economic evaluation of a water-based PV/T system for a single-family home to generate electricity and domestic hot water applications in 85 locations around the world. Simulation studies were performed using a validated tool with a one-hour time step. The results showed that the PV/T system has better energy and exergy performance for places where the annual ambient temperature is low. Also load profile, hot water storage volume etc. It has been observed that system boundaries can have a significant impact on the annual heat and electricity production of the system. Two different economic models were used in the study and show that the average net present values per unit collector area among 85 cities are 1800 and 2200 Euros respectively. The study showed that the payback periods of PV/T systems are competitive with other systems (Penaka et al., 2020). Saeed Abdul-Ganiyu et al established a PV and PV/T system in Ghana to investigate the technical and economic feasibility of the PV/T system. The technical and economic performances of both installed systems were analysed over a 25-year period. The results showed that the estimated average annual total exergy of PV and PV/T systems was 159.42 kWh/m^2 and 330.15 kWh/m^2, respectively. (Abdul, 2021). Three different systems using PV, PV/PCM (Phase Change Material) and PV/T-PCM (Thermal Phase Change Material) were investigated in Jiangxi, China. The study was conducted on two scenarios: fixed installation capacity and fixed state investment. Three alternative scenarios have been developed to determine the heat and electricity production potential and investment requirement in both scenarios. The results showed that under “fixed installation capacity” scenarios, conventional PV can produce 313 GWh/year of energy and PV/T-PCM can produce more

than 340 GWh/year of energy (Rafiq et al., 2022). A PV/T system was designed for a detached house in London, considering hourly weather data and thermal and electrical energy demand profiles. The annual performance of the system was compared with a reference system using a gas boiler and mains electricity. The results show that the PV/T system can achieve an annual electricity self-sufficiency of 87% and an annual thermal energy demand coverage rate of 99%, as well as an annual primary energy saving and a relative carbon emission reduction rate of 35% and 37%. to the reference system (Jurčević et al., 2023). An economic analysis of the PV-T system with an installed power of 20.5 kWp was made in Gujarat, India. It has been determined that this system in Gujarat produces approximately 5% more electrical energy compared to a PV power plant of the same capacity and saves approximately 2900 Kg of LPG for heating needs. The results showed that the investment could provide a discounted payback period of 5 years and 3 months with a project IRR of 21%. It has been reported that the payback period may vary depending on the heat energy change and the available fuel source (coal, biomass, biogas, LPG, PNG, FO, SKO, etc.) (Patel and Khurana, 2023).

Technical and economic analysis studies of PV/T systems in the literature have shown that PV/T systems have reached an economically feasible level. Providing electricity and thermal energy from a single source is advantageous, especially due to the lack of space on residential roofs. The use of PV/T systems in residences is very important to create energy self-sufficient residences. In addition, PV/T systems should not be evaluated economically but also in terms of their contribution to the environment. Providing electricity and thermal energy from a single source significantly reduces the use of fossil-based resources.

Limitation of Previous Studies

A detailed literature review has shown that there are still limitations or gaps in the economic analysis of PV/T systems. These gaps in the literature are listed below.

- The amount of the thermal and electrical energy that the PV/T collector can generate is calculated using generally monthly meteorological data. Moreover, these data are often obtained from various simulation programs rather than being measured. However, performance and economic analysis studies using monthly average data do not give accurate technical and economic results because panel performance and efficiency values are not calculated exactly. Some studies consider TMY datasets as hourly values. The disadvantage is that the method may be applied only to one parameter (e.g.DNI), and although the selected months in TMY are close to the long-term average, the distribution of (sub) hourly values (histogram) in the chosen months may not well represent the distribution of values in the original data.
- Many studies ignore the annual performance degradation for electricity and thermal production of the PV/T. Hence, the annual generated thermal and electrical energy amount doesn't change over the lifecycle of the system.
- The required electrical energy to circulate the water and the resulting loss of earnings wasn't considered in the economic analysis.
- In many studies, an economic analysis was performed based on only the panel. There are no economic analysis studies for the entire PV/T system.
- In many studies, the economic analysis was performed on the simple PBP by ignoring the economic parameters such as interest rate, inflation rate and discounted rate. Also, the NPV value required to make an investment decision is often not calculated. PV/T systems are becoming feasible due to changing investment and financial costs. However, especially in recent years only a few economic studies have been listed for the PV/T systems.
- In some countries there is no heating price. That is, as the thermal energy is not purchased from the grid, such as electrical energy, the price is not specified. Therefore, heating prices should be determined correctly for the study region for the economic analysis of the PV/T systems. None of the articles has stated how the heat prices are determined.
- In almost all studies, the electrical and thermal efficiencies of the PV/T collector were taken constant while conducting economic analysis. Whereas electrical and thermal efficiency varies depending on many factors.

Aim and Novelty of This Work

The chief aim of this article is to analyse the thermal-electrical performance of a PV/T collector and to conduct the economic feasibility of water-based PV/T systems under real measured meteorological data. For this purpose, the meteorological data such as irradiation and temperature were collected every 5 minutes for one year. The economic analysis was performed by considering all financial and technical parameters such as annual degradation rate, inflation rate, dept to equity ratio, interest rate based on the yearly energy output. Therefore, this study will provide a critical view on design and the associated parameters that affect the PV/T system performance and economic results.

In previous studies on PV/T systems, a single average performance value is taken for PV/T collectors. Taking a single average value for 8760 hours of working time per year causes a large erroneous calculation of the amount of energy to be produced. In this study, the efficiency of the PV/T collector on an hourly basis was determined and the electricity and thermal energy to be produced were calculated. In addition, there is a decrease of 0.07% in the amount of electrical energy to be produced each year in photovoltaic systems. In previous studies, the decrease in the amount of energy to be produced was not considered when making the 25-year economic analysis. Therefore, the results of the NPV and LCOE values of the system could be inaccurate. In this study, the amount of energy to be produced from the system is calculated on an hourly basis, considering all uncertainties and losses. Therefore, this study has the potential to make a significant contribution to original research, current practices and teaching involving capital investment issues. The novelty and contribution of this study is that the gaps listed above in the literature have been studied separately. These are summarized as follows.

Hourly performance and heat and electricity production were performed for one year using real meteorological data. Then the annual performance degradation rate implemented for life cycle of the PV/T collector.

While calculating the efficiency of the PV/T collectors, the ambient temperature as well as the main water temperature was taken into consideration and the heat and electrical energy to be produced were calculated by taking the efficiency values calculated on an hourly basis.

The economic analysis was conducted using the most commonly used NPV, LCOE, and PBP techniques in the literature, considering all parameters. We present these techniques by considering the technical, financial, and geographical factors that influence the cost of heat and electricity production for PV/T systems.

- The losses and the annual degradation of the entire system are included in the calculation.
- Hot water supply cost has been determined using the average unit price of some of the central hot water plants in Türkiye and it has been determined by considering the costs that will occur in case of using natural gas for heating.

DESCRIPTION OF THE PV/T SYSTEM, LOCATION, DATA SET, COMPONENTS AND REFERENCE HOUSE

The PV/T systems are systems that produce electrical and low-grade thermal energy from solar irradiation simultaneously. Therefore, PV/T systems require less space than PV and solar thermal systems. In addition to the advantage of these systems producing electricity and thermal energy at the same time, the cooling of the PV cell while the thermal energy is obtained has a positive effect on the PV efficiency. Water is the most widely used fluid in PV/T systems due to its low price, availability, and cooling properties. Water-carrying pipes under the PV/T collector are intended to draw heat from the PV panel, thereby improving the output voltage and current of the PV panel. At the same time, this heat is used for heating domestic water. In this study, the PV/T system consists of 7 panels, converter, inverter, solar absorbing tube, storage tank and circulating pump.

Location of the PV/T System

Aksaray was selected for the evaluation of the proposed PV/T system. The reason for this is that we were able to obtain the needed meteorological data from a solar power plant in Aksaray. The data was taken through the solar power plant's remote reading system, with the permission of the plant owner. The solar power plant from which the data is obtained is located close to the center of Aksaray. Due to the personal data protection law, the name and exact location of the solar power plant was not shared upon the request of the plant owner. Aksaray is located at a longitude of between 33-35° E, latitude of between 37-38° N and at an altitude of 980 m. The yearly average solar irradiation is 1.603 kWh/m^2, with a yearly total irradiation period of over 2880 h and the average yearly annual temperature is 10 °C in Aksaray.

The data such as irradiation and temperature were collected every 5 minutes from May 2016 to June 2018. Among the data measured between these years, it was found appropriate to use the data belonging to 2017. Because the rate of missing data in 2017 is quite low compared to other years. The data set for the year 2017 used in this study is the actual data measured that year. In PV power plants, data loss can occur due to various reasons such as power outages, interruptions during solar panel maintenance/cleaning, inverter failures, or communication module faults. In this study, it was observed that there was less than 1% data loss during 2017. To eliminate the disadvantages of the TMY dataset, it was preferred to use real measured data. Some critical features of the Data logger are presented in Table 1.

Table 1. Technical Features of Data Logger

Parameter	Value
Power supply	20-60 V DC
Consumption	5 W
Protection	DIN EN 61000-4-2
Operating temperature	-20-70 °C
Storage temperature	-20-85 °C
Protection class	IP 20
Raising	2000 m
Humidity	80%
Precision (Voltage input)	0-10 V, 2 mV
	0-1 V, 0,5 mV
	0-100 mV, 50 µV
Precision (Current input)	0-20 mA, 4 µA

Kipp&Zonen SMP11 pyranometer was used for irradiation (GHI, POA) measurement. Table 2 shows the typical measurement uncertainties of this device. PT1000 (with integrated converter) and PT1000 (resistance) temperature sensors were used to measure the ambient temperature and the panel cell temperature, respectively.

Table 2. Measurement uncertainties of Kipp&Zonen SMP11

Parameter	Value
Response Time	<2 s
Offset	< 2 W/m^2
Temperature Dependency	<1%
Non-stability	**<0.5%**
Non-linearity	<0.2%

During 2017, 105120 data were recorded from the PV/T system. For the results to be accurate, the data must be quality controlled and filtered. For example, since there is no radiation at night, the data measured during these hours must be filtered. Apart from that, the irradiation values at sunrise and sunset are quite small and are not effective for electricity production and may contain abnormal values. Therefore, the data in the mentioned time periods were filtered. In addition, there were missing data for various reasons in some time periods during the year. Since the data were recorded at 5-minute intervals, new values were written according to the previous and next measured values instead of the few missing data. After the filter process, the data set contains 43800 values (Scharmer and Greif, 2023; Reindl et al., 1990).

Specification of PV/T Collector

PV/T collector is provided electricity and usable thermal hot water at the same time from one collector. As far as we know, there is only one PV/T panel manufacturer in Turkey (Solimpex). At the time we conducted this study, there were 72 glass-covered PV cells and 66 tubes in the PV/T panel we could obtain from this manufacturer. The gross area of this collector is 1.28 m^2. Maximum temperature and maximum working pressure are 101°C and 6 bar respectively.

Reference House

In this study, Simple House SFH15, which is used by IEA in Task44 project, was chosen as the reference for the analysis of the PV/T system (Heimrath and Haller, 2007). The floor area of this house is 140 m^2. The roof area on the south and north side is 59.7 m^2, 28.9 m^2 respectively. The roof pitch of the southern facade is 20° and the roof pitch of the north facade is 45°. It was

assumed that 4 people lived in this house. The total residential usage area of 14.962.998 house for which Building Permits were obtained in Turkey between 2002 and 2024 is 1.767.099.964 m^2 (data.tuik.gov.tr, 2024). So, an average house is 118 m^2. All these houses have from 1 to 5 rooms. Therefore, a 4-room apartment for a standard family of 4 people is expected to be around 140 m^2 on average. The heating energy demand of the reference house with a floor area of 140 m^2 is given as 15 kWh/m^2a in Strasbourg climate conditions. The annual lowest temperature values and the number of rainy days in Strasbourg and Aksaray are similar (mgm.gov.tr, 2024; tr.weatherspark.com, 2024). Therefore, the selected reference flat is suitable for the conditions of Aksaray. The average collector area of considered collector is 1.37 m^2 for one panel. Therefore, it was thought that the panels would be placed only on the southern facade. The average daily water consumption is 111 litres per capita in Türkiye according to 2014 data of State Planning Organization. 40% of clean domestic water is consumed as hot water. According to this statistic, hot water consumption of a standard 4-person house was accepted as 50 L per month. In this study, electricity consumption of a standard 4-person house was accepted as 200 kWh per month.

Market Analysis and Assumptions

The energy market in Türkiye is growing day by day. Photovoltaic energy is increasing its importance in the energy mix day by day. At the end of 2020, the world installed PV capacity has exceeded 760 GW. Photovoltaic panel costs are decreasing day by day due to technological developments and rapid increase in installed power (IEA PVPS, 2021). Photovoltaic energy applications are expected to increase rapidly in the coming years due to cost reduction and environmental sensitivities. The solar thermal system market was initiate during the 1970s to meet the hot water demand in parallel with the growth of the tourism industry. Türkiye has 10 million m^2 of flat plate collectors installed. Türkiye offers opportunities in PV/T area because of the high potential of solar energy and experience in solar technology (IEA, 2021). The fact that PV / T systems have less installation costs than the installation of both individual PV and solar thermal collectors is one of the important advantages for the expansion of the PV/T market. In addition, because the PV market is directed to grid-connected distributed systems and national policies are developed for low-energy buildings, it is expected that the PV/T market will expand mostly in building sector in Türkiye.

The unit electricity prices in Türkiye are determined by Energy Market Regulatory Authority (EPDK). The unit price of electricity was determined as 1.92 TL/kWh (0.0597$/kWh) for Single Term Residential Subscribers in February 2024. When calculating the net energy price to be billed, distribution price (It has been determined by EPDK as 0.1171147 TL/kWh (0.0196$/kWh) in July 2019), energy fund price (1% of energy price), TRT share price (2% of energy price) and energy consumption tax (5% of energy price) are added to unit electricity price. When all taxes and rates are added to the unit price, the price of electricity for household users is calculated as 0,07 E/kWh (EPDK, 2024).

The cost of thermal energy in an example geothermal power plant in Türkiye is calculated as follows. The amount of thermal energy is determined by the calorimeter. This amount of energy is multiplied by the unit price of heat. Then, the apartment share fee, system improvement maintenance and repair fee and VAT are charged to the thermal energy price. However, if there is no possibility of using the central heating system water can be heated by electricity. In this case, the cost of heating water with electricity can be calculated by utilizing basic heat formulas. However, this method would be more expensive than obtaining heat from central heating plants. Furthermore, installing a separate heating system will have an additional investment cost. Heating cost is determined as 0.02 Euro/kWh when using natural gas (İzmir Jeotermal, 2024).

Although the installation costs are decreasing day by day, the results of economic analysis will differ between countries due to variables such as policies, feed-in tariff, interest rate and inflation. Therefore, it should be considered in financial parameters and policies as well as installation costs.

The key input variables required for economic analysis can be classified as geographical, technical, and financial. The geographical variables include irradiation, altitude, and ambient temperature. These variables were measured with high precision instruments and used in the economic analysis.

According to the market investigation results, the average cost of whole reference PV/T system was determined to be between 250 and 350 dollars per square meter. This price includes project cost, installation cost and all necessary equipment costs. In this study, pro forma invoices were received from two companies for the turnkey price of the system mentioned. The price of the system was determined by taking the average of the price quotes provided by the two companies. Accordingly, the total price of the system is determined to be 2355 Euros.

The project can be financed with equity, using an amount of bank loan, or using bank loan entirely. To make the economic analysis results realistic, it is stipulated to use bank loans. Therefore, credit interest rates should be determined. The regulations in the energy law allow small and medium-sized enterprises to generate electricity up to 1 MW without licensing and establishing a company. Many banks in Türkiye provide loan to small and medium-sized enterprises to produce their own renewable energy. Within this framework, financial support prepared with appropriate maturity and interest rates can be utilized for all turn-key costs such as purchase of equipment, installation, and construction. The loan interest rate varies from country to country and depends on the economic and political conditions of the countries. For this reason, it is more suitable to determine the loan interest rates by taking the average of long years rather than based on the interest rates in the year of installation. Renewable energy loan interest rate in Türkiye varies between 4% and 8%.

According to the Türkiye Statistical Institute data, considering the annual percentage change in the price index between 2005 and 2024, the average interest rate was 15.85% annually (Tcmb, 2024).

The O&M cost of the PV/T system may vary depending on the agreements and from country to country. It is determined from the literature that the O&M cost of these systems is around 1% of the total cost of the project (Kalogirou and Tripanagnostopoulos, 2006; Rasoul et al., 2017; Gu et al., 2018). When calculating the electrical energy and thermal energy produced by PV/T collectors, the annual loss of efficiency should be included in the calculation. Due to the aging of the materials, PV panels lose their efficiency each year compared to the previous year. This value is stated as 0.07% annually in the manufacturers' catalogues.

TECHNO-ECONOMİC MODELLİNG METHODS

Thermal Model of PV/T

The performance analysis of the PV/T collector can be performed by evaluating the electrical and thermal efficiency together. Electrical and thermal efficiency affect environmental factors such as irradiation and temperature. To perform thermal analysis, the useful heat gain should first be calculated. The useful heat gain represented with Eq.1 (Farghally et al., 2015).

$$Q = AF_R[(\tau\alpha)_{PV} * G - U_{loss}(T_i - T_a) \quad (1)$$

where, Q is the useful heat gain (W), A is the collector area (m^2), F_R is the heat removal efficiency factor, $\tau\alpha$ is the transmittance absorptance product of the PV cells, G is the irradiation (W/m^2), U_{loss} is the heat loss coefficient ($W/m^2°C$), T_i is the inlet temperature (°C) and the Ta is the ambient temperature (°C). The heat removal efficiency factor is calculated using Eq.2 (Calise et al., 2012).

$$F_R \frac{mC_p}{AU_{loss}}[1\exp(-\frac{AU_{loss}F'}{mC_p}] \quad (2)$$

where, m is the mass flow rate in the collector (lps), Cp is the collector cooling medium and F' is the corrected fin efficiency. The corrected fin efficiency and the fin efficiency (F) are calculated with Eq.3 and Eq.4, respectively (Calise et al., 2012).

$$F' = \left[\frac{\frac{1}{U_{loss}}}{U_{loss}(d+(w-d)F)}\right] + \frac{1}{wh_{PVA}} + \frac{1}{\pi dh_{fluid}} \quad (3)$$

$$F = \frac{\tanh(M\frac{w-d}{2})}{M\frac{w-d}{2}} \quad (4)$$

where, M is the coefficient term which accounts for the thermal conductivity of the absorber and PV cell, w is the tube spacing (m), d is the diameter of the tube (m), h_{fluid} is the heat transfer coefficient of fluid ($W/m^2°C$) and h_{PVA} is the heat transfer coefficient ($W/m^2°C$). The M is determined using Eq.5.

$$M = \sqrt{\frac{U_{loss}}{k_{abs}l_{abs}+k_{PV}l_{PV}}} \quad (5)$$

The loss coefficient (U_{loss}) can be divided to three parts. These are the top loss coefficient (Ut), bottom loss coefficient (U_b) and the edge loss coefficient (U_e). These loss coefficients can be calculated using Eq.6, 7, 8 and 9 (Farghally et al, 2015).

$$U_{loss} = U_t + U_b + U_e \quad (6)$$

$$U_t = \left\{\frac{N_g}{\frac{C}{Tpm(\frac{Tpm-Ta}{Ng+f})^e}} + \frac{\sigma(T_{pm}+T_a)(T_{pm}^2+T_a^2)}{(\varepsilon_p+0{,}0059N_g h_W)^{-1}+\frac{2N_g+f^{-1+0{,}33C_p}}{\varepsilon_g}-N_g}\right\} \quad (7)$$

$$U_b = \frac{K_b}{L_b} \quad (8)$$

$$U_e = \frac{(UA)_{edge}}{A_c} \quad (9)$$

To calculate the loss coefficient, the value of c, e, f, hw (the convection heat transfers due to the wind), Ue (edge loss coefficient) and Tpm (the mean collector plate temperature) should be determined. These parameters are calculated with following equations (Anderson et al., 2009).

$$c = 520(1 - 0{,}000051\beta^2) \quad (10)$$

$$e = 0{,}43(1 - \frac{100}{T_{pm}}) \quad (11)$$

$$f = 0(1 + 0{,}089)^{h_W} - 0{,}1166h_W\varepsilon_p)(1 + 0{,}07866N) \quad (12)$$

$$h_W = 5{,}7 + 3{,}8v \quad (13)$$

$$T_{pm} = T_i + \frac{\frac{Q_u}{A_e}}{F_R U_L}(1 - F_R) \quad (14)$$

where, N_g is the number of covered glasses, ε_p is the plate emittiance, ε_g is the glass emittance, T_{pm} is the mean plate temperature, h_W is the wind transfer coefficient, v is the wind speed, β is the tilt angel of collector, p is the collector perimeter and L is the absorber thickness.

Thermal efficiency is a function of inlet temperature, ambient temperature, packing factor (S) and irradiation, while electrical efficiency is a function of nominal operating cell temperature ($NOCT$) and T_{pm}. Eq.15 expresses thermal efficiency (Green, 1998).

$$\eta_{thermal} = F_R(S * \tau\alpha_{PV}) + (1 - S * \tau\alpha_T) - F_R U_{loss}\frac{T_i - T_a}{G} \quad (15)$$

Electrical Energy Model of the PV/T

The PV panels convert solar irradiation into the direct current. However, some of the devices we use in daily life operate on alternating current (AC), while others operate on direct current (DC). Battery charging of devices operating with direct voltage is also done from an alternative voltage source using various converter equipment. The electrical grid in homes also operates on alternating current. Therefore, the voltage produced in PV panels must be converted to alternating current. In addition, maximum power point tracker (MPPT) is required to operate the PV panel at maximum power point under all conditions. Otherwise, if the system is off grid, a storage device is needed. Although the electrical energy produced in PV panels depends on a large amount of irradiation, panel area and panel efficiency also affect the generated electricity. The hourly electricity generated by the PV panel is calculated using Eq.16 (Ayan et al., 2022).

$$E_{A,h} = G_{I,h} \cdot A_a \cdot \eta_{PV} \quad (16)$$

where the $G_{I,h}$is the hourly total in-plane irradiance (kWh/m^2), A_a is the PV/T available area (m^2) and η_{PV} is the overall PV system efficiency (%). The overall PV system efficiency is affected by the PV panel efficiency (η_{module}), inverter efficiency (η_{inv}), the PV panel temperature efficiency (η_{temp}), power conditioning efficiency (η_{pc}) and the annual PV module degradation (η_d). The overall PV panel efficiency is calculated with Eq.17 (Amine et al., 2023).

$$\eta_{PV} = \eta_{module} \cdot \eta_{pc} \cdot \eta_{temp} \cdot \eta_{inv} \cdot [1 - \{(t-1).(\eta_d)\}] \quad (17)$$

where t is the index for years. The output DC energy of the PV panel, hence the panel efficiency decreases linearly with increasing temperature. This efficiency depends on the temperature power coefficient (β) of the panel and the cell temperature ($T_{c,h}$).

$$\eta_{temp} = [1 - \beta(T_{c,h} - T_{c,ref})] \quad (18)$$

The cell temperature also varies depending on the ambient temperature ($T_{a,h}$), irradiation and ($NOCT$).

$$T_{c,h} = T_{a,h} + \left[{}^{(NOCT-20)}/_{800}\right].H_{I,h} \quad (19)$$

β and $NOCT$ vary according to panel technology and are determined from PV panel catalogues. Eq.20 expresses electrical efficiency.

$$\eta_e = 0{,}15(1 - 0{,}005(T_{pm} - NOCT)) \quad (20)$$

Economic Analysis Model

In this article, the LCOE, NPV and PBP values are determined by economic analysis of the PV/T system. LCOE is a widely accepted index which is indicates the total unit energy cost of installing and operating an energy system over its lifetime. Since LCOE represents the unit cost of generated electricity, it enables economic comparison of different energy generation technologies and the installation of similar systems in different regions. LCOE should contain many factors such as investment costs, financial costs, fuel costs, revenues, and heat and electricity production amount during its lifetime. The formula of LCOE is given in Eq.21.

$$LCOE = \sum_{j=0}^{n-1} \frac{C_t}{(1+r)^t} / \sum_{t=0}^{n-1} \frac{E_t}{(1+r)^t} \quad (21)$$

where C_t is the total cost in the year of t (€),n is the lifetime of the PV/T (year) and r is the discount rate (%).

The total cost of PV/T system contains investment expenditures in the initial year, financing loan cost (L_t), operating and management cost (OM_t) and tax paid for energy generation ($T_{a,t}$).

$$C_t = I_0 + L_t + OM_t + T_{a,t} \quad (22)$$

Investment expenditure is the capital investment provided by the proprietor. It depends on the debt-to-equity ratio in accordance with the agreement with the bank. The investment expenditure for the first year is calculated by Eq.23.

$$I_0 = C_0 x(1 - DE) \quad (23)$$

where C_0 is the capital cost (€) and DE is the dept to equity ratio (%). The loan cost is equal to the sum of the annual invested capital with the interest rate on the invested capital.

$$L_t = C_0 \,.\, DE/n + C_0 \,.\, DE(1 - t/n) \,.\, Itr_t \quad (24)$$

where Itr_t is the interest rate in the year t (%). Another method used to evaluate a project, measure economic efficiency, and make decisions is NPV. Probably the most popular method among all methods is the NPV and it is considered the most theoretically reliable. The NPV involves discounting all future cash flows (both in- and out-flow) at a discount rate and then combining them. The NPV can be defined in one formulation. The required historical data to calculate the NPV can be obtained from public sources, engineering documents, and past projects. By using historical data, the approximate probability density of costs, benefits, and discount factors can be formulated for the expected life of the project. Thereby, uncertainty in the project economy is taken into consideration. The NPV can be defined by Eq.25 (Žižlavský, 2014; Marchioni and Magni, 2018; Heyd, 2018).

$$NPV = -C_0 + \sum_{t=0}^{n-1} \frac{CF_t}{(1+r)^t} \quad (25)$$

where CF_t is the cash flow of the year t (€). The CF_tcan be calculating by Eq.26.

$$CF_t = S_{et} + S_{tht} - C_t \quad (26)$$

S_{et} and S_{tht} describe the electrical and thermal energy savings respectively. S_{et} and S_{tht} can be calculated by using Eq.27 and Eq.28.

$$S_{et} = EP_t \,.\, E_{et} \cdot (1 + Ifr_t) \quad (27)$$

$$S_{tht} = HP_t \,.\, E_{tht} \cdot (1 + Ifr_t) \quad (28)$$

where EP_t is the electricity price in the year t (€/kWh), HP_t is the heating price in the year t (€/kWh), Ifr_t is the inflation rate in the year t.

The payback period (PBP) is the simplest investment appraisal method. The PBP refers to the required time to offset the initial cash outflow by cash inflows generated by a project. In most cases, a longer PBP means a less lucrative investment, while a shorter PBP means that the capital cost can get back earlier. It is possible to calculate PBP using averaging or subtraction methods. The averaging method is used when cash flows are expected to be steady in subsequent years and the subtraction method is used when cash flows are expected to vary in subsequent years. Due to various factors such as variable inflation and loan interest rates, the long PBP makes the investment risky (Imteaz and Ahsan, 2018; Lawrence et al., 2019). The PBP is expressed by Eq.29.

$$PBP = T_{CF_t} \geq 0 \quad (29)$$

In this study, the assumed key input economic parameters are given in Table 3.

Table 3. Key Parameters for the financial analysis

Description	Symbol	Average	Unit
Electricity Price		0.101	€/kWh
Heating Price		0.08	€/kWh
Effective PV/T Area		8.96	m²
Project Life Cycle		25	Years
Electrical Efficiency (STC)		14.7	%
Thermal Efficiency		62.3	%
Degradation Rate		0.7	%/year
Capital Cost		7287	€
Debt to Equity		0.2	%
Interest Rate		6	%/year
Loan Term		25	Years
Effective Tax		18	%/year
Nominal Discount Rate		4	%/year
O&M Cost		1	%/year
Inflation Rate		9	%/year

RESULTS

There are several factors that influence the thermal and electrical efficiency of the PV/T collector, such as mass flow rate, absorbent plate parameters (such as tube spacing, pipe diameter, and fin thickness), thermal conductivity of the fluid in the absorbent plate, packing factor (S) inlet temperature and irradiation. Although s and $\tau\alpha_{pv}$ are effective on electrical and thermal efficiency, these are taken as a constant value since they are the coefficients of the materials used in the PV/T collector. However, the effect of S and $\tau\alpha_{pv}$ on the

electrical and thermal efficiency is shown in figure 1. The increases of the *S* means that more collector areas are covered by PV cells. Therefore, the increase of the absorber block area has the effect of decreasing the heat increase in PV cells. This means that more areas are heated under the same irradiation. Therefore, there will be a decrease in thermal efficiency due to the increase of *S*. So, increasing the *S* increases the electrical efficiency and decreases the thermal efficiency. Therefore, an optimal value for the *S* should be determined (Koç and Başaran, 2019). When the absorption properties of PV cells are examined, it is observed that they respond well to short wavelengths in the range typically from about 400 nm to approximately 1200 nm. However, the solar spectrum extends up to around 2500 nm, and these longer wavelengths tend to be reflected from PV cells while being absorbed by solar thermal collectors. Therefore, increasing $\tau\alpha_{pv}$ enhances thermal efficiency. Since $\tau\alpha pv$ has minimal impact on electrical efficiency, a $\tau\alpha_{pv}$ value close to 1 is preferred.

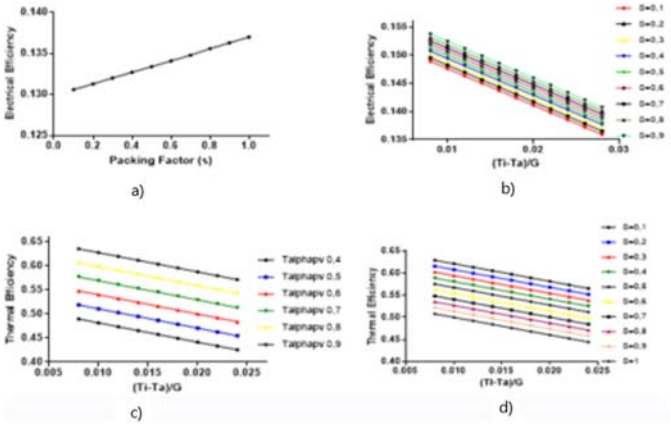

Figure 1. The effect of the *s* and $\tau\alpha_{pv}$ on the efficiency a) packing factor versus thermal efficiency, b) electrical efficiency at varying packing factor, c) thermal efficiency for varying transmittance/absorptance products, d) thermal efficiency at varying packing factor

The aim of this Simulink model is to determine the thermal and electrical efficiency of the PV/T collector depending on the temperature and irradiation. To determine the effect of the temperature and irradiation on the electrical and thermal efficiency, $\tau\alpha_{pv}$ and *S*, was kept constant at 0.8 and 0.4, respectively. Thus, only the effect of the temperature and irradiation on the efficiency was observed. Inlet water temperature (Ti), ambient temperature (Ta) and irradiation (G) affect the thermal efficiency of PV/T as shown in equation 15. Therefore, the change in (Ti-Ta)/G affects the thermal efficiency. As seen in Figure 3, the increase in (Ti-Ta)/G reduces the thermal efficiency. Although thermal efficiency theoretically depends on these three variables, the change in ambient temperature or inlet water temperature during the day is not as sudden as the change in irradiation. For this reason, thermal efficiency varies especially depending on irradiation. In addition, irradiation changes the panel internal temperature more than it changes the ambient temperature, that is, it indirectly changes the temperature for the PV/T panel. This affects PV/T efficiency. Also, PV panels are the current source. That is, the current produced by the panel change rapidly depending on the irradiation. Therefore, the decrease in irradiation reduces both the electrical efficiency and the thermal efficiency. After the optimal values of *S* and $\tau\alpha_{pv}$ were determined, the electrical and thermal efficiency of the PV/T collector was determined depending on the temperature values and radiation value in each 1-hour period during the year. During the year, the lowest electrical efficiency was calculated as 13.5% and the lowest thermal efficiency as 54.1%. The highest electrical efficiency was calculated as 15.1% and the highest thermal efficiency as 58.2%.

There may be serious differences between measured irradiation values and DNI values in the database of simulation programs, especially on an hourly basis. Aksaray's irradiation values were obtained from the database of the PVGis program and compared with the actual values obtained from the irradiation sensor. Figure 2 shows the DNI values of the PVGis program and measured irradiation values for the first week of January for Aksaray. As can be seen in Figure 2, there are big differences between the DNI values in the database of the simulation program and the measured irradiation values. For example, while DNI was 124.61 kWh/m^2 at midday on January 2, the measured value by the pyronometer was 586.9 kWh/m^2. The large difference between these two values causes large differences in technical and economic analyses.

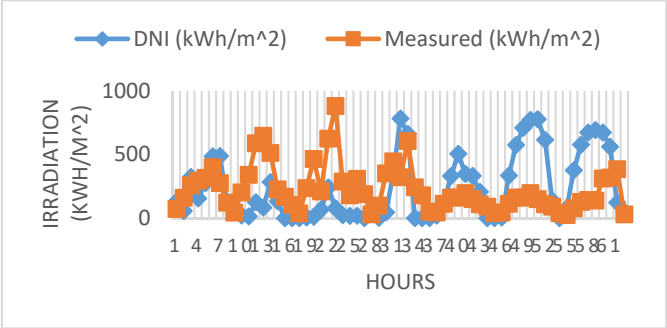

Figure 2. Sample DNI and measured irradiation

Although meteorological data were measured at 5-minute intervals in the study, hourly average values were used in the calculations to avoid complexity in the electrical and thermal efficiency of the PV/T panel. Figure 3 shows hourly average irradiation and the ambient temperature.

Figure 3. Hourly average irradiation and ambient temperature

The lowest ambient temperature and PV cell temperature were measured in January at -9.7 °C and -8.42 °C, respectively. The highest ambient temperature and PV cell temperature were measured in June at 42.78 °C and 60.19 °C, respectively. The monthly average minimum ambient temperature and PV cell temperature were measured in January at 3.78 °C and 8.6 °C, respectively. The monthly maximum ambient temperature and PV cell temperature were measured at 29.61 °C and 37.55 °C, respectively, in July.

In the MATLAB/Simulink model, the electrical and thermal efficiency of the PV/T collector was determined by using hourly data. These data were used when calculating the electrical and thermal energy production values of PV/T collector. The inlet water temperature, ambient temperature and the irradiation are affecting the thermal efficiency, while the collector cell temperature is affected electrical efficiency. Figure 4 shows the thermal and electrical efficiency of the PV/T collector. Annual average thermal and electrical efficiency was calculated as 62.3% and 14.7%, respectively.

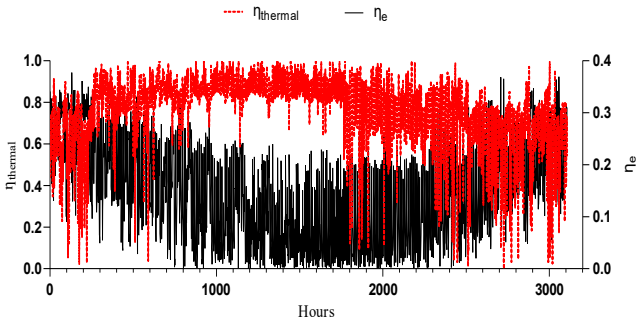

Figure 4. Efficiency of the PV/T collector

To meet the annual energy needs of the reference house, seven PV/T collectors should be used. Accordingly, the amount of electrical energy and thermal energy produced by the designed PV/T system was calculated on an hourly basis. The current efficiency value of the PV/T collector was used for hourly calculation. It has been calculated that the system will generate 2333.18 kWh electrical energy and 10864.43 kWh thermal energy in the first year. Figure 5 shows the amount of electricity and thermal energy that the system will produce hourly for a month in each season.

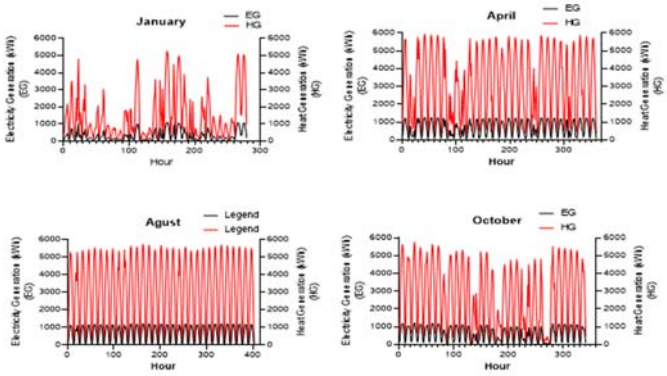

Figure 5. Monthly electricity and heat generation

Electricity and heat production occurred at minimum levels in January and peaked in August. Specifically, electricity production in January and August was 85.6 kWh and 266,639 kWh, respectively. Thermal energy production in January and August was 398.7 kWh and 1,241.6 kWh, respectively. As seen in Figure 4, electricity and heat production remain relatively constant during the summer months, while they exhibit significant variability during the winter months. On a daily basis, the lowest electricity and heat production occurred in March. These results indicate that the production of electricity and thermal energy is highly dependent on meteorological conditions.

Figure 6 shows the monthly average mains water temperature which is used as inlet water temperature of the PV/T collector.

Figure 6. Mains Water Temperature

Mains water temperature is associated with soil temperature. As the temperature of the soil does not change as fast as the ambient temperature, mains water temperature does not change very fast. Therefore, it has been found appropriate to use monthly average mains water temperature.

Table 4. shows the values in the sample years for the economic parameters calculated for the 25-year economic life. In the economic analysis, the degradation rate of the panel and the electricity consumption of the pump were taken into consideration. While the amount of electrical energy to be produced by PV/T in the first year was 2333.2 kWh, the amount of energy to be produced in the 25th year decreased by 0.07% in the following years to 1971.2 kWh. Similarly, the amount of thermal energy to be produced by PV/T in the first year is 10864 kWh, and the amount of energy to be produced in the 25th year has decreased by 0.07% in the following years to 9178.9 kWh. Considering that the electric pump consumes 511 kWh of energy annually, the net electrical energy amount to be obtained from the PV/T system is 1822.2 kWh, and the net thermal energy amount is 10864 kWh.

Table 4. The Estimation of Financial Results during the Life Cycle of PV/T System

Year	1	6	12	18	24
Cost saving from energy generation					
Electricity generation (kWh)	2316.8	2236.9	2144.6	2056.1	1971.2
Electric Pump Consumption	511	511	511	511	511
Totol electricity generation (kWh)	1805.8	1725.9	1633.6	1545.1	1460.2
Heat generation (kWh)	10788	10416	9986.1	9574	9178.9
Electricity savings (kWh)	146,45	139,96	132,47	125,30	118,41
Heating savings (kWh)	249,97	241,34	231,38	221,83	212,67
TOTAL ENERGY GENERATION (kWh)	13105	12653	12131	11630	11150
TOTAL ENERGY SAVING (kWh)	396,41	381,30	363,85	347,13	331,09
OM cost and Tax					
OM cost ($)	23,55	23,55	23,55	23,55	23,55
Tax for electricity (€)	26,36	25,19	23,85	22,55	21,31
TOTAL (Omt) (€)	49,91	48,74	47,40	46,10	44,86
Financial cost					
Loan payment (€)	19	19	19	19	19
Loan interest (€)	27	21	15	8	1
TOTAL (Lt) (€)	45,97	40,32	33,54	26,75	19,97
Discounted cash flow and energy generation					
Net Profit (CFt)	300,53	292,24	282,92	818.68	797.55
Discounted Cost (Ct)	95,88	89,06	80,93	186.27	163.6
Discounted Energy Generation (kWh)	12601	9999.8	7576.8	5740.9	4349.9
Cash Flow	-1332	145,35	1865,85	3532,7	5150,04
Evaluation Metrics					
NPV	**2718.5**				
LCOE	**0.091**				
Payback Period	**6 year**				

The LCOE, NPV and PP were calculated 0.091 €/kWh, 2718.5 € and 6 years, respectively. These results showed that the system is economically viable. PV/T systems are not yet widely used in daily life. Therefore, initial investment costs are still high. However, PV/T systems are still economically viable today. In the economic analysis, input variables were used by taking their averages over many years. Inflation and changes in the Euro exchange rate may change the economic analysis results. The long-term averages of both variables were taken and future perspectives of various institutions according to the current conditions were considered to minimize the impact of these changes.

CONCLUSION

Türkiye's average irradiation and sunshine duration are higher than the average of European countries. For these reasons, both electrical energy and thermal energy supply from solar energy are increasing rapidly. Since the consumption of energy at the place where it is produced reduces losses, distributed power plants have started to be preferred instead of central long-distance power plants. The easiest way to build a distributed power plant is to utilize solar energy. With the developing technology and the decrease in costs, solar energy applications are seen in many buildings. However, these systems are often installed separately either to obtain thermal energy or to obtain electrical energy. However, there is very limited space for the installation of such systems in buildings. Therefore, installing PV/T systems that can generate electricity and thermal energy at the same time provides advantages. There are limited studies on the performance and economic analysis of PV/T systems in the current literature. In this study, for the first time in Türkiye, the performance and economic analysis were performed using real meteorological data. It is aimed to provide hot water and electrical energy of a house by using water-based PV/T collectors. The results of this study are briefly summarized below.

- The ambient temperature of the area where the system is installed varies between -9.7 and 42.78 °C, and the PV cell temperature varies between -8.42 and 60.19 °C.
- Annual average thermal and electrical efficiency were calculated as 62.3% and 14.7%, respectively.
- The system can generate 2333.18 kWh of electrical energy and 10864.43 kWh of thermal energy for the first year.
- The LCOE was calculated as 0.0911 €/kWh while NPV and PBP are respectively estimated at 2718.5 € and 6 years.

In the literature, electrical efficiencies of PV/T collectors vary between 11.4% and 13.6%, thermal efficiencies vary between 55% and 62%, LCOE vary between 0.42 USD/kWh and 0.092 kWh, and PBP vary between 10.3 and 15 years. As a result of this study, the LCOE, NPV, PBP, average electrical and thermal efficiencies were found as 0.0911 €/kWh, 2718.5 €, 6 years, 14.7% and 62.3%, respectively, for a project size of 8.96 m^2 in a 25-year life cycle. It should be noted that these results depend on meteorological conditions. It is seen that the results obtained within the scope of this study are better than the results in the literature.

With the MATLAB/Simulink model of the PV/T collector developed within the scope of this study, the S and $\tau\alpha_{pv}$, which are important design parameters, can be determined optimally for the PV/T collector to be installed in any region (according to the temperature and radiation values of the region) to operate it at optimum electrical and thermal efficiency. In addition, the annual deterioration rate of the collector and the fact that devices such as electric pumps were considered, showed that the economic model created was more successful in the analyses to be made for many years. Paying attention to these in economic analysis studies for PV/T collectors to be made in any region will provide important gains. The use of renewable energy sources will reduce fossil fuel consumption. Among the renewable energy sources, especially in cities, the use of solar energy is relatively easier and more economical. In countries such as Türkiye, whose irradiation and temperature averages are above the world average, electricity and heat needs must be met from solar energy. The results obtained in this study show that PV/T systems are an economical way to supply electricity and heat. For this reason, it is very important to prepare both incentive mechanisms and technical standards by regulators for the spread of PV/T systems. It is necessary to prepare typical projects and facilitate legal procedures, especially for small powerful systems to be used in residential. It is expected that this study and its results will lead to the use of PV/T based systems in buildings.

REFERENCES

Wolf, M. (1976). Performance analysis of combined heating and photovoltaic power systems for residences. *Energy Conversation* 16(1),79–90.

Boer, K.W. (2003). Tamm G. Solar conversion under consideration of energy and entropy. Solar Energy 74(1), 525–8.

Florschuetz, L.W. (1979). Extension of the Hottel–Whillier model to the analysis of combined photovoltaic/thermal flat plate collectors. *Solar Energy*, 22(1), 361–6.

Hendrie, S.D. (1982). Photocoltaic/Thermal Collector Development Program-Final Report. The U.S. Department of Energy Under Contract NO DE-AC02-76ET20279

Cox, C.H. (1985). Raghuraman P. Desig.n considerations for flat-plate photovoltaic/thermal collectors. *Solar Energy*, 35(3),227–41.

Suzuki, A. Kitamura, S. (1979). Combined photovoltaic and thermal hybrid collector. *Japan J Phys*, 19(2), 79–83.

Karl, H. (1979). Photovoltaischer Hybridkollektor. In: Fourth international congress laser, 79 opto-electronics, Munchen.

Komp, R.J. (1985). Field experience and performance evaluation of a novel photovoltaic-thermal hybrid solar energy collector. *Intersol*, 85.

Schwartz, R. Rao, K.H.S. Tscharner, R. (1983). Computer-aided analysis of thermal images of solar cells and solar PV/T collectors. In: Fifth EPSEC, Athens.

Lalovic, B. Kiss, Z. Weakliem, H. (1986). A hybrid amorphous silicon photovoltaic and thermal solar collector. *Solar Cells*, 19(1), 131–8.

Lalovic, B. Pavlovic, T. Kiss, Z. Dine, J. (1988). The application of hybrid a-Si:H PV and thermal collectors for different usages. In: Eighth EPSEC.

Zondag, H.A. Vries, D.W. Helden, W.G.J. Zolingen, R.J.C. Steenhoven, A.A. (2003). The yield of different combined PV-thermal collector designs. *Solar Energy*, 74(1), 253–69.

Leenders, F. Schaap, A.B. Ree, B.C.G. Helden, W.G.J. (2000). Technology review on PV/Thermal concepts. In: 16th EPSEC, Glasgow.

Bakker, M. Zondag, H.A. Helden, W.G.J. (2002). Design of a dual flow photovoltaic/thermal combi panel. In: PV in Europe, Rome.

Bakker, M. Zondag, H.A. Elswijk, M.J. Ottenbros, M.T.N. Helden, W.G.J. (2004). Outdoor performance of uncovered PV/Thermal panels. In: 19th EPSEC, Paris.

Rockendorf, G. Sillmann, R. Podlowski, L. Litzenburger, B. (1999). PV-hybrid and thermo-electric collectors. *Solar Energy*, 67(4–6), 227–37.

Hausler, T. Rogass, H. (2000). Latent heat storage on photovoltaics. In: 16th EPSEC, Glasgow.

Soerensen, B. (2001). Modelling of hybrid PV-thermal systems. In: 17th EPSEC, Munich.

Tripanagnostopoulos, Y. Nousia, T.H. Souliotis, M. Yianoulis, P. (2002). Hybrid photovoltaic/thermal solar systems. *Solar Energy*, 72(3), 217–34.

Tselepis, S. Tripanagnostopoulos, Y. (2002). Economic analysis of hybrid photovoltaic/thermal solar systems and comparison with standard PV modules. In: PV in Europe, Rome.

Kalogirou, S.A. (2001). Use of TRNSYS for modelling and simulation of a hybrid PV-thermal solar system for Cyprus. *Renewable Energy*, 23(1), 247–60.

Bergene, T. Løvvik, O.M. (1995). Model calculations on a flat-plate solar heat collector with integrated solar cells. *Sol Energy*, 55(6), 453–62.

Meir, M.G. Rekstad, J.B. Løvvik, OM. (2002). A study of a polymer-based radiative cooling system. *Solar Energy*, 73(6), 403–17.

Sandnes, B. Rekstad, J. (2002). A photovoltaic/thermal (PV/T) collector with a polymer absorber plate. Experimental study and analytical model. *Solar Energy*, 72(1), 63–73.

Hayakashi, B. Muzusaki, K. Satoh, T. Hatanaka, T. (1989). Research and development of photovoltaic/thermal hybrid solar power generation system. In: ISES Solar World Congress, Kobe.

Fujisawa, T. Tani, T. (1997). Binary utilization of solar energy with photovoltaic-thermal hybrid collector. In: ISES Solar World Congress, Korea.

Ito, S. Miura, N. Wang, K. (1999). Performance of a heat pump using direct expansion solar collectors. *Solar Energy*, 65(3), 189–96.

Huang, B.J. Lin, T.H. Hung, W.C. Sun, F.S. (1999). Solar photo-voltaic/thermal co-generation collector. In: ISES Solar World Congress, Jerusalem.

Huang, B.J. Lin, T.H. Hung, W.C. (2001). Sun FS. Performance evaluation of solar photovoltaic/thermal systems. *Solar Energy*, 70(5), 443–8.

Garg, H.P. Agarwal, R.K. (1995). Some aspects of a PV/T collector/forced circulation flat plate solar water haeter with solar cells. *Energy Conversation and Management,* 36(2),87–99.

Thomas, H.P. Hayter, S.J. Martin, R.L. Pierce, L.K. (2000). PV and PV/hybrid products for buildings. In: 16th EPSEC, Glasgow.

Krauter, S. Araujo, G. Schroer, S. Hanitsch, R. Salhi, M.J. Triebel, C. (1999). Combined photovoltaic and solar thermal systems for fac-ade integration and building insulation. *Solar Energy*, 67(4–6), 239–48.

Krauter, S. Salhi, M.J. Schroer, S. Hanitsch, R. (2001). New fac-ade system consisting of combined photovoltaic and solar thermal generators with building insulation. In: Seventh IBPSA, Rio de Janeiro, Brazil.

Jai, P. (1994). Transient analysis of a photovoltaic-thermal solar collector for co-generation of electricity and hot air/water. *Energy Conversion and Management*, 35(11), 967-972.

Kim, J. (2012). Comparison of Electrical and Thermal Performances of Glazed and Unglazed PVT Collectors. *International Journal of Photoenergy,* 1(4), 7.

Aste, N. Leonforte, F. Pero, C. (2015). Design, modeling and performance monitoring of a photovoltaic–thermal (PVT) water collector. *Solar Energy,* 112(2), 85–99.

JieJia, H. Tin-tai, C. Hua, Y. Jianping, L. WeiHe, S. (2006). Effect of fluid flow and packing factor on energy performance of a wall-mounted hybrid photovoltaic/water-heating collector system. *Energy and Buildings*, 38(12), 1380-1387.

Saitoh, H. Hamada, Y. Kubota, H. Nakamura, M. Ochifuji, K. Yokoyama, S. (2003). Field experiments and analyses on a hybrid solar collector. *Applied Thermal Engineering,* 23(16), 2089–105.

Minglu, Q. Jianbo, C. Linjie, N. Fengshu, L. Qian, Y. (2016). Experimental study on the operating characteristics of a novel photovoltaic/thermal integrated dual-source heat pump water heating system. *Applied Thermal Engineering,* 94(2), 819–82.

Niccolò, A. Claudio, P. Fabrizio, L. Massimiliano, M. (2016). Performance monitoring and modeling of an uncovered photovoltaic-thermal (PVT) water collector. *Solar Energy,* 135(1), 551–568.

Fudholi, A. Sopian, K. Yazdi, M.H. Ruslan, M.H. Ibrahim, A. Kazem, H.A. (2014). Performance analysis of photovoltaic thermal (PVT) water collectors. *Energy Conversion and Management,* 78(1), 641–651.

Ibrahim, A. Fudholi, A. Sopian, K. Othman, M.Y. Ruslan, M.H. (2014). Efficiencies and improvement potential of building integrated PV thermal (BIPVT) system. *Energy Conversion and Management,* 77(1), 527–34.

Kiran, S. Devadiga, U. (2014). Performance analysis of hybrid PV/Thermal systems. *Int J Emerg Technol Adv Eng,* 4(3),80–6.

Alzaabi, A.A. Badawiyeh, N.K. Hantoush, H.O. Hamid, A.K. (2014). Electrical/thermal performance of hybrid PV/T system in Sharjah, UAE. International. *J Smart Grid Clean Energy,* 3(2), 385–9.

Rosa-Clot, M. Rosa-Clot, P. Tina, G.M. Ventura, C. (2016). Experimental PV-thermal power plants based on TESPI panel. *Solar Energy*, 133(1), 305–14.

Yazdanifard, F. Ebrahimnia-Bajestan, E. Ameri, M. (2016). Investigating the performance of a water-based PV/thermal (PV/T) collector in laminar and turbulent flow regime. *Renewable Energy,* 99(1), 295–306.

Daghigh, R. Ibrahim, A. Jina, G.L. Ruslan, M.H. Sopian, K. (2011). Predicting the performance of amorphous and crystalline silicon based PV solar thermal collectors. *Energy Conversation and Management,* 52(3), 1741–7.

Herrando, M. Markides, C.N. Hellgardt, K. (2014). A UK-based assessment of hybrid PV and solar-thermal systems for domestic heating and power: System performance. *Applied Energy,* 122(1), 288–309.

Madalina, B. Monica, S. George, D. (2023). Performance Analysis and Comparison of an Experimental Hybrid PV, PVT and Solar Thermal System Installed in a Preschool in Bucharest, Romania. *Energies*, 16(14), 5321.

Kegui, L. Qiongwan, Y. Bin, Z. Gang, P. (2023). Performance analysis of a novel PV/T hybrid system based on spectral beam splitting*, Renewable Energy*, 207(5), 398-406.

Dongxing, S. Wenbo, T. Bo, A. Ke, W. (2024). Twofold spectrum split enabling spectral selectivity tailoring and deep temperature decoupling for high exergy efficiency in a concentrating photovoltaic/thermal (PV/T) system, *Energy Conversion and Management,* 303(3), 118153.

Siyan, C. Bin, Z. Qiongwan, Y. Ken, C. Kongfu, H. Gang, P. (2024). Seasonal heat regulation in photovoltaic/thermal collectors with switchable backplate technology: Experiments and simulations, *Renewable Energy*, 224(4), 120139.

Buker, M.S. Mempouo, B. Riffat, S.B. (2014). Performance evaluation and techno-economic analysis of a novel building integrated PV/T roof collector: an experimental validation. *Energy and Buildings,* 76(1), 164–75.

Riggs, B.C. Biedenharnb, R. Dougher, C. (2017). Techno-economic analysis of hybrid PV/T systems for process heat using electricity to subsidize the cost of heat. *Applied Energy,* 208(1), 1370–8.

Wilson, R. Young, A. (1996). The embodied energy PP of photovoltaic installations applied to buildings in the UK. *Building and Environment,* 31(4), 299–305.

Zhang, X. Shen, J. Adkins, D. (2015). The early design stage for building renovation with a novel loop-heat-pipe based solar thermal facade (LHP-STF) heat pump water heating system: Techno-economic analysis in three European climates. *Energy Conversation and Management,* 106(1), 964–86.

Michael, J.J. Selvarasan, I. (2017). Economic analysis and environmental impact of flat plate roof mounted solar energy systems. *Solar Energy*, 142(3), 159–70.

Coventry, J.S. Lovegrove, K. (2003). Development of an approach to compare the 'value' of electrical and thermal output from a domestic Pv/thermal system. *Solar Energy*, 75(5), 63–72.

Tripanagnostopoulos, Y. Souliotis, M. Battisti, R. Corrado, A. (2005). Energy, cost and LCA results of PV and hybrid PVT solar systems. *Progress Photovoltaics,* 13(3), 235–250.

Kalogirou, S.A.,Tripanagnostopoulos, Y. (2007). Industrial application of PVT solar energy systems. *Appl. Therm. Eng*. 27(8–9), 1259–1270.

Mishra, R.K. Tiwari, G.N. (2013). Energy matrices analyses of hybrid photovoltaic thermal (HPVT) water collector with different PV technology. *Solar Energy,* 91(1), 161–173.

Mahmut, S.B. Blaise, M. Saffa, B.R. (2014). Performance evaluation and techno-economic analysis of a novelbuilding integrated PV/T roof collector: An experimental validation. *Energy and Buildings,* 76(2), 164–175.

Ka-Kui, Tse. Tin-Tai, C. Yan, S. (2016). Performance evaluation and economic analysis of a full scalewater-based photovoltaic/thermal (PV/T) system in an office building. *Energy and Buildings,* 122(1), 42–52.

Alba, R. Maria, A.C. Ilaria, G. James, F. Christos, N.M. (2017). Hybrid photovoltaic-thermal solar systems for combined heating, cooling and power provision in the urban environment. *Energy Conversion and Management,* 150(2), 838–850.

Augusto, B. Alessandro, G. Marco, P. Cesare, S. (2017). Photovoltaic/thermal (PV/T) solar system: Experimental measurements, performance analysis and economic assessment. *Renewable Energy,* 111(1), 543-555.

Jacovides, C.P. Tymvios, F.S. Assimakopoulos, V.D. Kaltsounides, N.A. (2016). Comparative study of various correlations in estimating hourly diffuse fraction of global solar radiation. *Renewable Energy,* 31(5), 2492-2504.

Gaurav, P. Lalit, K.K. (2023). Techno-Economic Analysis of Photovoltaci-Thermal (PV/T) in the Perspective of MSME Sector, *PDEU Journal of Energy and Management*, 9(1), 29-35.

Armel, Z.K. Modeste, K.N. Elie, S. Franck, A.T.K. Mahamat, H.B. Boris, A.P.P. Venant, S.C. (2024). Techno-economic and environmental analysis of a hybrid PV/T solar system based on vegetable and synthetic oils coupled with TiO_2 in Cameroon, *Heliyon*, 10(7), e24000.

Mustapha, A.O. Jingyuan, X. Christos, N.M. Yasser, M. (2022). Techno-economic analysis of a hybrid photovoltaic-thermal solar-assisted heat pump system for domestic hot water and power generation, *Renewable Energy,* 196(1), 720-736.

Penaka, S.R. Saini, P.K. Zhang, X. Amo, A. (2020). Digital Mapping of Techno-Economic Performance of a Water-Based Solar Photovoltaic/Thermal (PVT) System for Buildings over Large Geographical Cities. *Buildings*, 10(5), 148-153.

Abdul-Ganiyu, S. Quansah, D.A. Ramde, E.W. Seidu, R. Adaramola, M.S. (2021). Techno-economic analysis of solar photovoltaic (PV) and solar photovoltaic thermal (PVT)

systems using exergy analysis. *Sustainable Energy Technologies and Assessments,* 47(10), 101520.

Rafiq, M.A. Zhang, L. Kung, C.C. (2022). A Techno-Economic Analysis of Solar Energy Developmental Under Competing Technologies: A Case Study in Jiangxi, China. *SAGE*, 12(2), 1-7.

Jurčević, M. Nižetić, S. Čoko, D. Arıcı, M. Hoang, A.T. Giama, E. (2023). Papadopoulos A. Techno-economic and environmental evaluation of photovoltaic-thermal collector design with pork fat as phase change material. *Energy Conversion and Management,* 284(5), 116968.

Patel, G. Khurana, L.K. (2023). Techno-Economic Analysis of Photovoltaic-Thermal (PV-T) in the Perspective of MSME Sector. *PDEU Journal of Energy and Management*, 9(5), 29-35.

Scharmer, K. Greif, J. (2000). European Solar Radiation Atlas, Vol. 1, Fundamentals and Maps', Published for the Commission of the European Communities by Presses de l'Ecole, Ecole des Mines de Paris, France.

Reindl, D.T. Beckman, W.A. Duffie, J.A. (1990). Diffuse fraction correlations, *Solar Energy,* 45(1), 1-7.

Heimrath, R. Haller, M. (2007). Advanced storage concepts for solar and low energy buildings, A Report of IEA Solar Heating and Cooling Programme. Task 32 Report A2 of Subtask A.

https://data.tuik.gov.tr/Bulten/Index?p=Yapi-Izin-Istatistikleri-I.-Ceyrek:-Ocak-Mart,-2024-53750 Accessed 10 June 2024

https://www.mgm.gov.tr/veridegerlendirme/il-ve-ilceler-istatistik.aspx?k=H&m=AKSARAY Accessed 10 June 2024

https://tr.weatherspark.com/y/75995/Strasburg-Mecklenburg-Vorpommern-Almanya-Ortalama-Hava-Durumu-Y%C4%B1l-Boyunca Accessed 10 June 2024

IEA PVPS, Strategic PV Analysis and Outreach Snapshot of Global PV Markets 2021, Report IEA-PVPS T1-39:2021 April 2021

IEA, Turkey 2021 Energy Policy Review, International Energy Agency

EPDK, Energy Market Regulatory Authority 2024 Activity Report.

Izmir Jeotermal, https://izmirjeotermal.com.tr/ucret-tarifeleri-2019-2020-isitma-sezonu. Accessed 04 April 2024.

Tcmb,http://www.tcmb.gov.tr/wps/wcm/connect/TR/TCMB+TR/Main+Menu/Istatistikler/Enflasyon+Verileri/Tuketici+Fiyatlari. Accessed 04 April 2024.

Kalogirou, S.A. Tripanagnostopoulos, Y. (2006). Hybrid PV/T solar systems for domestic hot water and electricity production. *Energy Conversion and Management*, 7(2), 3368–3382.

Rasoul, S. A. Nikoofard, S. Ugursal, V.I. Morrison, I.B. (2017). Techno-economic assessment of photovoltaic (PV) and building integrated photovoltaic/thermal (BIPV/T) system retrofits in the Canadian housing stock. *Energy and Buildings,* 152(2), 667-679.

Gu, Y. Zhang, X. Myhren, J.A. Han, M. Chen, X. Yuan, Y. (2018). Techno-economic analysis of a solar photovoltaic/thermal (PV/T) concentrator for building application in Sweden using Monte Carlo method. *Energy Conversion and Management*, 165/6), 8-24.

Farghally H.M. Ahmed N.M. El-madany N.M. Atia D.M. Fahmy F.H. (2015). Design and Sensitivity Analysis of Photovoltaic/Thermal Solar Collector, *International Energy Journal,* 15(1), 21-32.

Calise, F. Accadia, M.D. Vanoli, L. (2012). Design and Dynamic Simulation of A Novel Solar Trigeneration System Based on Hybrid Photovoltaic/Thermal Collectors (PVT), *Energy Conversion and Management,* 60(1), 214–225.

Anderson, T.N. Duke, M. Morrison, G.L. Carson, K.J. (2009). Performance of A Building Integrated Photovoltaic/Thermal (BIPVT) Solar Collector, *Solar Energy*, 83(1), 445-455.

Green, M. (1998). Solar Cells: Operating Principles, Technology and System Applications, The University of New South Wales, Kensington, Australia.

Ayan, B. Anurag, S. Ravindra, M.P. Sanjiv, K.J. Santosh, G.N. Mukesh, S. (2022). Design, Modelling, and Analysis of Novel Solar PV System using MATLAB, *Materials Today: Proceedings*, 51(1), 756-763.

Amine, A. Shafiqur, R. Mahmut, S.B. Zafar, S. (2023). Recent technical approaches for improving energy efficiency and sustainability of PV and PV-T systems: A comprehensive review, *Sustainable Energy Technologies and Assessments,* 56(1), 103026,

Žižlavský, O. (2014). Net present value approach: method for economic assessment of innovation projects. 19th International Scientific Conference; Economics and Management, 23-25 April 2014, Riga, Latvia

Marchioni, A. Magni, C.A. (2018). Investment decisions and sensitivity analysis: NPV-consistency of rates of return. *European Journal of Operational Research*, 268(1), 361-372.

Heyd, G.T. (2018). The Probabilistic Evaluation of Net Present Value of Electric Power Distribution Systems Based on the Kaldor–Hicks Compensation Principle. *IEEE Transactions on Power Systems,* 33(4), 1-7.

Imteaz, M.A. Ahsan, A. (2018). Solar panels: Real efficiencies, potential productions and payback periods for major Australian cities. *Sustainable Energy Technologies and Assessments*, 25(2), 119-125.

Lawrence, A. Karlsson, M. Nehler, T. Thollander, P. (2019). Effects of monetary investment, payback time and firm characteristics on electricity saving in energy-intensive industry. *Applied Energy*, 240(4), 499-512.

Koç, İ. Başaran K. (2019). PV/T tabanlı bir sistemde MATLAB/Simulink kullanılarak yapılan performans analizi, *Politeknik Dergisi,* 22(1), 229-236

Journal Homepage: https://dergipark.org.tr/tr/pub/isibted

Isı Bilimi ve Tekniği Dergisi

Archive: https://tibtd.org.tr/dergi

Drag Reduction of Truck and Trailer Combination with Different Passive Flow Control Methods

Cihan BAYINDIRLI [1, *], Yahya Erkan AKANSU [2], M. Sahir SALMAN [3]

[1] *Nigde Omer Halisdemir Üniversitesi, Niğde Teknik Bilimler MYO, Motorlu Araçlar ve Ulaştırma Teknolojileri Bölümü, Merkez, 512000, Niğde, Türkiye*
[2] *Nigde Omer Halisdemir Üniversitesi, Mühendislik Fakültesi, Makine Mühendisliği Bölümü, Merkez, 512000, Niğde, Türkiye*
[3] *Gazi Üniversitesi, Teknoloji Fakültesi, Otomotiv Mühendisliği Bölümü, Teknikokullar 06500, Ankara, Türkiye*

A R T I C L E I N F O

2024, vol. 44, no.2, pp. 374-381

doi: 10.47480/isibted.1515727

Research Article
Received: 13 July 2024
Accepted: 24 August 2024

* *Corresponding Author*
e-mail: cbayindirli@ohu.edu.tr

Keywords:
Drag force
Wind tunnel
Passive flow control
Truck-trailer
Drag coefficient

ORCID Numbers in author order:
0000-0001-9199-9670
0000-0003-0691-3225
0000-0000-0000-0000

A B S T R A C T

In this study, drag force and surface pressure measurements were conducted on a 1/32 scaled truck-trailer combination model. The experimental tests were carried out between the ranges of 312×10^3- 844×10^3 Reynolds Numbers in a suction type wind tunnel. The aerodynamic drag coefficient (C_D) and distribution of pressure coefficient (C_P) were experimentally determined for the truck and trailer combination. The regions with a large amount of pressure coefficients were determined on the truck-trailer by using flow visualizations. The aerodynamic structure of truck-trailer combination models was improved by passive flow control methods on 4 different models. By using a newly designed spoiler on Model 1, the drag coefficient was reduced by 10.01 %. On Model 2, after adding a trailer rear extension with a spoiler, the reduction was obtained at 11.35 %. For the model 3 which is obtained by adding a side skirt to model 2, the improvement reached 18.85 %. The model 4 was composed of model 2 and a bellow between the truck and trailer. The drag force improvement was obtained at 22.80 % for model 4.

Çekici Römork Kombinasyonunda Sürükleme Kuvvetinin Farklı Pasif Akış Kontrol Yöntemleri İle Azaltılması

M A K A L E B İ L G İ S İ

Anahtar Kelimeler:
Sürükleme kuvveti
Rüzgar tüneli
Pasif akış kontrolü
Kamyon-treyler
Sürtünme katsayısı

Ö Z E T

Bu çalışmada, 1/32 ölçekli çekici-römork kombinasyon modelinde sürükleme kuvveti ve yüzey basıncı ölçümleri yapılmıştır. Deneysel testler, emme tipi rüzgar tünelinde 312x103- 844x103 Reynolds Sayısı aralığında gerçekleştirilmiştir. Çekici ve römork kombinasyonu için aerodinamik sürükleme katsayısı (C_D) ve basınç katsayısı dağılımları (C_P) deneysel olarak belirlenmiştir. Çekici ve römork üzerinde büyük miktarda basınç katsayısına sahip bölgeler akış görselleştirmeleri kullanılarak belirlenmiştir. Kamyon-treyler kombinasyon modellerinin aerodinamik yapısı, 4 farklı modelde pasif akış kontrol yöntemleri ile iyileştirilmiştir. Model 1'de yeni tasarlanan spoiler kullanılarak sürükleme katsayısı % 10,01 oranında azaltılmıştır. Model 2'de, spoylerli bir treyler arka uzantısı eklendikten sonra sürükleme katsayısı % 11,35 oranında azaltılmıştır. Model 2'ye yan etek eklenerek elde edilen Model 3'te iyileştirme % 18,85'e ulaşmıştır. Model 4, model 2 ve kamyon ile treyler arasında bir körükten oluşuyordu. Model 4 için sürtünme kuvveti iyileştirmesi %22,80 olarak elde edildi.

NOMENCLATURE

C_D	Drag coefficient
C_P	Pressure coefficient
Re	Reynolds number
CFD	Computational fluid dynamics
Afc	Active flow control
Pfc	Passive flow control
Fsv	Free stream velocity
A	Frontal area of model vehicle, m^2
F_D	Drag force, (N)
Exp.	Experimental
$U\infty$	Free flow velocity, m/s
s	Spoiler
s+re	Spoiler+rear extension
s+re+ss	Spoiler+rear extension+side skirt

INTRODUCTION

The control of flow around of ground vehicles is the main research and development subject of automotive designers and researchers. The aerodynamic properties of vehicles are directly related to fuel consumption, energy balance and emissions. It is very important to examine the flow structures around the vehicles using both experimental and numerical methods and to optimize the vehicles in terms of aerodynamics. Aerodynamic drag force is directly proportional to vehicle speed. Therefore, drag force is of great importance in terms of fuel consumption, engine performance and emissions in vehicles that drive at high speeds. The subject of this study was used at high vehicle speeds between the cities and drove thousands of kilometers in a year. Aerodynamic drag force in trucks and trailers is mainly due to pressure. It is very advantageous in terms of production cost and time to determine the aerodynamic situation, flow separations, forces and moments that act on the vehicles quickly, easily and at a low cost, without producing the prototype of the vehicles in real dimensions by using computer software based on digital fluid dynamics or in a wind tunnel. The summaries of some experimental and CFD studies in the literature are presented below. The drag force which is based on pressure forms a large percent of total drag force particularly on the front surface of road vehicles (Bayindirli et al. 2015). Vehicle performance, energy consumption and traction exhaust emissions are directly related to aerodynamic specifications. Moreover, ventilation, vehicle noise, engine life, and heating and cooling systems of vehicles have been affected by aerodynamic forces (Bayindirli et al. 2016, Wahba et al. 2012, Gilhaus, 1981 and Chowdhury et al. 2013) Vehicle speed is the critical factor determining aerodynamic force (Miralbes, 2012, Cengel and Cimbala, 2008 and Sahin, 2008) . Therefore improving of aerodynamic force of heavy vehicles is very important for transportation costs. 60% of engine power is spent to overpower drag forces at 100 km/h for a passenger car (Wood and Bauer, 2003). Thanks to flow control methods in vehicles, remarkable improvement rates in fuel consumption have been achieved (Bayindirli et al. 2020, Hu and Wong, 2011 and Lokhande et al. 2003). There are two approaches to flow control around vehicles. Perzon and Davidson (2000) obtained a 4-7% aerodynamic improvement in a study. The coefficient was reduced by 7% by using a chassis skirt. 1/24 scaled model cars model were investigated in wind tunnel. The drag coefficients of cars were found between the rates of 14%-7.8% deviation according to real car models (Solmaz, 2010). The influence of windshield angle on drag coefficient was investigated in a study. As angle increased coefficient decreased on a commercial vehicle (Sari, 2007). The C_D of a truck trailer mode was reduced by 12.5% and 28% using vertical and horizontal spoiler by Modi et al (1995). The C_D value of the truck and trailer was determined 0.6 in another study (Mccallen et al. 2000). This result supports the accuracy of this experimental study. 20% drag minimization be obtained by flow control on trucks and trailers (Ogburn and Ramroth, 2007) The effect of spoiler design as a passive flow control element on aerodynamic drag coefficient was investigated on a 1/8 scale truck- trailer model by CFD method and wind tunnel experiments. The aerodynamic drag coefficients were improved up to 19% in the 5.5×10^5 Reynolds number by different spoiler models (Jeong et al. 2017). The C_D values of a truck model were calculated under an average 7.1° yaw axis experimentally and numerically. They used MATLAB Simulink program as a numerical calculation method. The drag coefficient was calculated on average at 0.77 after the result of the numerical analysis and 0.805 after the experimental method (Barden and Gerova 2016). Pickup and sedan cars were analyzed under laminar flow, turbulent flow, and boundary layer flow at different wind angles (Liu et al. 2016). The drag force and flow structure of a truck-trailer combination were examined in CFD. The C_D value of the truck trailer was decreased by 21% with some pfc components which are spoiler, afterbody and vortex generator (Chilbule et al. 2014). Pfc includes modification of vehicles or attachment of some parts to decrease the drag force. They have significant advantages compared to afc because they are cheaper and consume no energy from the engine (Altaf et al. 2014). The large drag force due to the vehicle geometry forms pressure-based drag which is the main contributor to total drag. According to Hucho and Sovran (1993), about 50% of vehicle's the fuel consumption results from this pressure-based drag at high vehicle speeds. CFD analysis was made of SUV model and ~~it~~ it was modified by attaching some kinds of pfc parts such as a lip kit to the bumper. According to the base model car, the pressure increased by about 3.5%, the velocity by 3%, the lift force 50.6% and the drag force by 5.8% in the modified SUV ground vehicle model (Yadav et al. 2021). In another study, dimples on a bus model were carried out numerically and experimentally. The dimple position, dimple number and, dimple orientation were tested to understand their effect on drag. It has been recommended that this method is effective in decreasing of drag force (Chen et al. 2021). In another study, the superior aerodynamic structure of tuna was investigated using an experimental method. 3 types of bionic surfaces were produced by inspired tuna fish. The effect of these surfaces reduced drag force. It was seen that a 7.22% drag reduction was achieved on the dual structure coupling surface. Using jet devices such as afc is a promising approach for reducing drag for vehicles. A CFD study was performed for afc around the Ahmed body model. Comparing three different actuation strategies was researched according to the height of the vehicle. It was shown that variations in the shear layer occured during the

blowing phase. The change in flow topology occurs with synthetic jets and suction. Because of this situation, rear-back pressure substantially advanced (Edwige et al. 2022).

This study focuses on reducing of C_D of truck-trailer combinations. Various unique pfc components were developed to obtain lower F_D. The effect of these parts on the F_D was experimentally investigated. Between the rates of 10.01% and 22.80%, drag reduction was achieved. The original part of the study is the drag reduction with the original developed parts and its effect on fuel consumption. The main difference of this study from the studies in the literature is the aerodynamic improvement rate provided by the passive flow control parts developed for this truck model produced in Türkiye. In addition, the study recommends factors to consider when choosing a trailer for a truck model and reveals the possible impact of the improvement in aerodynamic drag force provided by passive flow control methods on the country's fuel imports.

MATERIALS AND METHOD

Experimental setup

The aerodynamic tests were conducted in a suction type wind tunnel as seen in Fig. 2a-b. The size of the test area is 40cm x 40cm x 100cm. The free stream speed was controlled to in the test area with a frequency inverter. It runs between 0Hz and 50Hz and 0.1 Hz steps. The 4000 W-powered fan axial fan motor was used to obtain fsv. A six-component load cell was used to measure Fx and Fy forces up to ± 32N and Fz force up to ± 100N. The load cell measures moments (Mx-My-Mz) in the range of ± 2.5Nm. In studies, turbulence intensity was lower than 1% in the wind tunnel. The maximum fsv was 28 m/s. To ensure kinematic similarity, the blocking rate was 6.31% in test area. The experimental setup and wind tunnel were presented in Fig. 1.

In wind tunnel tests, the model vehicle was positioned on a solid stable ground. This plate is fixed on airfoil legs, 5 cm above the ground. It is connected to the load cell by a shaft. Thus, the vehicle is affected by the free flow velocity in the fully developed flow region. The drag force acting on the plate at each test speed was determined and this value was subtracted when calculating the net drag force values of the vehicle.

Fig. 1. Experimental setup

As seen in Fig. 2a and 2b total of 32 taps were formed on symmetry axis of the truck trailer. 13 taps were on the truck and 19 taps were on the trailers to conduct pressure measurement.

Fig.2a. The locations of the pressure probes on model vehicle

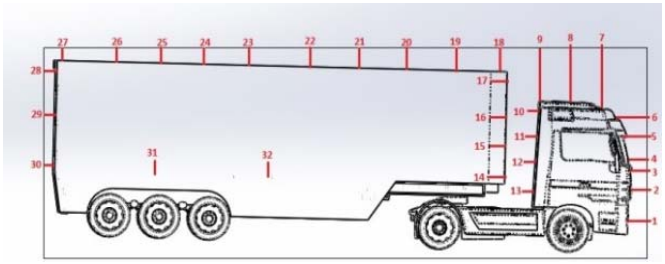

Fig.2b. The locations of the pressure probes on model vehicle

The tests of pressure measurements were made between the range of 89 000 - 286 000 Re for the truck. It was carried out in the range of 253 000 - 794 000 Re for the truck-trailer combination. The dynamic pressure was measured from the pressure taps at the inlet and outlet of the contraction cone of the wind tunnel. Two differential-type pressure converters were used in the tests. It was an Omega PX163-2.5BD5V model. The output voltage of 0V-5V detection time was 1 millisecond. The pressure transducers were calibrated before the pressure measurements. 800 values were taken in a second to calculate surface pressure. These values are below the pressure transducer detection time capacity (1000 Hz). In total 16384 values were taken for each measurement in 20.48 seconds. The dynamic pressure is the difference between the static pressure and the total pressure (Bayindirli et al 2016).

$$P_{dyn} = P_{total} - P_{st} \quad (1)$$

$$P_{dyn} = \tfrac{1}{2} \rho V \quad (2)$$

$$C_P = \frac{\Delta P}{\tfrac{1}{2} \rho V^2 A} \quad (3)$$

In wind tunnel tests, room temperature, the pressure of the atmosphere, the dynamic pressure and fsv were gauged with digital micromanometer (Manoair 500 model).

The C_D is expressed with the parameters of fsv (V) force (F_D), air density (ρ), and frontal area of the vehicle (A).

$$C_D = \frac{F_D}{\tfrac{1}{2} \rho V^2 A} \quad (4)$$

The force measurement tests were conducted on 6 different free stream velocities (5, 10, 15, 20, 25, and 27 m/s). The 2 results were calculated per second in 1 minute. The C_D values were calculated based on these 120 results.

Similarity Conditions

Three similarity conditions must be provided to ensure the accuracy of test results. In this study, a licensed model car was used to obtain geometric similarity. The kinematic

similarity is related to the blockade ratio in the wind tunnel test area. It is explained as the ratio of vehicle frontal area to test section surface area. The blockade ratio was 6.31%. As seen in this experimental study, and it is recommended in literature that it must be below the 7.5 % (Cengel and Cimbala, 2008). As shown in Fig.3, Reynolds independency tests were conducted to provide dynamic similarity with this study. The fully turbulent free stream velocities were determined, and related tests were carried out after Reynolds independency.

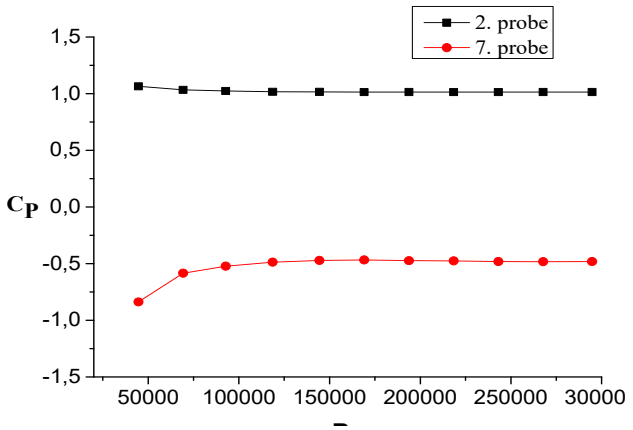

Fig. 3. Reynolds independency in tests (Bayindirli et al. 2016)

Uncertainty Analyses of Measured Parameters

Uncertainty rate of Reynolds number was obtained as 3.87% in Eq. 5.

$$u_{Re} = \frac{w_{Re}}{Re} = \left[(u_\rho)^2 + (u_{Pitot})^2 + (u_H)^2 + (u_\mu)^2\right]^{1/2} \quad (5)$$

The drag force uncertainty was acquired as 4.5% in 10 m/s and 312×10³ Reynolds Number in Eq. 6.

$$\frac{w_{F_D}}{F_D} = \left[\left(\frac{w_{X_1}}{X_1}\right)^2 + \left(\frac{w_{X_2}}{X_2}\right)^2 + \left(\frac{w_{X_3}}{X_3}\right)^2 + \left(\frac{w_{X_4}}{X_4}\right)\left(\frac{w_{X_4}}{X_4}\right) + \left(\frac{w_{X_5}}{X_5}\right)^2\right]^{1/2} \quad (6)$$

The uncertainty value of C_D was calculated as 4.7% by writing related parameters such as F, ρ, and A arguments in Eq. 7.

$$u_{C_D} = \frac{w_{C_D}}{C_D} = \left[(u_{F_D})^2 + (u_\rho)^2 + 4(u_{pitot})^2 + (u_A)^2\right]^{1/2} \quad (7)$$

The C_P uncertainty was calculated as 2.11% in Eq.8.

$$u_{C_P} = \frac{w_{C_P}}{C_P} = \left[(u_{\Delta_P})^2 + (u_\rho)^2 + 4(u_{pitot})^2\right]^{1/2} \quad (8)$$

RESULTS AND DISCUSSION

The CP distribution on model vehicle

The aerodynamic force of the base truck trailer was determined by Bayindirli et. al. (2016). This study aims to improve the drag force of the base model truck trailer. Take into consideration the pressure coefficient (C_P) distributions in Fig 4. Passive flow control parts were developed to decrease pressure-based drag force. There is a negative pressure area at the rear between the truck-trailer and the rear of trailer.

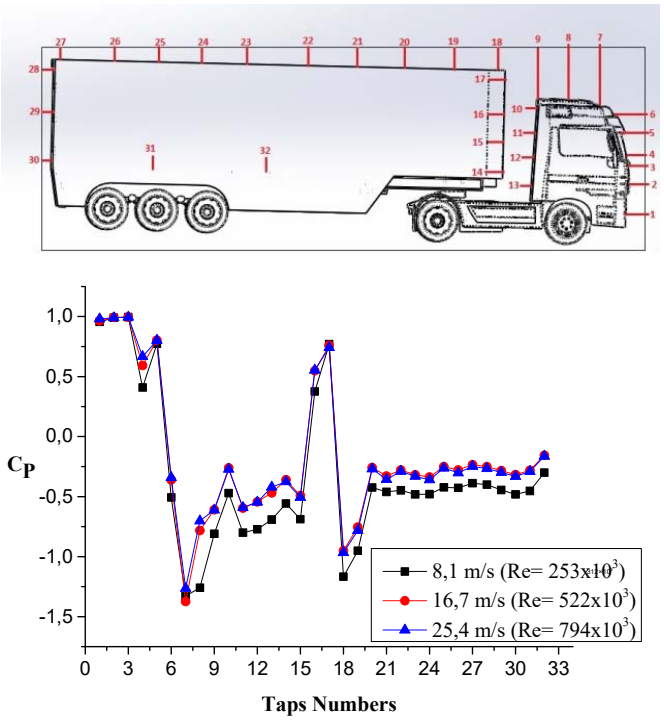

Fig. 4. The CP distributions on base model truck-trailer (Bayindirli et al. 2016)

The drag force measurements

The average C_D of the base model was determined to be 0.704, as seen in Table 1 and Fig 5. The addition of the trailer to the truck increased the drag coefficient (C_D) by 15.8%. The C_P is very high on 17th and 18th probes. There is a huge amount of pressure-based drag force in that area. The aerodynamic structure of model vehicle and flow separation were determined by flow visualization in Fig 6.

Table 1. The C_D values of base model /Bayindirli et al. 2016)

Re	Aerodynamic Drag Force (N)	Base Model C_D
3.12×10⁵	0.467	0.707
4.69×10⁵	1.036	0.697
6.25×10⁵	1.889	0.714
7.81×10⁵	2.917	0.706
8.44×10⁵	3.359	0.697

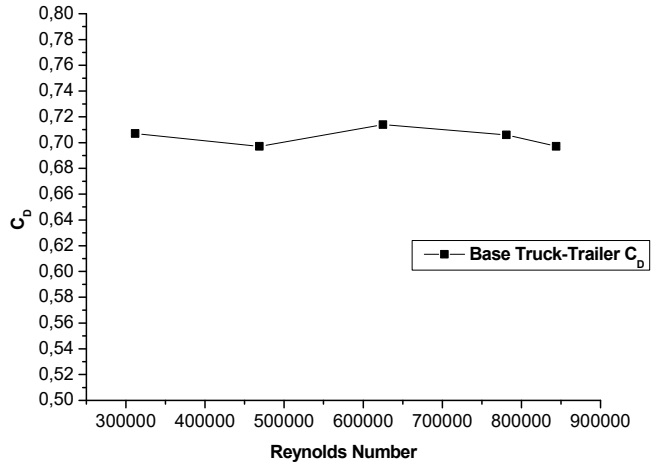

Fig. 5. C_D graph of base truck-trailer model according to Reynolds Number

Fig.6. Flow separations around base model truck-trailer (Bayindirli et al. 2016)

Passive flow control technique

A certain flow structure prevails around the object in the flow medium. The process of removing this flow structure from the normal flow structure is called flow control. Depending on the amount of energy consumed there are two methods flow control. These are named pfc and afc. In pfc method, there is no energy consumption from the vehicle, and this situation provides a big advantage compared to afc. Generally, the geometry of vehicles is optimized with some parts in order to gain better aerodynamic structure in pfc.

Drag reduction with spoiler (Model 1)

After the pressure coefficient distributions were determined that the C_P value was found to be high for the tap number of 17. The vehicles with the standard spoiler pressure coefficient in this region (15., 16., and 17. taps) were obtained to be close to the stagnation pressure like on the front bumper.

A spoiler model was produced with 30° inclination angle to reduce drag force in this area. The truck and trailer combination with newly designed spoiler is given in Fig.7. As shown in Table 2. the wind tunnel tests were conducted in 5 different Re numbers and average C_D was calculated as 0.633 of model 1 (truck and trailer). The C_D of the base truck-trailer model was 0.704.

Fig. 7. Model 1 truc k-trailer

Table 2. The C_D values of Model 1

Re	Aerodynamic Drag Force (N)	Model 1 C_D
3.12×10^5	0.57	0.613
4.69×10^5	1.332	0.65
6.25×10^5	2.338	0.637
7.81×10^5	3.579	0.63
8.44×10^5	4.222	0.638

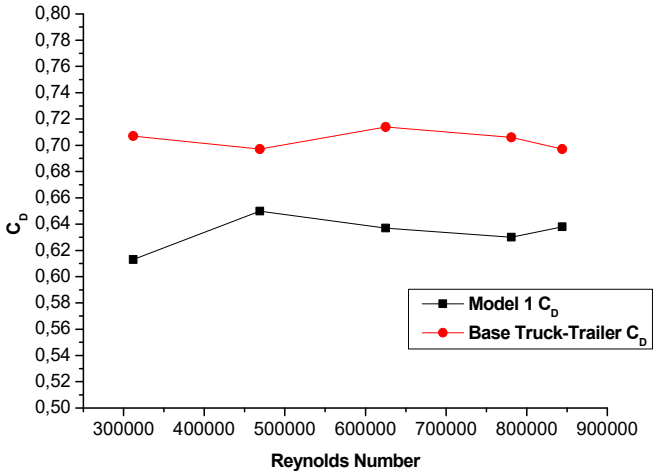

Fig. 8. C_D graph of base truck-trailer model-Model 1 according to Reynolds Number

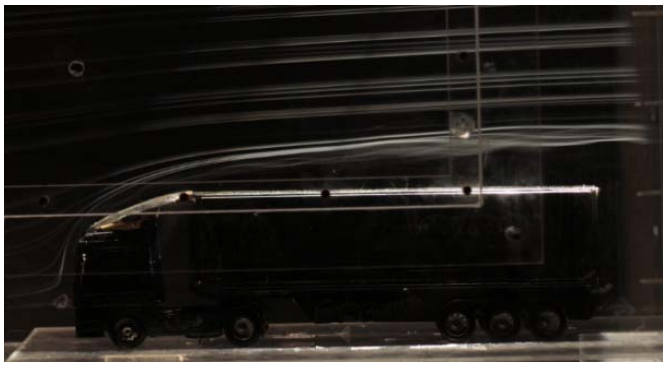

Fig.9. Flow visualization of model 1

As seen in Fig. 4, the flow that affects the upper front region of the trailer (17. taps) was redirected to upper part of the trailer (18., 19., and 20. taps) by the newly designed spoiler. Hence pressure-based drag force was reduced by 10.01% on average.

Drag reduction with spoiler and trailer rear extension (Model 2)

A large amount of negative pressure occurs in rear of the trailers. In truck-trailer combinations, a significant amount of total aerodynamic originates from this negative pressure area. In model 2, it was aimed to create a smaller negative pressure area behind the trailer. A rear trailer extension is designed and added to model 1 truck trailer to obtain aerodynamic improvement. Model 2 truck-trailer and designed rear trailer extension are given in Fig.10.

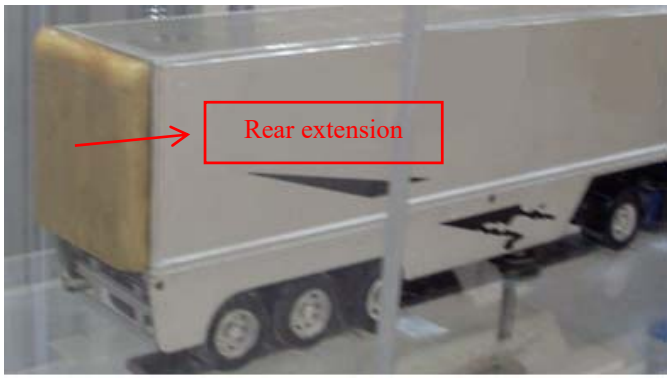

Fig. 10. Model 2 truck-trailer

As seen in Table 3 and Fig 10, the C_D was obtained as 0.624 for model 2. The obtaining aerodynamic improvement obtained was 11.35% with the newly designed spoiler and rear trailer extension (model 2). The aerodynamic improvement gained was 1.35% for rear trailer extension only.

Table 3. The C_D values of Model 2

Re	Aerodynamic Drag Force (N)	Model 2 C_D
3.12×10^5	0.405	0.612
4.69×10^5	0.928	0.624
6.25×10^5	1.672	0.632
7.81×10^5	2.573	0.623
8.44×10^5	3.034	0.630

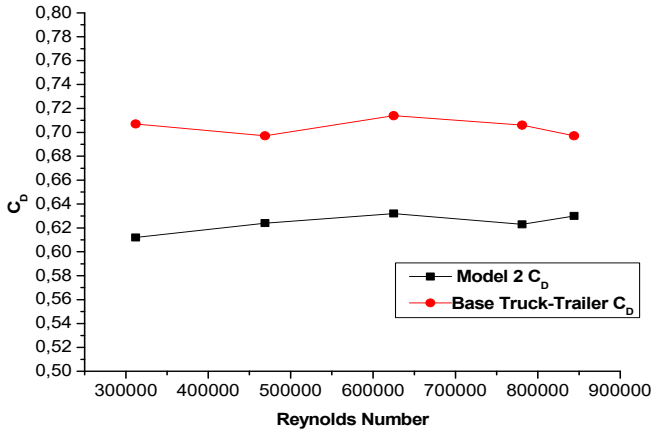

Fig. 10. C_D graph of base truck-trailer model-Model 2 according to Reynolds Number

Drag reduction with spoiler, trailer, rear extension and side skirt (Model 3)

The wheels may cause 5% of the total drag on the truck-trailer combination (Bayindirli et al. 2015). The trailer wheels of model 2 vehicle were closed with side skirt as presented in Fig.11.

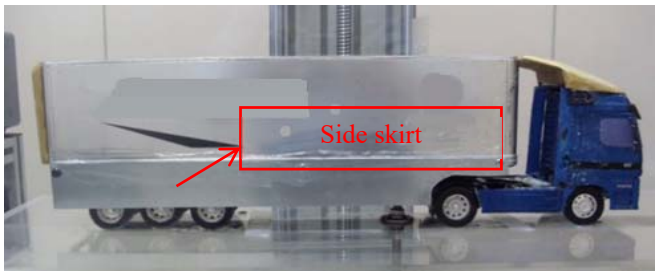

Fig.11. Model 3 truck-trailer

As shown in Table 4. and in Fig 12, the C_D was reduced to 0.571 in model 3 truck and trailer. Consequently the aerodynamic improvement attained was18.85% by of the newly designed spoiler. rear trailer extension and side wind skirt (model 3). By using only side skirt, a 7.5% aerodynamic improvement was obtained.

Table 4. The C_D values of Model 3

Re	Aerodynamic Drag Force (N)	Model 3 C_D
3.12×10^5	0.387	0.586
4.69×10^5	0.842	0.566
6.25×10^5	1.482	0.56
7.81×10^5	2.298	0.556
8.44×10^5	2.832	0.558

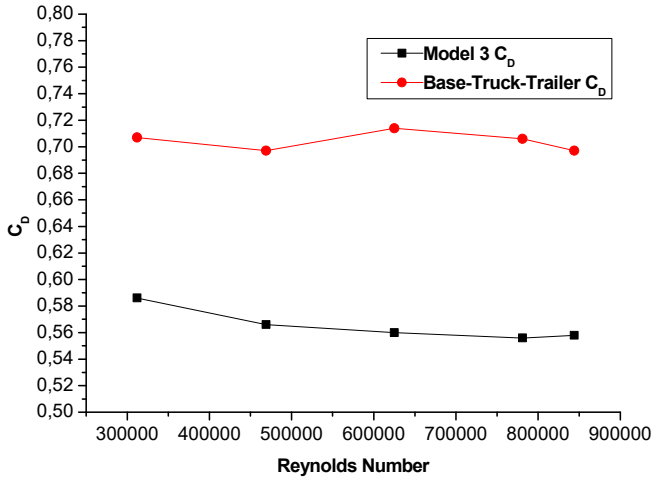

Fig. 12. C_D graph of base truck-trailer model-Model 3 according to Reynolds Number

Drag reduction with spoiler, trailer rear extension and bellow (Model 4)

In experimental studies, negative pressure was formed in the gap between the trailer and the truck. As presented in the Fig.13, gap between the truck and the trailer of model 2 was closed with a bellows in this aerodynamic improvement study. It was aimed at providing an aerodynamic improvement by using bellow to prevent inflow between the truck and the trailer.

Fig. 13. Model 4 truck and trailer

The C_D value was calculated as 0.543 for model 4 truck-trailer as shown in Table 5 and Fig 14. According to the base model total aerodynamic improvement was 22.80% with a spoiler, trailer rear extension and bellow. The aerodynamic improvement rate achieved was 11.45% by only adding bellow.

Table 5. The C_D values of Model 4

Re	Aerodynamic Drag Force (N)	Model 4 C_D
3.12×10^5	0.36	0.544
4.69×10^5	0.821	0.552
6.25×10^5	1.422	0.538
7.81×10^5	2.249	0.544
8.44×10^5	2.602	0.54

The aerodynamic modification of vehicle geometry ensures drag reduction. It contributes to decreasing of fuel consumption of vehicles. Vehicle body outlines, spoilers, after-body parts, diffusers, side skirts etc. are examples of body modification in vehicles. These applications on vehicles improve stability and increase downward forces (Marklund et al. 2013).

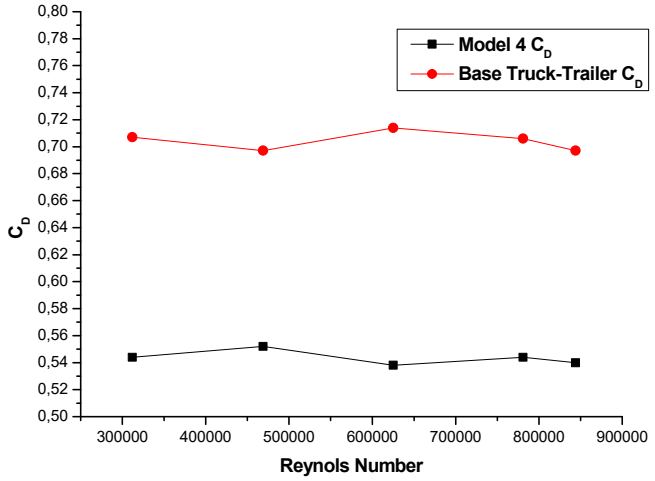

Fig. 14. C_D graph of base truck-trailer model-Model 4 according to Reynolds Number

Keeping the flow at the surface, delaying flow separation, and reducing the negative pressure area reduce the pressure-induced drag force (Yanqing et al. 2023, Edwige et al. 2022 and Altaf et al. 2022) As seen in Fig.15., by using 4 different passive flow control parts respectively 10.01%. 11.35%. 18.85%. 22.80%, respectively, aerodynamic improvement was obtained.

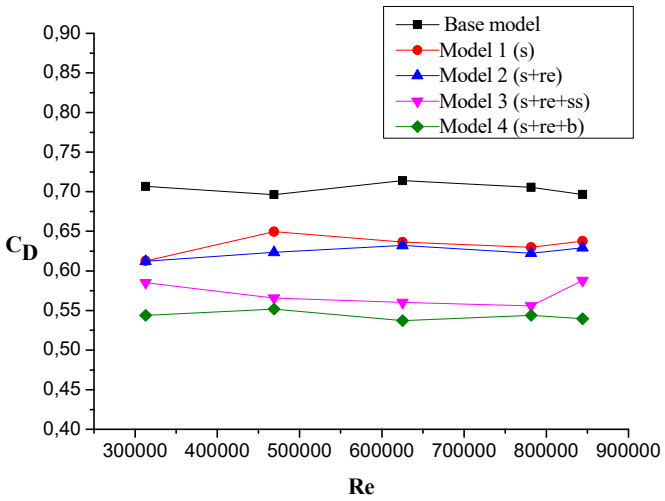

Fig.15. The C_D comparison graph of base model, model 1, model 2, model 3, model 4

When the C_D was reduced by 2% and fuel consumption was reduced by 1% at high speeds for road vehicles. Trucks and trailers are extensively used in intercity freight transportation. These vehicles drive at high speeds. Aerodynamic forces are of great importance when the vehicle speed exceeds 50 km. The vehicle's engine consumes extra fuel to overcome this aerodynamic force. These vehicles also travel many kilometers each year. The maximum drag reduction rate was 22.80% in this study. The 22.80% aerodynamic improvement can reduce fuel consumption by 12%. Assuming that, a truck trailer travels an average of 100.000 kilometers annually and consumes 25 liters for every 100 kilometers. The annual fuel consumption of a vehicle will be 25.000 liters. Thanks to the aerodynamic improvement provided by these passive flow control methods, this vehicle can consume 12% less fuel per year. This means that each car will consume 3000 liters less fuel annually. This aerodynamic improvement will reduce transportation costs and reduce exhaust emissions from engines.

CONCLUSIONS

A summary of this wind tunnel experiments was presented below.

- ✓ A standard trailer addition on the truck model increased the drag coefficient of the truck (C_D) by 15.80%.
- ✓ In model 1, a 10.01% drag reduction was obtained by the newly designed spoiler. This drag reduction rate reduces fuel consumption by 5%. This result has revealed the importance of suitable spoiler selection and design in truck trailers.
- ✓ The C_D was reduced by 11.35% with the newly designed spoiler and rear trailer extension in model 2.
- ✓ 18.85% drag reduction was obtained by the newly designed spoiler, rear trailer extension and side skirt in model 3.
- ✓ The maximum aerodynamic improvement ratio was 22.80% in model 4. According to the literature, this drag reduction rate can reduce fuel consumption of truck trailer by about 12 % over at 96 km/h.

It is recommended, as a result of this study that 4 pfc methods can be applied at the same time to aerodynamically improve of the truck-trailers

REFERENCES

Altaf A., Omar A., and Asrar1 W. (2022). Passive Drag Reduction of the Square Back Truck Body. International Journal of Automotive and Mechanical Engineering, 19-3, 9892- 9908.

Altaf A., Omar A., and Asrar W. (2014). Review of passive drag reduction techniques for bluff road vehicles. IIUM Engineering Journal, 15(1). 61-69.

Barden J., and Gerova K. (2016). An On-Road İnvestigation İnto The Conditions Experienced By A Heavy Goods Vehicle Operating Within The United Kingdom. Transportation Research Part D, 48. 284–297.

Bayindirli C., Akansu Y.E., Celik M. (2020). Experimental And Numerical Studies On Improvement Of Drag Force Of A Bus Model Using Different Spoiler Models. Int. J. Heavy Vehicle Systems, 27-6. 743-776.

Bayindirli C., Akansu Y.E., Salman M.S., Colak D. (2015). The Numerical Investigation Of Aerodynamic Structures Of Truck And Trailer Combinations. International Journal Of Automotive Engineering And Technologies, 4-3. 139 – 145.

Bayindirli C., Akansu Y.E., Salman, M.S. (2016). The Determination Of Aerodynamic Drag Coefficient Of Truck And Trailer Model By Wind Tunnel Tests. International Journal Of Automotive Engineering And Technologies, 5-2. 53 – 60.

Cengel A.Y., and Cimbala J.M. (2008). Fluid Mechanics Fundamentals And Applications, Güven Bilimsel.

Chen D., Chen H., and Cui X. (2022). Dual-coupling drag reduction inspired by tuna skin: Fan-shaped imbricated fish

scale composited with flexible coating. AIP Advances 12, 035218 doi: 10.1063/5.0066195

Chilbule C., Upadhyay A., Mukkamala Y. (2014). Analyzing The Profile Modification Of Truck-Trailer To Prune The Aerodynamic Drag And Its Repercussion On Fuel Consumption. Procedia Engineering, 97. 1208 – 1219.

Chowdhury H., Moria H., Ali A., Khan I., Alam F., and Watkins S. (2013). A Study On Aerodynamic Drag Of A Semi-Trailer Truck. 5th Bsme International Conference On Thermal Engineering. 56. 201–205.

Edwige S., Gilotte P., Mortazavi, I. (2022). Computational Analysis of Actuation Techniques Impact on the Flow Control around the Ahmed Body. Fluids, 7, 52,doi.org/10.3390/ fluids

Gilhaus A. (1981). The Influence Of Cab Shabe On Air Drag Of Trucks. Journal Of Wind Engineering And Industrial Aerodynamics, 9. 77-87.

Hu X.X., and Wong E.T.T. (2011). A Numerical Study On Rear-Spoiler Of Passenger Vehicle. World Academy Of Science, Engineering And Technology, 57. 636-641.

Hucho W.H., and Sovran G. (1993). Aerodynamics of road vehicles. Annual Review of Fluid Mechanics, 25(1). 485-537.

Jeong J.K., Sangseung L., Myeongkyun K., Donghyun Y., Sang J.L. (2017). Drag Reduction Of A Heavy Vehicle Using Modified Cab-Roof Fairings. Journal Of Wind Engineering & Industrial Aerodynamics, 164. 138–151.

Liu X., Han Y., Cai C.S., Levitan M., and Nikitopoulos D. (2016). Wind Tunnel Tests For Mean Wind Loads On Road Vehicles. Journal Of Wind Engineering & Industrial Aerodynamics, 150. 15–21.

Lokhande B., Sovani S., and Khalighi B. (2003). Transient Simulation Of The Flow Field Around A Generic Pickup Truck. Sae Technical Paper Series, 01-1313. 1- 19.

Marklund J., Lofdahl L., Danielsson H., and Olsson G. (2013). Performance of an automotive under-body diffuser applied to a sedan and a wagon vehicle. SAE International Journal of Passenger Cars, 6(1). 293-307.

Mccallen R., Flowers, D., Owens T.D., Owens J., Browand F., Hammache M., Leonard A., Brady M., Salari K., Rutledge W., Ross J., Storms B., Heineck J.T., Driver D., Bell J., Walker S., and Zilliac G. (2000). Aerodynamic Drag Of Heavy Vehicles Class 7-8: Simulation And Benchmarking, Sae Technical Paper Series, 01-2209. 1-19.

Miralbes R. (2012). Analysis Of Some Aerodynamic Improvements For Semi-Trailer Tankers. Proceedings Of The World Congress On Engineering 3, 4-6 July. London U.K.

Modi V.J., Hill S.St., and Yokomimizo T. (1995). Drag Reduction Of Trucks Through Boundary-Layer Control. Journal Of Wind Engineering And Industrial Aerodynamics, 54/55. 583-594.

Ogburn M.J., and Ramroth L.A. (2007). A Truck Efficiency And Ghd Reduction Opportunities In The Canadian Truck Fleet (2004-2007), Rocky Mountain Instutue Report, Canadian. 1-13.

Palanivendhan M., Chandradass J., Saravanan C., Philip J., and Sharan R. (2021). Reduction in aerodynamic drag acting on a commercial vehicle by using a dimpled surface. Materials Today: Proceedings, 45, 7072–7078.

Perzon S., and Davidson L. (2000). On Transient Modeling Of The Flow Around Vehicles Using The Reynolds Equation, International Conference On Applied Computational Fluid Dynamics (Acfd), Beijing China. 720-727.

Sahin C. (2008). Prediction Of Aerodynamic Drag Coefficient For Heavy Vehicles With Computational Fluid Dynamics Method, İstanbul Technical Universty. Institute Of Science And Technology, Master Thesis. 3-21.

Sari M.F. (2007). The Aerodynamic Analysis Of Air Resistance Affecting The Front Form Of Light Commercial Vehicles And Its Effect On Fuel Consumption, Osmangazi University. Institute Of Science And Technology. Master Thesis. Eskişehir. 28-54.

Solmaz H. (2010). Determination Drag Coefficient Of Different Vehicle Models In A Wind Tunnel. Gazi University. Institute Of Science And Technology. Master Thesis. Ankara. 43-47.

Wahba C. E. M., Al-Marzooqı H., Shaath M. Shahın., and El Dhamashawy T. (2012). Aerodynamic Drag Reduction For Ground Vehicles Using Lateral Guide Vanes. Cfd Letters. 4-2. 68-78.

Wood R.M., and Bauer S.X.S. (2003). Simple And Low Cost Aerodynamic Drag Reduction Devices For Tractor-Trailer Trucks. Sae Technical Paper, 01–3377. 1-18

Yadav R., Islam A., Chaturvedi, R. (2021). Efficient reduction of the consumption of fuel in road vehicles using aerodynamic behavior in CDF analysis. Materials Today: Proceedings 45, 2773–2776

Yanqing W., Ding W., Yuju W., Yuan M., Lei C., and Jiadao, W. (2023). Aerodynamic Drag Reduction on Speed Skating Helmet by Surface Structures. Applied Sciences, 13, 130, doi.org/10.3390/app1301013

TÜRK ISI BİLİMİ VE TEKNİĞİ DERNEĞİ

TURKISH SOCIETY FOR THERMAL SCIENCE AND TECHNOLOGY

TIBTD